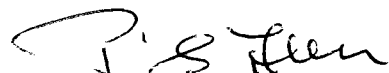


**University of Alberta**

**Faculty of Graduate Studies and Research**

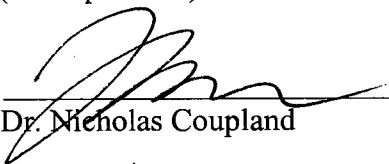
The undersigned certify that they have read, and recommend to the Faculty of Graduate Studies and Research for acceptance, a thesis entitled *In-Vivo Methodologies of <sup>13</sup>C NMR Spectroscopy* submitted by **Atiyah Yahya** in partial fulfillment of the requirements for the degree of **Doctor of Philosophy in Medical Sciences - Biomedical Engineering**.



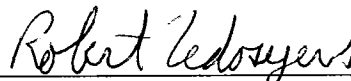
Dr. Peter S. Allen  
(Co-supervisor)



Dr. Abdulhakem Elezzabi  
(Co-supervisor)



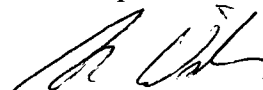
Dr. Nicholas Coupland



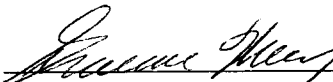
Dr. Robert Fedosejevs



Dr. Christopher C. Hanstock



Dr. Alan H. Wilman



Dr. Graeme F. Mason  
(External Examiner)

DATE: *January 8, 2006*

*“And walk not on the earth with conceit and arrogance. Verily, you can neither rend nor penetrate the earth, nor can you attain a stature like the mountains in height.”*

*The Holy Quran, chapter 17, verse 37*

University of Alberta

*IN-VIVO* METHODOLOGIES OF  $^{13}\text{C}$  NMR SPECTROSCOPY

by

Atiyah Yahya



A thesis submitted to the Faculty of Graduate Studies and Research in partial fulfillment of the requirements for the degree of **Doctor of Philosophy**

in

Medical Sciences - Biomedical Engineering

Department of Electrical and Computer Engineering

Edmonton, Alberta  
Spring 2006



Library and  
Archives Canada

Bibliothèque et  
Archives Canada

Published Heritage  
Branch

Direction du  
Patrimoine de l'édition

395 Wellington Street  
Ottawa ON K1A 0N4  
Canada

395, rue Wellington  
Ottawa ON K1A 0N4  
Canada

*Your file* *Votre référence*

*ISBN: 0-494-14066-6*

*Our file* *Notre référence*

*ISBN: 0-494-14066-6*

#### NOTICE:

The author has granted a non-exclusive license allowing Library and Archives Canada to reproduce, publish, archive, preserve, conserve, communicate to the public by telecommunication or on the Internet, loan, distribute and sell theses worldwide, for commercial or non-commercial purposes, in microform, paper, electronic and/or any other formats.

The author retains copyright ownership and moral rights in this thesis. Neither the thesis nor substantial extracts from it may be printed or otherwise reproduced without the author's permission.

#### AVIS:

L'auteur a accordé une licence non exclusive permettant à la Bibliothèque et Archives Canada de reproduire, publier, archiver, sauvegarder, conserver, transmettre au public par télécommunication ou par l'Internet, prêter, distribuer et vendre des thèses partout dans le monde, à des fins commerciales ou autres, sur support microforme, papier, électronique et/ou autres formats.

L'auteur conserve la propriété du droit d'auteur et des droits moraux qui protègent cette thèse. Ni la thèse ni des extraits substantiels de celle-ci ne doivent être imprimés ou autrement reproduits sans son autorisation.

---

In compliance with the Canadian Privacy Act some supporting forms may have been removed from this thesis.

Conformément à la loi canadienne sur la protection de la vie privée, quelques formulaires secondaires ont été enlevés de cette thèse.

While these forms may be included in the document page count, their removal does not represent any loss of content from the thesis.

Bien que ces formulaires aient inclus dans la pagination, il n'y aura aucun contenu manquant.

  
**Canada**

# University of Alberta

## Library Release Form

**Name of Author:** Atiyah Yahya

**Title of Thesis:** *In-Vivo* Methodologies of  $^{13}\text{C}$  NMR Spectroscopy

**Degree:** Doctor of Philosophy

**Year this Degree Granted:** 2006

Permission is hereby granted to the University of Alberta Library to reproduce single copies of this thesis and to lend or sell such copies for private, scholarly, or scientific research purposes only.

The author reserves all other publication and other rights in association with the copyright in the thesis, and except as herein before provided, neither the thesis nor any substantial portion thereof may be printed or otherwise reproduced in any material form whatsoever without the author's prior written permission.

---

Atiyah Yahya  
3214-104A Street  
Edmonton, Alberta  
T6J 2Z6, Canada

**Date:** 8 January, 2006

To the memory of my father,

Syed Mohammad Yahya

# Abstract

The work conducted in this thesis is the first part of a research programme to develop the tools and procedures to introduce dynamic measurements of neurotransmitter metabolism into collaborative projects with psychiatrists and neurologists on patients with brain disorders or diseases. Carbon-13,  $^{13}\text{C}$ , magnetic resonance spectroscopy (MRS) is a valuable tool in the determination of metabolic flux rates. Because  $^{13}\text{C}$  is only 1.1% naturally abundant, infusing  $^{13}\text{C}$  labelled substrates into a subject allows the time courses of  $^{13}\text{C}$  label incorporation into metabolic products such as neurotransmitter glutamate, and hence a key metabolic flux rate to be measured. Carbon-13 is challenging to measure directly, and therefore methodologies that involve both the  $^{13}\text{C}$  and  $^1\text{H}$  nuclei, known as double resonance techniques, are employed to enhance specificity and sensitivity. Such techniques exploit the heteronuclear scalar coupling that exists between  $^{13}\text{C}$  nuclei and the bonded  $^1\text{H}$  nuclei to take advantage of the higher sensitivity of  $^1\text{H}$  spins.

The objectives of this thesis were to enhance the volume range, sensitivity and specificity of dynamic  $^{13}\text{C}$  measurements. The first two were addressed by the design, construction, and testing of a dual-tuned open radiofrequency coil. The advantage of this coil is that as a single-unit it provides uniform radiofrequency fields at both  $^{13}\text{C}$  and  $^1\text{H}$  frequencies over a larger territory of brain than the coil commonly used in  $^{13}\text{C}$  studies. The final, and most substantial objective (specificity) involved the incorporation of homonuclear  $^1\text{H}$  coupling as well as heteronuclear ( $^1\text{H}$ - $^{13}\text{C}$ ) coupling in the NMR model. Homonuclear  $^1\text{H}$  coupling has been uniformly neglected in the literature. The result of its

inclusion, demonstrated both theoretically and experimentally, was that it can lead to quantification errors of the order of several tens of percent and in some cases to less than optimal sequence design. The inclusion of  $^1\text{H}$  homonuclear coupling was evaluated in a number of direct (three in all) and indirect (two in all) techniques for measuring  $^{13}\text{C}$  spectra from a localized volume.



# Acknowledgments

I would first like to acknowledge my supervisor, Dr. Peter Allen, for his efforts and input throughout my Ph.D. program. I feel privileged to have been the graduate student of such an outstanding researcher in the field of NMR. I would also like to thank Dr. Abdulhakem Elezzabi for being my co-supervisor and for all his stimulating electromagnetics questions. I appreciate the time invested by the other members of my supervisory committee, Dr. Alan Wilman and Dr. Robert Fedosejevs. I am also grateful to Dr. Nick Coupland and Dr. Chris Hanstock for serving as examiners on my candidacy and defense examinations. In addition, I wish to thank Dr. Hanstock for his patience when answering my many questions, especially during the first couple of years of my graduate studies. I thank Dr. Kelvin Jones and Dr. Christian Beaulieu for chairing my candidacy and defense examinations, respectively. Moreover, I feel honoured to have had Dr. Graeme Mason, an expert in the field of  $^{13}\text{C}$  NMR spectroscopy, as my external examiner.

I am grateful to Dr. Richard Thompson whose Ph.D. work was crucial for my own, and I thank Dr. Vivian Mushahwar for taking time out of her busy schedule to help improve our presentation skills.

I am indebted to Dr. Nicola DeZanche, a previous fellow graduate student and sincere friend, for teaching me all that I know about RF coil design and for answering my never ending questions. I also must thank another previous fellow graduate student, Dr. Hyeonjin Kim, for helping me enhance my understanding of NMR spin interactions, and for sharing with me his optimistic views on life. I acknowledge Dr. Jim Wild, for being an academic role model, and for all the wise advice (e.g. "Atiyah, it is important to eat") and support which he still provides me with all the way from England.

I owe so much to Dan Gheorghiu for assisting me with the initial hardware setup I needed for my experiments, and for making sure that the NMR equipment ran smoothly everyday. I thank Beau Sapach for solving all my serious (and petty) computer problems, and for always being there to help me set up the projector for presentations. I am grateful to Maisie Goh for ensuring I got my monthly pay, and for taking care of many other administrative issues. Life would have been so much more difficult without Carol Hartle, whom I thank for assisting with manuscripts, scholarship applications, and above all for being a friend. Thanks also to Brenda Carrier who warmly greeted me every morning when I went to check the mail.

It is essential to acknowledge all my fellow graduate students who have made the workplace an enjoyable place to be. I sincerely thank the following: Yusuf Bhagat for being an entertaining office companion, Luis Concha for showing me exciting computer animations almost every day, Jacob Ellegood for dropping by my office every so often to make sure I am ok, Amir Eissa for always being in a good mood no matter what the circumstances, Jeff Snyder for making me realize the importance of Venezuela, Sherif El

Basiouny for his continuous support and words of wisdom, Daniel Hallihan for being someone you can count on, Anthony Tessier for keeping me company in the NMR facility in the evenings, Alison, Angela and Lindsay for providing female companionship in the lab, and Rob Stobbe for educating me about bike helmets. Although I have only known the new students to the department a few months, I feel like it has been much longer. I appreciate Marc and Catherine Lebel keeping me company at lunchtime and I have enjoyed sharing my office with Farnaz Khosrow-Khavar. Also, thanks to Osama Abushenaf for being a wonderful listener (or successfully pretending to be one). I am also grateful to former graduate students in our lab Dr. Keith Wachowicz, Osama Al-Kwafi, Steven Thomas, Jason Mendes, Chilo Bonilla, and Sasha Holden for all the interesting conversations, support and encouragement.

I appreciate the time sacrificed by all my magnet volunteers. Special thanks to Muhammad Jabakhanji for being willing to show up at any time and for never failing to make the session entertaining.

I greatly appreciate the funding provided to me by AHFMR, NSERC, and iCORE.

Most importantly I must thank my family. I am grateful to my brother for being “my number one fan” and to my sister for being my best friend. Finally, nothing in my life could have been accomplished without my parents. My father, to whom this thesis is dedicated, implanted in me the value of education from the time I was a child and developed in me the desire to always strive towards excellence. My mother has been the means and the source of strength through which I manage to achieve it. I am eternally grateful to her for selflessly and tirelessly being there day after day for her family.

# Table of Contents

	Page
<b>Chapter 1 Introduction</b>	
1.1 Introduction to the Thesis.....	1
1.2 Physical Principles of NMR.....	4
1.2.1 Nuclear magnetic moments.....	4
1.2.2 Interaction of nuclear magnetic moments with a static field.....	5
1.2.3 The NMR experiment .....	8
1.2.3.1 Classical overview .....	8
1.2.3.2 The rotating frame.....	10
1.2.3.3 The Hamiltonian for the application of an RF pulse.....	11
1.2.4 Relaxation.....	12
1.2.4.1 Longitudinal relaxation.....	12
1.2.4.2 Transverse relaxation and the concept of a spin echo.....	12
1.3 Phenomena of Chemical Shift and Scalar Coupling in MRS.....	15
1.3.1 Chemical shift.....	16
1.3.2 Indirect scalar coupling (J-coupling).....	16
1.3.2.1 Weak coupling.....	17
1.3.2.2 Strong coupling.....	17
1.3.2.3 Homonuclear coupling.....	18
1.3.2.4 Heteronuclear coupling.....	19
1.4 Spatial Localization.....	20
1.4.1 Linear magnetic field gradients and slice selection.....	20
1.4.2 Other applications of magnetic field gradients.....	21
1.4.3 Three dimensional (3D) single voxel localization.....	22
1.4.3.1 PRESS.....	22
1.4.3.2 STEAM.....	23
1.4.3.3 ISIS.....	23
1.4.4 The voxel shift effect.....	24
1.5 Some Theoretical Aspects of NMR.....	25
1.5.1 Matrix representation of spin operators.....	25
1.5.2 The density matrix, the density operator, and the concept of coherence.....	26
1.5.3 The density matrix for two interacting spins and the concept of multiple quantum coherence (MQC).....	28
1.5.4 Evolution of the density operator.....	30
1.5.5 Gradients for coherence selection.....	31
1.6 RF Coils.....	32
1.6.1 Surface coils and linear excitation.....	33
1.6.2 Birdcage coils and quadrature excitation.....	34
1.6.3 Impedance matching.....	35
1.6.4 The quality factor.....	36

1.6.5 The SNR of an NMR experiment.....	36
1.7 $^1\text{H}$ MRS and $^{13}\text{C}$ MRS.....	38
1.8 Double Resonance.....	42
1.8.1 Proton decoupling during acquisition.....	42
1.8.2 Polarization transfer.....	43
1.8.3 Indirect $^{13}\text{C}$ detection.....	44
1.8.4 RF coils for double resonance.....	46
1.9 References.....	47

## ***Chapter 2 A Dual-Tuned Transceiver for $^{13}\text{C}\{^1\text{H}\}$ NMR Spectroscopy: Two Open Coils in One***

2.1 Introduction.....	55
2.2 Theory.....	57
2.2.1 An open coil design.....	57
2.2.2 The dual-tuned open birdcage design.....	59
2.3 Experimental Methods.....	60
2.3.1 RF probe design and constructions.....	60
2.3.1.1 The dual-tuned half-birdcage design.....	60
2.3.1.2 Adriany-Gruetter design.....	61
2.3.2 Performance testing.....	62
2.3.2.1 Imaging.....	62
2.3.2.2 $^{13}\text{C}\{^1\text{H}\}$ spectroscopy.....	63
2.3.2.3 Measuring the quality factor.....	63
2.3.2.4 Port isolation.....	64
2.4 Results.....	64
2.4.1 Quality factors and isolation.....	64
2.4.2 $B_1$ homogeneity at the proton frequency.....	65
2.4.3 <i>In-Vivo</i> decoupling power requirements.....	68
2.4.4 Sensitivity and homogeneity at the $^{13}\text{C}$ frequency.....	69
2.4.5 Efficacy of the dual-tuned half birdcage <i>in vivo</i> .....	70
2.5 Discussion.....	72
2.6 Conclusion.....	73
2.7 References.....	74

## ***Chapter 3 Numerical Method of Spin Evolution Analysis***

3.1 Introduction.....	76
3.2 Numerical Method of Analysis.....	77
3.2.1 The Hamiltonian for a proton spin system.....	77
3.2.2 Modifications made to incorporate a $^{13}\text{C}$ nucleus.....	78
3.2.3 Algorithm for the calculations.....	79
3.3 A Double Resonance Example: Response of $\text{CH}_2$ to DEPT.....	80
3.4 References.....	83

## **Chapter 4 Indirect $^{13}\text{C}$ Observation I: PRESS-Localized POCE**

4.1 Introduction.....	84
4.2 Methods.....	85
4.2.1 Numerical method.....	85
4.2.2 Experimental methods.....	86
4.3 Results.....	88
4.3.1 Simultaneous strong homonuclear coupling and weak homonuclear Coupling during PRESS.....	88
4.3.2 Simultaneous strong homonuclear coupling and weak homonuclear Coupling during POCE.....	92
4.3.3 Simultaneous strong homonuclear coupling and weak homonuclear Coupling during PRESS-localized POCE.....	94
4.3.4 Field strength dependence.....	99
4.4 Discussion.....	100
4.5 Conclusion.....	101
4.6 References.....	102

## **Chapter 5 Indirect $^{13}\text{C}$ Observation II: Single-Shot PRESS-Localized ge-HMQC**

5.1 Introduction.....	105
5.2 Theory.....	106
5.2.1 Ge-HMQC pulse sequence.....	106
5.2.1.1 General overview of the sequence.....	106
5.2.1.2 Gradient ratios.....	107
5.2.2 Combining PRESS and the ge-HMQC technique.....	109
5.3 Methods.....	109
5.4 Results.....	110
5.4.1 Verification of sequence efficacy.....	110
5.4.2 Comparing the efficiency of PRESS-localized HMQC to that of PRESS-localized POCE.....	112
5.4.3 Effect of strong homonuclear proton coupling on the outcome of the basic ge-HMQC sequence.....	113
5.4.4 Effect of strong homonuclear proton coupling on the outcome of A PRESS-localized ge-HMQC sequence.....	114
5.5 Discussion.....	118
5.6 Conclusion.....	121
5.7 References.....	123

## **Chapter 6 Direct $^{13}\text{C}$ Observation I: PRESS Combined with a Modified DEPT Sequence**

6.1 Introduction.....	125
-----------------------	-----

6.2 Theory.....	126
6.2.1 INEPT.....	126
6.2.1.1 The basic INEPT sequence.....	126
6.2.1.2 The refocussed INEPT sequence.....	127
6.2.2 DEPT.....	128
6.2.2.1 The basic DEPT sequence.....	128
6.2.2.2 The modified DEPT sequence.....	128
6.2.3 PRESS combined with modified DEPT.....	129
6.3 Methods.....	130
6.4 Results.....	134
6.4.1 Efficacy of the sequence.....	134
6.4.2 Feasibility of the sequence <i>in vivo</i> .....	135
6.4.3 The effect of strong homonuclear proton coupling on the outcome of the sequence, illustrated with glutamate at 3.0 T.....	135
6.5 Discussion.....	144
6.6 References.....	146

### ***Chapter 7 Direct <sup>13</sup>C Observation II: Modified INEPT***

7.1 Introduction.....	148
7.2 Methods.....	149
7.2.1 Numerical method.....	149
7.2.2 Experimental methods.....	149
7.3 Results.....	153
7.4 Discussion.....	156
7.5 Conclusion.....	157
7.6 References.....	158

### ***Chapter 8 Concluding Remarks***

8.1 A <sup>13</sup> C/ <sup>1</sup> H Dual-Tuned Half-Birdcage Coil.....	160
8.2 The Effect of Simultaneous Strong Homonuclear Proton Coupling and Heteronuclear Coupling on Spin Responses.....	161
8.3 Future Directions.....	162
8.4 References.....	164

***Appendix 1: Transformation Tables for Two Weakly-Coupled Spins*** 166

***Appendix 2: The Difference in Evolution between Strongly-Coupled  
  Spins and Weakly-Coupled Spins*** 168

***Appendix 3: Transformation Under the Influence of a Gradient Pulse*** 171

***Appendix 4: Evolution of an IS Heteronuclear Spin System during  
  the ge-HMQC Sequence*** 172

# *List of Tables*

	<b>Page</b>
<b><i>Chapter 1 Introduction</i></b>	
1.1 Chemical shift and scalar coupling values of the protons of glutamate.....	19
<b><i>Chapter 2 A Dual-Tuned Transceiver for <math>^{13}\text{C}\{^1\text{H}\}</math> MR Spectroscopy: Two Open Coils in One</i></b>	
2.1 Measured RF probe quality factors.....	65
2.2 Coil port couplings at each of the two frequencies.....	65
<b><i>Chapter 4 Indirect <math>^{13}\text{C}</math> Observation I: PRESS-Localized POCE</i></b>	
4.1 Chemical shift and scalar coupling parameters for both the protons and the carbons of glutamate.....	85
<b><i>Chapter 5 Indirect <math>^{13}\text{C}</math> Observation II: Single-Shot PRESS-Localized Ge-HMQC</i></b>	
5.1 Gradient ratios in a ge-HMQC sequence for rephasing of selected pathways.....	108
<b><i>Chapter 6 Direct <math>^{13}\text{C}</math> Observation I: PRESS Combined with a Modified DEPT Sequence</i></b>	
6.1 Phase cycling scheme implemented for DEPT.....	133
6.2 List of Glu proton SQCs that yield $^{13}\text{C}$ observable signal by DEPT.....	140
<b><i>Chapter 7 Direct <math>^{13}\text{C}</math> Observation II: Modified INEPT</i></b>	
7.1 Phase cycling scheme implemented in the modified INEPT sequence.....	151

# *List of Figures*

	<b>Page</b>
<b><i>Chapter 1 Introduction</i></b>	
1.1 Energy levels of a spin 1/2 nucleus in a static field $B_0$ .....	6
1.2 Orientations of a spin 1/2 nucleus when placed in a static field $B_0$ .....	7
1.3 Directions of applied fields in an NMR experiment.....	8
1.4 Induced emf in the time domain and in the frequency domain.....	9
1.5 Precession of $\overline{M}_\rho$ and $\overline{B}_{eff}$ in the rotating frame.....	11
1.6 Dephasing of spins in the transverse plane of the rotating frame.....	13
1.7 A spin echo pulse sequence.....	14
1.8 Spin refocussing in the rotating frame of reference by the application of a spin echo pulse sequence.....	15
1.9 Calculated proton spectrum of Glu at 3.0 T.....	18
1.10 Calculated $^{13}\text{C}$ spectrum of a $\text{CH}_3$ molecular group.....	19
1.11 Distribution of in-phase $I_Y$ magnetization of a single uncoupled spin after the application of a $180^\circ$ slice selective refocusing pulse.....	21
1.12 Basic PRESS localization sequence.....	22
1.13 Basic STEAM localization sequence.....	23
1.14 Basic ISIS localization sequence.....	24
1.15 Illustration of the voxel shift effect.....	25
1.16 Energy level diagram of two weakly-coupled spins in a static field $B_0$	29
1.17 Diagram of an RF surface coil.....	33
1.18 A linearly polarized field.....	34
1.19 General structure of a birdcage coil.....	35
1.20 Proton and carbon spectra of glutamate and glutamine at 3.0 T.....	40
1.21 $^{13}\text{C}$ labelling of the tricarboxylic acid cycle upon infusion of $[1-^{13}\text{C}]$ glucose.....	41
1.22 An illustration of the consequence of proton decoupling.....	43
1.23 The DEPT pulse sequence.....	44
1.24 The POCE sequence.....	45
1.25 The Adriany-Gruetter coil design.....	46
 <b><i>Chapter 2 A Dual-Tuned Transceiver for <math>^{13}\text{C}\{^1\text{H}\}</math> MR Spectroscopy: Two Open Coils in One</i></b>	
2.1 Adriany-Gruetter proton coil.....	56
2.2 High-pass and low-pass network structures.....	58
2.3 Representation of a low-pass half-birdcage coil.....	58
2.4 Schematic diagram of the half-birdcage circuit.....	59
2.5 Schematic diagram of the dual-tuned open coil.....	60
2.6 Matching elements of the dual-tuned half birdcage.....	61
2.7 Tune and match circuits used for the surface coils.....	62



2.8	Proton RF field maps of the half birdcage and the Adriany-Gruetter coils	67
2.9	$^{13}\text{C}$ lipid spectra obtained with the half birdcage from a human calf.....	69
2.10	$^{13}\text{C}$ sensitivity profiles of the half-birdcage and the $^{13}\text{C}$ surface coil.....	70
2.11	Axial and coronal spin echo images of a human calf obtained with the half birdcage.....	71
2.12	Natural abundance $^{13}\text{C}_1$ glycogen spectrum obtained from the calf of a normal volunteer with the half-birdcage RF probe.....	71
2.13	Natural abundance localized $^{13}\text{C}$ spectrum obtained from the calf of a normal volunteer with the half-birdcage RF probe.....	72

### **Chapter 3 Numerical Method of Spin Evolution Analysis**

3.1	Calculated $^{13}\text{C}$ response of a $\text{CH}_2$ molecular group to the DEPT sequence in the presence and in the absence of proton decoupling.....	82
3.2	Calculated signal intensity of the decoupled peak of a $\text{CH}_2$ molecular group in response to DEPT as a function of the theta flip angle.....	82

### **Chapter 4 Indirect $^{13}\text{C}$ Observation I: PRESS-Localized POCE**

4.1	A PRESS-localized POCE sequence for indirect $^{13}\text{C}$ detection.....	87
4.2	An illustration of the different response to a proton PRESS sequence by the MNPQ protons of Glu depending on whether the $\text{C}_3$ carbon is labelled with $^{13}\text{C}$ or not.....	89
4.3	The lineshape of four SQC terms of the P proton of Glu.....	90
4.4	Distribution of 17 Glu M, N, P, and Q SQC terms present at the onset of acquisition of a PRESS sequence ( $\text{TE}_1 = 20$ ms, $\text{TE}_2 = 10$ ms) in the situations where the MN protons are either $^{13}\text{C}$ -labelled or not.....	92
4.5	The response of $^{13}\text{C}_3$ - and $^{13}\text{C}_4$ -Glu to the POCE sequence.....	94
4.6	Changes in a selection of Glu proton SQCs that illustrate the effect of switching the POCE $^{13}\text{C}$ inversion pulse on or off.....	95
4.7	A diagram showing the spectral consequences of the POCE inversion pulse on the MN and PQ multiplets of Glu, when either the $\text{C}_3$ or $\text{C}_4$ carbon is $^{13}\text{C}$ -labelled.....	98
4.8	Field strength dependence of the response of the MNPQ protons of Glu to the POCE sequence.....	99

### **Chapter 5 Indirect $^{13}\text{C}$ Observation II: Single-Shot PRESS-Localized Ge-HMQC**

5.1	Standard 2D ge-HMQC pulse sequence.....	106
5.2	PRESS-localized ge-HMQC sequence.....	109
5.3	PRESS-localized ge-HMQC sequence obtained from a natural abundance acetic acid phantom.....	111
5.4	Comparison of the efficiency of POCE and ge-HMQC.....	112
5.5	Response of $^{13}\text{C}_3$ - and $^{13}\text{C}_4$ -Glu to the ge-HMQC sequence.....	114

5.6	Intensity of the MN protons of $^{13}\text{C}_3$ -Glu to the PRESS-localized ge-HMQC sequence as a function of the two PRESS echo times.....	115
5.7	Intensity of the PQ protons of $^{13}\text{C}_4$ -Glu to the PRESS-localized ge-HMQC sequence as a function of the two PRESS echo times.....	116
5.8	Response of natural abundance Glu to the PRESS-localized ge-HMQC sequence when $\text{TE}_1 = \text{TE}_2 = 10$ ms.....	117
5.9	Response of $^{13}\text{C}_3$ - and $^{13}\text{C}_4$ -Glu to the PRESS-localized ge-HMQC sequence when $\text{TE}_1 = \text{TE}_2 = 10$ ms .....	119
5.10	Response of natural abundance Glu to the PRESS-localized ge-HMQC sequence when $\text{TE}_1 = 70$ ms, and $\text{TE}_2 = 30$ ms.....	121

### **Chapter 6 Direct $^{13}\text{C}$ Observation I: PRESS Combined with a Modified DEPT Sequence**

6.1	The INEPT and refocussed INEPT sequences.....	128
6.2	The modified DEPT sequence.....	129
6.3	A diagram illustrating PRESS combined with modified DEPT.....	130
6.4	Phantom used to verify the efficacy of the PRESS-DEPT sequence.....	132
6.5	Sequence used to calibrate the phase of the DEPT theta pulse.....	132
6.6	Verifying the efficacy of the PRESS-DEPT sequence.....	134
6.7	Natural abundance $^{13}\text{C}$ spectrum obtained with the sequence <i>in vivo</i> .....	135
6.8	Dominant coherence pathways taken by ten proton SQCs during DEPT	139
6.9	$^{13}\text{C}_3$ -Glu peak intensity as a function of PRESS echo times.....	141
6.10	$^{13}\text{C}_4$ -Glu peak intensity as a function of PRESS echo times in response to the PRESS-DEPT sequence.....	142
6.11	$^{13}\text{C}_3$ - and $^{13}\text{C}_4$ Glu peak intensities as a function of PRESS echo times in response to a PRESS-refocussed INEPT sequence.....	143
6.12	$^{13}\text{C}$ spectrum acquired from a natural abundance 1.8 M Glu phantom with the PRESS-DEPT sequence ( $\text{TE}_1 = \text{TE}_2 = 10$ ms).....	145

### **Chapter 7 Direct $^{13}\text{C}$ Observation II: Modified INEPT**

7.1	The INEPT, modified INEPT, and modified refocussed INEPT sequences.....	152
7.2	Difference in $^{13}\text{C}$ signal between when the $^{13}\text{C}$ inversion pulse is placed $1/4J_{\text{CH}}$ after the first proton pulse and when it is placed $1/4J_{\text{CH}}$ before the third proton pulse.....	154
7.3	Expectation values of $2M_x X_z$ and $2N_x X_z$ present immediately prior to the third proton pulse of the modified INEPT sequence.....	155
7.4	Contributions of $M_y$ , $N_y$ , $P_y$ , and $Q_y$ to the formation of $2M_x X_z$ and $2N_x X_z$ at the echo time of the modified INEPT sequence.....	156

***Appendix 2: The Difference in Evolution between Strongly-Coupled Spins and Weakly-Coupled Spins***

A2.1 Response of an uncoupled spin I to a spin echo experiment as a function of the echo time.....168

A2.2 Response of the A spin of a weakly-coupled AX spin system to a spin echo experiment as a function of the echo time .....169

A2.3 Response of the A spin of a strongly-coupled AB spin system to a spin echo experiment as a function of the echo time showing the creation of the coherence term  $2A_zB_x$ .....169

A2.4 Response of the A spin of a strongly-coupled AB spin system to a spin echo experiment as a function of the echo time showing the creation of the coherence terms  $B_x$  and  $2A_zB_x$ .....170

A2.5 Response of the A spin of a strongly-coupled AB spin system to a spin echo experiment as a function of the echo time showing the creation of the coherence terms  $B_y$  and  $2A_zB_y$ .....170

# *List of Symbols and Abbreviations*

$\vec{B}_0$	Static magnetic field
BW	Bandwidth
$\vec{B}_1(t)$	Radiofrequency magnetic field
$\vec{B}_{eff}$	Effective radiofrequency magnetic field in the rotating frame
$^{13}\text{C}$	Carbon-13
$^1\text{H}$	Hydrogen
DEPT	Distortionless Enhancement by Polarization Transfer
DQC	Double Quantum Coherence
$E_{Zeeman}$	Zeeman energy
emf	Electromotive force
FDA	Food and Drug Administration
FID	Free Induction Decay
ge-HMQC	Gradient Enhanced-Heteronuclear Multiple Quantum Coherence
$\vec{G}$	Gradient strength
Glu	Glutamate
Gln	Glutamine
Glx	Glutamate and Glutamine
$\mathcal{H}_{B_0}$	Zeeman Hamiltonian
$\mathcal{H}_{RF}$	Radiofrequency Hamiltonian
$\mathcal{H}_{chemical\ shift}$	Chemical shift Hamiltonian
$\mathcal{H}_{scalar\ coupling}$	Scalar coupling Hamiltonian
$\mathcal{H}_{gradient}$	Gradient pulse Hamiltonian
I	Spin quantum number
$I_x, I_y, I_z$	Cartesian spin operators
INEPT	Insensitive Nuclei Enhanced by Polarization Transfer
ISIS	Image-Selected <i>In-Vivo</i> Spectroscopy

$\vec{J}$	Angular momentum of the nucleus
J	Scalar coupling constant
k	Boltzmann's constant
MQC	Multiple Quantum Coherence
MRI	Magnetic Resonance Imaging
MRS	Magnetic Resonance Spectroscopy
$\vec{M}_o$	Magnetization
$\vec{M}_z$	Longitudinal magnetization
$\vec{M}_\rho$	Magnetization in the rotating frame
$M_{xy}$	Transverse magnetization
$N_\uparrow$	Number of spins parallel to the static field
$N_\downarrow$	Number of spins anti-parallel to the static field
$N_s$	Total number of spins
NMR	Nuclear Magnetic Resonance
POCE	Proton Observe Carbon Edited
ppm	Parts per million
PRESS	Point RESolved Spectroscopy
Q	Quality factor
r	Spatial position
$R_{coil}$	Coil resistance
$R_{sample}$	Sample resistance
RF	Radiofrequency
SAR	Specific Absorption Rate
SNR	Signal to Noise Ratio
SQC	Single Quantum Coherence
STEAM	STimulated Echo Acquisition Mode
T	Tesla
$T_1$	Spin-lattice relaxation time
$T_2$	Spin-spin relaxation time
TE	Echo time

$TE_1$	First echo time
$TE_2$	Second echo time
TCA	Tricarboxylic acid cycle
U	Unitary operator
$V_{\text{noise}}$	Noise voltage
$V_{\text{signal}}$	Signal voltage
ZQC	Zero Quantum Coherence
$\Delta E$	Energy difference
$\hbar$	Planck's constant divided by $2\pi$
$\Delta\delta$	Chemical shift difference
$\gamma$	Gyromagnetic ratio
$\gamma_H$	Gyromagnetic ratio of hydrogen
$\gamma_C$	Gyromagnetic ratio of carbon-13
$\Delta x$	Slice thickness
$\theta_{\text{gradient}}$	Phase accumulated during a gradient pulse
$\vec{\mu}$	Magnetic moment
$\rho$	Density operator
$\rho_{\text{eq}}$	Density operator at thermal equilibrium
$\sigma$	Shielding constant
$\eta$	Filling factor
$\omega_o$	Larmor frequency
$\psi$	Wavefunction
§	Section

# Chapter 1

## Introduction

### 1.1 Introduction to the Thesis

Nuclear magnetic resonance (NMR) provides a non-destructive, and non-invasive method for studying human tissues *in vivo*. Magnetic resonance imaging (MRI) is the most common diagnostic application of NMR, and it has a wide variety of uses clinically. MRI uses the NMR signal from water protons to form an image. It has achieved its clinical standing because of its non-destructive nature (no ionizing radiation is used) and because of the ability to modulate the NMR signal intensity with numerous measurements that are reflective of pathology.

Magnetic resonance spectroscopy (MRS) applied *in vivo*, allows for the regional and temporal measurement of local steady-state metabolite concentrations, thereby enabling the evaluation of metabolism's steady state and its modification by pathology and therapy. MRS of the brain has been shown to be useful in the study of diseases and disorders such as Parkinson's disease (1-4), multiple sclerosis (5-9), stroke (10,11), brain tumours (12-14), epilepsy (15-18), Alzheimer's disease (19-21), bipolar disorder (22-24) and schizophrenia (25-27). It has also been utilized in drug studies (28). Furthermore,  $^1\text{H}$ ,  $^{31}\text{P}$ ,  $^{15}\text{N}$ , and  $^{13}\text{C}$  MRS have been used to monitor temporal changes of metabolites over the course of minutes or hours in cases of sensory stimulation, exercise, ischemia, seizure, and pharmacological manipulations. However, due to the difficulties that are encountered in acquiring and analyzing spectra, MRS is still not employed routinely in the clinical domain. The main limitation of an *in-vivo* NMR spectroscopy experiment is the low signal to noise ratio (SNR) of the resulting spectrum, because the concentrations of the metabolites being detected are only on the order of mmols (mM) (compared to a water concentration of  $\approx 55\text{ M}$ ). The SNR can be improved by signal averaging ( $\text{SNR} \propto \sqrt{N}$ , where  $N$  = number of averages); however, one has to comply with a time-window for the experiment that is determined by patient tolerance. In addition, it is often complicated to analyze metabolite spectra because unlike the water spectrum which is a

single resonance, most metabolites exhibit homonuclear (e.g.  $^1\text{H}$ - $^1\text{H}$ ) and heteronuclear (e.g.  $^1\text{H}$ - $^{13}\text{C}$ ) scalar coupling which causes the resonances to split into multiplets (see §1.3.2). In particular, this is a problem in proton ( $^1\text{H}$ ) spectra, where the whole spectrum occupies a narrow frequency range, and gives rise to a significant overlapping of peaks from different metabolites. Moreover, at clinical field strengths such as 1.5–3.0 T, many of the metabolites exhibit strong homonuclear coupling which further complicates spectra. The scalar coupling also causes the final signal intensity and lineshape of the spin responses to be dependent on parameters such as the pulses and the intervals between them involved in the pulse sequences employed for spatial localization. Therefore, for accurate quantification and interpretation of spectra it is essential to be able to predict the response of a given spin system to a given pulse sequence.

Despite the obstacles preventing MRS from being part of a routine clinical setting, the use of MRS in research has led to significant insight into the etiology of disease. Proton MRS has been commonly used to determine differences in steady state metabolite concentrations between normal and patient populations. Although such differences can be used as an indicator for a disease, the mechanisms that give rise to the steady-state concentrations are still not clear. Deeper insight into the functioning of the various pathways that give rise to the steady-state concentrations can be obtained, nevertheless, by exploiting the low natural abundance of  $^{13}\text{C}$ . By infusing a  $^{13}\text{C}$ -labelled substrate into a subject and monitoring the rate of  $^{13}\text{C}$  label incorporation into the various metabolite pools, dynamic measurements of metabolism can be made. Specifically, the use of  $^{13}\text{C}$  MRS following an infusion of glucose with its  $\text{C}_1$  99% enriched in  $^{13}\text{C}$  has enabled the determination of important brain metabolic rates such as the tricarboxylic acid (TCA) rate and the rate of the glutamate-glutamine cycle in both humans and rats (29-36). Moreover, the changes in these rates have been investigated under conditions of visual stimulation (37,38), increased neuronal activity (39,40), and under diseased conditions, for example in patients suffering from Alzheimer's disease (41) or hepatic encephalopathy (42).

The topics included in this thesis pertain to *in-vivo* methods of  $^{13}\text{C}$  NMR spectroscopy. There are two methods of observing signal from  $^{13}\text{C}$  nuclei. The signal can be observed directly, or indirectly through the protons coupled to the  $^{13}\text{C}$  nuclei by



exploiting the scalar coupling that exists between them. Often the scalar coupling is also exploited in direct  $^{13}\text{C}$  observation in order to enhance the detected  $^{13}\text{C}$  signal. In either approach, enhanced direct  $^{13}\text{C}$  detection or indirect  $^{13}\text{C}$  detection, the pulse sequences employed usually involve pulses at both the frequencies of  $^1\text{H}$  and  $^{13}\text{C}$ , and are thus referred to as double resonance pulse sequences. Such experiments require a radiofrequency (RF) coil that operates at both the frequencies of  $^1\text{H}$  and  $^{13}\text{C}$ . There were three main objectives of this thesis. The first was to design, construct, and test a half volume dual-tuned single-unit ( $^1\text{H}/^{13}\text{C}$ ) RF coil (chapter 2), that has the advantage of providing an adequately uniform RF field at both frequencies at depths that are of greater neurological interest compared to a commonly used design which involves three separate surface coils (43).

The second objective was to develop and to use a numerical method of analysis (outlined in chapter 3) to calculate the responses of heteronuclear (specifically  $^1\text{H}-^{13}\text{C}$ ) spin systems to a given pulse sequence. Previously it has been assumed that the only interaction taking place in such sequences is the heteronuclear coupling. Our numerical method incorporates both the effects of proton homonuclear coupling and proton-carbon heteronuclear coupling. The method was employed in this thesis (chapters 4-7) to illustrate, using glutamate (Glu) at 3.0 T as an example, the effect of simultaneous strong homonuclear ( $^1\text{H}-^1\text{H}$ ) and heteronuclear ( $^1\text{H}-^{13}\text{C}$ ) scalar coupling on the spin evolution during a number of pulse sequences used in both direct and indirect  $^{13}\text{C}$  detection. In chapter 4, the effect of simultaneous strong homonuclear ( $^1\text{H}-^1\text{H}$ ) and heteronuclear ( $^1\text{H}-^{13}\text{C}$ ) scalar coupling on the spin response was calculated for the spatial localization sequence Point RESolved Spectroscopy, PRESS (44), the Proton Observe Carbon Edited, POCE (45), sequence (an indirect  $^{13}\text{C}$  detection method), and the PRESS sequence incorporating POCE (46). It was demonstrated how neglecting to take into account the proton homonuclear coupling can lead to quantification errors in  $^{13}\text{C}$  labelling on the order of tens of percent.

The third objective of this thesis was to develop single-shot pulse sequences for both direct and indirect  $^{13}\text{C}$  observation. The commonly used sequences, POCE in indirect  $^{13}\text{C}$  detection and proton localization using Image-Selected *In-vivo* Spectroscopy (ISIS) (47) in localized direct  $^{13}\text{C}$  detection, rely on the subtraction or addition of scans

which makes them susceptible to motion artifacts and errors due to hardware instabilities. Chapters 5 and 6 describe alternative sequences that acquire the desired data in a single scan. Chapter 5 shows how the PRESS sequence can be combined with the gradient enhanced Multiple Quantum Coherence technique, ge-HMQC (48), to allow indirect detection of  $^{13}\text{C}$  signal from three dimensional volumes in a single scan, while chapter 6 demonstrates how PRESS can be combined with the Distortionless Enhancement by Polarization Transfer (DEPT) method (49) to achieve the same for direct  $^{13}\text{C}$  detection. The effects of concurrent proton homonuclear coupling and heteronuclear coupling on the outcome of these two sequences was also investigated, and again it was shown how neglecting to take into account the proton homonuclear coupling can lead to significant errors in signal quantification. The PRESS sequence was chosen since it is used in many laboratories because of its single-shot nature and because maximum signal from uncoupled spins can be obtained by it. Chapter 7 deals with a modified version of the Insensitive Nuclei Enhanced by Polarization Transfer (INEPT) sequence (50) and demonstrates once more the significance of not taking into account proton homonuclear coupling.

The numerical method utilized in this thesis can be employed to plan and design  $^{13}\text{C}/^1\text{H}$  double resonance pulse sequences and to predict the response of spin systems to such sequences. It is important to note that the calculations in this thesis were carried out assuming ideal conditions (e.g. homogeneous RF fields). These assumptions are fair for *in-vitro* experiments such as the ones conducted on small phantoms in this thesis to verify the calculations. However, when predicting spin responses *in vivo* the effects due inhomogeneous RF fields and relaxation need to be taken into account to make the simulations realistic; spectra from appropriately designed phantoms can provide the complementary information required.

## **1.2 Physical Principles of NMR**

### **1.2.1 Nuclear magnetic moments**

For a nucleus to be NMR viable, it must possess a nuclear magnetic moment. The nuclear magnetic moment is denoted by a vector quantity  $\vec{\mu}$  which is related to the total

angular momentum of the nucleus,  $\vec{J}$ , by a constant  $\gamma$  ( $\vec{\mu} = \gamma\vec{J}$ ), known as the gyromagnetic ratio of the nucleus, and is specific for different nuclei (e.g.  $\gamma_H = 4.26 \times 10^7 \text{ T}^{-1}\text{s}^{-1}$ , and  $\gamma_C \approx \gamma_H / 4$ , where  $\gamma_H$  is the gyromagnetic ratio of a  $^1\text{H}$  nucleus, and  $\gamma_C$  is that of a  $^{13}\text{C}$  nucleus).  $\vec{J}$  is related to a dimensionless angular operator  $\vec{I}$ , by  $\vec{J} = \hbar\vec{I}$ , where  $\hbar$  is Planck's constant divided by  $2\pi$ . The magnitude of  $\vec{I}$  is given by  $\sqrt{I(I+1)}$ , where  $I$  is the spin quantum number and can be either an integer, or a half-integer. Since this thesis deals with  $^1\text{H}$  and  $^{13}\text{C}$  nuclei, both of which have  $I = 1/2$ , all further descriptions will be limited to nuclei of spin  $1/2$ .

### 1.2.2 Interaction of nuclear magnetic moments with a static field

The NMR experiment involves placing magnetic nuclei in a strong static field,  $\vec{B}_o$ , which is conventionally taken to be pointing along the z-axis. The interaction energy of the field with the magnetic moment is given by Eq. (1.1).

$$\mathcal{E} = -\vec{\mu} \cdot \vec{B}_o = -\gamma\hbar\vec{I} \cdot \vec{B}_o \quad (1.1)$$

Since  $\vec{B}_o$ , only has a z-component, the Hamiltonian (operator form) of the interaction energy can be written as

$$\mathcal{H}_{B_o} = -\gamma\hbar B_o I_z. \quad (1.2)$$

From the time-independent Schrödinger equation (1.3), the energy eigenvalues,  $E$ , of the system can be calculated for the energy eigenstates  $\Psi$ .

$$\mathcal{H}_{B_o} \Psi = E\Psi \quad (1.3)$$

The eigenvalues of the operator  $I_z$  are  $1/2$  and  $-1/2$  (when  $I = 1/2$ ) and correspond to the spin being aligned either parallel (energy eigenstate denoted by  $|\alpha\rangle$ ) or antiparallel (energy eigenstate denoted by  $|\beta\rangle$ ) to the magnetic field, respectively. Thus, there exist two energy eigenvalues, namely,  $E = \pm\gamma\hbar B_o / 2$ , as illustrated in Fig. 1.1. The energy separation (Zeeman splitting) can be written as  $\hbar\omega_o$ , where  $\omega_o = \gamma B_o$ , and is called the Larmor frequency; transitions between the two states results in a characteristic spectral line at this frequency.

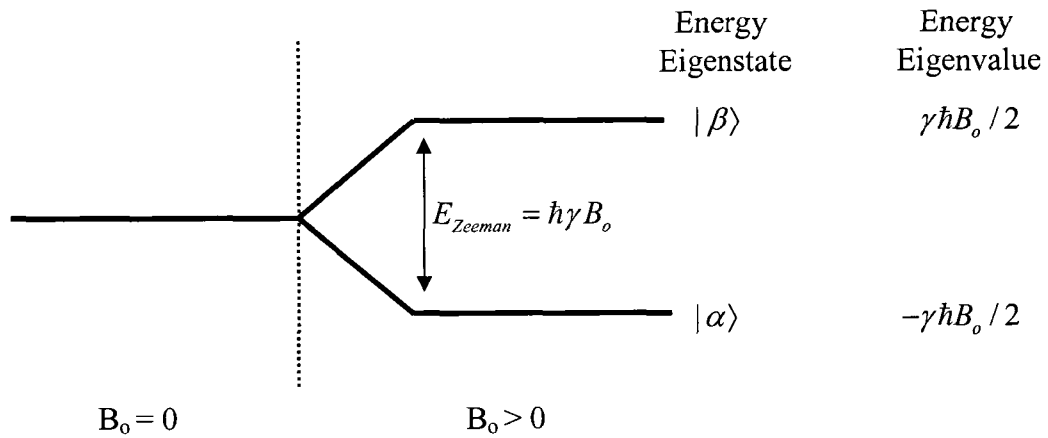


Figure 1.1: Energy levels of a spin 1/2 nucleus in a static field  $B_0$ . The state  $|\alpha\rangle$  corresponds to the spin being parallel to  $B_0$  while  $|\beta\rangle$  corresponds to the antiparallel state. The energy separation of the two states is  $\hbar\omega_0$ , where  $\omega_0$  is the Larmor frequency of the nucleus and equals  $\gamma B_0$ .

To be precise, the magnetic moment itself is not parallel or antiparallel to the field, but because of its magnitude and its z-component, it forms an angle of  $54.74^\circ$  to it, and it precesses at the Larmor frequency on the surface of a cone, as shown in Fig. 1.2. Quantum mechanically, at any instant, the spin has a finite probability of being in the  $|\alpha\rangle$  or the  $|\beta\rangle$  state; that is it can be represented by a general wavefunction given in Eq. (1.4), where the two states are orthonormal to each other, that is  $\langle\alpha|\alpha\rangle = \langle\beta|\beta\rangle = 1$ , and  $\langle\alpha|\beta\rangle = \langle\beta|\alpha\rangle = 0$ , and the probability of it being in the  $|\alpha\rangle$  state is  $|c_\uparrow|^2$ , and similarly, the probability of it being in the  $|\beta\rangle$  state is  $|c_\downarrow|^2$ .

$$\Psi = c_\uparrow |\alpha\rangle + c_\downarrow |\beta\rangle \quad (1.4)$$

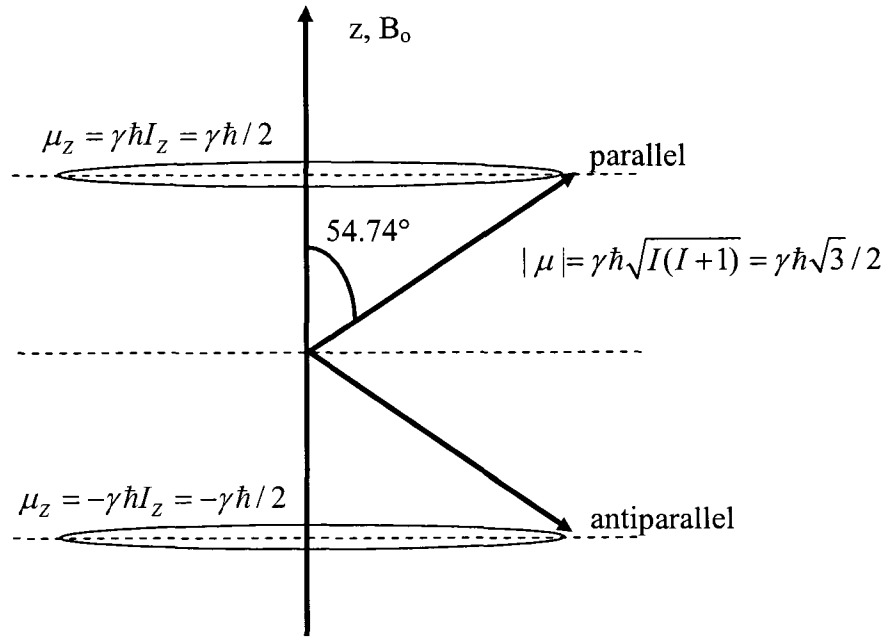


Figure 1.2: Orientations of a spin 1/2 nucleus when placed in a static field  $B_0$  pointing in the  $z$ -direction. Strictly speaking, it is the  $z$ -component of the magnetic moment which is either parallel or antiparallel to the field.

In reality, the NMR experiment involves a macroscopic number of nuclei. In the absence of a magnetic field, these nuclei are all randomly oriented; however, when they are placed in the static field,  $\vec{B}_0$ , they align themselves to yield a net magnetization,  $\vec{M}_0$ , pointing in the direction of the field (the more favourable state). The random precessional phases of the spins results in a zero net component in the plane perpendicular to the field (the  $xy$  plane, or the transverse plane). The magnetization  $\vec{M}_0$  can be written as

$$|\vec{M}_0| = |\vec{M}_z| = \frac{\gamma\hbar}{2}(N_\uparrow - N_\downarrow), \quad (1.5)$$

where  $N_\uparrow$  and  $N_\downarrow$  represent the number of spins aligned parallel and antiparallel to  $\vec{B}_0$ , respectively, and are related to the probabilities of finding the spins in a state  $|\alpha\rangle$  or  $|\beta\rangle$  through the coefficients in Eq. (1.4). From the Boltzman relationship, where  $T$  is the temperature of the spin system,  $k$  is Boltzman's constant ( $1.38 \times 10^{-23}$  J/K), and  $\Delta E = \gamma\hbar B_0 \ll kT$

$$\frac{N_{\uparrow}}{N_{\downarrow}} = \exp\left(\frac{\Delta E}{kT}\right) \approx 1 + \frac{\gamma \hbar B_o}{kT}, \quad (1.6)$$

and from the fact that  $N_{\uparrow} + N_{\downarrow} = N_s$  (the total number of spins), we obtain

$$N_{\uparrow} - N_{\downarrow} = \frac{N_s \gamma \hbar B_o}{2kT}, \quad (1.7)$$

and therefore (51),

$$M_o = \frac{\gamma^2 \hbar^2 B_o N_s}{4kT}. \quad (1.8)$$

If we assume we are working with protons at 1 T at a temperature of 300K, Eq. (1.7)

yields  $\frac{N_{\uparrow} - N_{\downarrow}}{N_s} = 3 \times 10^{-6}$ , implying that only 3 in a million protons are responsible for the NMR signal.

### 1.2.3 The NMR experiment

#### 1.2.3.1 Classical overview

If an RF field,  $\vec{B}_1(t)$ , is applied such that it rotates around  $\vec{B}_o$  in a plane orthogonal to it, as shown in Fig. 1.3, then the magnetization  $\vec{M}_o$  will experience a torque causing it to move away from the z-axis in a spiralling manner. If  $\vec{B}_1(t)$  is turned off after a certain time, called a 90° pulse, and defined such that  $\vec{M}_o$  will have relocated in the  $xy$  plane, the nuclear system is said to be in an excited state.

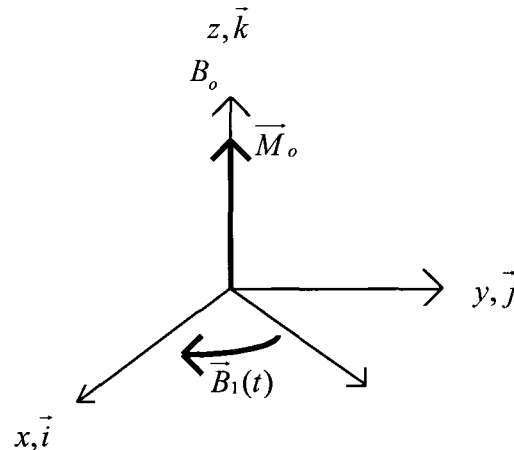


Figure 1.3: Directions of applied fields in an NMR experiment.  $\vec{i}$ ,  $\vec{j}$ , and  $\vec{k}$  represent unit vectors in the x,y, and z directions, respectively. The oscillating RF field is applied perpendicular to the static field.

The magnetization will now experience a torque due to  $\vec{B}_o$ , which will cause it to precess around  $\vec{B}_o$  in the  $xy$  plane according to Eq. (1.9) at its Larmor frequency,  $\omega_o$ . For nuclei with positive  $\gamma$ , the precession is in a negative sense (clockwise). Note that for excitation to take place the applied RF field must oscillate close to the Larmor frequency of the nuclei and in the same precessional sense as the nuclei.

$$\frac{d\vec{M}}{dt} = \gamma \vec{M} \times \vec{B}_o \quad (1.9)$$

To detect the NMR signal an RF coil is required. The same coil may also be used to produce the desired  $\vec{B}_1(t)$  field. The NMR signal is received by the fact that the rotating magnetization induces an electromotive force, emf, in the coil according to Faraday's law of electromagnetic induction. Due to spin-spin and spin-lattice interactions that the nuclear moments experience while precessing around  $B_o$ , the magnetization, will relax back to its equilibrium state (parallel to  $\vec{B}_o$ ) with an exponential time constant (see §1.2.4). The resulting signal is a decaying sinusoidal emf, known as the free induction decay (FID), shown in Fig. 1.4(a). In frequency space this emf can be viewed as a broadened delta function at  $\omega_o$ . Such a representation is called a spectrum, and the area under it is proportional to the number of nuclei that contribute towards it.

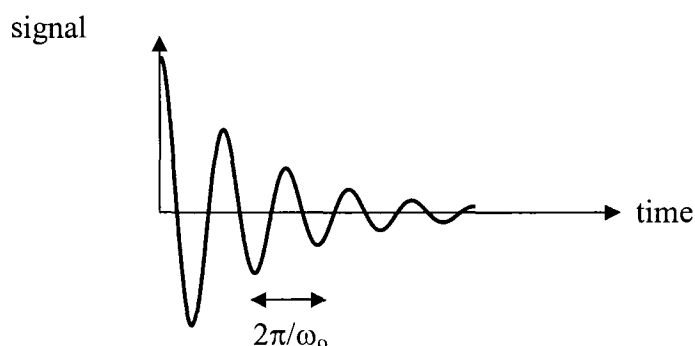


Figure 1.4a: Induced emf in the time domain.

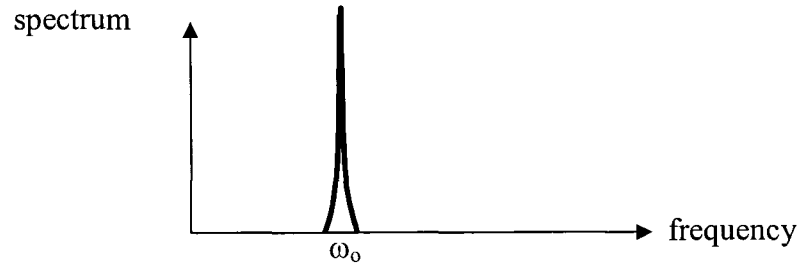


Figure 1.4b: Induced emf in the frequency domain.

### 1.2.3.2 The rotating frame

The stationary frame of reference used in the previous section is named the laboratory frame. To simplify conceptually the effects of RF pulses, a rotating frame of reference is often used. The transverse plane of this frame rotates with the  $\vec{B}_1$  field in a synchronized manner, that is, it rotates in a negative sense at  $\omega$ , the angular frequency of the  $\vec{B}_1$  field. The new coordinate system is given with respect to the laboratory frame by the transformations in Eqs. (1.10a-1.10c) (51), where  $\vec{i}$ ,  $\vec{j}$ , and  $\vec{k}$  are defined in Fig. 1.3.

$$\vec{i}_\rho = \cos(\omega t)\vec{i} - \sin(\omega t)\vec{j} \quad (1.10a)$$

$$\vec{j}_\rho = \sin(\omega t)\vec{i} + \cos(\omega t)\vec{j} \quad (1.10b)$$

$$\vec{k}_\rho = \vec{k} \quad (1.10c)$$

In this frame of reference, the combined effects of  $\vec{B}_o$  and  $\vec{B}_1(t)$  on the nuclei can be described by the equation of motion (1.11) where the effective field,  $\vec{B}_{eff}$ , is defined in Eq. (1.12), and  $\vec{M}_\rho$  is a vector consisting of the three orthogonal components of the magnetization in the rotating frame.

$$\frac{d\vec{M}_\rho}{dt} = \gamma \vec{M}_\rho \times \vec{B}_{eff} \quad (1.11)$$

$$\vec{B}_{eff} = B_1 \vec{i}_\rho + (B_o + \omega / \gamma) \vec{k}_\rho \quad (1.12)$$

These equations tell us that in the rotating frame,  $\vec{M}_\rho$  will precess on the surface of a cone whose central axis is  $\vec{B}_{eff}$  at an angular frequency  $\omega_{eff} = \gamma B_{eff}$ . The situation is illustrated in Fig. 1.5.



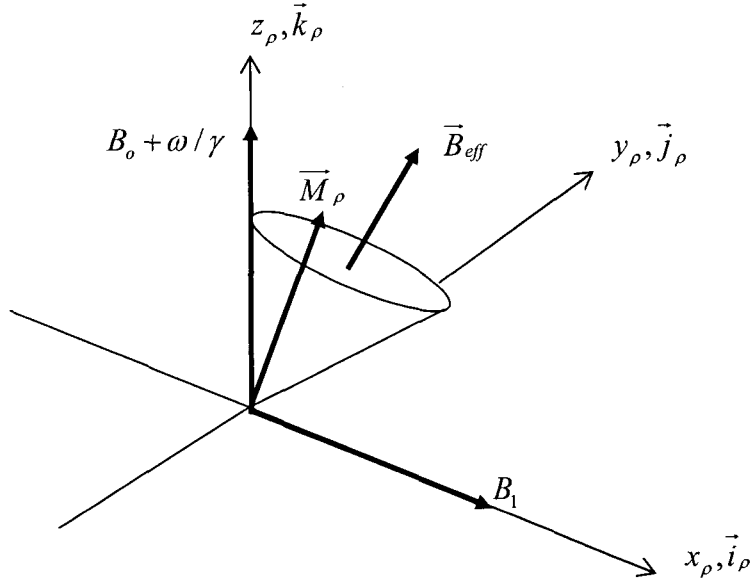


Figure 1.5: Precession of  $\vec{M}_\rho$  around  $\vec{B}_{eff}$  in the rotating frame.

If  $\vec{B}_1(t)$  is rotating in a negative sense at the Larmor frequency of the nuclei,  $\gamma B_0$ , Eq. (1.12) reduces to  $\vec{B}_{eff} = B_1 \vec{i}_\rho$ , and the cone of precession flattens to the  $z_\rho y_\rho$  plane. This is called the resonance condition and  $\vec{M}_\rho$  will rotate in the  $z_\rho y_\rho$  plane around  $\vec{B}_1$  at an angular frequency  $\omega_1 = \gamma B_1$ . If  $\vec{B}_1$  is turned off after a time  $t$ , such that  $t = \pi / (2\gamma B_1)$ , the magnetization vector will be placed along the  $y_\rho$  axis. Such a pulse is referred to as a  $90^\circ$  excitation pulse. If the RF pulse is left on for twice as long, the result would be a  $180^\circ$  inversion pulse that would align  $\vec{M}_\rho$  with the  $-z$  axis.

### 1.2.3.3 The quantum mechanical Hamiltonian for the application of an RF pulse

The RF pulse Hamiltonian can be written in the rotating frame of reference as (52,53)

$$\mathcal{H}_{RF} = \gamma \hbar B_1(t) [(\cos \varphi) I_x + (\sin \varphi) I_y], \quad (1.13)$$

where  $B_1(t)$  is the amplitude of the RF pulse envelope,  $\varphi$  is the phase of the pulse relative to the x-axis of the rotating frame, and  $I_x$  and  $I_y$  are transverse spin operators such that

$[I_x, I_y] = iI_z$ ,  $[I_y, I_z] = iI_x$ , and  $[I_z, I_x] = iI_y$ .  $I_x, I_y$ , and  $I_z$  are termed Cartesian operators.

### 1.2.4 Relaxation

Although the solution to Eq. (1.9) appears to imply that after excitation, the nuclear magnetization precesses endlessly in the transverse plane, in reality it returns back to its thermal equilibrium state, at a rate governed by two relaxation times, the longitudinal and the transverse relaxation time constants, known as  $T_1$  and  $T_2$ , respectively. While  $T_1$  concerns relaxation of the longitudinal magnetization,  $M_z$ ,  $T_2$  concerns that of the transverse magnetization,  $M_{xy}$ . Each can be considered separately. The *Bloch equation* given below takes into account relaxation.

$$\frac{d\vec{M}}{dt} = \gamma \vec{M} \times \vec{B}_o - \frac{M_x \vec{i} + M_y \vec{j}}{T_2} - \frac{(M_z - M_o) \vec{k}}{T_1} \quad (1.14)$$

#### 1.2.4.1 Longitudinal relaxation

Longitudinal, or  $T_1$ , relaxation is caused by the randomly fluctuating magnetic fields within the environment (lattice) the nucleus experiences, and thus is sometimes referred to as spin-lattice relaxation (53). The recovery of  $M_z$  can be taken to be determined by the first order rate equation (1.15), the solution of which is given by Eq. (1.16).

$$\frac{dM_z(t)}{dt} = -\frac{1}{T_1} [M_o - M_z(t)], \quad (1.15)$$

$$M_z(t) = M_o + [M_z(0) - M_o] \exp\left(-\frac{t}{T_1}\right) \quad (1.16)$$

#### 1.2.4.2 Transverse relaxation and the concept of a spin echo

The microscopic fields created by neighbouring dipoles is one of the sources that causes the field at the nucleus to become time dependent (53). The total local field can be expressed as

$$B = B_o + b(x, y, z, t) \quad (1.17)$$

and thus individual spins experience precession frequencies  $\omega_{precess}$  which fall in the range

$$\omega_{precess}(x, y, z, t) = \omega_o + \Omega(x, y, z, t), \quad (1.18)$$

where  $\Omega(x, y, z, t)$  can add or subtract from the resonance frequency,  $\omega_o$ , causing the coherent magnetization vector to dephase as shown in Fig. 1.6. This dephasing leads to an irreversible decay of  $M_{xy}$  back to its equilibrium value of zero. For a fluid medium, this decay can also be modelled as a first order equation (1.19), the solution to which is (1.20).

$$\frac{dM_{xy}}{dt} = -\frac{1}{T_2}[0 - M_{xy}(t)] \quad (1.19)$$

$$M_{xy}(t) = M_{xy}(0) \exp\left(-\frac{t}{T_2}\right) \quad (1.20)$$

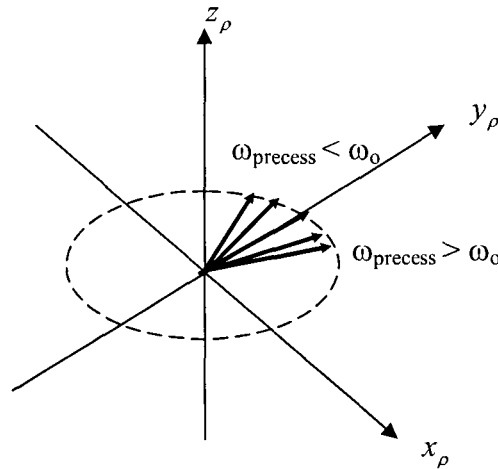


Figure 1.6: Dephasing of spins in the transverse plane of the rotating frame.

Further variations in the precessional frequencies arise due to imperfections in the main magnet design resulting in the static field not being perfectly homogeneous. This extra field variation can be denoted as  $\phi(x, y, z)$  and can be added to Eq. (1.17) to yield

$$B = B_o + b(x, y, z, t) + \phi(x, y, z). \quad (1.21)$$

The effect of this additional term is to increase the rate of dephasing and shorten the relaxation time to a new value called  $T_2^*$ . However, while the effects due to the time dependent local fields are irreversible, those due to static field inhomogeneities can be reversed by implementing a standard spin echo sequence (54), shown in Fig. 1.7.

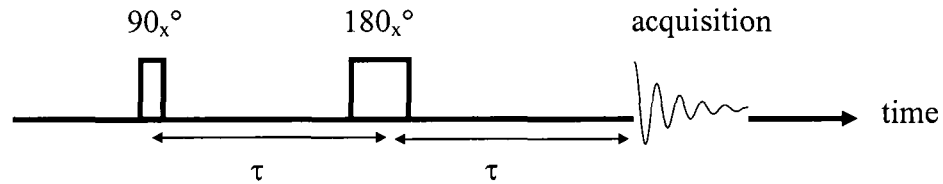


Figure 1.7: A spin echo pulse sequence consists of a  $90^\circ$  excitation pulse followed by a delay  $\tau$  (half the echo time), a  $180^\circ$  pulse and the same delay. The pulse subscripts denote the phase of a pulse. For example, a phase of x implies that the  $B_1$  field in the rotating frame is along the  $x_\rho$  axis.

After the  $90_x^\circ$  pulse, the spins are aligned along the  $y_\rho$  axis of the rotating frame as illustrated in Fig. 1.8(a). Considering only static field homogeneities, during the delay  $\tau$ , the spins dephase (Fig. 1.18(b)). The  $180_x^\circ$  pulse causes the spins to flip around the  $x_\rho$  axis (Fig. 1.8(c)), causing both sets of spins to move towards the  $-y_\rho$  axis and to eventually refocus at the end of the second delay  $\tau$  (Fig. 1.8(d)) along  $-y_\rho$ . Note that if the  $180^\circ$  pulse had been applied with a phase of y, the spins would have refocused along the  $y_\rho$  axis. The time  $2\tau$  is conventionally called the echo time, TE.

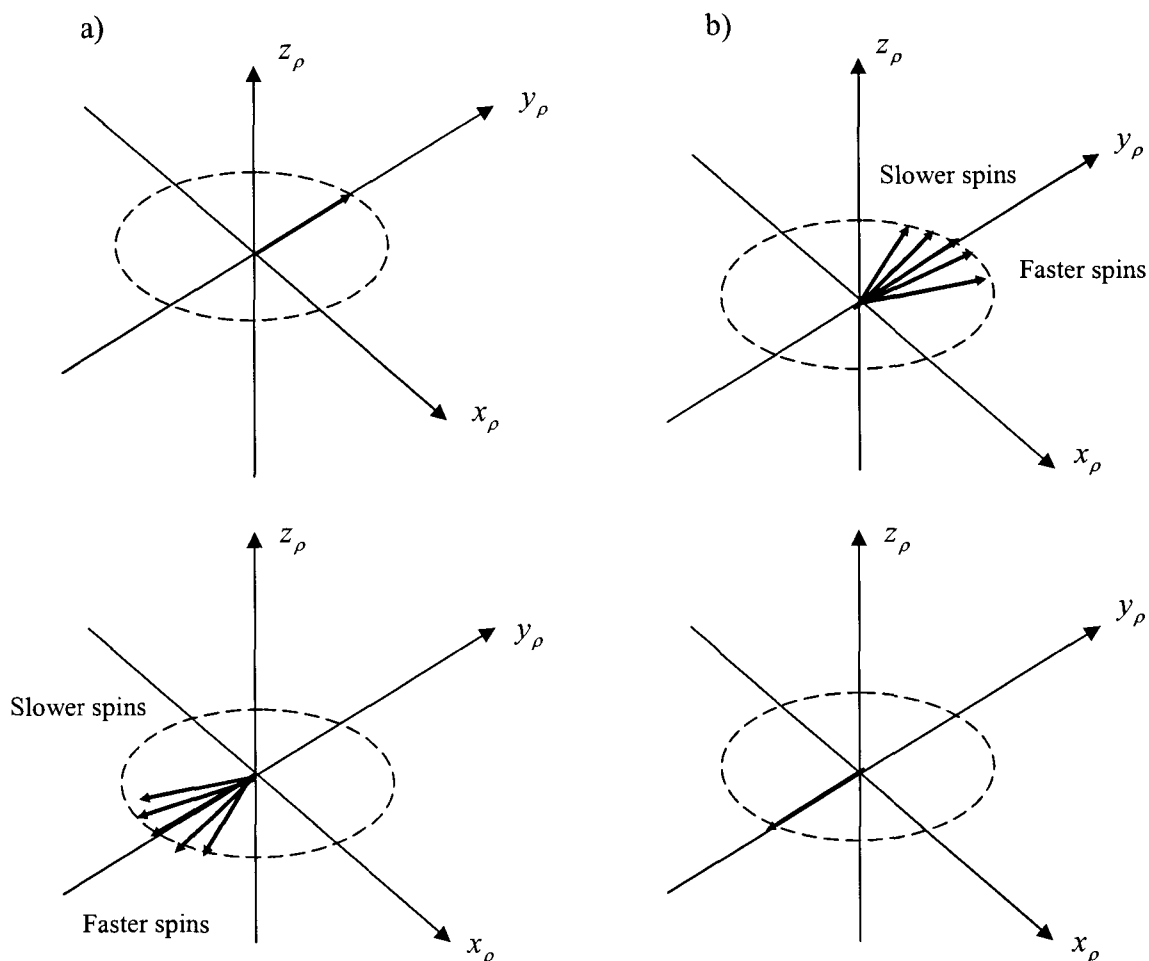


Figure 1.8: Illustration of spin refocussing in the rotating frame of reference by the application of a spin echo pulse sequence. The  $90_x^\circ$  excitation pulse results in a coherent magnetization vector as shown in (a). During the delay,  $\tau$ , the spins dephase (b). The  $180_x^\circ$  causes the spins to rotate  $180^\circ$  about the  $x$ -axis of the rotating frame as illustrated in (c). The spins now move towards each other to eventually refocus a time  $\tau$  later (d).

### **1.3 Phenomena of Chemical Shift and Scalar Coupling in MRS**

The analytical power of NMR spectroscopy stems from two interactions experienced by the nuclei, namely, chemical shielding, and indirect scalar coupling, also referred to as J-coupling.

### 1.3.1 Chemical shift

From the equation for the Larmor frequency,  $\omega_o = \gamma B_o$ , it would appear that all nuclei of the same species, for example all  $^1\text{H}$  nuclei, resonate at the same frequency in a given static field. This, however, is not the case. Nuclei in different chemical environments experience slightly different magnetic fields, due to the imbalanced orbital currents that are induced in their surrounding electron clouds by the static field  $B_o$ . This current imbalance produces a small local magnetic field at the site of the nucleus that is directly proportional to  $B_o$ , but opposite in direction. Hence, the resonance frequency for a specific nucleus can be written as Eq. (1.22) where  $\sigma$  is known as the chemical shielding, and is dependent on the electronic structure, and where  $\gamma B_o \sigma$  is the chemical shift frequency.

$$\omega_o = \gamma B_o (1 - \sigma) \quad (1.22)$$

It is the metabolite specific chemical shift pattern that allows us to distinguish between different metabolites and even between different atoms in a metabolite molecule. Chemical shifts are usually expressed in dimensionless units of ppms (parts per million). Thus a specific peak will always have the same chemical shift value in terms of ppm regardless of the field strength.  $^1\text{H}$  and  $^{13}\text{C}$  chemical shifts are measured with respect to the proton and carbon resonances, respectively, of the molecule tetramethylsilane (TMS),  $(\text{CH}_3)_4\text{Si}$ .

The chemical shift rotating frame Hamiltonian is given by Eq. (1.23) where,  $\omega_a$  is the chemical shift offset frequency.

$$\mathcal{H}_{\text{chemical shift}} = \hbar \omega_a I_Z \quad (1.23)$$

### 1.3.2 Indirect scalar coupling (J-coupling)

Scalar coupling involves neighbouring nuclear spins interacting with each other via electrons in the bonds joining the nuclei. This phenomenon arises from the hyperfine contact interaction between a nucleus and an s-electron, which has a finite probability of

existing at the nucleus (53). Consider two nuclei bonded to each other via an electronic covalent bond. The electron near a nucleus favours an anti-parallel alignment to the nucleus. The Pauli exclusion principle states that the two electrons in the covalent bond must have opposing states; this implies that the second electron in the covalent bond will favour an alignment antiparallel to the first electron (parallel to the original nucleus). The second nucleus “senses” the spin state of the first nucleus by the polarization of its nearby electron. Therefore, by the hyperfine contact interaction and the electrons’ compliance with the Pauli exclusion principle an indirect coupling between the two nuclear spins exists. Because this interaction is sensitive to the various orientations of the nuclei, it causes individual chemically shifted peaks in a spectrum to split into multiplets. The amount of the splitting is given by the scalar coupling constant,  $J$ , in units of Hz. The scalar coupling Hamiltonian between two spins  $I_1$  and  $I_2$  is given by

$$\mathcal{H}_{\text{scalar coupling}} = 2\pi J_{12} \vec{I}_1 \cdot \vec{I}_2. \quad (1.24)$$

The majority of brain metabolites exhibit scalar coupling.

### 1.3.2.1 Weak coupling

Perturbation theory shows that when the chemical shift difference of the two nuclei is much larger than the scalar coupling constant ( $J / \Delta\delta \ll 1$ ), the scalar coupling Hamiltonian can be approximated as (52)

$$\mathcal{H}_{\text{scalar coupling}} = 2\pi J_{12} I_{Z_1} I_{Z_2}. \quad (1.25)$$

In general, in a weakly-coupled spin system, if a nucleus of intrinsic spin  $I = 1/2$  is coupled to  $n$  equivalent nuclei of spin  $1/2$ , the resonance will split into  $n + 1$  lines, with relative intensities given by the binomial distribution. Weak coupling is usually denoted by labelling the nuclei with letters far apart from each other in the alphabet, for example an AX spin system represents two nuclei that are weakly-coupled.

### 1.3.2.2 Strong coupling

In strongly-coupled spin systems, the difference in the resonance frequencies of the two nuclei is of the same order of magnitude as the coupling constant and the complete Hamiltonian given by Eq. (1.24) must be used. There is no general rule for the multiplicity structure of strongly-coupled spins. Strong coupling is usually denoted by

labelling the nuclei with letters close to each other in the alphabet, for example an AB spin system represents two nuclei that are strongly-coupled. Note that because the chemical shift difference between two spins,  $\Delta\delta$ , increases with increasing field strength (see Eg. (1.2.2)), the degree to which two spins are strongly coupled decreases as the field strength increases.

### 1.3.2.3 Homonuclear coupling

Homonuclear coupling refers to scalar coupling existing between two nuclei of the same species, for example,  $^1\text{H}$ - $^1\text{H}$  homonuclear coupling. At clinical field strengths, such as 3.0 T, the majority of brain metabolites, for example, glutamate (Glu), glutamine (Gln), myo-inositol (MI), and aspartate (Asp) all exhibit strong homonuclear coupling. Fig. 1.9 shows the molecular structure of Glu and its numerically calculated proton spectrum at 3.0 T illustrating the complex splitting due to the homonuclear coupling its protons exhibit. The protons of Glu can be represented as an AMNPQ spin system, where the MNPQ protons are strongly coupled to each other and the A proton is weakly coupled to the MN protons. Table 1.1 lists the chemical shifts (at a pH of about 7) and homonuclear scalar coupling constants of the proton spin system of Glu.

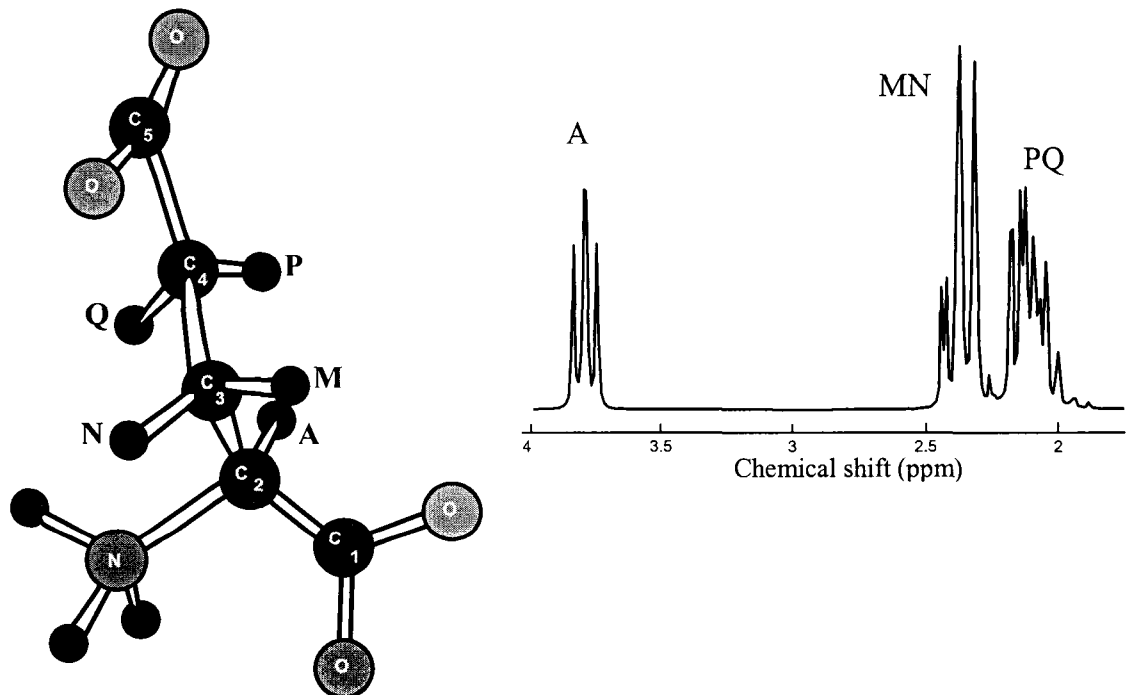


Figure 1.9: Calculated proton spectrum of Glu (molecular structure shown on the left) at 3.0 T



Table 1.1: Chemical shift and scalar coupling values of the protons of glutamate.

Chemical Shifts (ppm)				
Spin 1	Spin 2	Spin3	Spin4	Spin5
A	M	N	P	Q
3.78	2.14	2.06	2.37	2.36
Scalar Coupling Constants (Hz)				
	M	N	P	Q
A	4.67	7.33		
M		-14.85	6.43	8.47
N			8.39	6.89
P				-15.89

#### 1.3.2.4 Heteronuclear coupling

Heteronuclear coupling refers to scalar coupling between nuclei of different species, for example,  $^1\text{H}$ - $^{13}\text{C}$  coupling. Heteronuclear coupling is always weak because the chemical shift difference between the two nuclei is on the order of MHz. The effect of heteronuclear coupling is not apparent in Fig. 1.9 due to the low natural abundance of  $^{13}\text{C}$  ( $\approx 1.1\%$ ). Fig. 1.10 shows a calculated  $^{13}\text{C}$  spectrum of a  $\text{CH}_3$  molecular group, where  $J_{\text{CH}} = 130\text{ Hz}$  (the scalar coupling between the carbon and each proton). As can be seen the  $^{13}\text{C}$  peak is split into a quartet because of the scalar coupling between the  $^{13}\text{C}$  nucleus and its three  $^1\text{H}$  neighbours. The three protons in the  $\text{CH}_3$  molecular group all have the same chemical shift and are known as magnetically equivalent (52). These protons do not exhibit any homonuclear coupling between themselves.

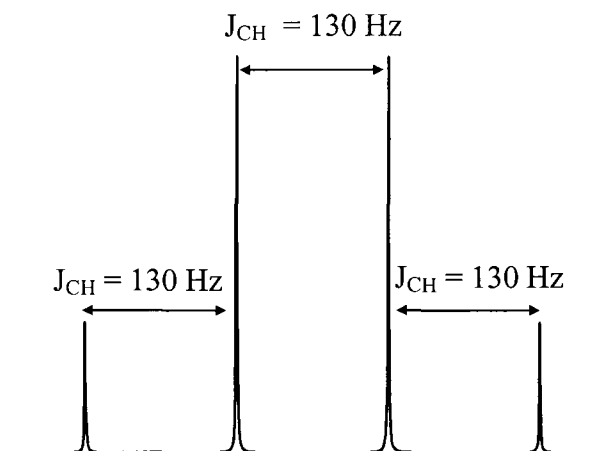


Figure 1.10: Calculated  $^{13}\text{C}$  spectrum of a  $\text{CH}_3$  molecular group.

## 1.4 Spatial Localization

### 1.4.1 Linear magnetic field gradients and slice selection

Superimposing a gradient field on the static field,  $B_o$ , renders the net magnetic field spatially dependent. Eq. (1.26) gives the resulting field at any point  $r$  from the origin of the gradient (usually coincident with the origin of the sample), where  $|\vec{G}|$  is the gradient strength, usually measured in G/cm or mT/m. The purpose of the gradient is to make the resonant frequency of the nuclei spatially dependent as shown in Eq. (1.27).

$$B = B_o + \vec{G} \cdot \vec{r} \quad (1.26)$$

$$\Rightarrow \omega = \omega_o + \gamma G r \quad (1.27)$$

The direction of the gradient field is always along the  $\pm z$ -axis, but its direction of variation can be along any axis. The rotating frame gradient Hamiltonian is

$$\mathcal{H}_{\text{gradient}} = -\gamma \hbar \vec{G} \cdot \vec{r} I_z. \quad (1.28)$$

A band-limited RF pulse is usually an amplitude modulated pulse (soft pulse), that has an excitation profile over a range of frequencies,  $\omega_o \pm \Delta\omega$ . Applying such a pulse in conjunction with a linear magnetic field gradient causes excitation within a selected slice in the sample. A soft pulse is defined by its duration (which is inversely proportional to its bandwidth) and its amplitude modulating envelope, which usually is some form of a sinc function ( $\text{sinc}(t) = \sin(t)/t$ ) because the Fourier transform of a sinc pulse is a rectangle. Thus the excitation profile is uniform across a range of frequencies that lie within the desired slice and zero outside that range. The required pulse bandwidth, BW, can be calculated from Eq. (1.29), where  $\Delta x$  is the desired slice thickness.

$$BW = \gamma G \Delta x \quad (1.29)$$

In reality, the sinc pulses cannot be infinite and therefore need to be truncated. To perform smooth truncation, often apodizing functions are applied to the RF pulse. One example is filtering the sinc pulse with a Gaussian function (sinc-Gaussian pulse). Moreover, because of the finite pulse duration, the pulse excitation profile deviates from the ideal case where nuclei are uniformly excited within the slice and completely unperturbed outside it; a more realistic calculated slice profile is shown in Fig. 1.11.

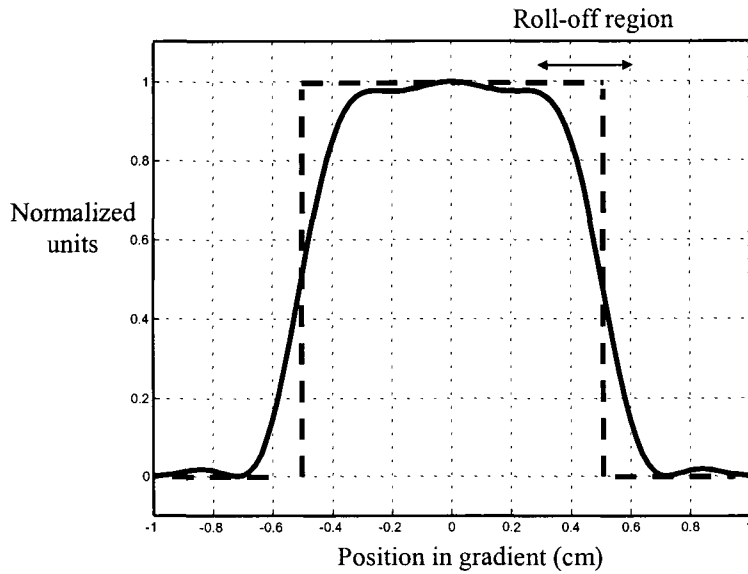


Figure 1.11: Distribution of in-phase  $I_Y$  magnetization of a single uncoupled spin after the application of a  $180^\circ$  slice selective refocusing pulse in a spin-echo sequence. The 2.75 ms pulse was applied in conjunction with a gradient of strength 3.6 mT/m in order to excite a 1 cm slice. As can be seen the realistic slice profile (solid line) deviates from the desired ideal profile (dashed line).

### 1.4.2 Other applications of magnetic field gradients

The influence of a gradient pulse can also be thought of as spatially dependent phase accumulations, where spins at position  $\vec{r}$  accumulate a phase in the transverse rotating frame according to

$$\theta_{\text{gradient}} = -\gamma \vec{G} \cdot \vec{r} t. \quad (1.30)$$

If a gradient pulse of a certain amplitude is left on for an appropriate time, the net sum of the transverse magnetization over the sample will approach zero. At this stage, it is said that the magnetization is completely dephased. Therefore, gradient pulses can be used to destroy, or *spoil*, unwanted signal. In reality, there is a rise time (hundreds of microseconds) associated with the switching on and off of gradient pulses and thus Eq. (1.30) can be written more precisely as,

$$\theta_{\text{gradient}} = -\gamma \int_0^{\Delta t} \vec{G} \cdot \vec{r} dt, \quad (1.31)$$

where  $\Delta t$  is the gradient duration.

Gradient pulses can also be used in coherence selection; this will be further discussed in §1.5.5.

### 1.4.3 Three dimensional (3D) single voxel localization

In *in-vivo* NMR experiments, it is desirable to localize signal to a specific spatial region. This can be done by the application of three slice-selective pulses each in conjunction with a gradient whose direction of variation is mutually orthogonal to that of the other two. Three important 3D-localization sequences are described below. The first two, namely, PRESS (Point RESolved Spectroscopy) (44) and STEAM (Stimulated Echo Acquisition Mode) (55), are single-shot sequences, that is they perform localization in a single scan, whereas the third, ISIS (Image-Selected *In-vivo* Spectroscopy) (47), requires eight acquisitions to perform localization.

#### 1.4.3.1 PRESS

Figure 1.12 displays a basic PRESS localization sequence. Essentially, it is a double spin echo with three slice-selective pulses applied in conjunction with mutually orthogonal gradients. The negative gradient applied after the slice-selective excitation pulse is termed a refocussing lobe and it has an area equal to one half of that of the main slice selection gradient. Its purpose is to rephase phase accumulations that take place during the excitation pulse. The gradients around the  $180^\circ$  refocussing pulses are referred to as spoiler gradients and their purpose is to dephase any signal that may arise as a result of imperfect  $180^\circ$  pulses.

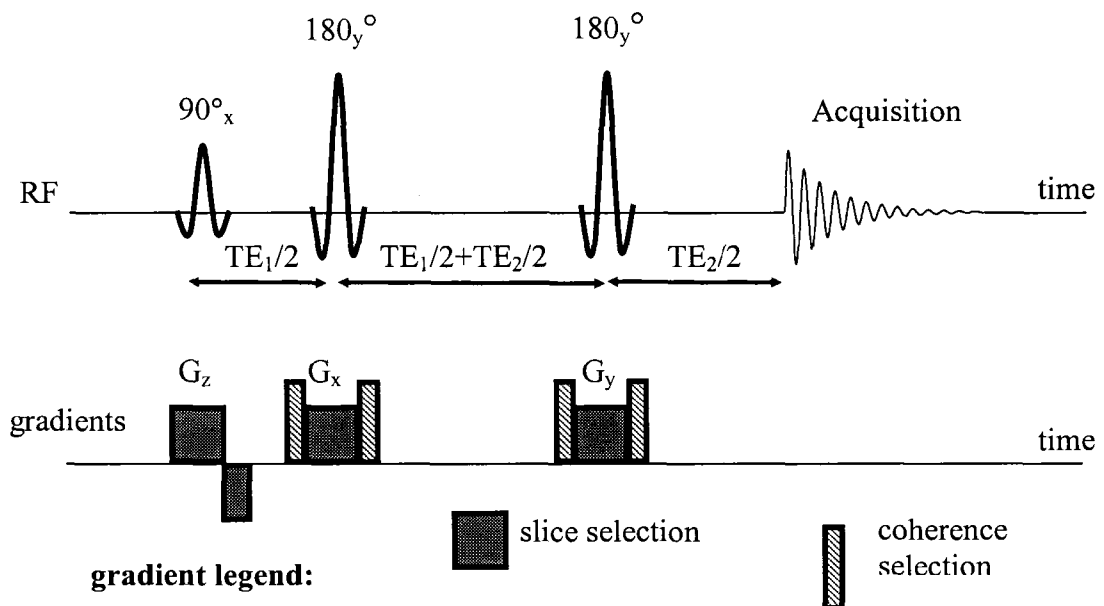


Figure 1.12: Basic PRESS localization sequence.

### 1.4.3.2 STEAM

A schematic diagram of the STEAM localization sequence is displayed in Fig. 1.13. The STEAM sequence consists of three  $90^\circ$  slice-selective pulses applied in conjunction with mutually orthogonal gradients and is based on the formation of a stimulated echo, not a spin echo as in PRESS. In principle, the STEAM signal loses half of the maximum signal available because of the nature of the stimulated echo. The coherence selection gradients are there to ensure the production of a “clean” stimulated echo. A more detailed, intuitive explanation of the STEAM sequence is given in Ref.

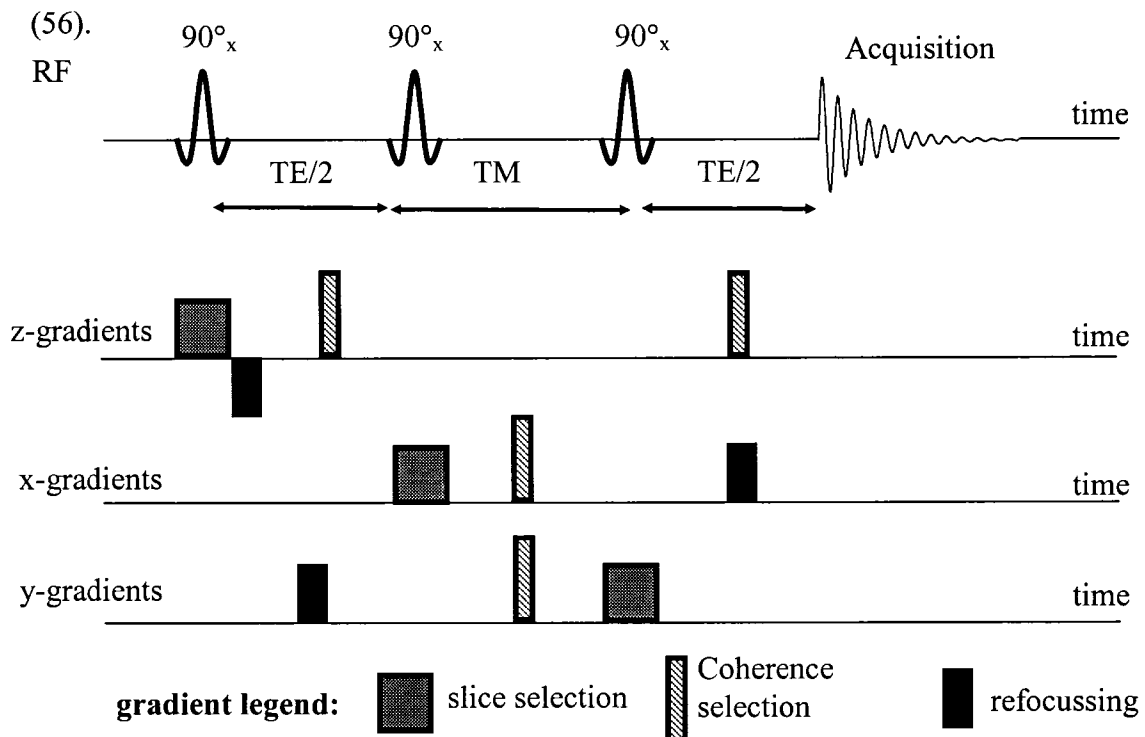


Figure 1.13: Basic STEAM localization sequence.

### 1.4.3.3 ISIS

The basic ISIS localization sequence is illustrated in Fig. 1.14. It consists of three slice-selective inversion pulses, each again applied with gradients mutually orthogonal to each other. In order to achieve localization over a 3D volume, eight acquisitions are required. Each acquisition consists of a different combination of one or more of the RF pulses being on, and the final localized signal is a linear combination of all eight acquisitions, each either being added or subtracted to yield the desired signal. A summary of the eight acquisitions is given below (47).

<i>Acquisition #</i>	<i>x-selective pulse</i>	<i>y-selective pulse</i>	<i>z-selective pulse</i>	<i>contribution</i>
1	off	off	off	+1
2	on	off	off	-1
3	off	on	off	-1
4	on	on	off	+1
5	off	off	on	-1
6	on	off	on	+1
7	off	on	on	+1
8	on	on	on	-1

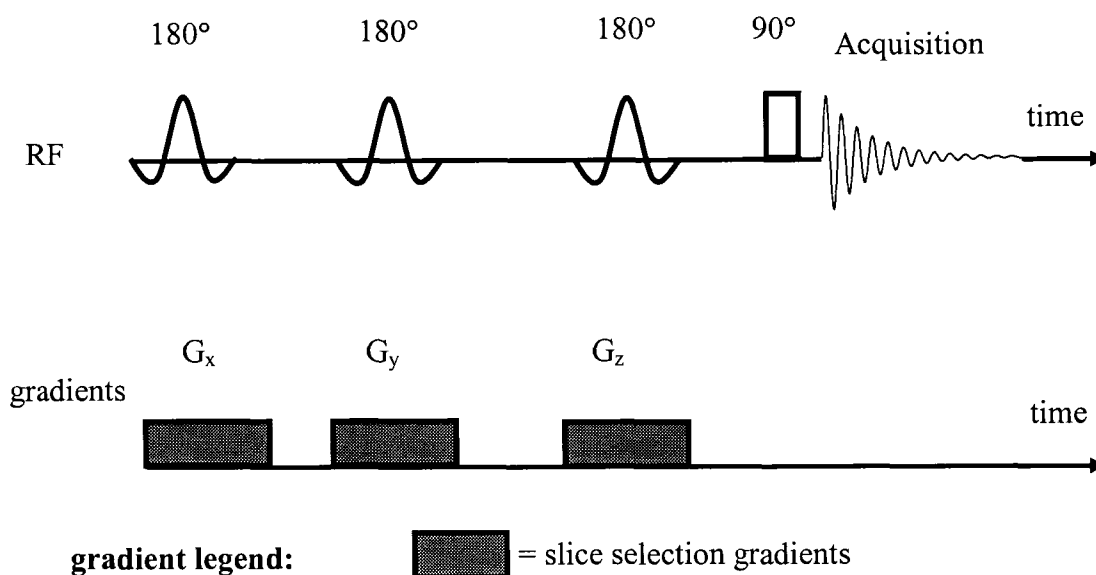


Figure 1.14: Basic ISIS localization sequence.

#### 1.4.4 The voxel shift effect

The voxel shift effect arises because different spins have their own specific chemical shift. For example, if two spins with a chemical shift difference of  $\Delta\delta$  are being excited by a slice-selective pulse, then the signal obtained will not be from the same slice for each spin, but rather from slices offset by an amount  $\Delta\delta / (\gamma G)$ , where  $G$  is the gradient strength. For coupled spins, the situation is made worse because spins on the same molecule are not experiencing the pulse in the same regions of space. Extending to 3D localization, it can be understood that the desired signal from a coupled spin system will only come from that region of space in which the three orthogonal slices overlap for

the coupled spins. Reference (57) demonstrates how this excitation band shift seriously affects the response of lactate (Lac) to the PRESS sequence.

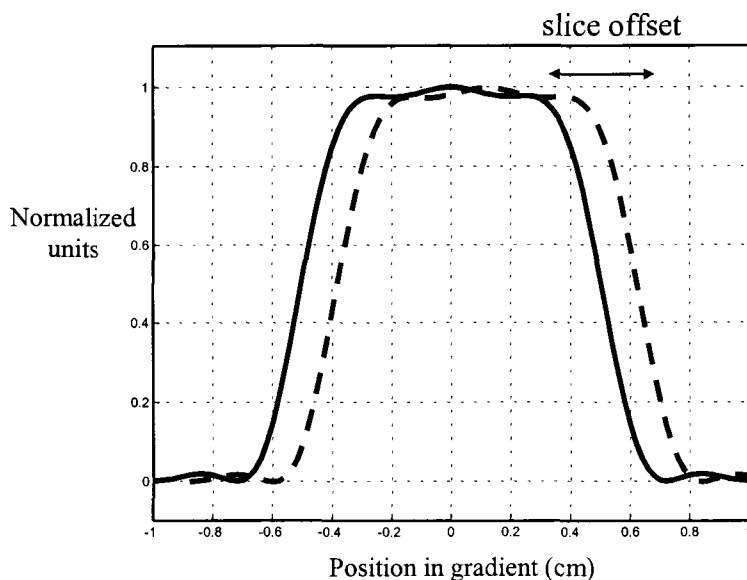


Figure 1.15: Distribution of in-phase  $I_Y$  magnetization of two uncoupled spins after the application of a  $180^\circ$  slice selective refocusing pulse in a spin-echo sequence. The 2.75 ms pulse was applied in conjunction with a gradient of strength 3.6 mT/m in order to excite a 1 cm slice. The two slices are offset from each other by an amount dependent on their chemical shift difference.

## 1.5 Some Theoretical Aspects of NMR

### 1.5.1 Matrix representation of spin operators

For a system of  $n$  spins, the general wavefunction,  $|\psi(t)\rangle$ , is a sum of product spin functions,

$$|\psi(t)\rangle = \sum_i c_i(t) |s_1 s_2 s_3 \dots s_n\rangle_i, \quad (1.32)$$

where  $c_i(t)$  are time dependent complex coefficients and  $s_i$  are the single spin functions which represent the Zeeman eigenstates. For a one spin system,  $s_i = |\alpha\rangle$  or  $|\beta\rangle$ . For a system of two interacting spins, for example, through scalar coupling,  $s_i s_m = |\alpha\alpha\rangle, |\alpha\beta\rangle, |\beta\alpha\rangle$ , or  $|\beta\beta\rangle$ .

An operator,  $A$ , can be expressed in matrix form as

$$A = \begin{bmatrix} \langle a_1 | A | a_1 \rangle & \langle a_1 | A | a_2 \rangle & \dots & \dots \\ \langle a_2 | A | a_1 \rangle & \langle a_2 | A | a_2 \rangle & \dots & \dots \\ \vdots & \vdots & \dots & \dots \\ \vdots & \vdots & \dots & \dots \end{bmatrix}, \quad (1.33)$$

where  $a_n$  represent the energy eigenstates. For a single spin,  $a_1 = |\alpha\rangle$ ,  $a_2 = |\beta\rangle$ ,  $I_z |\alpha\rangle = 1/2 |\alpha\rangle$ , and  $I_z |\beta\rangle = -1/2 |\beta\rangle$  (52). Thus the operator  $I_z$  can be expressed as

$$I_z = 1/2 \begin{bmatrix} 1 & 0 \\ 0 & -1 \end{bmatrix}. \quad (1.34)$$

From the definitions for the raising and lowering operators (spherical operators),  $I_+ = I_x + iI_y$  and  $I_- = I_x - iI_y$ , respectively, and from the relations  $I_+ |\beta\rangle = |\alpha\rangle$ ,  $I_- |\alpha\rangle = |\beta\rangle$ ,  $I_+ |\alpha\rangle = I_- |\beta\rangle = 0$ , matrix forms for the operators  $I_x$  and  $I_y$  can be derived.

$$I_x = 1/2 \begin{bmatrix} 0 & 1 \\ 1 & 0 \end{bmatrix} \quad (1.35)$$

$$I_y = i/2 \begin{bmatrix} 0 & -1 \\ 1 & 0 \end{bmatrix} \quad (1.36)$$

Similarly, for two interacting spins,

$$I_{z_1} = 1/2 \begin{bmatrix} 1 & 0 & 0 & 0 \\ 0 & 1 & 0 & 0 \\ 0 & 0 & -1 & 0 \\ 0 & 0 & 0 & -1 \end{bmatrix}, I_{z_2} = 1/2 \begin{bmatrix} 1 & 0 & 0 & 0 \\ 0 & -1 & 0 & 0 \\ 0 & 0 & 1 & 0 \\ 0 & 0 & 0 & -1 \end{bmatrix} \quad (1.37)$$

$$I_{x_1} = 1/2 \begin{bmatrix} 0 & 0 & 1 & 0 \\ 0 & 0 & 0 & 1 \\ 1 & 0 & 0 & 0 \\ 0 & 1 & 0 & 0 \end{bmatrix}, I_{x_2} = 1/2 \begin{bmatrix} 0 & 1 & 0 & 0 \\ 1 & 0 & 0 & 0 \\ 0 & 0 & 0 & 1 \\ 0 & 0 & 1 & 0 \end{bmatrix}, \text{ and} \quad (1.38)$$

$$I_{y_1} = i/2 \begin{bmatrix} 0 & 0 & -1 & 0 \\ 0 & 0 & 0 & -1 \\ 1 & 0 & 0 & 0 \\ 0 & 1 & 0 & 0 \end{bmatrix}, I_{y_2} = i/2 \begin{bmatrix} 0 & -1 & 0 & 0 \\ 1 & 0 & 0 & 0 \\ 0 & 0 & 0 & -1 \\ 0 & 0 & 1 & 0 \end{bmatrix}. \quad (1.39)$$

### 1.5.2 The density matrix, the density operator, and the concept of coherence

The expectation value of an observable associated with the operator  $A$ , is given by

$$\langle A \rangle = \langle \psi(t) | A | \psi(t) \rangle. \quad (1.40)$$



If we consider a single spin with a wavefunction stated in Eq. (1.4), we obtain the following expression for the expectation value of  $A$ ,

$$\langle A(t) \rangle = c_{\uparrow}^* c_{\uparrow} \langle \alpha | A | \alpha \rangle + c_{\uparrow}^* c_{\downarrow} \langle \alpha | A | \beta \rangle + c_{\downarrow}^* c_{\uparrow} \langle \beta | A | \alpha \rangle + c_{\downarrow}^* c_{\downarrow} \langle \beta | A | \beta \rangle \quad (1.41)$$

$$= Tr \left\{ \begin{bmatrix} c_{\uparrow}^* c_{\uparrow} & c_{\downarrow}^* c_{\uparrow} \\ c_{\uparrow}^* c_{\downarrow} & c_{\downarrow}^* c_{\downarrow} \end{bmatrix} \begin{bmatrix} \langle \alpha | A | \alpha \rangle & \langle \alpha | A | \beta \rangle \\ \langle \beta | A | \alpha \rangle & \langle \beta | A | \beta \rangle \end{bmatrix} \right\}, \quad (1.42)$$

where  $Tr$  is the trace of a matrix (the sum of its diagonal elements), and the  $*$  denotes a complex conjugate. In reality, we have more than a single spin, and thus an ensemble average needs to be taken as well, that is we wish to calculate  $\overline{\langle A(t) \rangle}$ .

$$\Rightarrow \overline{\langle A(t) \rangle} = Tr \left\{ \begin{bmatrix} \overline{c_{\uparrow}^* c_{\uparrow}} & \overline{c_{\downarrow}^* c_{\uparrow}} \\ \overline{c_{\uparrow}^* c_{\downarrow}} & \overline{c_{\downarrow}^* c_{\downarrow}} \end{bmatrix} \begin{bmatrix} \langle \alpha | A | \alpha \rangle & \langle \alpha | A | \beta \rangle \\ \langle \beta | A | \alpha \rangle & \langle \beta | A | \beta \rangle \end{bmatrix} \right\} \quad (1.43)$$

The left hand matrix in the product is termed the density matrix and its elements can be derived from a density operator,  $\rho$ , such that  $\langle \alpha | \rho | \alpha \rangle = \overline{c_{\uparrow}^* c_{\uparrow}}$ ,  $\langle \alpha | \rho | \beta \rangle = \overline{c_{\downarrow}^* c_{\uparrow}}$ ,  $\langle \beta | \rho | \alpha \rangle = \overline{c_{\uparrow}^* c_{\downarrow}}$ , and  $\langle \beta | \rho | \beta \rangle = \overline{c_{\downarrow}^* c_{\downarrow}}$ . It can be shown that

$$\overline{\langle A(t) \rangle} = Tr(\rho A). \quad (1.44)$$

Using the high temperature approximation of the Boltzmann distribution and the conservation of probability, the density operator at thermal equilibrium can be calculated to be

$$\rho_{eq} = \frac{1}{2} I_d + \frac{\gamma \hbar B_o}{2kT} I_z, \quad (1.45)$$

where  $k$  is Boltzmann's constant,  $T$  is the temperature in Kelvins, and  $I_d$  is the identity matrix. The identity matrix is a static term and can be discarded; in most calculations the proportionality constant  $\frac{\gamma \hbar B_o}{2kT}$  is also dropped leaving us with

$$\rho_{eq} = I_z. \quad (1.46)$$

It is apparent from Eq. (1.43) that every density matrix element can be expressed as a product  $c_a^* c_{a'}$ , where the coefficients are complex numbers, therefore

$$c_a^* c_{a'} = |c_a| |c_{a'}| \exp(i(\theta_a - \theta_{a'})). \quad (1.47)$$

From the above relation, it is clear that in order to have a finite value for a density matrix element, there must exist a statistical correlation, or *coherence*, between the states  $|a\rangle$  and  $|a'\rangle$  so that  $\overline{\exp(i(\theta_a - \theta_{a'}))} \neq 0$ . For diagonal elements, where  $a = a'$ ,  $c_a^* c_a = |c_a|^2$  which is always a real quantity and therefore coherence is not necessary to obtain finite diagonal elements. In fact, the diagonal elements give the probability of finding the spin in state  $|a\rangle$ . The off-diagonal elements, which if finite, imply coherence between the  $|\alpha\rangle$  and  $|\beta\rangle$  states for a single spin and are called single quantum coherences, SQCs.

### 1.5.3 The density matrix for two interacting spins and the concept of multiple quantum coherence (MQC)

For a system of two coupled spins, the general form of the density matrix is

$$\begin{array}{cccc}
 & |\alpha\alpha\rangle & |\alpha\beta\rangle & |\beta\alpha\rangle & |\beta\beta\rangle \\
 |\alpha\alpha\rangle & \overline{c_{\uparrow\uparrow}^* c_{\uparrow\uparrow}} & \overline{c_{\uparrow\downarrow}^* c_{\uparrow\uparrow}} & \overline{c_{\downarrow\uparrow}^* c_{\uparrow\uparrow}} & \overline{c_{\downarrow\downarrow}^* c_{\uparrow\uparrow}} \\
 |\alpha\beta\rangle & \overline{c_{\uparrow\uparrow}^* c_{\uparrow\downarrow}} & \overline{c_{\uparrow\downarrow}^* c_{\uparrow\downarrow}} & \overline{c_{\downarrow\uparrow}^* c_{\uparrow\downarrow}} & \overline{c_{\downarrow\downarrow}^* c_{\uparrow\downarrow}} \\
 |\beta\alpha\rangle & \overline{c_{\uparrow\uparrow}^* c_{\downarrow\uparrow}} & \overline{c_{\uparrow\downarrow}^* c_{\downarrow\uparrow}} & \overline{c_{\downarrow\uparrow}^* c_{\downarrow\uparrow}} & \overline{c_{\downarrow\downarrow}^* c_{\downarrow\uparrow}} \\
 |\beta\beta\rangle & \overline{c_{\uparrow\uparrow}^* c_{\downarrow\downarrow}} & \overline{c_{\uparrow\downarrow}^* c_{\downarrow\downarrow}} & \overline{c_{\downarrow\uparrow}^* c_{\downarrow\downarrow}} & \overline{c_{\downarrow\downarrow}^* c_{\downarrow\downarrow}}
 \end{array}, \quad (1.48)$$

with the diagonal elements again corresponding to the populations of each state, and off-diagonal elements corresponding to coherences between states. If the two spins, one with frequency  $\omega_1$ , the other with frequency  $\omega_2$  (in the rotating frame of reference), are weakly-coupled ( $\omega_1 - \omega_2 \gg 2\pi J$ ), then the rotating frame Hamiltonian is  $\mathcal{H} = -\hbar(\omega_1 I_{z_1} + \omega_2 I_{z_2} - 2\pi J I_{z_1} I_{z_2})$ . Putting this Hamiltonian in matrix representation allows the energies of each state to be calculated. Figure 1.16 shows the energy level diagram for the four states. The difference of the quantum numbers associated with the energy levels involved in a transition defines the order of the coherence (either zero, single, or double quantum coherence). Note that the double quantum coherence (DQC) transition involves the sum of the chemical shift frequencies, whereas the zero quantum coherence (ZQC) transition involves their difference. Both ZQCs and DQCs are termed multiple quantum coherences (MQCs). Only SQCs can directly induce observable magnetization. To obtain SQCs, a single RF pulse is required to perturb the spin system

from thermal equilibrium, whereas to produce MQCs, at least two RF pulses are required with a delay between them. For an N-spin system, the maximum possible coherence order is N.

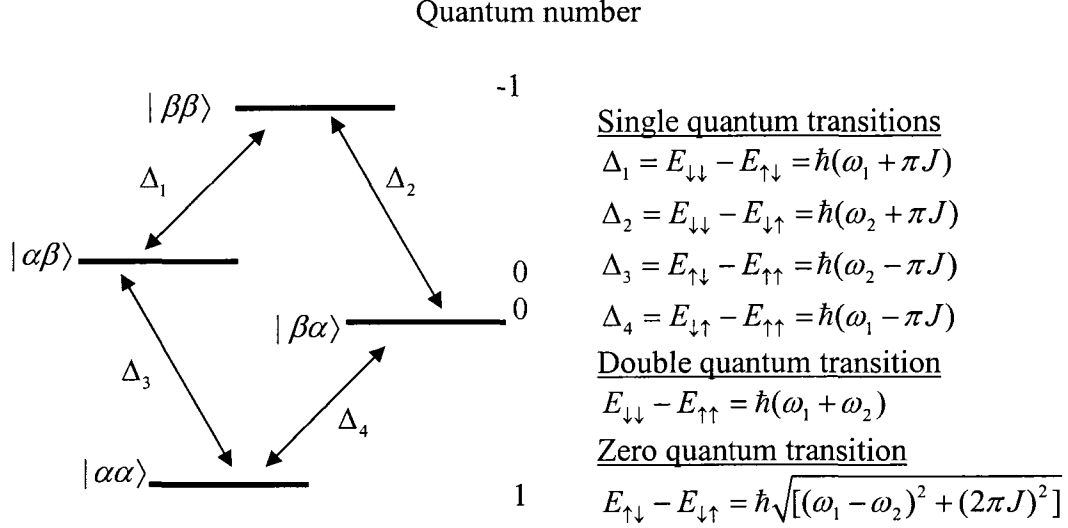


Figure 1.16: Energy level diagram of two weakly-coupled spins in a static field  $B_0$ .

The matrix below shows which elements in the density matrix are associated with the different coherence orders. The subscripts 1 and 2, correspond to spin 1 and spin 2, respectively, and Popn. refers to population.

	$ \alpha\alpha\rangle$	$ \alpha\beta\rangle$	$ \beta\alpha\rangle$	$ \beta\beta\rangle$	
$ \alpha\alpha\rangle$	Popn.	SQC <sub>2</sub>	SQC <sub>1</sub>	DQC	
$ \alpha\beta\rangle$	SQC <sub>2</sub>	Popn.	ZQC	SQC <sub>1</sub>	(1.49)
$ \beta\alpha\rangle$	SQC <sub>1</sub>	ZQC	Popn.	SQC <sub>2</sub>	
$ \beta\beta\rangle$	DQC	SQC <sub>1</sub>	SQC <sub>2</sub>	Popn.	

While the single-spin density operator can be expressed as a linear combination of four basis operators ( $I_x, I_y, I_z$ , and  $I_d$ ), the two-spin system basis consists of 16 operators, namely, four longitudinal operators:  $I_{z_1}, I_{z_2}, I_{z_1}I_{z_2}$ , and  $I_d$ , four transverse in-phase operators:  $I_{x_1}, I_{x_2}, I_{y_1}$ , and  $I_{y_2}$ , four transverse anti-phase operators:  $I_{x_1}I_{z_2}, I_{y_1}I_{z_2}, I_{z_1}I_{x_2}$ , and  $I_{z_1}I_{y_2}$ , and four multiple quantum operators:  $I_{x_1}I_{x_2}, I_{y_1}I_{y_2}, I_{x_1}I_{y_2}$ ,

and  $I_{Y_1}I_{X_2}$ . The first two longitudinal terms represent the thermal equilibrium magnetizations, and for a two spin system the density operator at thermal equilibrium is the sum of these two operators. The third longitudinal term is rarely produced in an *in-vivo* NMR experiment, and the identity matrix is discarded because it is a static contribution. The transverse in-phase and anti-phase coherences are all SQCs because they represent coherence between states that have quantum numbers that differ by 1. The in-phase terms are responsible for observable magnetization; the anti-phase terms while not directly observable, can evolve into in-phase magnetization. The difference between the two types of coherence can be illustrated by their matrix representations.

$$I_{X_1} = \frac{1}{2} \begin{bmatrix} 0 & 0 & 1 & 0 \\ 0 & 0 & 0 & 1 \\ 1 & 0 & 0 & 0 \\ 0 & 1 & 0 & 0 \end{bmatrix} \quad 2I_{X_1}I_{Z_2} = \frac{1}{2} \begin{bmatrix} 0 & 0 & 1 & 0 \\ 0 & 0 & 0 & -1 \\ 1 & 0 & 0 & 0 \\ 0 & -1 & 0 & 0 \end{bmatrix} \quad (1.50)$$

The finite elements represent coherences corresponding to the transitions  $\Delta_1$  and  $\Delta_4$  in Fig. 1.16. The negative values in the matrix  $2I_{X_1}I_{Z_2}$  indicate a 180° phase shift between the two transitions, and thus the coherence is termed anti-phase. For  $I_{X_1}$  both the transitions are in phase and thus it is termed an in-phase coherence. The phase difference evolves under the influence of scalar coupling.

The ZQC contribution has real ( $ZQC_X$ ) and imaginary ( $ZQC_Y$ ) components;  $ZQC_X = I_{X_1}I_{X_2} + I_{Y_1}I_{Y_2}$ , and  $ZQC_Y = I_{X_1}I_{Y_2} - I_{Y_1}I_{X_2}$ . The ZQC represents a transition between the  $|\alpha\beta\rangle$  and the  $|\beta\alpha\rangle$  states. The transition associated with the ZQC is directly undetectable. Similarly, the DQC has real and imaginary components;  $DQC_X = I_{X_1}I_{X_2} - I_{Y_1}I_{Y_2}$ , and  $DQC_Y = I_{X_1}I_{Y_2} + I_{Y_1}I_{X_2}$ . The DQC represents a transition between the states  $|\alpha\alpha\rangle$  and  $|\beta\beta\rangle$ , which differ by a quantum number of 2, and like the ZQC transition, it is not directly detectable.

#### 1.5.4 Evolution of the density operator

Equation (1.46) gives the density operator at thermal equilibrium while Eq. (1.44) indicates how the expectation value of an operator at a certain time can be calculated if

the density operator at that time is known. Therefore, if the evolution of the density operator can be tracked throughout a pulse sequence, then so can the expectation values of any operators of interest. The Liouville-von Neumann equation stated below allows us to do this.

$$\frac{\partial}{\partial t} \rho = \frac{i}{\hbar} [\rho, \mathcal{H}(t)], \quad (1.51)$$

where  $\mathcal{H}$  is the Hamiltonian including the effects of all interactions (chemical shift, scalar coupling, RF and gradient pulses). This relation arises from the time dependent Schrödinger equation,  $i\hbar \frac{\partial}{\partial t} \psi(t) = \mathcal{H} \psi(t)$ . When  $\mathcal{H}$  is time-independent, the solution to Eq. (1.51) is

$$\rho(t) = \exp(-i\mathcal{H}t/\hbar) \rho(0) \exp(i\mathcal{H}t/\hbar), \quad (1.52)$$

where  $\rho(0)$  is the initial condition of the density operator. By breaking up a pulse sequence into a number of segments, each with its own time-independent Hamiltonian, the density operator can be calculated for each segment. Using Eq. (1.52) transformation tables have been derived for two-spin weakly-coupled systems illustrating how operators transform under the influence of the Zeeman interaction, scalar coupling, and RF pulses. This method of manual spin evolution calculation is called the product operator approach and is useful for systems consisting of one or two spins (58). These transformation tables are given in Appendix 1. Similar tables have been derived for spin systems with two strongly-coupled spins (59). Appendix 2 illustrates the more complicated evolution of a strongly-coupled spin pair compared to that of a weakly-coupled pair.

For spin systems such as glutamate that contains four strongly-coupled spins, it is quite impractical to rely on the product operator approach, and numerical methods of analysis need to be utilized. The numerical method of analysis used in this thesis is described in detail in chapter 3.

### 1.5.5 Gradients for coherence selection

Equation (1.31) applied to a coherence of order 1. For a coherence of order  $p$ , the phase accumulation can be given by

$$\theta_{gradient} = -\rho\gamma \int_0^{\Delta t} \vec{G} \cdot \vec{r} dt. \quad (1.53)$$

Appendix 3 gives the transformations under the influence of a gradient. Because coherences of different order accumulate phases differently in the presence of a magnetic field gradient, gradients with specific ratios can be used to dephase and subsequently rephase only desired signal. For example, if a gradient with area A is applied to dephase an SQC and a DQC, the DQC will accumulate twice the phase as the SQC, and if an RF pulse is then applied to transform the DQC into an SQC, a gradient of area 2A will be required to rephase the term which originally existed as a DQC. This gradient will not, however, rephase the original SQC. This method of selectively retaining only certain coherences is known as gradient filtering, and is useful, for example, in eliminating signal from uncoupled spins which cannot exist as MQCs. Pulse sequences that choose specific coherence levels are known as multiple quantum filters.

## **1.6 RF Probes (Coils)**

As was mentioned in §1.2.3, the role of the RF coil is to provide the rotating field  $\vec{B}_1(t)$  and to receive the NMR signal. Ideally, the RF coil should transmit a transverse, circularly polarized magnetic field that is uniform over its volume so that nuclei in different regions respond in the same manner to the RF field. The principle of reciprocity (60) states that if a unit of direct current applied to the coil produces a field  $\vec{B}_1$  at a certain location in the sample, then the induced emf in the coil by the precessing excited magnetization will be proportional to the created field. This implies that if a coil efficiently excites nuclei at a certain location in space then it will also efficiently receive signal from them.

An RF coil can be thought of a resonating LC circuit tuned to the Larmor frequency of interest. There are two main categories of RF coils, namely, surface coils, and volume coils. Surface coils are relatively small and can be placed directly over the region of the body from which signal is desired. However, they do not produce homogeneous fields and are only sensitive within a fraction of their diameter along the axial direction. Surface coils are usually desirable for receiving only because their small field of view limits the amount of noise picked up from the subject. In the case that a

surface coil is being employed for reception only, a larger coil, a volume coil, is used for transmission. The birdcage coil (61) is the most widely used volume coil and it is known for its field homogeneity.

### 1.6.1 Surface coils and linear excitation

Figure 1.17 shows a diagram of a surface coil placed around a sample (which if not a subject, is referred to as a phantom). The capacitor  $C$  is selected to resonate with the inductance  $L$  provided by the loop wire, at the desired resonance frequency  $\omega_o$ .

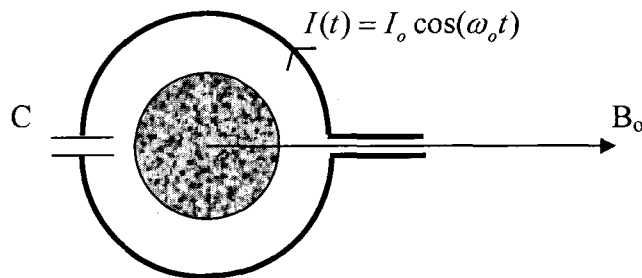


Figure 1.17: Simple diagram of an RF surface coil. The coil axis is into the page.

If a sinusoidally varying current is passed through the coil as shown in the figure, a linearly polarized field  $B(t)$  will be produced along the coil's axis as shown in Fig. 1.18. At any instant of time, this field can be broken into two counter-rotating components of constant amplitude  $\frac{1}{2}B$ . The nuclei will only couple with the component rotating in a negative sense like the nuclei (if  $\gamma > 0$ ); in other words, one of the counter-rotating components is the effective  $B_1(t)$  required to excite the spins. The other component only contributes to losses and by reciprocity to noise during reception.

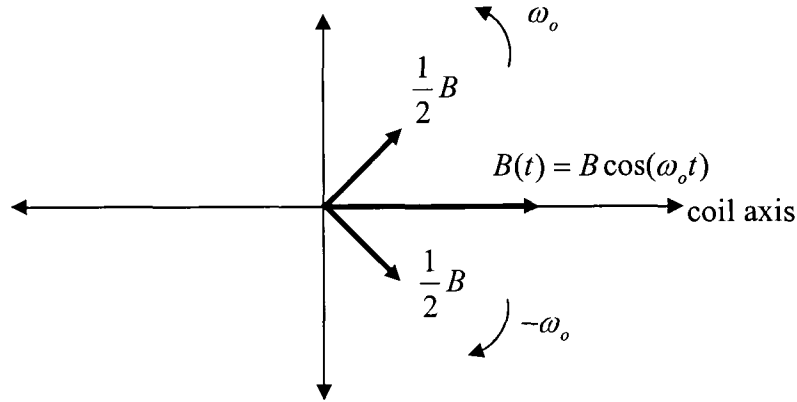


Figure 1.18: A linearly polarized field can be broken up into two counter rotating components each of constant amplitude  $B/2$ . The nuclei only interact with the component rotating in the same sense of them. This means the negative sense for nuclei with positive  $\gamma$ . The static field strength direction is into the page.

### 1.6.2 Birdcage coils and quadrature excitation

The birdcage coil design is based on the fact that a uniform transverse magnetic field can be created by a longitudinal current density confined to the surface of an infinitely long circular cylinder with a sinusoidal dependence on the azimuthal angle (62). The birdcage coil employs  $N$  equally spaced current carrying conductors (termed the legs of the coil) on the surface of a cylinder and an LC ladder network in order to create the required current distribution (61). Figure 1.19 shows the structure of a birdcage coil and its LC ladder network elements. For a birdcage coil of  $N$  legs, the current in each leg at time  $t = 0$  is given by

$$I_n = I_o \cos\left(2\pi \frac{M}{N}[n-1]\right), \text{ or } I_n = I_o \sin\left(2\pi \frac{M}{N}[n-1]\right), \quad (1.54)$$

where  $n$  denotes the leg number and  $M$  the mode number; the two solutions represent two degenerate modes of the coil. The mode  $M=1$ , where the total phase shift around the coil is equal to  $2\pi$ , is the useful mode for NMR. Because the birdcage coil has two degenerate modes, it has the capability of producing a purely circularly polarized field by quadrature excitation. Quadrature excitation refers to exciting the coil at two points physically  $90^\circ$  apart on the surface of the cylinder with currents that are  $90^\circ$  out of phase with each other. The result is a circularly polarized  $B_1$  field that rotates in the  $xy$  plane. The advantage of quadrature operation over linear operation is a  $\sqrt{2}$  enhancement in



sensitivity and a factor of 1/2 reduction in required power because there is no “wasted” counter-rotating component (63).

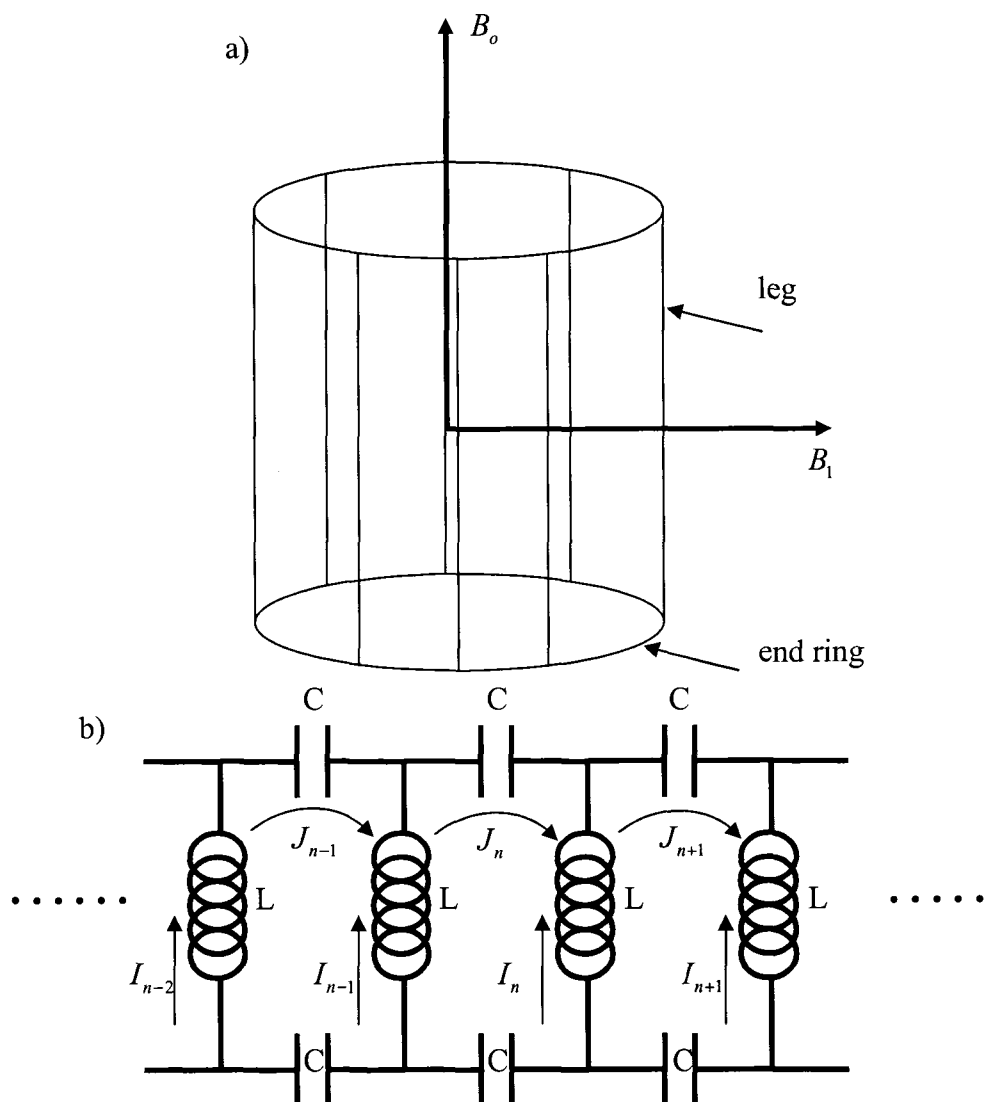


Figure 1.19: a) The general structure of a birdcage coil. b) A section of the ladder network which consists of the same pattern repeated  $N$  times and joined at the ends to form the circular structure in (a). The inductors represent the inductances of the copper strips or wire used to form the legs. Although not shown in the figure, the end rings are also formed by copper strips and have some inductance associated with them. The leg currents are related to the mesh currents by  $I_n = J_{n+1} - J_n, n = 0, 1, \dots, (N - 1)$ .

### 1.6.3 Impedance matching

To ensure maximum power transfer to and from the coil, and to prevent wave reflections, it is required to match the impedance of the coil to that of the characteristic impedance of the coaxial cable (usually  $50 \Omega$ ). This is done by using discrete capacitors

and inductors. Often the matching network is configured so that it transforms an unbalanced voltage, such as that with a coaxial cable, where one conductor is always at ground potential, to a balanced voltage, where the signals on the two conductors of the balanced transmission line are equal and opposite in sign relative to the ground potential, and vice versa (64,65). The benefit of balancing the RF coil is that the maximum voltage to ground is reduced, thereby reducing dielectric losses.

#### 1.6.4 The quality factor

An important measurement of a coil is its quality factor,  $Q$ , which gives the ratio of the maximum energy stored at resonance to that of the energy dissipated per cycle. The quality factor is usually measured by

$$Q = \frac{\omega_o}{BW}, \quad (1.55)$$

where  $BW$  is the 3 dB width of the resonance curve. The  $Q$  of a coil is an indicator of its performance; in particular, the ratio  $\frac{Q_{unloaded}}{Q_{loaded}}$  (the subscript unloaded describes the situation of no load, and loaded refers to the introduction of a magnetically lossy sample such as saline in the vicinity of the coil) should be as high as possible because this indicates that sample losses dominate those of the coil itself.

#### 1.6.5 The SNR of an NMR experiment

The emf induced in the coil during signal reception is given by Faraday's law of electromagnetic induction

$$\mathcal{E} = -\frac{d\phi}{dt}, \quad (1.56)$$

where  $\phi$  is the magnetic flux.

$$\Rightarrow \mathcal{E} = -\frac{\partial}{\partial t} \oint \vec{M}_{xy}(t) \cdot \vec{da} \quad (1.57)$$

$$\begin{aligned} \Rightarrow \mathcal{E} &\propto -\frac{\partial}{\partial t} M_{xy}(t) \\ &= -iM\omega_o \exp(-i\omega_o t) \\ &= -iM\gamma B_o \exp(-i\omega_o t) \end{aligned} \quad (1.58)$$

Combining Eqs. (1.6) and (1.56) we see that the detected NMR signal (assuming a 90° excitation pulse was applied) is proportional to the square of the static field strength and to the cube of the gyromagnetic ratio of the nucleus. The NMR signal is also proportional to  $\eta$ , the coil filling factor which is a measure of the sample volume to the total coil volume (66). The signal is also proportional to the “reception quality” of the coil, which by reciprocity can be thought of as the amount of transverse  $B_T$  produced by the coil for a unit current. Thus we can write the following proportionality relation for the signal voltage

$$V_{signal} \propto M\omega_o\eta B_T. \quad (1.59)$$

It is apparent from the above relation that the higher the filling factor, the larger the signal voltage and thus coils that have been carefully tailored to the part of the anatomy being studied are expected to yield a higher SNR (67).

Noise in the NMR experiment mainly arises from noise generated by the thermal excitation of charge carriers in the body and in the coil itself. The amplitude of this noise is described by the standard deviation of the noise voltage (68)

$$V_{noise} = \sigma_n = \sqrt{4kTR_i\Delta f}, \quad (1.60)$$

where  $k$  is Boltzmann’s constant,  $T$  is the absolute temperature, and  $\Delta f$  is the receiver bandwidth.  $R_i$  is the resistance of the receiver coil and the resistance of the sample as seen by the coil. We can consider these two resistances as series resistors,  $R_{coil}$  and  $R_{sample}$ . Moreover, the resistance is proportional to the power dissipated for a unit current into the coil and thus

$$\Rightarrow V_{noise} \propto \sqrt{4KT_{coil}\Delta fP_{coil} + 4KT_{sample}\Delta fP_{sample}}. \quad (1.61)$$

For a good conductor, the skin depth (penetration depth of an electromagnetic field) is given by (69)

$$\delta = \sqrt{\frac{2}{\mu\sigma\omega}}, \quad (1.62)$$

where  $\omega$  is the frequency of operation,  $\sigma$  is the conductivity, and  $\mu$  is the magnetic permeability of the conductor. The resistance of a conductor,  $R_{cond}$ , is equal to  $\frac{l}{\sigma A}$ , where  $l$  is the length of the conductor, and  $A$  is the cross sectional area of conduction and

is proportional to  $\delta$ . This implies that  $R \propto \frac{1}{\delta}$ , which results in  $R_{coil} \propto P_{coil} \propto \sqrt{\omega}$ . The power dissipated in the sample, on the other hand, is proportional to  $E^2$  (62), where E is the magnitude of the electric field produced by the coil. From Faraday's law,  $E \propto -\frac{dB}{dt} \propto -\frac{d}{dt} \exp(-i\omega_o t)$ ; this implies that  $E \propto \omega_o$ . Therefore,  $P_{sample} \propto \omega_o^2$ .

$$\Rightarrow \frac{V_{signal}}{V_{noise}} \propto \frac{\omega_o^2}{\sqrt{a\omega_o^{1/2} + b\omega_o^2}}, \quad (1.63)$$

where a and b contain factors such as coil and sample geometries and temperatures (70). Although for *in-vivo* NMR at field strengths above a fraction of a tesla where sample noise dominates and thus

$$\Rightarrow \frac{V_{signal}}{V_{noise}} \propto \omega_o \propto B_o, \quad (1.64)$$

proper coil design is still essential for optimal SNR. For example, ensuring that the field of view of the coil is limited to the region of interest of the sample will minimize the amount noise acquired.

## **1.7 $^1\text{H}$ MRS and $^{13}\text{C}$ MRS**

The  $^1\text{H}$  nucleus is the most commonly used nucleus in *in-vivo* MRS because it is 100% naturally abundant and has the largest magnetic moment of the nuclei in the body, thus giving the greatest SNR compared to other nuclei. However, there are complications that arise with  $^1\text{H}$  MRS *in vivo*. One complication is the large water concentration (about 55M) present compared to metabolite concentrations which are on the order of mM. This results in a large water peak that is about  $10^4$  times larger than metabolite peaks, making it necessary to include water suppression techniques in any experiment in order to observe the metabolites. The residual water signal after suppression may still affect the determination of other signal intensities (71). Another problem is the fact that most of the metabolite information in an *in-vivo*  $^1\text{H}$  spectrum lies in a narrow chemical shift range of about 5 ppm (72). Thus a  $^1\text{H}$  spectrum contains many overlapping peaks from many metabolites often complicating the interpretation of results. Also, certain metabolites, for example, glutamate (Glu) and glutamine (Gln) have very similar chemical structures

which results in them having very similar multiplet spectral structures, thereby making it difficult to distinguish between the two (73). Furthermore, the majority of key metabolites are strongly coupled which introduces further complications to the interpretation of *in-vivo* proton spectra (73).

Carbon-13, which is only 1.1% naturally abundant, is the only NMR viable isotope of carbon. An advantage of  $^{13}\text{C}$  NMR is that the signals occupy a wide range of chemical shifts (about 200 ppm) (74) and hence spectral resolution is much better than that obtained with  $^1\text{H}$  NMR, as shown in Fig. 1.20.

In addition, the absence of a strong water peak removes the problems associated with water suppression, and the effects of the residual water signal on the resulting spectrum. However, the sensitivity of  $^{13}\text{C}$  is less than that of  $^1\text{H}$  because  $\gamma_{\text{C}} \approx \gamma_{\text{H}} / 4$ . The low sensitivity of  $^{13}\text{C}$  in conjunction with its low natural abundance results in an SNR factor of  $\approx 1600$  less than that obtainable with  $^1\text{H}$ . Although the low natural abundance may appear to be a disadvantage at first sight, it can be turned to advantage by incorporating  $^{13}\text{C}$  enriched and labelled substrates into the body and measuring time courses of the  $^{13}\text{C}$  label into the products of metabolism. Figure 1.21 shows a simple illustration of how this labelling occurs when infusing the most commonly used enriched substrate, 99% [ $1\text{-}^{13}\text{C}$ ]-glucose (glucose that is 99%  $^{13}\text{C}$  enriched at its  $\text{C}_1$  carbon site). By acquiring  $^{13}\text{C}$  spectra at regular intervals during the time course of an infusion study, the rates of increase of the carbon peaks can be observed and thus measures for the rates of associated cycles can be determined.

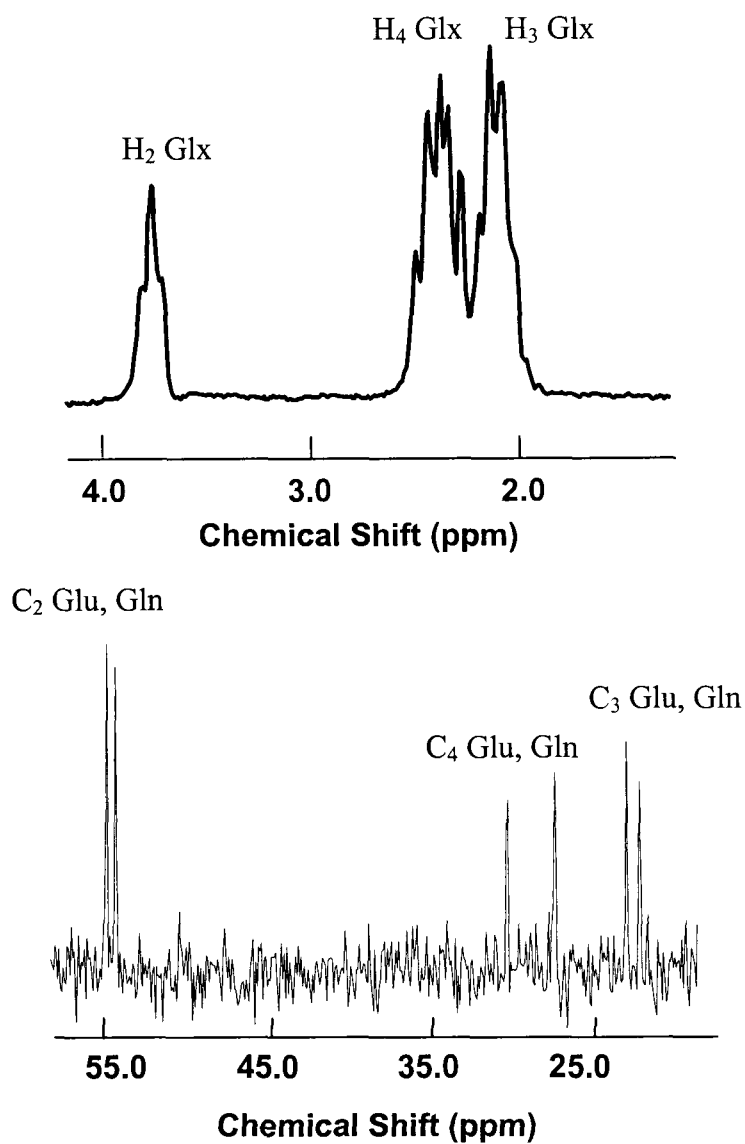


Figure 1.20: The top spectrum is a proton spectrum of a phantom consisting of 200 mM Glu and 200 mM Gln (collectively termed Glx) obtained at 3.0 T ( $\approx$  128 MHz). H<sub>2</sub>, H<sub>3</sub>, and H<sub>4</sub> refer to the protons bonded to the C<sub>2</sub>, C<sub>3</sub>, and C<sub>4</sub> carbons, respectively (the A, MN, and PQ protons in Fig. 1.9, respectively.). Observe the strong overlap between the Glu and Gln peaks. The bottom spectrum is a  $^{13}\text{C}$  spectrum of the same solution obtained at 3.0 T. The larger  $^{13}\text{C}$  chemical shifts allows better discrimination of Glu and Gln.

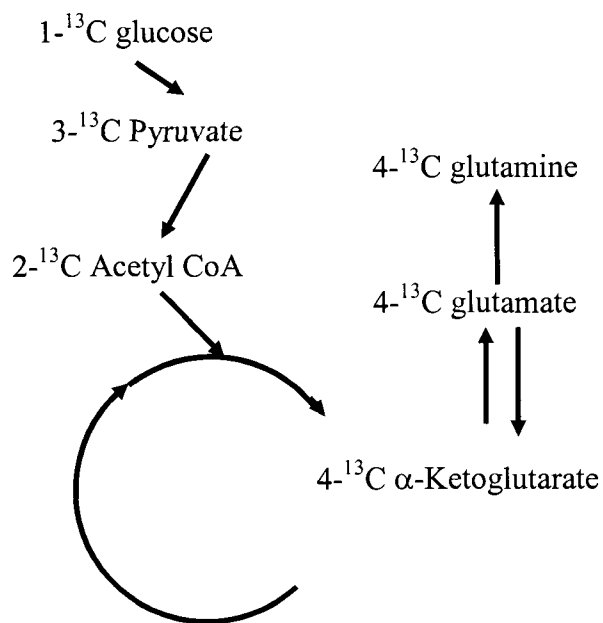


Figure 1.21: Infusion of [1-<sup>13</sup>C] glucose leads to <sup>13</sup>C label accumulating in the products of the tricarboxylic acid cycle. On the first round of the cycle, the C<sub>4</sub> of Glu is labelled and conversion of Glu to Gln via the Glu/Gln cycle in the astrocytes leads to label accumulation on the C<sub>4</sub> site of Gln.

Of particular interest are the rates of the tricarboxylic acid (TCA) cycles in neurons and in astrocytes and the rate of the Glu/Gln cycle and how these rates change under diseased conditions. Glutamate is a major excitatory neurotransmitter and any excess amounts of it in the synaptic cleft are rapidly taken up by astrocytes, preventing over-activation of Glu receptors. In the astrocytes, Glu is converted to Gln, an inert metabolite, which is then transported back to the neuron where it can be converted to Glu (75). Only naming a few diseases, abnormalities in the levels of Glu or Gln have been reported in mood disorders (76,77), schizophrenia (26,78), amyotrophic lateral sclerosis (ALS) (79,80), and Alzheimer's disease (81,82). Although proton MRS has played a valuable role in determining differences in concentration levels of relevant metabolites between normal and diseased brains, being able to measure the rates of the cycles that yield these end-point concentration provides much deeper insight into the mechanisms involved in the disorders. Thus the power of <sup>13</sup>C NMR in conjunction with the infusion of <sup>13</sup>C enriched substrates is apparent. A number of <sup>13</sup>C studies have been carried out to measure the rates of the TCA cycle and the Glu/Gln cycle both in humans and in rats (29-36).

## 1.8 Double Resonance

Double resonance NMR experiments involve two nuclear species and hence utilize two radiofrequency (RF) channels. The channel which transmits at the frequency of the “observe” nucleus, i.e. the species which is responsible for the observed signal, is known as the observing channel. The other channel, which excites the other nuclear species and decouples the two species, is known as the decoupling channel. For example, in a direct  $^{13}\text{C}$  experiment,  $^{13}\text{C}$  is the observe nucleus and  $^1\text{H}$  is the decoupling nucleus. This relationship is often denoted as  $^{13}\text{C} \{^1\text{H}\}$ , where the decoupling nucleus is placed between brackets. In an indirect  $^{13}\text{C}$  experiment (see §1.8.3), the  $^{13}\text{C}$  signal is observed indirectly by detecting signal from protons coupled to the  $^{13}\text{C}$  nuclei of interest, and in such a situation,  $^1\text{H}$  would be the observe nucleus, and  $^{13}\text{C}$  the decoupling nucleus, represented by  $^1\text{H}\{^{13}\text{C}\}$ .

### 1.8.1 Proton decoupling during acquisition

The scalar coupling between  $^{13}\text{C}$  and  $^1\text{H}$  nuclei causes individual chemically shifted  $^{13}\text{C}$  peaks in a spectrum to split into multiplets (see §1.3.2), thereby complicating the spectrum and making it more difficult to interpret. Proton decoupling involves irradiating at the proton frequency during the  $^{13}\text{C}$  signal acquisition period of the experiment. To be effective, this field (usually termed  $B_2$ ) requires an amplitude such that  $\gamma_{\text{H}}B_2 \gg nJ$ , where  $J$  is the heteronuclear scalar coupling constant, and  $n$  is the number of lines in the multiplet (83). Proton decoupling eliminates the spectral effects of scalar coupling between  $^{13}\text{C}$  and  $^1\text{H}$  and therefore a structurally distinguishable  $^{13}\text{C}$  atom produces only a single resonance peak whose area is equal to the sum of the area under the scalar coupled multiplet peaks. Usually, the proton irradiation is carried out using the WALTZ-16 decoupling scheme which is a cycle consisting of  $90^\circ$ ,  $180^\circ$ ,  $270^\circ$ , and  $360^\circ$  hard pulses, where each pulse is  $180^\circ$  out of phase with the previous one (84). Figure 1.22 demonstrates the effect of proton decoupling.



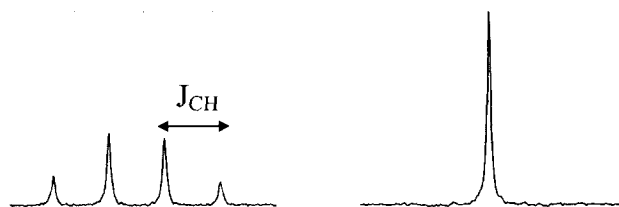


Figure 1.22: The spectrum on the left is a 3.0 T  $^{13}\text{C}$  spectrum of the  $\text{CH}_3$  molecular group of a 10 M acetic acid phantom. The splitting between the peaks is equal to the heteronuclear scalar coupling constant ( $\approx 130$  Hz). The spectrum on the right is a WALTZ-16 proton decoupled spectrum of that on the left. The multiplets have collapsed into a singlet, thereby simplifying the spectrum and enhancing the SNR.

### 1.8.2 Polarization transfer

To obtain greater increases in SNR than that provided by broadband decoupling,  $^1\text{H}$  polarization can be transferred to the  $^{13}\text{C}$  signal by exploiting the scalar coupling between  $^1\text{H}$  and  $^{13}\text{C}$ . Two such polarization transfer sequences are the Inensitive Nuclei Enhanced by Polarization Transfer (50), and the Distortionless Enhancement by Polarization Transfer (49) sequences, termed INEPT and DEPT, respectively. To give some insight into the mechanism of polarization transfer, the DEPT sequence will be further discussed here. Figure 1.23 shows a diagram of the DEPT sequence. To understand how the sequence works, consider a CH molecular group, which can be represented as an  $IS$  spin system, where I represents the proton, and S the  $^{13}\text{C}$  nucleus. The evolution of the spin system can be followed by using the product operator approach (see Appendix 1). At thermal equilibrium the density operator equals  $\gamma_I I_Z + \gamma_S S_Z$  (the  $\gamma$  factor is usually not included; however it is included here to demonstrate the source of signal enhancement). Upon application of the proton excitation pulse,  $\gamma_I I_Z + \gamma_S S_Z \xrightarrow{90_x(I)} -\gamma_I I_Y + \gamma_S S_Z$ , and following the delay  $\tau$  which is set to  $1/2J_{IS}$ ,  $-\gamma_I I_Y + \gamma_S S_Z \xrightarrow{1/2J_{IS}} \gamma_I 2I_X S_Z + \gamma_S S_Z$ , forming proton antiphase magnetization. The  $180^\circ$  pulses are there to refocus any chemical shift evolutions. The  $180^\circ$  pulses will be ignored in the analysis because the pulses are assumed to be on resonance. The  $^{13}\text{C}$  excitation pulse forms a multiple quantum state and in-phase transverse magnetization for uncoupled  $^{13}\text{C}$  nuclei,  $\gamma_I 2I_X S_Z + \gamma_S S_Z \xrightarrow{90_x(S)} -\gamma_I 2I_X S_Y - \gamma_S S_Y$ . Following the delay and

application of the  $\theta$  pulse, which is set to  $90^\circ$  for optimal signal from a CH group,  $-\gamma_I 2I_x S_Y - \gamma_S S_Y \xrightarrow{90^\circ_y(I)} \gamma_I 2I_z S_Y - \gamma_S S_Y$ , resulting in a  $^{13}\text{C}$  antiphase coherence. After the final delay,  $\gamma_I 2I_z S_Y - \gamma_S S_Y \xrightarrow{1/2J_{IS}} -\gamma_I S_X - \gamma_S S_Y$ . To eliminate signal from uncoupled  $^{13}\text{C}$  nuclei, the phase of the last proton pulse is alternated between  $\pm y$  and the two scans are subtracted. This yields only signal from  $^{13}\text{C}$  nuclei that are  $^1\text{H}$  coupled. The factor of  $\gamma_I$  indicates that the resulting signal is  $\gamma_I/\gamma_S \approx 4$  times greater than the signal that would be observed by direct excitation of the  $^{13}\text{C}$  nuclei.

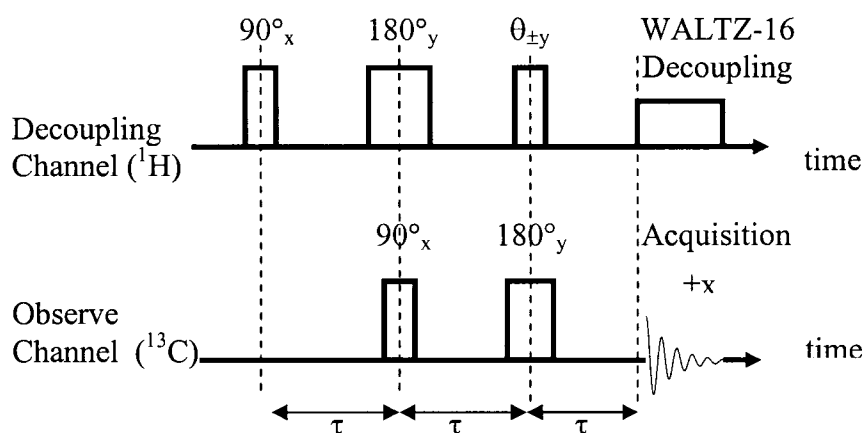


Figure 1.23: The DEPT pulse sequence, where  $\tau = 1/2J_{CH}$ .

The intensity of the final signal is actually trigonometrically dependent upon the flip angle  $\theta$  and upon the molecular group (49). For example, CH molecular groups have a resulting signal intensity given by  $\gamma_H/\gamma_C \sin\theta$ . Hence CH groups will be maximally enhanced by a factor of  $\gamma_H/\gamma_C \approx 4$  when  $\theta = 90^\circ$ .  $\text{CH}_2$  molecular groups are also maximally enhanced by a factor of  $\gamma_H/\gamma_C$  but when  $\theta = 45^\circ$  because the signal intensity is given by  $\gamma_H/\gamma_C \sin(2\theta)$ .  $\text{CH}_3$  molecular groups have signal intensities of  $0.75(\gamma_H/\gamma_C)\{\sin(3\theta)+\sin(\theta)\}$ , and hence their signals exhibit a maximum of  $1.15\gamma_H/\gamma_C$  when  $\theta = 35.26^\circ$ .

### 1.8.3 Indirect $^{13}\text{C}$ detection

Direct  $^{13}\text{C}$  detection means that the signal observed during acquisition is from the  $^{13}\text{C}$  nuclei themselves. Indirect  $^{13}\text{C}$  detection refers to observing signal from protons

coupled to  $^{13}\text{C}$  nuclei. The scalar coupling that exists between protons and  $^{13}\text{C}$  nuclei results in the appearance of satellite peaks on  $^1\text{H}$  NMR spectra. These peaks are not detectable in  $^1\text{H}$  *in-vivo* NMR spectra because of the low natural abundance of  $^{13}\text{C}$  (1.1%). However, when a  $^{13}\text{C}$  enriched and labelled substrate (for example [1- $^{13}\text{C}$ ] glucose) is administered to the subject being studied, the metabolic products of the substrates become  $^{13}\text{C}$  enriched at various carbon atoms, causing the corresponding satellite peaks on the  $^1\text{H}$  spectrum to grow. The rate at which the peaks increase is proportional to the rate of appearance of the  $^{13}\text{C}$  label on the coupled  $^{13}\text{C}$  nuclei. The main advantage of indirect  $^{13}\text{C}$  detection over direct  $^{13}\text{C}$  detection is the higher sensitivity of the  $^1\text{H}$  nucleus, resulting in a signal gain of  $\gamma_H^3 / \gamma_C^3 \approx 64$ . This higher signal allows for improved temporal resolution as less signal averaging is required to obtain sufficient SNR for each data point in  $^{13}\text{C}$  label incorporation time courses.

A common pulse sequence for indirect  $^{13}\text{C}$  detection is the Proton Observe Carbon Edited, POCE, pulse sequence (45). The basic sequence is displayed in Fig. 1.24. The  $^{13}\text{C}$  inversion pulse is applied  $1/2J_{CH}$  seconds prior to acquisition on alternate scans which are then subtracted. The inversion pulse inverts signal only from  $^{13}\text{C}$ -coupled protons so that upon subtracting the two POCE scans, any signal from protons not coupled to  $^{13}\text{C}$  nuclei is eliminated, while the desired signal is retained. In chapter 4, it is shown that this holds true only when the  $^{13}\text{C}$ -coupled protons are not strongly coupled to any other protons, an issue that has not been previously addressed.

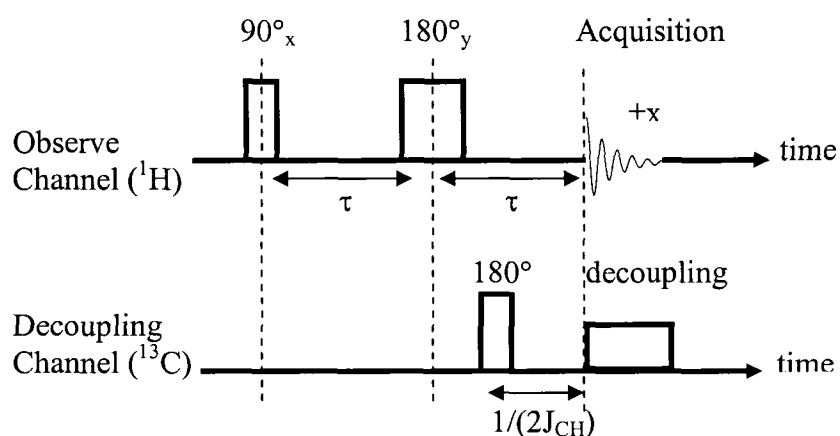


Figure 1.24: The POCE sequence. The  $^{13}\text{C}$  inversion pulse is applied on every alternate scan. Subtracting the scans from each other yields only signal from  $^{13}\text{C}$ -coupled protons.  $^{13}\text{C}$  decoupling can be applied during acquisition in order to simplify the spectrum.

#### 1.8.4 RF coils for double resonance

It is apparent that in a  $^{13}\text{C}\{^1\text{H}\}$  or  $^1\text{H}\{^{13}\text{C}\}$  double resonance experiment, a coil system that resonates at both the frequencies of  $^1\text{H}$  and  $^{13}\text{C}$  is required. If two separate coils are being used for each frequency, it is important that both coils have similar areas of sensitivity, but that they display no electromagnetic interaction with each other. It is also desirable that a sensitive receiver coil is employed and that an efficient homogeneous coil is used for decoupling. The acquisition part of a pulse sequence is on the order of hundreds of milliseconds, and thus when decoupling, care must be taken to ensure that the power deposited in the patient is minimized and that SAR (Specific Absorption Rates) values are within FDA (Food and Drug Administration) guidelines. The SAR is defined as the energy per unit volume per unit time that is delivered to a subject, and is an indicator of how much sample heating can occur during an NMR pulse sequence (62). The current FDA guidelines prevent the use of any NMR sequence that has a SAR greater than 4 W/kg averaged over a body part other than the head for a period of 15 minutes or longer, or a SAR greater than 3 W/kg averaged over the head for a period of 10 minutes or longer. The SAR must also not exceed 8 W/kg in any gram of tissue in the head or torso, or 12 W/kg in any gram of tissue in the extremities, for a period of 5 minutes or longer (85). An inhomogeneous decoupling coil may satisfy the average SAR criteria but may exceed local SAR requirements, particularly in regions in close proximity to the coil.

An efficient coil design that meets the above criteria and that has become popular in  $^{13}\text{C}\{^1\text{H}\}$  studies is the half volume coil designed by Adriany and Gruetter (43). This coil has been used in a number of brain (29,33,34,37,42,84) and leg studies (86). The coil involves two orthogonal proton surface coils operating in quadrature and a single  $^{13}\text{C}$  sensitive surface coil for both transmission and reception as illustrated in Fig. 1.25.

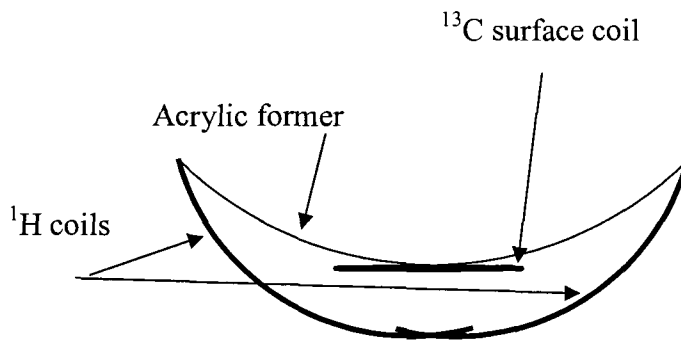


Figure 1.25: Schematic diagram of the half volume coil designed by Adriany and Gruetter. The coil consists of two proton surface coils operating in quadrature to reduce power requirements and to produce a more uniform decoupling field. A single  $^{13}\text{C}$  surface coil is used for both transmission and reception.

## **1.9 References**

1. Baik HM, Choe BY, Son BC, Jeun SS, Kim MC, Lee KS, Lee JM, Lee HK, Suh TS. Proton MR spectroscopic changes in Parkinson's diseases after thalamotomy. *European Journal of Radiology* 2003;47:179-187.
2. Brooks DJ. Advances in imaging Parkinson's disease. *Current Opinion in Neurology* 1997;10:327-331.
3. Davie CA, Wenning GK, Barker GJ, Tofts PS, Kendall BE, Quinn N, McDonald WI, Marsden CD, Miller DH. Differentiation of multiple system atrophy from idiopathic Parkinson's disease using proton magnetic resonance spectroscopy. *Annals of Neurology* 1995;37:204-210.
4. Hoang TQ, Bluml S, Dubowitz DJ, Moats R, Kopyov O, Jacques D, Ross BD. Quantitative proton-decoupled  $^{31}\text{P}$  MRS and  $^1\text{H}$  MRS in the evaluation of Huntington's and Parkinson's diseases. *Neurology* 1998;50:1033-1040.
5. Fernando KT, McLean MA, Chard DT, MacManus DG, Dalton CM, Miszkil KA, Gordon RM, Plant GT, Thompson AJ, Miller DH. Elevated white matter myo-inositol in clinically isolated syndromes suggestive of multiple sclerosis. *Brain* 2004;127:1361-1369.
6. Inglese M, Liu S, Babb JS, Mannon LJ, Grossman RI, Gonen O. Three-dimensional proton spectroscopy of deep gray matter nuclei in relapsing-remitting MS. *Neurology* 2004;63:170-172.
7. Rovaris M, Filippi M. The value of new magnetic resonance techniques in multiple sclerosis. *Current Opinion in Neurology* 2000;13:249-254.
8. Sarchielli P, Presciutti O, Tarducci R, Gobbi G, Alberti A, Pelliccioli GP, Chiarini P, Gallai V. Localized  $^1\text{H}$  magnetic resonance spectroscopy in mainly cortical gray matter of patients with multiple sclerosis. *Journal of Neurology* 2002;249:902-910.
9. Vrenken H, Barkhof F, Uitdehaag BMJ, Castelijns JA, Polman CH, Pouwels PJW. MR spectroscopic evidence for glial increase but not for neuro-axonal damage in MS normal-appearing white matter. *Magnetic Resonance in Medicine* 2005;53:256-266.
10. Kobayashi M, Takayama H, Suga S, Mihara B. Longitudinal changes of metabolites in frontal lobes after hemorrhagic stroke of basal ganglia: a proton magnetic resonance spectroscopy study. *Stroke* 2001;32:2237-2245.

11. Saunders DE. MR spectroscopy in stroke. *British Medical Bulletin* 2000;56:334-345.
12. Burtscher IM, Holtas S. Proton magnetic resonance spectroscopy in brain tumours: clinical applications. *Neuroradiology* 2001;43:345-352.
13. Majos C, Alonso J, Aguilera C, Serrallonga M, Perez-Martin J, Acebes JJ, Arus C, Gili J. Proton magnetic resonance spectroscopy <sup>1</sup>H MRS of human brain tumours: assessment of differences between tumour types and its applicability in brain tumour categorization. *European Radiology* 2003;13:582-591.
14. Lee PL, Gonzalez RG. Magnetic resonance spectroscopy of brain tumors. *Current opinion in oncology* 2000;12:199-204.
15. Seyfert S, Bernarding J, Braun J. Volume-selective 1H MR spectroscopy for in vivo detection of valproate in patients with epilepsy. *Neuroradiology* 2003;45:295-299.
16. Wellard RM, Briellmann RS, Prichard JW, Syngeniotis A, Jackson GD. Myoinositol abnormalities in temporal lobe epilepsy. *Epilepsia* 2003;44:815-821.
17. Laxer KD. Clinical applications of magnetic resonance spectroscopy. *Epilepsia* 1997;38(Suppl. 4):S13-S17.
18. Hájek M, Dezortová M, Komárek V. <sup>1</sup>H MR spectroscopy in patients with mesial temporal epilepsy. *Magnetic Resonance Materials in Physics, Biology, and Medicine* 1998;7:95-114.
19. Adalsteinsson E, Sullivan EV, Kleinhans N, Spielman DM, Pfefferbaum A. Longitudinal decline of the neuronal marker N-acetyl aspartate in Alzheimer's disease. *The Lancet* 2000;355:1696-1697.
20. Jones RS, Waldman AD. 1H-MRS evaluation of metabolism in Alzheimer's disease and vascular dementia. *Neurological Research* 2004;26:488-495.
21. Herminghaus S, Frolich L, Gorriz C, Pilatus U, Dierks T, Wittsack HJ, Lanfermann H, Maurer K, Zanella FE. Brain metabolism in Alzheimer disease and vascular dementia assessed by in vivo proton magnetic resonance spectroscopy. *Psychiatry Research* 2003;123:183-190.
22. Cecil KM, DelBello MP, Morey R, Strakowski SM. Frontal lobe differences in bipolar disorder as determined by proton MR spectroscopy. *Bipolar Disorders* 2002;4:357-365.

23. Winsberg ME, Sachs N, Tate DL, Adalsteinsson E, Spielman D, Ketter TA. Decreased dorsolateral prefrontal N-Acetyl aspartate in bipolar disorder. *Biological Psychiatry* 2000;47:475-481.
24. Davanzo P, Thomas MA, Yue K, Oshiro T, Belin T, Strober M, McCracken J. Decreased anterior cingulate myo-inositol/creatine spectroscopy resonance with lithium treatment in children with bipolar disorder. *Neuropsychopharmacology* 2001;24:359-369.
25. Bertolino A, Weinberger DR. Proton magnetic resonance spectroscopy in schizophrenia. *European Journal of Radiology* 1999;30:132-141.
26. Tibbo P, Hanstock C, Valiakalayil A, Allen P. 3-T proton MRS investigation of glutamate and glutamine in adolescents at high genetic risk for schizophrenia. *American Journal of Psychiatry* 2004;161:1116-1118.
27. Sigmundsson T, Maier M, Toone BK, Williams SC, Simmons A, Greenwood K, Ron MA. Frontal lobe N-acetylaspartate correlates with psychopathology in schizophrenia: a proton magnetic resonance spectroscopy study. *Schizophrenia Research* 2003;64:63-71.
28. Griffiths JR, Glickson JD. Monitoring pharmacokinetics of anticancer drugs: non-invasive investigation using magnetic resonance spectroscopy. *Advanced Drug Delivery Reviews* 2000;41:75-89.
29. Gruetter R, Seaquist ER, Kim S, Ugurbil K. Localized *in vivo*  $^{13}\text{C}$ -NMR of glutamate metabolism in the human brain: initial results at 4 tesla. *Developmental Neuroscience* 1998;20:380-388.
30. Blüml S, Moreno-Torres A, Shic F, Nguy CH, Ross BD. Tricarboxylic acid cycle of glia in the *in vivo* human brain. *NMR in Biomedicine* 2002;15:1-5.
31. Behar KL, Rothman DL. *In vivo* nuclear magnetic resonance studies of glutamate-gamma-aminobutyric acid-glutamine cycling in rodent and human cortex: the central role of glutamine. *Journal of Nutrition* 2001;131:2498S-2504S.
32. Sibson NR, Mason GF, Shen J, Cline GW, Herskovitz AZ, Wall JEM, Behar KL, Rothman DL, Shulman RG. *In vivo*  $^{13}\text{C}$  NMR measurement of neurotransmitter glutamate cycling, anaplerosis and TCA cycle flux in rat brain during [2- $^{13}\text{C}$ ]glucose infusion. *Journal of Neurochemistry* 2001;76:975-989.
33. Shen J, Petersen KF, Behar KL, Brown P, Nixon TW, Mason GF, Petroff OAC, Shulman GI, Shulman RG, Rothman DL. Determination of the rate of the glutamate/glutamine cycle in the human brain by *in vivo*  $^{13}\text{C}$  NMR. *Proc Natl Acad Sci USA* 1999;96:8235-8240.

34. Lebon V, Petersen KF, Cline GW, Shen J, Mason GF, Dufour S, Behar KL, Shulman GI, Rothman DL. Astroglial contribution to brain energy metabolism in humans revealed by  $^{13}\text{C}$  nuclear magnetic resonance spectroscopy: elucidation of the dominant pathway for neurotransmitter glutamate repletion and measurement of astrocytic oxidative metabolism. *The Journal of Neuroscience* 2002;22:1523-1531.
35. Rothman DL, Sibson NR, Hyder F, Shen J, Behar KL, Shulman RG. *In vivo* nuclear magnetic resonance spectroscopy studies of the relationship between the glutamate-glutamine neurotransmitter cycle and functional neuroenergetics. *Phil Trans R Soc Lond* 1999;354:1165-1177.
36. Shen J, Rothman DL. Magnetic resonance spectroscopic approaches to studying neuronal:glial interactions. *Biological Psychiatry* 2002;52:694-700.
37. Chhina N, Kuestermann E, Halliday J, Simpson LJ, Macdonald IA, Bachelard HS, Morris PG. Measurement of human tricarboxylic acid cycle rates during visual activation by  $^{13}\text{C}$  magnetic resonance spectroscopy. *Journal of Neuroscience Research* 2001;66:737-746.
38. Chen W, Zhu X-H, Gruetter R, Seaquist ER, Adriany G, Ugurbil K. Study of tricarboxylic acid cycle flux changes in human visual cortex during hemifield visual stimulation using  $^1\text{H}\{-^{13}\text{C}\}$  MRS and fMRI. *Magnetic Resonance in Medicine* 2001;45:349-355.
39. Sibson NR, Dhankar A, Mason GF, Rothman DL, Behar KL, Shulman GI. Stoichiometric coupling of brain glucose metabolism and glutamatergic neuronal activity. *Proc Natl Acad Sci USA* 1998;95:316-321.
40. Hyder F, Chase RJ, Behar KL, Mason GF, Siddeek M, Rothman DL, Shulman RG. Increased tricarboxylic acid cycle flux in rat brain during forepaw stimulation detected with  $^1\text{H}\{^{13}\text{C}\}$  NMR. *Proc Natl Acad Sci USA* 1996;93:7612-7617.
41. Lin AP, Shic F, Enriquez C, Ross BD. Reduced glutamate neurotransmission in patients with Alzheimer's disease-an *in vivo*  $^{13}\text{C}$  magnetic resonance study. *Magnetic Resonance Materials in Physics, Biology and Medicine* 2003;16:29-42.
42. Blüml S, Moreno-Torres A, Ross BD.  $[1-^{13}\text{C}]$  glucose MRS in chronic hepatic encephalopathy in man. *Magnetic Resonance in Medicine* 2001;45:981-993.
43. Adriany G, Gruetter R. A half-volume coil for efficient proton decoupling in humans at 4T. *Journal of Magnetic Resonance* 1997;125:178-184.
44. Bottomley PA; Selective volume method for performing localized NMR spectroscopy. US Patent 4, 480,228. 1984.



45. Bendall MR, Pegg DT, Doddrell DM, Field J. NMR of protons coupled to  $^{13}\text{C}$  nuclei only. *Journal of the American Chemical Society* 1981;103:934-936.
46. Chen W, Adriany G, Zhu XH, Gruetter R, Ugurbil K. Detecting Natural Abundance Carbon Signal of NAA Metabolite Within 12-cm<sup>3</sup> Localized Volume of Human Brain Using  $^1\text{H}$ - $\{^{13}\text{C}\}$  NMR Spectroscopy. *Magnetic Resonance in Medicine* 1998;40:180-184.
47. Ordidge RJ, Connelly A, Lohman JAB. Image-selected in vivo spectroscopy (ISIS). A new technique for spatially selective NMR spectroscopy. *Journal of Magnetic Resonance* 1986;66:283-294.
48. Hurd RE, Boban JK. Gradient-enhanced proton-detected heteronuclear multiple quantum coherence spectroscopy. *Journal of Magnetic Resonance* 1991;91:648-653.
49. Doddrell DM, Pegg DT, Bendall MR. Distortionless enhancement of NMR signals by polarization transfer. *Journal of Magnetic Resonance* 1982;48:323-327.
50. Morris G, Freeman R. Enhancement of nuclear magnetic resonance signals by polarization transfer. *Journal of the American Chemical Society* 1979;101:760-762.
51. Liang ZP, Lauterbur PC. *Principles of Magnetic Resonance Imaging: A Signal Processing Perspective*. New York: IEEE Press; 2000.
52. Canet D. *Nuclear Magnetic Resonance, Concepts and Methods*. Ontario: John Wiley & Sons; 1996.
53. Levitt MH. *Spin Dynamics, Basics of Nuclear Magnetic Resonance*. Chichester: John Wiley & Sons; 2001.
54. Hahn EL. Spin Echoes. *Physical Review* 1950;80:580-594.
55. Frahm J, Merboldt KD, Haniöke W. Localized proton spectroscopy using stimulated echos. *Journal of Magnetic Resonance* 1987;72:502-508.
56. Burstein D. Stimulated echoes: description, applications, practical hints. *Concepts in Magnetic Resonance* 1996;8:269-278.
57. Thompson RB, Allen PS. Sources of variability in the response of coupled spins to the PRESS sequence and their potential impact on metabolite quantification. *Magnetic Resonance in Medicine* 1999;41:1162-1169.

58. Sorensen OW, Eich GW, Levitt MH, Bodenhausen G, Ernst RR. Product operator formalism for the description of NMR pulse experiments. *Progress in NMR Spectroscopy* 1983;16:163-192.
59. Kay L, McClung R. A product operator description of AB and ABX spin systems. *Journal of Magnetic Resonance* 1988;77:258-273.
60. Hoult DI, Richards RE. The signal-to-noise-ratio of the nuclear magnetic resonance experiment. *Journal of Magnetic Resonance* 1976;24:71-85.
61. Hayes CE, Edelstein WA, Schenck JF, Mueller OM, Eash M. An efficient, highly homogeneous radiofrequency coil for whole-body NMR imaging at 1.5 T. *Journal of Magnetic Resonance* 1985;63:622-628.
62. Jin J. *Electromagnetic Analysis and Design in Magnetic Resonance Imaging*. New York: CRC Press; 1999.
63. Chen CN, Hoult DI, Sank VJ. Quadrature detection coils-a further improvement in sensitivity. *Journal of Magnetic Resonance* 1983;54:324-327.
64. Peterson DM, Duensing GR, Fitzsimmons JR. MRI basics and coil design principles. *RF Design* January 1997:56-64.
65. Chen CN, Hoult DI. *Biomedical Magnetic Resonance Technology*. Philadelphia: Institute of Physics Publishing; 1995.
66. Hill HDW, Richards RE. Limits of measurement in magnetic resonance. *Journal of Scientific Instruments* 1968;1:977-983.
67. De Zanche N, Allen PS. Sensitivity calculations and comparisons for shielded elliptical and circular birdcage coils. *Magnetic Resonance in Medicine* 2002;47:364-371.
68. Johnson JB. Thermal agitation of electric charge in conductors. *Physical Review* 1934;32:97-109.
69. Griffiths DJ. *Introduction to Electrodynamics*. New Jersey: Prentice-Hall Inc.; 1989.
70. Hoult DI. The sensitivity of the zeumatographic experiment involving human samples. *Journal of Magnetic Resonance* 1979;34:425-433.
71. De Beer R, Van den Boogaart A, Van Ormondt D, Pijnappel WWF. Application of time - domain fitting in the quantification of in vivo <sup>1</sup>H spectroscopic imaging data sets. *NMR in Biomedicine* 1992;5:171-178.

72. Behar KL, Ogino T. Assignment of resonances in the  $^1\text{H}$  spectrum of rat brain by two-dimensional shift correlated and J-resolved NMR spectroscopy. *Magnetic Resonance in Medicine* 1991;17:285-303.
73. Allen PS, Thompson RB, Wilman AH. Metabolite-specific NMR spectroscopy in vivo. *NMR in Biomedicine* 1997;10:434-444.
74. Bomsdorf H, Roschmann P, Weiland J. Sensitivity enhancement in whole-body natural abundance  $^{13}\text{C}$  spectroscopy using  $^{13}\text{C}/^1\text{H}$  double-resonance techniques at 4 tesla. *Magnetic Resonance in Medicine* 1991;22:10-22.
75. Hertz L, Dringen R, Schousboe A, Robinson SR. Astrocytes: Glutamate Producers for Neurons. *Journal of Neuroscience Research* 1999;57:417-428.
76. Pfliederer B, Michael N, Erfurth A, Ohrmann P, Hohmann U, Wolgast M, Fiebich M, Arolt V, Heindel W. Effective electroconvulsive therapy reverses glutamate/glutamine deficit in the left anterior cingulum of unipolar depressed patients. *Psychiatry Research* 2003;122:185-192.
77. Sanacora G, Gueorguieva R, Epperson CN, Wu YT, Appel M, Rothman DL, Krystal JH, Mason G. Subtype-specific alterations of gamma-aminobutyric acid and glutamate in patients with major depression. *Archives of General Psychiatry* 2004;61:705-713.
78. Theberge J, Al-Semaan Y, Williamson PC, Menon RS, Neufeld RW, Rajakumar N, Schaefer B, Densmore M, Drost DJ. Glutamate and glutamine in the anterior cingulate and thalamus of medicated patients with chronic schizophrenia and healthy comparison subjects measured with 4.0-T proton MRS. *American Journal of Psychiatry* 2003;160:2231-2233.
79. Bradley WG, Bowen BC, Pattany PM, Rotta F.  $^1\text{H}$ -magnetic resonance spectroscopy in amyotrophic lateral sclerosis. *Journal of the Neurological Sciences* 1999;169:84-86.
80. Pioro EP, Majors AW, Mitsumoto H, Nelson DR, Ng TC.  $^1\text{H}$ -MRS evidence of neurodegeneration and excess glutamate + glutamine in ALS medulla. *Neurology* 1999;53:71-79.
81. Hattori N, Abe K, Sakoda S, Sawada T. Proton MR spectroscopic study at 3 Tesla on glutamate/glutamine in Alzheimer's disease. *Neuroreport* 2002;13:183-186.
82. Antuono PG, Jones JL, Wang Y, Li SJ. Decreased glutamate + glutamine in Alzheimer's disease detected in vivo with  $(^1\text{H})\text{-MRS}$  at 0.5 T. *Neurology* 2001;56:737-742.

83. Gadian DG. Nuclear Magnetic Resonance and its Applications to Living Systems. New York: Oxford University Press; 1982.
84. Shaka AJ, Keeler J, Freeman R. Evaluation of a new broadband decoupling sequence : WALTZ-16. Journal of Magnetic Resonance 1983;53:313-340.
85. Guidance for Magnetic Resonance Diagnostic Devices. US Food and Drug Administration: Centre for Devices and Radiological Health. Available from: <http://www.fda.gov/cdrh/magdev.html>. Accessed March 2005.
86. Carey P, Halliday J, Snaar J, Morris P, Taylor R. Direct assessment of muscle glycogen storage after mixed meals in normal and type 2 diabetic subjects. American Journal of Physiology: Endocrinology and Metabolism 2003;284:688-694.

# Chapter 2

## A Dual-Tuned Transceiver for $^{13}\text{C}\{^1\text{H}\}$ MR Spectroscopy: Two Open Coils in One

### 2.1 Introduction

For the application of  $^{13}\text{C}\{^1\text{H}\}$  NMR spectroscopy, it is clear that a coil system that resonates at both the  $^{13}\text{C}$  and  $^1\text{H}$  frequencies is required. Often two separate coils are used, one operating at the  $^{13}\text{C}$  Larmor frequency and the other at the  $^1\text{H}$  frequency. In such a coil system, it is important that the two coils have the same field of view, but that they do not experience any electromagnetic interaction with each other. In addition, it is essential for the  $^{13}\text{C}$  coil to be sensitive and for the  $^1\text{H}$  coil not to produce local hot spots during proton decoupling. It is, moreover, particularly important for the coil system to produce homogeneous fields at both frequencies, so that the spins are excited uniformly and thus behave in a predictable manner to the pulse sequence being applied. Previous solutions have included (e.g. (1-4)), a surface coil for both transmission and reception at the  $^{13}\text{C}$  frequency, together with a larger surface coil concentric with the  $^{13}\text{C}$  coil for proton irradiation; however, this configuration is not efficient for decoupling  $^{13}\text{C}$ -proton interactions because the inner  $^{13}\text{C}$  coil blocks the proton flux, and degrades the decoupling power. Furthermore, such a configuration does not create uniform RF fields at either frequency. The design of Roussel et al. (5) where a linear  $^{13}\text{C}$  birdcage coil is placed inside a slightly larger  $^1\text{H}$  linear birdcage coil provides homogeneous RF fields for both  $^{13}\text{C}$  and  $^1\text{H}$ . Nevertheless, this arrangement requires careful orientation of the two coils with respect to each other in order to avoid electromagnetic coupling; moreover, because a larger volume contributes to the noise when using a birdcage coil for reception, the signal to noise ratio (SNR) suffers. The dual-tuned volume coil transmission line design of J.T. Vaughan (6) has been used previously for the indirect detection of  $^{13}\text{C}$  during a labelled glucose infusion study (7); however this coil implementation is labour-intensive because the coil currents in each leg need to be individually adjusted. The most popular solution has been a design of Adriany and Gruetter (8) which was reported to

have overcome some of the aforementioned problems. Their design consists of two orthogonal proton surface coils operating in quadrature to provide a uniform circularly polarized RF field (see Fig. 2.1) together with a  $^{13}\text{C}$  surface coil for transmission and reception. The Adriany-Gruetter system has been employed in  $^{13}\text{C}\{^1\text{H}\}$  leg (9) as well as a number of brain studies (10-12). The strategy of this design is that by placing the two  $^1\text{H}$  RF surface probes orthogonal to each other and feeding them with currents that are  $90^\circ$  out of phase with each other (achieved by the quadrature hybrid), a circularly polarized  $B_1$  will be produced. As was mentioned in §1.6.2, the advantage of quadrature operation over linear operation is a  $\sqrt{2}$  enhancement in sensitivity and a factor of 1/2 reduction in required power (13). The  $^{13}\text{C}$  part of this RF system consists of a single surface coil used for both reception and transmission and was placed above the two proton loops as was shown previously in Fig. 1.25. This design, however, has limited  $^{13}\text{C}$  RF homogeneity and spatial range, the latter restricting its application to the occipital lobe region of the brain. For the study of neurological disorders, deeper areas of the brain are the principal regions of pathology. In addition, the three coils of this design need to be positioned in a meticulous manner in order to minimize interactions between them.

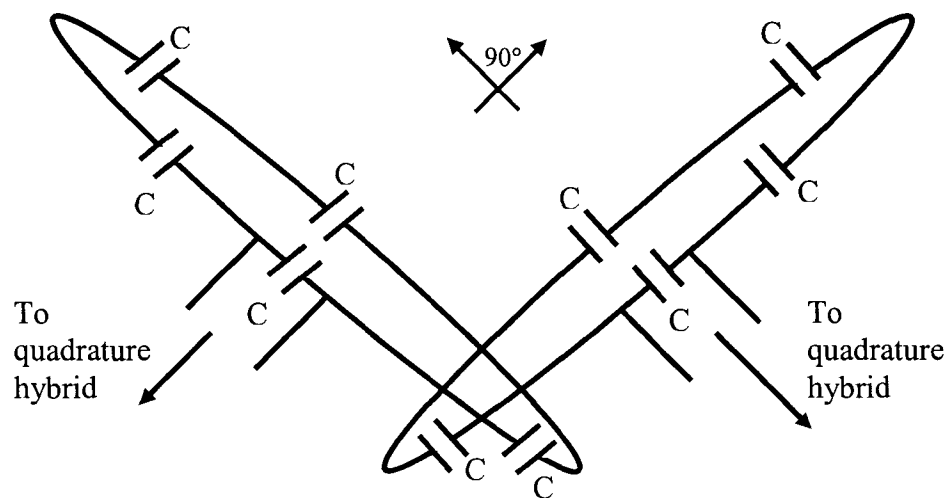


Figure 2.1: The proton quadrature surface RF probe design used by Adriany and Gruetter to provide the decoupling field.

The objective of the work reported in this thesis was to investigate an alternative design, namely, that of a dual-tuned coil which would be able to excite and detect signal

from deeper regions of the brain with acceptable sensitivity while providing adequately uniform fields at both frequencies. The solution is based on the open half birdcage design, that has been shown to provide acceptable field homogeneity (14,15), and was made for operation at 3.0 T ( $\approx 128$  MHz for  $^1\text{H}$ , and 32 MHz for  $^{13}\text{C}$ ). In order to make the open dual-tuned transceiver, it was designed as a low-pass network with eleven legs, each alternate leg contributing to resonance at one or other of the two frequencies (six of the legs contributed to the proton frequency). Isolation of the two frequencies was achieved by placing a trap circuit in every leg, such that it resonated at the unwanted frequency in that leg. A coil based on the design of Adriany and Gruetter (8) was also constructed, and the performance of the dual-tuned half-birdcage was compared to the performance of the published design, in terms of field homogeneity,  $^{13}\text{C}$  sensitivity, isolation between the two frequencies, and proton decoupling power requirements. The efficacy of the half birdcage design *in vivo* was verified on the human calf.

## **2.2 Theory**

### **2.2.1 An open coil design**

The proposed design can be thought of as a half-birdcage coil (see §1.6.2 for a description of the birdcage configuration). Schematic diagrams of low-pass and high-pass open networks are shown in Fig. 2.2, their difference being the location of the capacitors (15). Since we based our coil on the low-pass network design, it will be discussed further. The most useful mode for producing a uniform  $B_1$  field in a full birdcage RF probe is the  $M = 1$  mode (15). The same is true for an open coil. However, whereas for a full birdcage this mode produces a full-wavelength standing wave around the ladder network, in a half birdcage, the result is still a standing wave but of integral half-wavelengths. Figure 2.3 displays a low-pass ladder network. The current distribution in the legs for this mode is sinusoidal with the current being maximum in the first and  $N^{\text{th}}$  legs, and zero in the  $(N+1)/2^{\text{th}}$  leg, if  $N$  is odd (14).

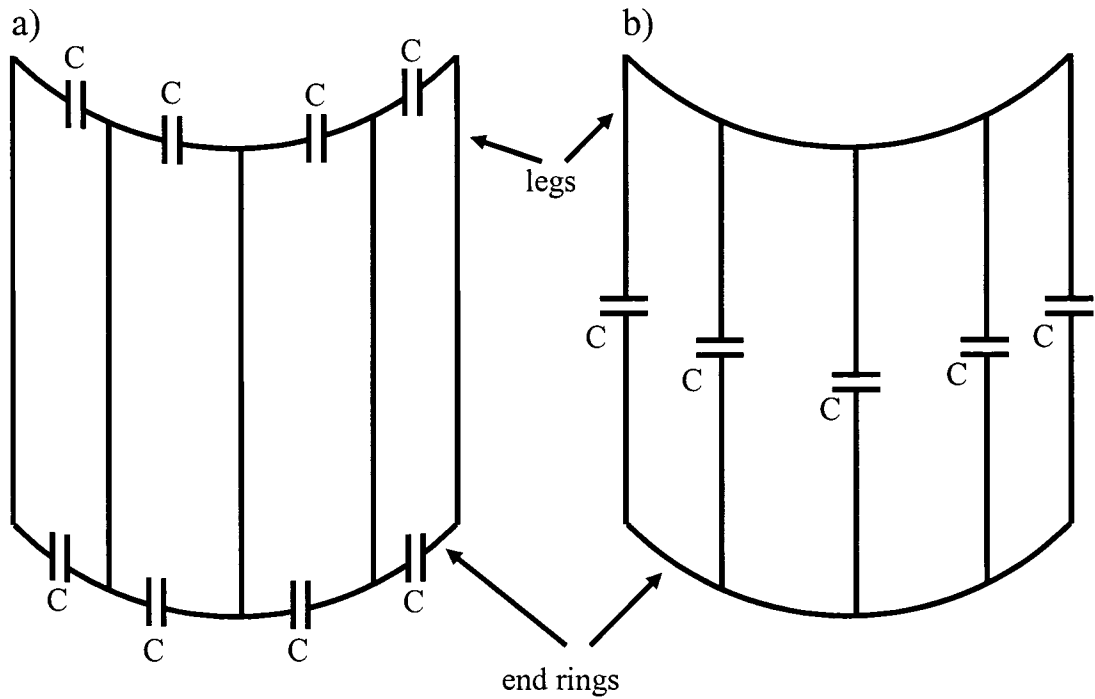


Figure 2.2: Structure of a) a high-pass open network and b) a low-pass open network. The capacitors are denoted by C and the end rings and the legs are usually made of copper strips that provide the inductance of the coil.

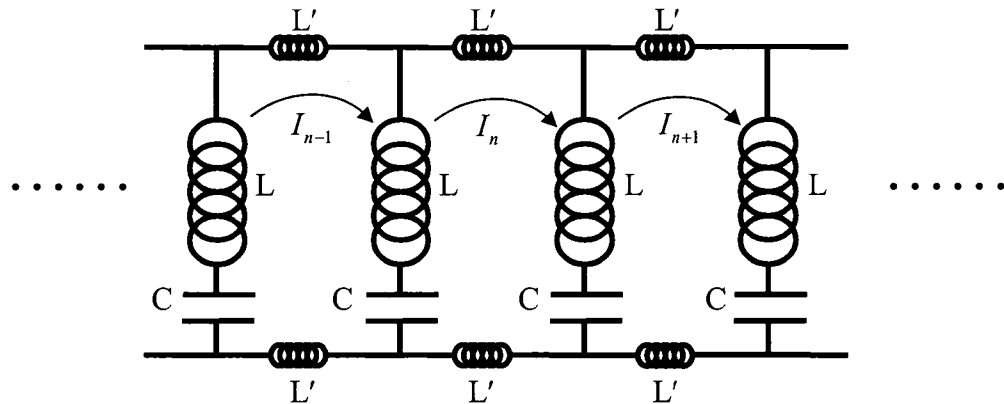


Figure 2.3: Representation of a low-pass network. L and L' denote the inductances of the coil legs and end rings, respectively.

The mesh current amplitudes,  $I_n$ , are given in Eq. (2.1), where A is a constant, n is the mesh number, and N is the total number of legs. Note that these solutions are not degenerate as they are with a full birdcage. Equation (2.2) relates the current in each leg to the mesh currents (14).

$$I_n = A \sin(n\pi / N) \quad (2.1)$$



$$i_n = I_n - I_{n-1} \quad (2.2)$$

### 2.2.2 The dual-tuned open birdcage design

Figure 2.4 displays a schematic diagram of the dual-tuned half-birdcage coil. Alternate legs containing the capacitors  $C_1$  and the  $L_1^*C_1^*$  trap circuits tune the RF probe to the proton frequency at 3 T, 128 MHz (the lowest resonating frequency mode in a low-pass open coil). The capacitors  $C_1$  tune the proton legs of the coil and  $L_1^*C_1^*$  form parallel resonating LC circuits at the carbon frequency, 32 MHz, thus blocking any current flow at that frequency in the proton legs. Similarly, the capacitors  $C_2$  tune the resonance created by the remaining legs to that of the carbon frequency, while  $L_2^*C_2^*$  form parallel resonating LC circuits at the proton frequency thus blocking any proton currents in the carbon legs. The decoupling by the trap circuits makes the open coil, in essence, two independent open coils (one for each frequency) integrated together. As shown in Fig. 2.4, the coil was matched and fed at each frequency at the end leg (14) for that frequency. Variable capacitors were placed parallel to the tuning capacitors at the opposite end legs for fine tuning at each frequency.

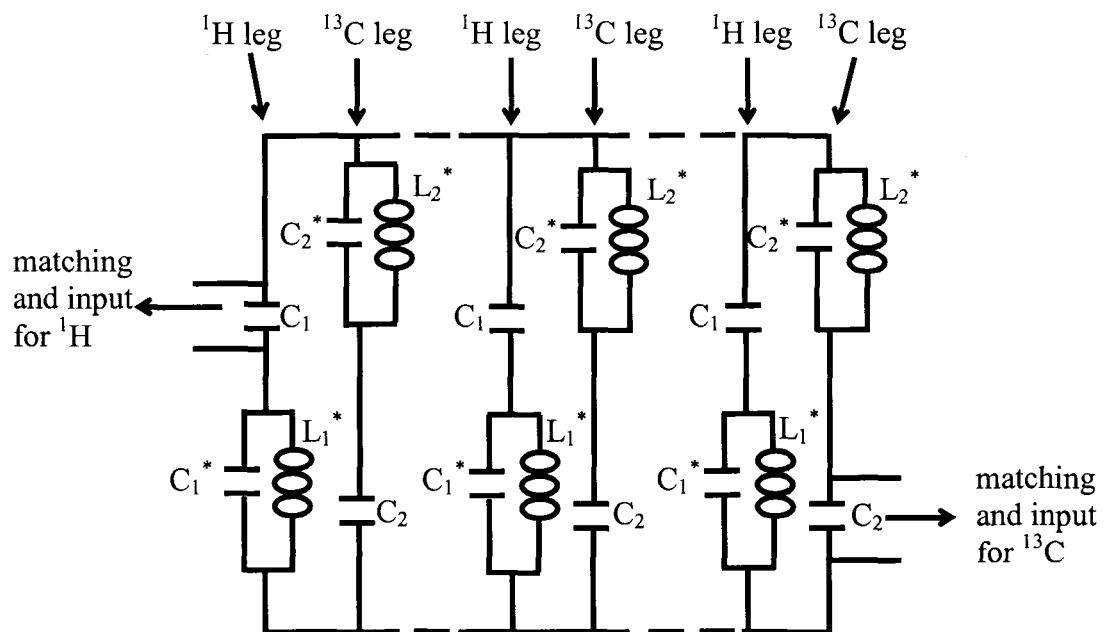


Figure 2.4: Schematic diagram of the half-birdcage circuit. The legs termed “ $^{13}\text{C}$  leg” refer to those legs forming the resonance at the  $^{13}\text{C}$  frequency and similarly the “ $^1\text{H}$  legs” are those creating resonance at the  $^1\text{H}$  frequency.

## 2.3 Experimental methods

All experiments were carried out in an 80 cm bore, 3.0 T magnet system (Magnex Scientific PLC, Abingdon, UK), using a SMIS spectrometer (Surrey Medical Imaging Systems PCL, Guildford, UK). All fixed capacitors were purchased from American Technical Ceramics (Jacksonville, FL) and the variable capacitors were purchased from Polyflon (Norwalk, CT).

### 2.3.1 RF probe design and construction

#### 2.3.1.1 The dual-tuned half-birdcage design

The half-birdcage circuit was constructed on an acrylic piece of cylinder 16 cm in diameter and was made of eleven legs 10.5 cm in length, all equally spaced around a semi circle. Six of the legs contribute to the proton frequency while the remaining five are responsible for the  $^{13}\text{C}$  frequency as shown in Fig. 2.5. Each proton leg (a 0.95 cm wide copper strip) consists of a 2.2 pF capacitor for tuning, corresponding to  $C_1$  in Fig. 2.4, and a trap circuit, a 330 pF capacitor in parallel with a 75 nH inductor (corresponding to  $C_1^*$  and  $L_1^*$  in Fig. 2.4 and resonating at the  $^{13}\text{C}$  frequency). Similarly, each  $^{13}\text{C}$  leg (also a 0.95 cm wide copper strip) consists of an 82 pF capacitor for tuning ( $C_2$  in Fig. 2.4) and a trap circuit, a 27 pF capacitor in parallel with a 58 nH inductor ( $C_2^*$  and  $L_2^*$  in Fig. 2.4 resonating at the  $^1\text{H}$  frequency). The end rings were made from copper strips 1.27 cm in width. The coil was matched to  $50\ \Omega$ , the characteristic impedance of the coaxial cable, at each frequency at the “input leg” as shown in Fig. 2.6. Variable capacitors were placed parallel to the tuning capacitors at the opposite end legs for fine tuning at each frequency.

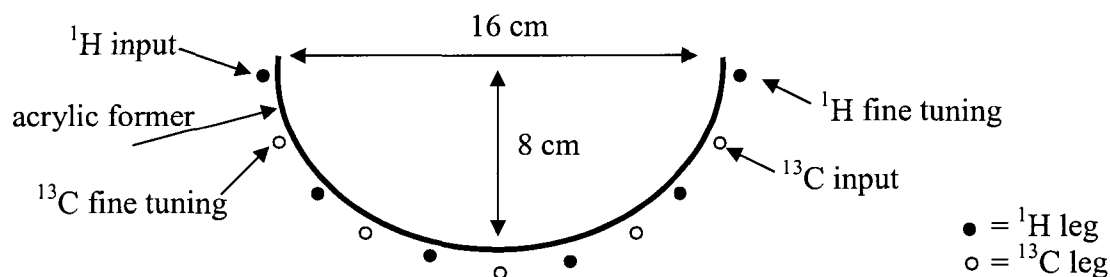


Figure 2.5: A schematic diagram of the dual-tuned open coil, illustrating the positions of the legs and the dimensions of the coil.

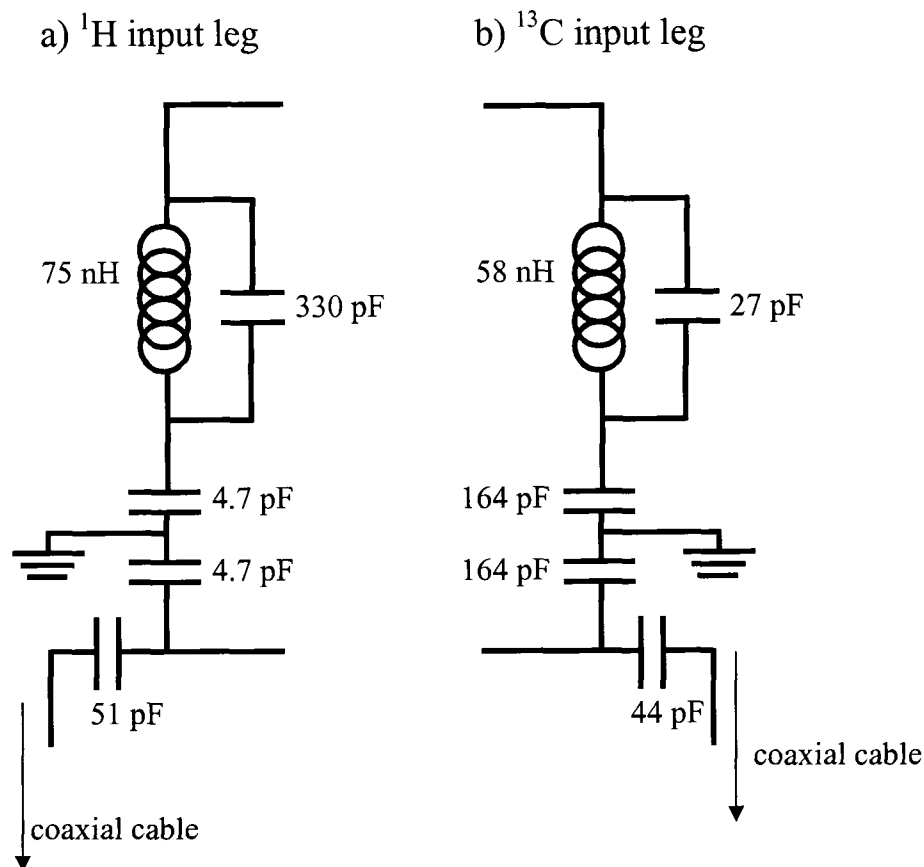


Figure 2.6: A representation of the legs through which RF at each frequency is fed. In each case, the tuning capacitor was split into two series capacitors. It was found that this balanced the coil better. A matching capacitor was then added in series with the coil and the coaxial cable. For the  $^1\text{H}$  leg, a 51 pF matching capacitor was used, while two 22 pF capacitors in parallel were employed for the  $^{13}\text{C}$  frequency.

### 2.3.1.2 Adriany-Gruetter design

The proton part consisting of two surface coils placed orthogonal to each other was made of two identical loops, each constructed from copper strips 0.635 cm in width on acrylic plastic loops 14.25 cm in diameter. Five 18 pF capacitors were distributed around the loops to tune them to the  $^1\text{H}$  frequency. A half-wavelength cable then connected each loop to a tune/match box (see Fig. 2.7) that contained two variable capacitors, one for tuning and the other for matching. The amount of overlap of the coils (see Fig. 2.1) was determined by using an HP 4396A analyzer (Hewlett Packard, Palo Alto, CA). When two loops resonating at the same frequency are brought close to each

other, the resonances split due to the mutual inductance between them. By overlapping the two loops appropriately, the mutual inductance between them can be minimized (16). This amount of overlap was determined by altering the positions of the two coils with respect to each other until no frequency splitting was observed on the resonance peak displayed by the network analyzer.

The  $^{13}\text{C}$  RF probe was also made from copper strips 0.635 cm in width and was made as a 10×10 cm square. Four 270 pF capacitors were distributed around the circuit to tune it to the  $^{13}\text{C}$  frequency, and it was matched with a 47 pF capacitor in a similar manner to that shown in Fig. 2.6(b). To eliminate the need for meticulous positioning of the  $^{13}\text{C}$  coil with respect to the proton coils in order to minimize electromagnetic interactions between them, we improved on the design of Ref. (8) and placed a trap circuit resonating at the  $^1\text{H}$  frequency in the  $^{13}\text{C}$  coil (the trap consisted of a 27 pF capacitor in parallel with a 58 nH inductor). This idea was implemented independently by Klomp et al. (17).

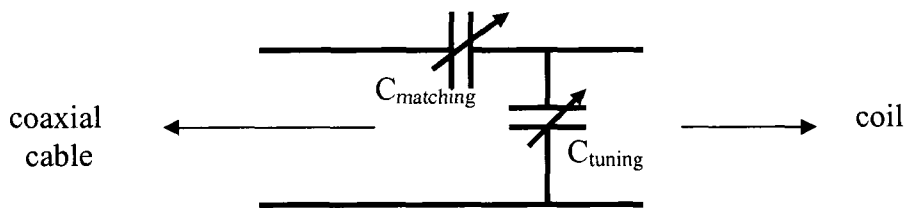


Figure 2.7: The tune and match circuits used for each of the proton surface coils.

## 2.3.2 Performance testing

### 2.3.2.1 Imaging

We previously carried out field mapping by using the double angle method (18) to compare the performance of two birdcage coils of different cross sectional shapes (19) and to compare the field homogeneity *in vivo* and in phantoms (20). In this work, we employed the same method of field mapping on an oil filled cylindrical phantom to compare the field homogeneities of the two coils at the proton frequency. Two spin-echo proton images were acquired using excitation flip angles  $\alpha_1 = 45^\circ$  and  $\alpha_2 = 2\alpha_1 = 90^\circ$  respectively. Acquisition of the two images was interleaved to eliminate registration problems. Using repetition times longer than five times the longest  $T_1$ , the flip angle at

each image pixel was calculated from  $\alpha_1 = \arccos(I_2/2I_1)$ , where  $I_1$  and  $I_2$  are the corresponding image intensities at each pixel. All acquisitions had the following parameters: An echo time (TE) of 20 ms, a field of view (FOV) of 30 cm, a repetition time (TR) of 2 s, a slice thickness of 5 mm, 128 phase encode points, and 256 frequency encode points. The two images were obtained by Fourier transformation of the acquired data zero-padded to 256×256. The  $\alpha_1$  distribution was calculated from the above relation. Field amplitude contours at 10% intervals of the maximum were overlaid on the resulting image.

For *in-vivo* imaging, images of a human calf were obtained using a spin echo imaging sequence with TE = 15 ms, FOV= 20 cm, TR = 3 s, a slice thickness of 7 mm, 128 phase encodes, and 256 frequency encode points.

#### 2.3.2.2 $^{13}\text{C}\{^1\text{H}\}$ spectroscopy

To verify the functioning of the coil at both frequencies, and to determine the decoupling power requirements *in vivo*, WALTZ-16 (21) proton decoupling was applied during acquisition (duration of which was 0.2048 s) following the application of a simple 500  $\mu\text{s}$   $^{13}\text{C}$  excitation pulse to detect the signal from the lipids in a human calf. A repetition time of 3 s was employed. For detection of the more demanding glycogen, the same sequence was used but the repetition time was reduced to 1.5 s to enable signal averaging within a practical time (the duration of the acquisition period of the sequence was also reduced to 0.1024 s to keep power deposition during proton decoupling within SAR limits).

#### 2.3.2.3 Measuring the quality factor

The quality factor was defined in §1.6.4. To measure the quality factor, Q, of a frequency mode of the RF probe, it was connected to the transmission port of the network analyzer (HP 4396A analyzer, Hewlett Packard, Palo Alto, CA) and a pickup loop was used to measure the coil's frequency response. The quality factor measured from this resonance response ( $Q_{\text{measured}} = \text{resonance frequency}/3\text{dB bandwidth}$ ) is affected by the loading due to the connections to the analyzer and the presence of the pick-up loop. Therefore,  $Q_{\text{measured}}$  is less than the actual quality factor of the RF coil,  $Q_{\text{coil}}$ , which,

however, can be determined from Eq. (2.3) (22). The value  $K$  can be obtained from the reflection coefficient,  $\rho$ , by Eq. (2.4) if the coil is overcoupled (coil matching improves with the introduction of more sample losses), or by Eq. (2.5) if it is undercoupled (coil match worsens with increasing losses) (22). The reflection coefficient can be determined by an  $S_{11}$  measurement.

$$Q_{coil} = (K + 1)Q_{measured} \quad (2.3)$$

$$K = \frac{1 + \rho}{1 - \rho} > 1 \quad (2.4)$$

$$K = \frac{1 - \rho}{1 + \rho} < 1 \quad (2.5)$$

#### 2.3.2.4 Port isolation

For the RF probe to function as efficiently as possible, it is essential to minimize the coupling between different coil ports. The isolation between any two ports was measured by an  $S_{21}$  measurement with the network analyzer.

## **2.4 Results**

### 2.4.1 Quality factors and isolation

Bench measurements of the quality factor,  $Q$ , of each coil were made under loaded and unloaded conditions. To simulate the loading effect of a human leg a 1 litre bottle of 100 mM saline was used. The results are summarized in Table 2.1. Measurements were also carried out to determine the degree of isolation between all coil ports at each of the two frequencies; these measurements are listed in Table 2.2.

From the measurements reported in the tables, it is apparent that a desirable isolation (>15 dB) between all coil ports has been achieved at each of the two frequencies with both coils. All  $Q_u/Q_l$  values are greater than two, corresponding to an efficiency of at least 50% (efficiency =  $1 - Q_l/Q_u$ ), which although not outstanding, is an acceptable standard. The ratios  $Q_u/Q_l$  are very similar for both coil designs, indicating that the dual-tuned open coil is just as efficient as each of the surface coils. However, experimentally it is expected that the open coil will require approximately twice the power for proton

decoupling because it is operating in a linear mode as opposed to the two surface coils which will be driven in a quadrature mode of operation.

Table 2.1: Summary of RF probe quality factors.  $Q_u$  represents the quality factor under the condition of no load and  $Q_l$  represents the quality factor when the coil was loaded with a 1 litre saline bottle that loads the coil like a human leg.  $H_a$  and  $H_b$  are the two orthogonal proton surface loops.

Dual-tuned open birdcage design								
$^{13}\text{C}$			$^1\text{H}$					
$Q_u$	$Q_l$	$Q_u/Q_l$	$Q_u$	$Q_l$	$Q_u/Q_l$			
130	56.7	2.3	105	43.6	2.4			
Adriany-Gruetter design								
$^{13}\text{C}$			$^1\text{H}_a$			$^1\text{H}_b$		
$Q_u$	$Q_l$	$Q_u/Q_l$	$Q_u$	$Q_l$	$Q_u/Q_l$	$Q_u$	$Q_l$	$Q_u/Q_l$
186	71.1	2.6	124	49.2	2.5	178	77.8	2.3

Table 2.2: Coil port couplings at each of the two frequencies.

Dual-tuned open coil design				
32 MHz ( $^{13}\text{C}$ )		127.7 MHz ( $^1\text{H}$ )		
-18 dB		-26 dB		
Adriany-Gruetter design				
$^{13}\text{C}$ and $^1\text{H}_a$		$^{13}\text{C}$ and $^1\text{H}_b$		$^1\text{H}_a$ and $^1\text{H}_b$
32 MHz ( $^{13}\text{C}$ )	127.7 MHz ( $^1\text{H}$ )	32 MHz ( $^{13}\text{C}$ )	127.7 MHz ( $^1\text{H}$ )	127.7 MHz ( $^1\text{H}$ )
-34 dB	-30 dB	-34 dB	-25 dB	-17 dB

#### 2.4.2 $B_1$ homogeneity at the proton frequency

As was explained in §1.8.4 it is important to have a homogeneous RF field at the  $^1\text{H}$  frequency in order to be sure that power deposition into the subject during proton decoupling does not exceed FDA (Food and Drug Administration) guidelines. An inhomogeneous decoupling field may satisfy the average SAR (Specific Absorption Rates) criteria but may exceed local SAR requirements, particularly in regions in close proximity to the coil. To compare the  $^1\text{H}$  RF field homogeneity of the half-birdcage open coil to that of the Adriany-Gruetter design, the RF field mapping technique described in §2.3.2.1 was used to map the  $^1\text{H}$  RF field of both RF probes in three orthogonal planes. The results are shown in Fig. 2.8. It can be seen that the half-birdcage design provides a more homogeneous field in all three planes. The axial and sagittal contour diagrams

obtained with the half-birdcage exhibit a less rapid decay of signal intensity with increasing distance from the coil elements. Specifically, along the central vertical cut of the axial image obtained with the half birdcage, the approximately linear rate of decay of the flip angle was calculated to be about 0.66 degrees/mm compared to a corresponding rate of about 1 degree/mm for the quadrature surface coil. Very similar values were obtained from the vertical central cuts of the sagittal images. This indicates that the half-birdcage coil would be more efficient in exciting deeper mid-brain structures which are of relevance in the study of neurological disorders. Also calculated along the central vertical lines of the axial and sagittal were the fractional standard deviations ( $fSTD = \text{standard deviation}/\text{mean}$ ) of the field values. It was found for the half birdcage that the  $fSTD$  (for both the axial and sagittal images) was about 80% that of the Adriany-Gruetter design, indicating that the open half-birdcage coil provides a more homogeneous field in the axial and sagittal planes. From the coronal contour diagrams, it is apparent that the half-birdcage also provides a more uniform field in the central region of interest. The improved RF homogeneity will allow more control on the outcome of experiments because the spins will behave more predictably.



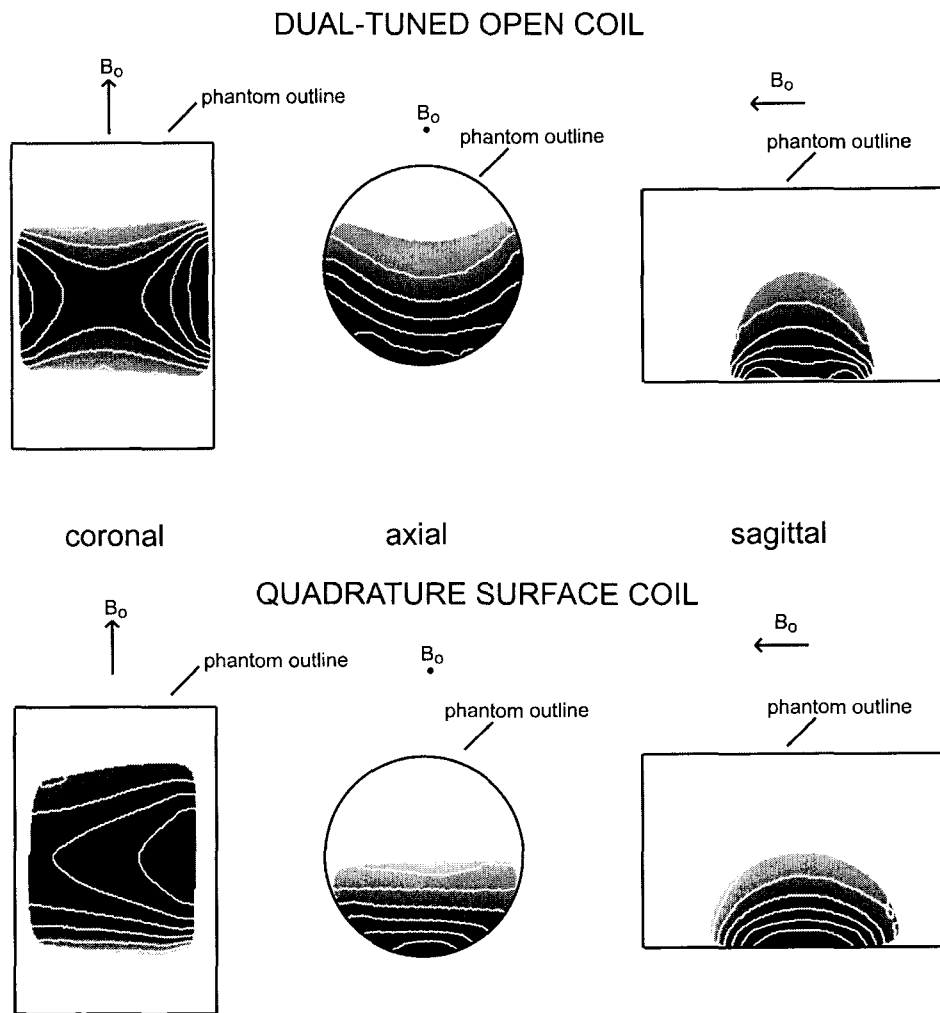


Figure 2.8: Proton RF field maps of the two RF probes. A cylindrical oil phantom of length 19.4 cm and diameter 13.7 cm was used. The maps display normalized  $B_1$  amplitude and contours at 10% intervals of maximum. As can be seen the half-birdcage (dual-tuned open coil) exhibits better uniformity than the Adriany-Gruetter coil design (quadrature surface coil). The surface loops are about 14 cm in diameter, whereas the legs of the half-birdcage are 10.5 cm in length; therefore a larger length of the phantom is 'seen' by the surface coils in the coronal and sagittal directions.

### 2.4.3 In-Vivo decoupling power requirements

Natural abundance  $^{13}\text{C}$  spectra from a human calf were acquired using the method described in §2.3.2.2. Figure 2.9(a) shows the fat spectrum acquired using the dual tuned half birdcage, whereas 2.9(b) shows the same spectrum but proton decoupled. The specific absorption rate (SAR) can be calculated from

$$SAR = P_{input} \times DC \times (1 - Q_{loaded} / Q_{unloaded}) / mass, \quad (2.3)$$

where DC = duty cycle of proton decoupling pulses and  $P_{input}$  = input power.

The expression takes into account the efficiency of the coil. Assuming the mass of the volume seen by the RF probes is about 2 kg, the SAR for proton decoupling using the half birdcage was about 3.2 W/kg, which is within the 4 W/kg FDA guidelines for NMR studies of extremities (DC = 6.8%,  $P_{input}$  = 160 W, and  $Q_{loaded}/Q_{unloaded}$  = 0.42). The corresponding SAR value using the Adriany-Gruetter design was calculated to be approximately 2.2 W/kg (DC = 6.8%,  $P_{input}$  = 110 W, and  $Q_{loaded}/Q_{unloaded}$  = 0.42). The power required for proton decoupling was lower using the quadrature coil design, as was expected however, only by 30% rather than the theoretical 50%. This can be explained by the fact that the two loops were not exactly orthogonal to each other; the optimum angle for minimizing coupling between the coils was about  $110^\circ$ . Therefore, a perfectly circularly polarized field was not achieved.

Although the SAR when employing the half birdcage was just above what is allowed for brain studies (3 W/kg), it can be brought within the guidelines by reducing the acquisition time, either by increasing the spectral width or by reducing the number of data points acquired during acquisition.

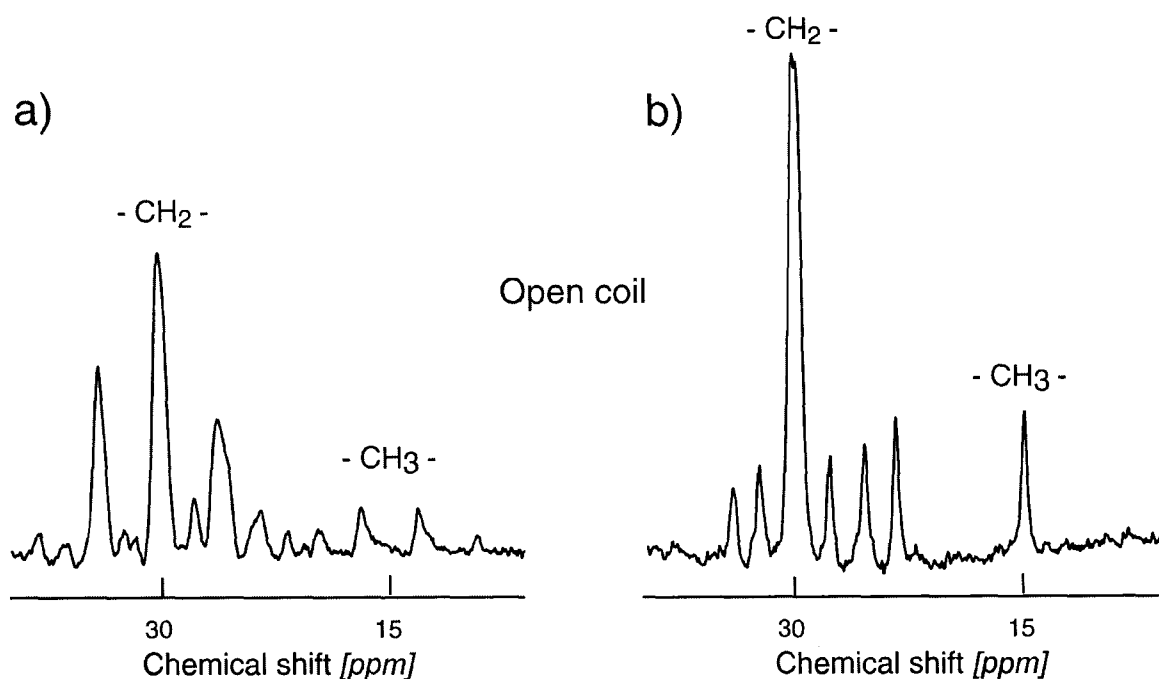


Figure 2.9: (a)  $^{13}\text{C}$  lipids spectra acquired from a human calf by a single  $^{13}\text{C}$  excitation pulse with the dual-tuned half birdcage. (b) Proton decoupling was applied during acquisition. All spectra were acquired in 32 averages. The efficiency of the decoupling can be observed from the  $\text{CH}_3$  signal. The four  $^{13}\text{C}$  peaks of the  $\text{CH}_3$  groups observed in (a) with intensities of ratio 1:3:3:1 are clearly decoupled in (b), where a singlet with a relative height intensity of about 8 is observed (sum of the four multiplets).

#### 2.4.4 Sensitivity and homogeneity at the $^{13}\text{C}$ frequency

To obtain  $^{13}\text{C}$  sensitivity profiles of both RF probes, DEPT enhanced spectra from a 2.5 cm diameter sphere containing 10 M natural abundance acetic acid were obtained with the phantom placed at different points along the coils' vertical axis. The separation between the phantom and the surface of the coil was increased in 1 cm increments, and the power of the pulses was recalibrated at each new phantom location to yield maximum signal. Figure 2.10 shows the variation of the SNR along each coil's vertical axis. The high sensitivity of the  $^{13}\text{C}$  RF surface probe rapidly decays with increasing separation between the phantom and the coil surface. At about one radius (5 cm) separation, both designs exhibit a sensitivity of about 32% of the maximum sensitivity obtained with the  $^{13}\text{C}$  surface coil. Because the  $^{13}\text{C}$  half-birdcage design exhibits a more linear decay of sensitivity, it is more sensitive at greater depths. Specifically, when the separation between the RF probe and the phantom is 7 cm, the half-birdcage is 37% more sensitive

than the surface probe (in other words, the surface coil is only about 73% as sensitive as the half-birdcage coil at that depth). The sensitivity profiles also reflect field homogeneity of the coils, illustrating that the half-birdcage coil provides a more uniform  $^{13}\text{C}$  RF field, down to a depth of about 8 cm, a region of greater neurological interest.

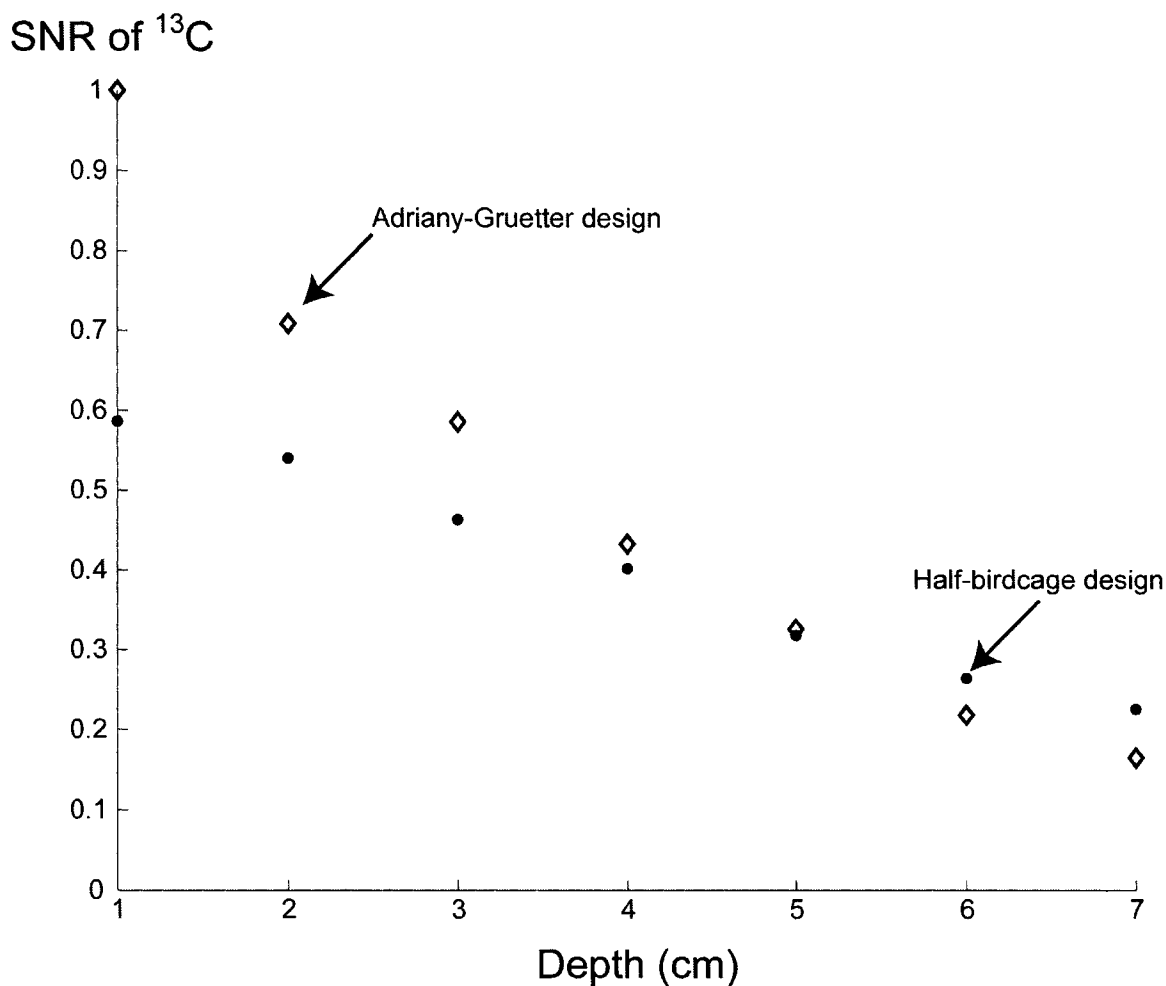


Figure 2.10: SNR of  $^{13}\text{C}$  DEPT enhanced spectra obtained with each coil from a 2.5 cm diameter sphere containing 10 M  $^{13}\text{C}$  natural abundance acetic acid. All values were normalized to the maximum intensity obtained, which was when the separation between the phantom and the  $^{13}\text{C}$  surface coil was 1 cm.

#### 2.4.5 Efficacy of the dual-tuned half birdcage *in vivo*

To verify the efficacy of the coil *in vivo* experiments were conducted on a human calf muscle. Figure 2.11 shows coronal and axial proton images of a human calf obtained with the half birdcage using the imaging parameters stated in §2.3.2.1. The signal to noise ratio of the  $^{13}\text{C}_1$  resonance of glycogen, acquired with the open half birdcage

together with the sequence parameters quoted in §2.3.2.2 was approximately 14. This spectrum is shown in Fig. 2.12.

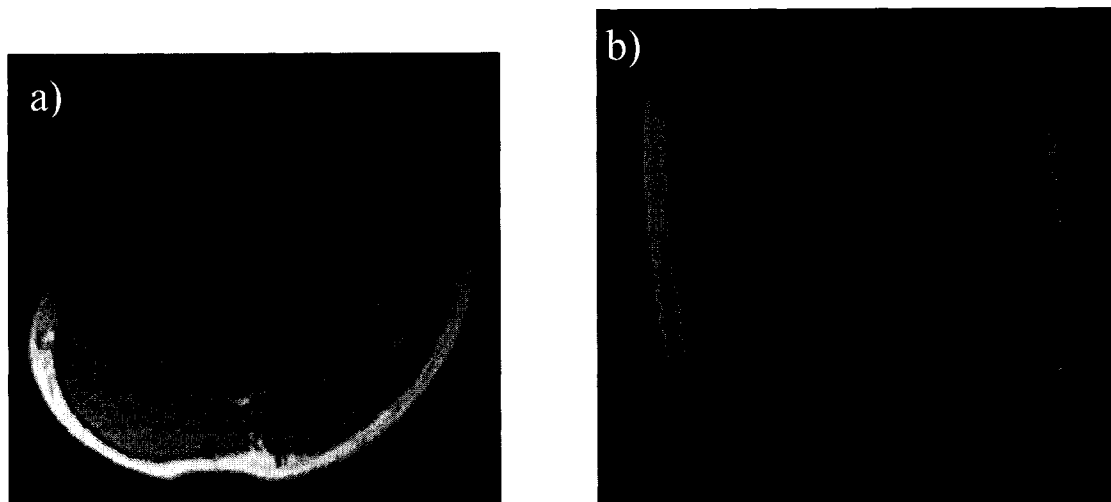


Figure 2.11: Axial (a) and coronal (b) spin echo images of a human calf obtained with the half-birdcage coil.

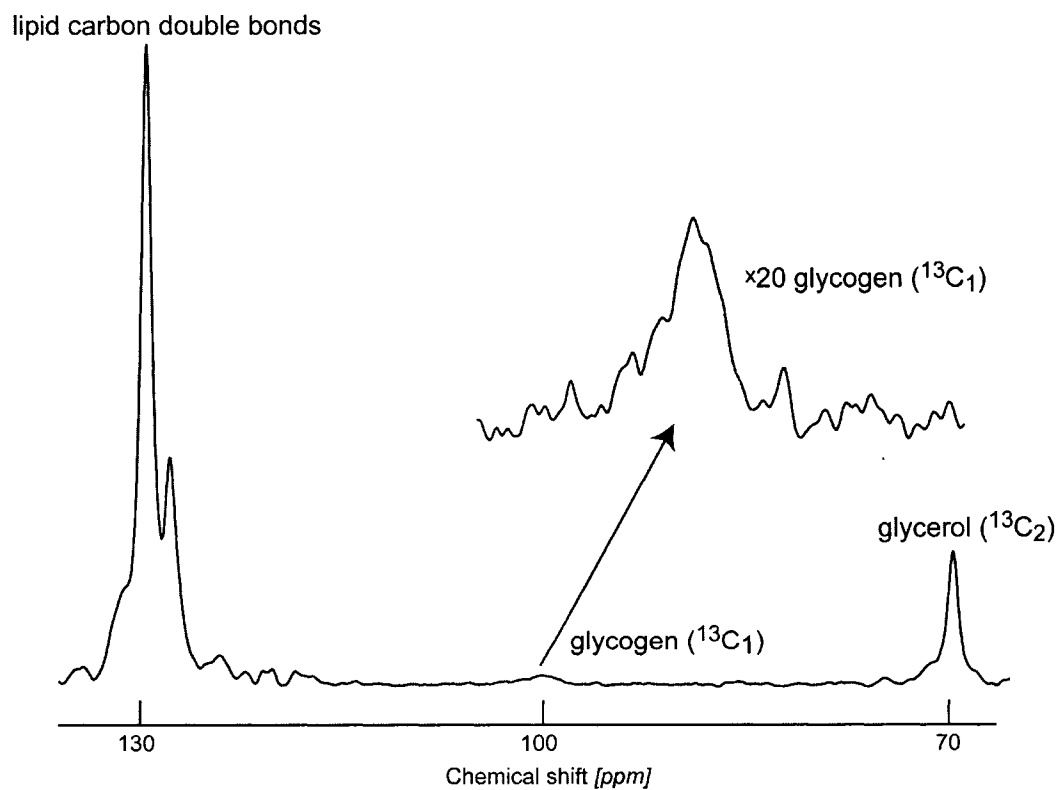


Figure 2.12: Natural abundance  $^{13}\text{C}_1$  glycogen spectrum obtained from the human calf of a normal volunteer. The spectrum was obtained in 1500 averages.

A localized spectrum from a  $3 \times 3 \times 7 \text{ cm}^3$  volume of the human calf was also acquired with the same coil, see Fig. 2.13, where the natural abundance  $^{13}\text{C}$  peaks of creatine (Cr) and of choline (Cho) were detected.

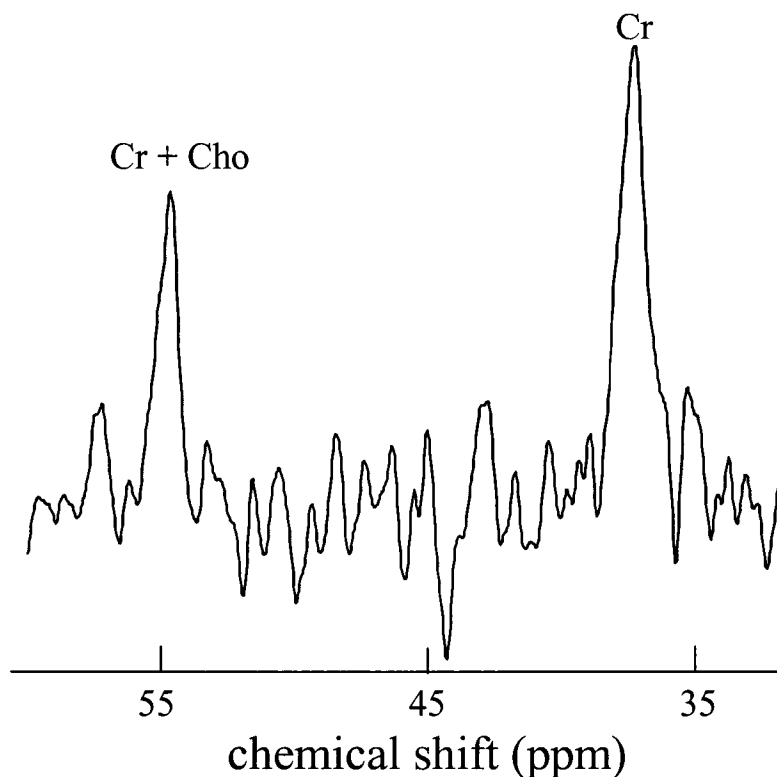


Figure 2.13: Natural abundance  $^{13}\text{C}$  spectrum acquired from a  $3 \times 3 \times 7 \text{ cm}^3$  voxel of a human calf of a normal volunteer using the sequence of Fig. 6.3 ( $\text{TE}_1 = \text{TE}_2 = 30 \text{ ms}$ , 1600 acquisitions) and the dual-tuned open coil. The spectrum shows peaks from the creatine methyl group at 37.5 ppm, and from the creatine methylene and choline methyl groups at 54.8 ppm.

## **2.5 Discussion**

We have demonstrated in this chapter that an open half birdcage can be made to resonate at two frequencies by designing it as a low-pass network and by tuning it in such a way that each of the two resonant signals arise from an alternate set of birdcage conductors. In order to isolate the two frequency modes, trap circuits resonating at the frequency to be blocked were placed in every leg. Such a dual-tuned half-birdcage  $^{13}\text{C}/^1\text{H}$  transceiver was constructed for operation at 3.0 T and was designed for  $^{13}\text{C}\{^1\text{H}\}$  studies of either the human calf or the head. A half-volume coil based on the design of

Adriany and Gruetter (8) was also constructed in order to compare the performance of the two designs. A desirable isolation ( $>15\text{dB}$ ) between the two coil ports at the two frequencies was achieved with the open half-birdcage, and it was shown to provide a more homogeneous RF field than the Adriany-Gruetter design. Although the Adriany-Gruetter system required about 68% of the power required by the half-birdcage (the benefit of quadrature operation), proton decoupling with the open coil can be achieved within FDA SAR guidelines. The major advantage of the half birdcage over the Adriany-Gruetter design is that it is a single unit that provides improved RF homogeneity at both frequencies. This is a significant advantage because an inhomogeneous field can change the distribution of spin coherences which will affect the outcome of any experiment with coupled spins. The half birdcage was also shown to be more sensitive at the  $^{13}\text{C}$  frequency compared to the  $^{13}\text{C}$  surface coil at points further than 5 cm (along its axis) from the coil surface. Moreover, the half birdcage is designed in such a manner that it can be modified to be used for  $^{13}\text{C}$  transmission only, while employing a separate  $^{13}\text{C}$  surface probe for reception if a higher sensitivity is desired for regions close to the coil surface. The use of two separate coils (one for transmission and the other for reception) can be achieved by using a passive decoupling approach where fast switching diodes are placed in both the transmitter and receiver coils (23,24). Because the half birdcage has certain legs that are assigned for  $^{13}\text{C}$  operation placing the diodes in them should not affect operation at the  $^1\text{H}$  frequency.

## **2.6 Conclusion**

We have described in this work a single-unit coil based on the half-birdcage design that can be employed in  $^{13}\text{C}\{^1\text{H}\}$  studies as an alternative to the three coil Adriany-Gruetter design (8). The advantage of this RF probe is that it provides a more uniform field than a surface coil at depths (greater than 7 cm) that are of neurological relevance. Although the coil was employed for  $^{13}\text{C}\{^1\text{H}\}$  experiments, the same coil concept can be employed for  $^1\text{H}\{^{13}\text{C}\}$  studies and should prove to be valuable in studying regions of the brain that are deeper than the occipital lobe.

## **2.7 References**

1. Beckmann N, Seelig J, Wick H. Analysis of glycogen storage disease by *in vivo*  $^{13}\text{C}$  NMR: comparison of normal volunteers with a patient. *Magnetic Resonance in Medicine* 1990;16:150-160.
2. Shulman GI, Rothman DL, Jue T, Stein P, DeFronzo R, Shulman RG. Quantitation of muscle glycogen synthesis in normal subjects and subjects with non-insulin-dependent diabetes by  $^{13}\text{C}$  nuclear magnetic resonance spectroscopy. *The New England Journal of Medicine* 1990;322:223-228.
3. Taylor R, Price TB, Rothman DL, Shulman RG, Shulman GI. Validation of  $^{13}\text{C}$  NMR measurement of human skeletal muscle glycogen by direct biochemical assay of needle biopsy samples. *Magnetic Resonance in Medicine* 1992;27:13-20.
4. Taylor R, Price TB, Katz LD, Shulman RG, Shulman GI. Direct measurement of change in muscle glycogen concentration after a mixed meal in normal subjects. *American Journal of Physiology: Endocrinology and Metabolism* 1993;265:224-229.
5. Roussel R, Carlier PG, Robert JJ, Velho G, Bloch G.  $^{13}\text{C}/^{13}\text{P}$  NMR studies of glucose transport in human skeletal muscle. *Proc Natl Acad Sci USA* 1998;95:1313-1318.
6. Vaughan JT, Hetherington HP, Pan JW, Noa PJ, Pohost GM. A high frequency double tuned resonator for clinical NMR. *Proceedings Annual Meeting SMRM*, 1993, p306.
7. Pan JW, Mason GF, Vaughan JT, Chu W-J, Zhang Y, Hetherington HP.  $^{13}\text{C}$  editing of glutamate in human brain using -refocused coherence transfer spectroscopy at 4.1T. *Magnetic Resonance in Medicine* 1997;37:355-358.
8. Adriany G, Gruetter R. A half-volume coil for efficient proton decoupling in humans at 4T. *Journal of Magnetic Resonance* 1997;125:178-184.
9. Carey PE, Halliday J, Snaar JE, Morris PG, Taylor R. Direct assessment of muscle glycogen storage after mixed meals in normal and type 2 diabetic subjects. *American Journal of Physiology: Endocrinology and Metabolism* 2003;284:688-694.
10. Blüml S, Moreno-Torres A, Ross BD.  $[1-^{13}\text{C}]$  glucose MRS in chronic hepatic encephalopathy in man. *Magnetic Resonance in Medicine* 2001;45:981-993.
11. Gruetter R, Seaquist ER, Kim S, Ugurbil K. Localized *in vivo*  $^{13}\text{C}$ -NMR of glutamate metabolism in the human brain: initial results at 4 tesla. *Developmental Neuroscience* 1998;20:380-388.



12. Shen J, Petersen KF, Behar KL, Brown P, Nixon TW, Mason GF, Petroff OAC, Shulman GI, Shulman RG, Rothman DL. Determination of the rate of the glutamate/glutamine cycle in the human brain by *in vivo*  $^{13}\text{C}$  NMR. *Proc Natl Acad Sci USA* 1999;96:8235-8240.
13. Chen CN, Hoult DI, Sank VJ. Quadrature detection coils-a further improvement in sensitivity. *Journal of Magnetic Resonance* 1983;54:324-327.
14. Ballon D, Graham M, Miodownik S, Koutcher J. A 64 MHz Half-Birdcage Resonator for Clinical Imaging. *Journal of Magnetic Resonance* 1990;90:131-140.
15. Jin J. *Electromagnetic Analysis and Design in Magnetic Resonance Imaging*. Boca Raton: CRC Press; 1999.
16. Roemer PB, Edelstein WA, Hayes CE, Souza SP, Mueller OM. The NMR Phased Array. *Magnetic Resonance in Medicine* 1990;16:192-225.
17. Klomp DW, Kentgens AP, Heerschap A. Loss-less blocking circuits to combine local quadrature  $^{13}\text{C}$  coils with quadrature  $^1\text{H}$  decoupling coils for human head at 3T. *Proceedings Annual Meeting ISMRM, Toronto, 2003*, p2376.
18. Stollberger R, Wach P. Imaging the active  $B_1$  field *in vivo*. *Magnetic Resonance in Medicine* 1996;35:246-251.
19. De Zanche N, Yahya A, Vermeulen FE, Allen PS. Analytical approach to noncircular section birdcage coil design: verification with a cassinian oval coil. *Magnetic Resonance in Medicine* 2005;53:201-211.
20. De Zanche N, Yahya A, Allen PS. Comparison of  $B_1$  field homogeneity *in vivo* vs. in uniform phantoms using a standard birdcage head coil. *Proceedings Annual Meeting ISMRM, Toronto, 2003*, p2388.
21. Shaka AJ, Keeler J, Freeman R. Evaluation of a New Broadband Decoupling Sequence: WALTZ-16. *Journal of Magnetic Resonance* 1983;53:313-340.
22. Ashley JR, Palka FM. Reflection coefficient measurement of microwave resonator Q factors. *The Microwave Journal* June 1971:35-39.
23. Edelstein WA, Hardy CJ, Mueller OM. Electronic decoupling of surface coils for NMR imaging and spectroscopy. *Proceedings Annual Meeting SMRM, 1985*, p1084.
24. Hyde JS, Rilling RJ, Jesmanowicz A. Passive decoupling of surface coils by pole insertion. *Journal of Magnetic Resonance* 1990;89:485-495.

# Chapter 3

## Numerical Method of Spin Evolution Analysis

### 3.1 Introduction

Chapter 1, §1.5.4, explained how the evolution of a spin system during an NMR pulse sequence can be followed by calculating the evolution of the density operator of that spin system. The evolution of the density operator can be calculated by solving the Liouville-von Neumann equation (1),

$$\frac{d}{dt}\rho(t) = \frac{i}{\hbar}[\rho(t), \mathcal{H}(t)] \quad (3.1)$$

which arises from the time-dependent Schrödinger equation, Eq. (3.2), where  $\mathcal{H}$  is the Hamiltonian under which spin evolution takes place.

$$i\hbar \frac{\partial}{\partial t} \Psi(t) = \mathcal{H} \Psi(t) \quad (3.2)$$

The solution to Eq. (3.1) is simple for cases where  $\mathcal{H}$  is time independent and is given by

$$\rho(t) = \exp(-i\mathcal{H}t / \hbar) \rho(0) \exp(i\mathcal{H}t / \hbar), \quad (3.3)$$

where  $\rho(0)$  is the density operator at time  $t = 0$ . The density operator at thermal equilibrium is given by  $I_z$  (see §1.5.2). In general, for an  $I = 1/2$  spin system consisting of  $N$  spins, the density matrix can be expressed at any instant as a weighted sum of  $2^{2N}$  product operator basis terms (1). Since tracking the evolution of these terms for a complicated five proton spin system such as that of glutamate or glutamine is quite impractical manually, numerical methods of analysis need to be employed. For the work presented in this thesis, an extension was made to the numerical framework originally implemented in MATLAB by R.B. Thompson (2-6) for density operator calculations of proton only spin systems. The extension was necessary in order to evaluate the heteronuclear evolutions taking place in  $^{13}\text{C}\{^1\text{H}\}$  and  $^1\text{H}\{^{13}\text{C}\}$  double resonance experiments. The heteronuclear coupling involved proton spin systems that were internally strongly coupled and a typical evolution would be that during the application of a proton PRESS localization sequence.

The next section of this chapter summarizes the algorithms involved in the calculations, and describes the changes introduced to the program in order for it to incorporate a  $^{13}\text{C}$  nucleus.

## **3.2 Numerical Method of Analysis**

### **3.2.1 The Hamiltonian for a proton spin system**

To solve Eq. (3.3), a time independent Hamiltonian must be defined for each of the interactions in which the spins are involved, namely, those due to the static field, the RF field, the gradient field, as well as the chemical shielding and scalar coupling interactions. The rotating frame Hamiltonian is given by  $\mathcal{H}_{rot} = \mathcal{H}_{chemical\ shift} + \mathcal{H}_{scalar\ coupling} + \mathcal{H}_{RF} + \mathcal{H}_{gradients}$ , where each of the individual Hamiltonian terms are defined below.

$$\mathcal{H}_{RF} = \gamma \hbar B_1(t)[(\cos \varphi)I_X + (\sin \varphi)I_Y], \quad (3.4)$$

where  $\varphi$  is the phase of the applied RF pulse with respect to the first pulse applied in the sequence, and  $B_1(t)$  is the amplitude of the RF pulse envelope (7). The chemical shift Hamiltonian in the rotating frame is given by

$$\mathcal{H}_{chemical\ shift} = \hbar \omega_a I_Z, \quad (3.5)$$

where  $\omega_a$  is the proton chemical shift. For the case of a spin system consisting of N protons (denoted by I), Eqs. (3.4) and (3.5) can be written as

$$\mathcal{H}_{chemical\ shift} + \mathcal{H}_{RF} = \hbar \sum_{n=1}^N \omega_{I_n} I_{Z_n} + \gamma_I \hbar B_1(t)[(\cos \varphi_I) \sum_{n=1}^N I_{X_n} + (\sin \varphi_I) \sum_{n=1}^N I_{Y_n}]. \quad (3.6)$$

Similarly, expressions can be written for the N proton spin system for the scalar coupling and gradient pulse Hamiltonians. The scalar coupling Hamiltonian is given by Eq. (3.7), where  $J_{mn}$  are scalar coupling constants between the spins  $I_m$  and  $I_n$  (8).

$$\mathcal{H}_{scalar\ coupling} = 2\pi \hbar \sum_{m=1}^{N-1} \sum_{n=m+1}^N J_{mn} (\vec{I}_m \cdot \vec{I}_n) \quad (3.7)$$

The gradient field varies spatially and involves only the  $I_Z$  operator. The gradient Hamiltonian for a rectangular gradient pulse is given by Eq. (3.8), where  $|\vec{G}|$  is the

gradient strength,  $r$  is the spatial position from the origin of the linear gradient field, and  $\tau$  is the gradient pulse duration.

$$\begin{aligned}\mathcal{H}_{\text{gradient}} &= -\gamma_I \hbar \vec{G} \cdot \vec{r} \sum_{n=1}^N I_{Z_n} & 0 \leq t \leq \tau \\ &= 0 & t > \tau\end{aligned}\quad (3.8)$$

Adding Eqs. (3.6), (3.7), and (3.8) together gives the complete Hamiltonian with which we describe the nuclear-spin system at any instant in time.

### 3.2.2 Modifications made to incorporate a $^{13}\text{C}$ nucleus

To incorporate a  $^{13}\text{C}$  nucleus into the proton-only numerical framework, it is necessary to modify the Hamiltonian equations. The inclusion of a  $^{13}\text{C}$  nucleus in an  $N$  proton spin system yields an  $N+1$  spin system with the  $N+1^{\text{th}}$  spin being the  $^{13}\text{C}$  spin. Denoting  $^{13}\text{C}$  by  $S$ , the four Hamiltonians can be modified as follows (9),

$$\mathcal{H}_{\text{chemical shift}} = \hbar \sum_{n=1}^N \omega_{I_n} I_{Z_n} + \hbar \omega_S S_Z, \quad (3.9)$$

$$\mathcal{H}_{\text{RF}} = \gamma_I \hbar B_{I_I}(t) [(\cos \varphi_I) \sum_{n=1}^N I_{X_n} + (\sin \varphi_I) \sum_{n=1}^N I_{Y_n}] + \gamma_S \hbar B_{I_S}(t) [(\cos \varphi_S) S_X + (\sin \varphi_S) S_Y], \quad (3.10)$$

$$\mathcal{H}_{\text{scalar coupling}} = 2\pi \hbar \sum_{m=1}^{N-1} \sum_{n=m+1}^N J_{mn} (\vec{I}_m \cdot \vec{I}_n) + 2\pi \hbar \sum_{n=1}^N J_{nS} (\vec{I}_n \cdot \vec{S}), \quad (3.11)$$

and

$$\mathcal{H}_{\text{gradient}} = -\gamma_I \hbar \vec{G} \cdot \vec{r} \sum_{n=1}^N I_{Z_n} - \gamma_S \hbar \vec{G} \cdot \vec{r} S_Z, \quad (3.12)$$

where  $\omega_S$  is the  $^{13}\text{C}$  Larmor frequency,  $B_{I_S}(t)$  is the amplitude of the  $^{13}\text{C}$  RF pulse envelope, and  $\varphi_S$  is the phase of the  $^{13}\text{C}$  pulse with respect to the first  $^{13}\text{C}$  pulse applied in the sequence. The chemical shift Hamiltonian represents the Zeeman terms frequency shifted from that of the rotating frame and incorporates all chemically shifted protons and the Larmor frequency shifted  $^{13}\text{C}$  spin. The  $^{13}\text{C}$  frequency relative to the proton frequencies was set to an arbitrary large value, so that  $\vec{I}_n \cdot \vec{S}$  in Eq. (3.11) could be replaced by  $I_{Z_n} S_Z$  (the heteronuclear coupling was explicitly defined as weak). During acquisition, the terms  $\mathcal{H}_{\text{RF}}$  and  $\mathcal{H}_{\text{gradient}}$  in the Hamiltonian become zero. In the presence

of  $^{13}\text{C}$  decoupling, all  $J_{nS}$  values were set to zero in Eq. (3.11), whereas in the presence of  $^1\text{H}$  decoupling all  $J_{nS}$  and  $J_{mn}$  values were set to zero.

### 3.2.3 Algorithm for the calculations

Equation (3.3) is the fundamental equation that allows the calculation of the evolution of the density operator for a number of NMR pulse sequences. From it the density operator (and thus the expectation value of any operator) can be obtained at any time point during the pulse sequence, and directly after it. Since every operator can be represented as a matrix, it is a practical way of representing them for numerical calculations. In order to simplify Eq. (3.3), it is desirable to transform the Hamiltonian into a diagonal matrix, because the exponential of a diagonal matrix is simply a diagonal matrix whose elements are the exponentials of the argument diagonal elements (8). The diagonal form of the Hamiltonian is given by  $\mathcal{H}_{diag} = U\mathcal{H}U^{-1}$ , where  $U$  is a unitary operator and its columns are the eigenvectors of  $\mathcal{H}$ . The eigenvalues of  $\mathcal{H}$  form the diagonal elements of  $\mathcal{H}_{diag}$ . In this new frame,  $\rho(0)_{diag} = U\rho(0)U^{-1}$ , and  $\rho(t)_{diag} = U\rho(t)U^{-1}$ . This transforms Eq. (3.3) into

$$\rho(t) = U^{-1} \exp(-i\mathcal{H}_{diag}t)U\rho(0)U^{-1} \exp(i\mathcal{H}_{diag}t)U. \quad (3.13)$$

In the numerical calculations, the number of spins, the chemical shift and scalar coupling constants are defined. The pulse sequence is then defined with all relevant parameters such as pulse flip angles, delay lengths, and gradient field strengths and durations. Each pulse sequence is treated as a series of independent segments, where each segment is characterized by its own time independent Hamiltonian. For example, in a sequence where a hard  $90^\circ$  pulse is applied followed by a delay, the pulse represents one segment and the delay another. In this discrete method of implementation Eq. (3.13) can be rewritten as

$$\rho_n = U_n^{-1} \exp(-i\mathcal{H}_{diag_n}t_n)U_n\rho_{n-1}U_n^{-1} \exp(i\mathcal{H}_{diag_n}t_n)U_n, \quad (3.14)$$

where  $\mathcal{H}_{diag_n}$  is the diagonal Hamiltonian of the  $n^{\text{th}}$  segment formed from the Hamiltonian of that segment,  $\mathcal{H}_n$ , defined by Eq. (3.15).  $U_n$  is the unitary matrix of that segment obtained from the eigenvectors of  $\mathcal{H}_n$ .

$$\mathcal{H}_n = \mathcal{H}_{RF_n} + \mathcal{H}_{chemical\ shift_n} + \mathcal{H}_{scalar\ coupling_n} + \mathcal{H}_{gradient_n} \quad (3.15)$$

By successive matrix multiplications according to Eq. (3.14), the density operator at the end of any segment can be evaluated.

For the gradient terms where there exists a spatial distribution of terms, the segment representing the gradient pulse is broken into sub-segments (for different spatial positions), where each sub-segment is defined by a Hamiltonian for that position in space. These operators are all combined in a storage matrix that efficiently allows their effects to be combined (4). For shaped slice selective pulses applied in conjunction with a gradient, the Hamiltonian is no longer time independent. However, in this situation, the pulse can be broken up into smaller discrete time segments, during which a time independent Hamiltonian can be defined. The integrated effects of the pulse over space can be combined into a transformation matrix that depends only on the characteristics of the spin system and not on the density matrix present prior to pulse application (4). Multiplying this transformation matrix by the coefficients of the density operator terms present prior to the pulse gives a matrix whose elements are the transformed coefficients of the density operator terms, that is, the state of the spin system after applying the slice selective pulse.

To calculate the final observable spectrum, the FID that is acquired during the acquisition period needs to be calculated. This is done by using the density operator at each of the discrete sample points,  $n\Delta t$ , during the acquisition period to calculate the expectation value of  $I_+$ , the raising operator at each point.

$$M_+(n\Delta t) \propto \langle I_+(n\Delta t) \rangle = Tr(I_+ \rho(n\Delta t)) \quad (3.16)$$

### **3.3 A Double Resonance Example: Response of CH<sub>2</sub> to DEPT**

To give an example of using the numerical program to analyze a double resonance experiment, a CH<sub>2</sub> molecular group and the application of the DEPT (§1.8.2) pulse sequence (10) at 3.0 T is considered. First the three spins are defined by their chemical shift and scalar coupling constants. The proton Larmor frequency ( $\approx 128$  MHz at 3.0 T) is also specified. Denoting chemical shift constants by  $\sigma$ , we let  $\sigma_{I_1} = \sigma_{I_2} = 2$  ppm,  $\sigma_S = 30$  ppm (an arbitrary large value for the <sup>13</sup>C frequency), and

$J_{1S} = J_{2S} = 135 \text{ Hz}$ , a typical  $^1\text{H}/^{13}\text{C}$  heteronuclear scalar coupling constant. The density matrix at time  $t = 0$  was set equal to  $\rho(0) = I_{z_1} + I_{z_2}$  ( $S_z$  is excluded because only  $^{13}\text{C}$  signal due to polarization transfer is of interest; experimentally any  $^{13}\text{C}$  signal arising from direct excitation by the  $^{13}\text{C}$   $90^\circ$  pulse is eliminated by phase cycling). The response of the spins was calculated using the DEPT sequence displayed in Fig. 1.23, where  $\tau$  was set to 3.7 ms. The pulse sequence shown in Fig. 1.23 can be broken into eight discrete segments. The first segment is for the  $90^\circ$  proton excitation pulse, the second is for the delay  $\tau$ , the third is for the  $180^\circ$  proton refocussing pulse, the fourth is for the  $^{13}\text{C}$  excitation pulse, the fifth is for the second  $\tau$  delay, the sixth is for the  $^{13}\text{C}$  refocussing pulse, the seventh is for the proton editing pulse where  $\theta$  is set to  $45^\circ$  for optimal signal from a  $\text{CH}_2$  molecular group, and the last segment is for the final  $\tau$  delay. Each of the eight segments has its own time independent Hamiltonian that characterizes it. During the acquisition period, the Hamiltonian consists only of the chemical shift and the scalar coupling Hamiltonians. Figure 3.1(a) shows the resulting  $^{13}\text{C}$  spectrum from the polarization transfer experiment. Three peaks with intensity ratios of 1:2:1 are observed as expected with their separation being equal to  $J_{\text{CH}}$ . Figure 3.2(b) shows the result of setting the scalar coupling Hamiltonian to zero during acquisition to implement the effect of proton decoupling. Finally, the angle theta was varied between 0 and  $\pi$  in increments of  $\pi/20$  and the resulting peak height is plotted as a function of theta in Fig. 3.2. The signal variation with theta matches the expected  $\sin(2\theta)$  dependence (10).

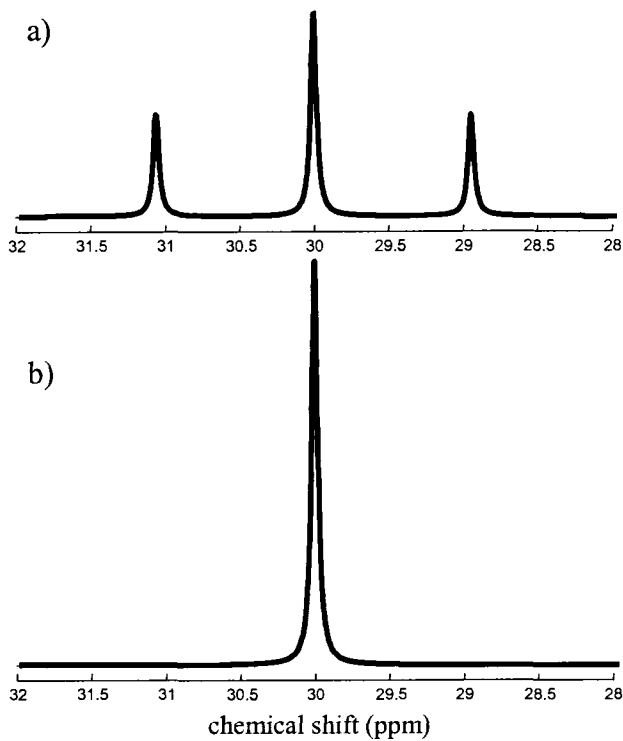


Figure 3.1: Calculated  $^{13}\text{C}$  spectra of a  $\text{CH}_2$  molecular group in response to DEPT in the case where a) no proton decoupling is applied, and b) proton decoupling is applied (all heteronuclear scalar coupling constants were set to zero during the acquisition period).

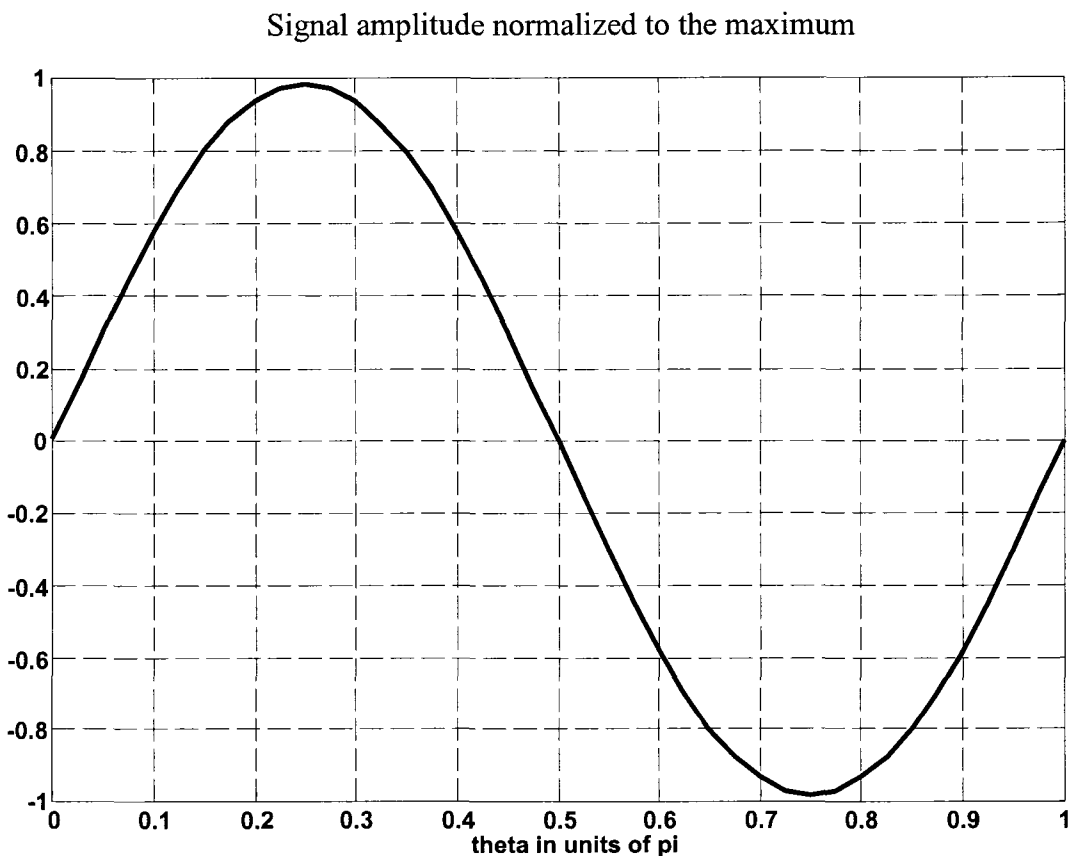


Figure 3.2: Calculated signal intensity of the decoupled peak of a  $\text{CH}_2$  molecular group in response to DEPT as a function of theta (the editing proton pulse in the DEPT sequence).



### **3.4 References**

1. Ernst RR, Bodenhausen G, Wokaun A. Principles of nuclear magnetic resonance in one and two dimensions. Oxford: Clarendon Press; 1987.
2. Thompson RB, Allen PS. A new multiple quantum filter design procedure for use on strongly coupled spin systems found in vivo: its application to glutamate. *Magnetic Resonance in Medicine* 1998;39:762-771.
3. Thompson RB, Allen PS. The role of the N-acetylaspartate multiplet in the quantification of brain metabolites. *Biochemistry and Cell Biology* 1998;76:497-502.
4. Thompson RB. *Coupled Proton MRS: In-Vivo Applications* [Ph.D. thesis]. Edmonton: University of Alberta; 1999.
5. Thompson RB, Allen PS. Sources of variability in the response of coupled spins to the PRESS sequence and their potential impact on metabolite quantification. *Magnetic Resonance in Medicine* 1999;41:1162-1169.
6. Thompson RB, Allen PS. The response of metabolites with coupled spins to the STEAM sequence. *Magnetic Resonance in Medicine* 2001;45:955-965.
7. Canet D. *Nuclear Magnetic Resonance, Concepts and Methods*. Chichester: John Wiley & Sons; 1996.
8. Levitt MH. *Spin Dynamics, Basics of Nuclear Magnetic Resonance*. Chichester: John Wiley & Sons; 2001.
9. Yahya A, Allen PS. Effect of strong homonuclear proton coupling on localized <sup>13</sup>C detection using PRESS. *Magnetic Resonance in Medicine* 2005;54:1340-1350.
10. Doddrell DM, Pegg DT, Bendall MR. Distortionless enhancement of NMR signals by polarization transfer. *Journal of Magnetic Resonance* 1982;48:323-327.

# Chapter 4

## Indirect $^{13}\text{C}$ Observation I: PRESS-Localized POCE<sup>1</sup>

### 4.1 Introduction

In vivo  $^{13}\text{C}$  NMR spectroscopy has been widely used to determine the rates of metabolic fluxes in both human (1-4) and rat (5-10) brain. The time course of  $^{13}\text{C}$  label incorporation into metabolic products has been carried out either by indirect  $^{13}\text{C}$  detection through  $^{13}\text{C}$  coupling to protons (1,5,8,10) or by direct  $^{13}\text{C}$  detection (2-4,6,7,9). The principal advantage of the indirect technique is the signal gain of  $\gamma_H^3 / \gamma_C^3 \approx 64$  (11) over direct  $^{13}\text{C}$  detection.

Localized indirect detection has been exploited with one or other of the ISIS (12) or the PRESS (13,14) localization schemes and may (1,10) or may not (15) have used the  $^{13}\text{C}$  inversion pulse that characterizes the POCE (Proton Observe Carbon Edited) indirect observation strategy (16). However, at the typical field strengths used for human brain studies, such as 3.0 T, the less than optimal spectral resolution offered by the proton tends to limit what can be measured to the  $\text{C}_3$  and  $\text{C}_4$  signals of glutamate (Glu). Nevertheless, the  $\text{C}_3$  and  $\text{C}_4$  signals of Glu were sufficient to measure aspects of neuronal oxidative metabolism such as the tricarboxylic acid (TCA) cycle rate from a PRESS localized volume without any  $^{13}\text{C}$  excitation (15), by observing the  $^{13}\text{C}$ -coupled sidebands on the protons coupled to  $\text{C}_3$  and  $\text{C}_4$ . Extending the PRESS sequence to incorporate the POCE  $^{13}\text{C}$  inversion pulse (1,17) was used at 4.0 T to measure changes in  $\text{C}_4$  Glu labelling, parallel to fMRI, during changes in neuronal activity in human brain (1).

When planning or interpreting the data from indirect detection methods, it has been convention to assume that the key interaction is the  $^1\text{H}$ - $^{13}\text{C}$  heteronuclear scalar coupling. The focus of this report is to demonstrate how the concurrent, strong-homonuclear proton scalar coupling that exists in many key brain metabolites affects the

---

<sup>1</sup> A version of this chapter has been published. Yahya A, Allen PS. Effect of strong homonuclear proton coupling on localized  $^{13}\text{C}$  detection using PRESS. *Magnetic Resonance in Medicine* 2005; 54, 1340-1350.

spectral response to the POCE sequence, and moreover, to demonstrate that even greater differences in spectral response are manifest when POCE is combined with PRESS, because of the modification of the proton spin coherence distribution during proton-PRESS localization. Using Glu at 3.0 T as an illustrative example, the effects of the simultaneous homo- and heteronuclear scalar couplings on the spectral evaluation of indirect  $^{13}\text{C}$  incorporation experiments are described. It is shown that when (homonuclear-coupling-induced) polarization transfer takes place between protons that are bound to  $^{13}\text{C}$  (and are therefore coupled) and those that are not, significant modifications of the scalar-coupling evolutions occur for both categories of proton. These changes in the scalar-coupling evolution lead to changes in the proton multiplets that arise both from protons that are  $^{13}\text{C}$ -coupled and from those that are not. These multiplet lineshape and intensity changes ultimately affect the estimates of  $^{13}\text{C}$  enrichment made by the indirect POCE method. An independent investigation of the POCE sequence was recently presented at the annual meeting of ISMRM in Miami by Dr. P-G Henry et al. (18).

## **4.2 Methods**

### **4.2.1 Numerical method**

The method of numerical analysis used in this chapter was outlined in chapter 3. The chemical shift and scalar coupling constants used (19,20) are displayed in Table 4.1.

Table 4.1: Chemical shift and scalar coupling parameters for both the protons and the carbons of glutamate. Since each of the protons can only be coupled to a single carbon, X can denote a  $^{13}\text{C}$  labelled  $\text{C}_2$ ,  $\text{C}_3$  or  $\text{C}_4$  carbon.

<b>Chemical Shift (ppm)</b>					
<b>A</b>	<b>M</b>	<b>N</b>	<b>P</b>	<b>Q</b>	<b>X</b>
3.78	2.14	2.06	2.37	2.36	arbitrarily large
<b>Scalar Coupling Constants (Hz)</b>					
	<b>M</b>	<b>N</b>	<b>P</b>	<b>Q</b>	<b>X</b>
<b>A</b>	4.67	7.33			155 ( <b>X=C<sub>2</sub></b> )
<b>M</b>		-14.85	6.43	8.47	135 ( <b>X=C<sub>3</sub></b> )
<b>N</b>			8.39	6.89	135 ( <b>X=C<sub>3</sub></b> )
<b>P</b>				-15.89	135 ( <b>X=C<sub>4</sub></b> )
<b>Q</b>					135 ( <b>X=C<sub>4</sub></b> )

### 4.2.2 Experimental methods

In the work reported, the PRESS sequence was used to provide spatial localization. To provide the sensitivity to  $^{13}\text{C}$ , the PRESS localization component, applied to protons, was followed by a POCE (16) sequence component to illustrate indirect  $^{13}\text{C}$  detection. The PRESS sequence consisted of a sinc-gaussian  $90^\circ$  slice selective excitation pulse of length 2.6 ms (bandwidth  $\approx 1500$  Hz) followed by two slice selective 2.75 ms sinc refocussing pulses (bandwidth  $\approx 1500$  Hz) each applied in conjunction with 3.6 mT/m gradients in order to refocus a slice thickness of 1 cm (a voxel size of  $1 \times 1 \times 1 \text{ cm}^3$  was achieved). The pulses were numerically optimized using the software MATPULSE (21) to minimize the spatial extent of the tip-angle transition region. The relatively short pulse lengths along with spoiler gradients of length 1 ms allowed a minimum total echo time of 20 ms ( $\text{TE}_1 = \text{TE}_2 = 10$  ms) to be achieved. A preceding hyperbolic secant inversion pulse was employed to minimize water contamination at the appropriate inversion time. The sequence also employed a repetition time, TR, of 3 s, and a WALTZ-16 (22) decoupling component for  $^{13}\text{C}$  decoupling during acquisition.

For indirect  $^{13}\text{C}$  detection, a POCE sub-sequence was incorporated into PRESS (17) as shown in Fig. 4.1. The  $^{13}\text{C}$  inversion pulse, applied on alternate scans  $1/2J_{\text{CH}}$  seconds prior to acquisition, inverted the  $^{13}\text{C}$  nuclear magnetization, thereby changing the sign of the heteronuclear antiphase coherences. This sign change enabled the heteronuclear coupled protons to be differentiated from all other protons by the subtraction of alternate scans. The  $^{13}\text{C}$  inversion pulse was a  $400 \mu\text{s}$  pulse applied 3.7 ms ( $J_{\text{CH}} = 135$  Hz) prior to acquisition. The addition of the POCE inversion pulse increased the minimum length of  $\text{TE}_2$  to 15 ms, thereby yielding a minimum total echo time of 25 ms.

All experiments were carried out in an 80 cm bore, 3.0 T magnet system (MagneX Scientific PLC, Abingdon, UK) using a SMIS spectrometer (Surrey Medical Imaging Systems PCL, Guildford, UK) with a home-built 7 cm diameter  $^1\text{H}$  birdcage RF coil, and a 3.5 cm diameter  $^{13}\text{C}$  surface coil. To verify the numerical calculations, two 2 cm diameter aqueous-solution phantoms of  $\text{pH} \approx 7$  were made, one containing 35 mM Glu,

with  $^{13}\text{C}$  in natural abundance and another containing 35 mM labelled Glu with the  $\text{C}_3$  carbon enriched 99% in  $^{13}\text{C}$  (Sigma-Aldrich Canada). Although  $[1-^{13}\text{C}]$  glucose yields labelled  $\text{C}_4$ -Glu on the first round of the TCA cycle, the ideas we wish to convey can be illustrated by  $\text{C}_3$ -labelled Glu which is readily available commercially. First of all, the perturbation of the  $^{13}\text{C}$ - $^1\text{H}$  heteronuclear-scalar-coupling evolution brought about by the strong homonuclear coupling during a proton PRESS sequence was evaluated. Using both natural abundance and enriched  $^{13}\text{C}$  Glu at 3.0 T the difference in the proton response of the Glu MNPQ spins was determined numerically and experimentally at a number of different echo times. The same procedure was then repeated using enriched Glu for the PRESS sequence incorporating POCE.

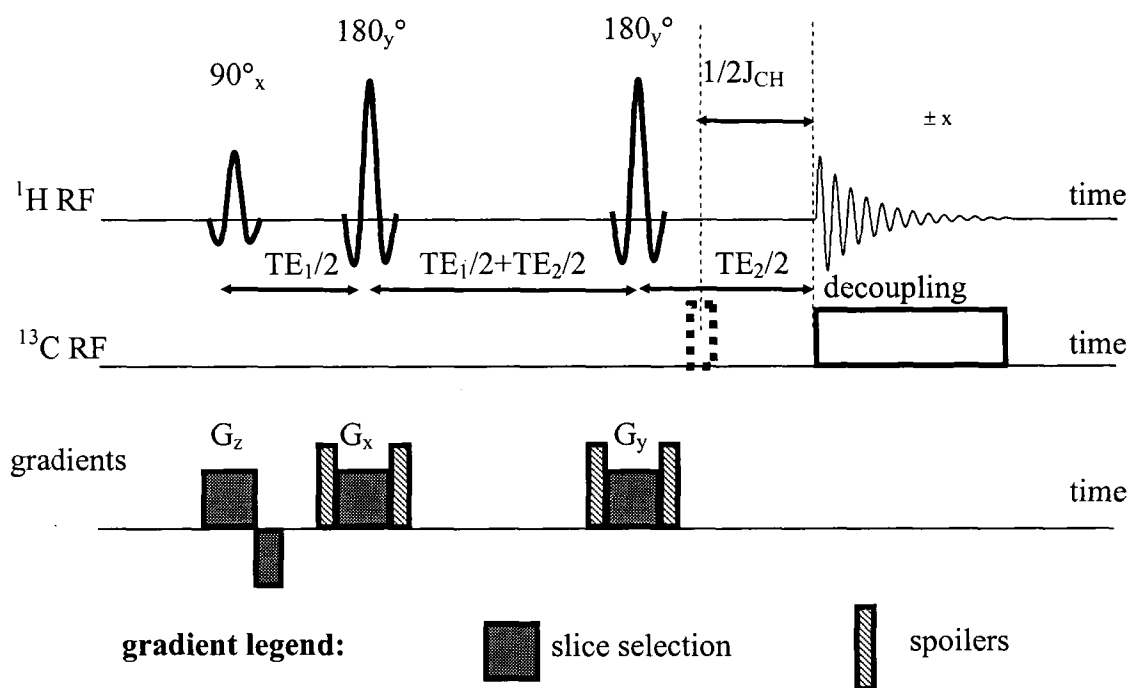


Figure 4.1: A localized POCE sequence for the indirect detection of  $^{13}\text{C}$  signals. The localization is brought about by a PRESS sub-sequence applied to the protons. The dashed rectangle represents the  $^{13}\text{C}$  inversion pulse (the POCE component) applied in each alternate scan.

## **4.3 Results**

### **4.3.1 Simultaneous strong homonuclear and weak heteronuclear coupling during PRESS**

The purpose of this section is to demonstrate the interplay between homo- and hetero-nuclear coupling on the proton PRESS response. To demonstrate the consequences of concurrent homonuclear and heteronuclear scalar coupling interactions involving the protons of Glu, it was essential to be able to switch “on”, or “off”, one of the interactions in both the numerical analysis and in the experiment. This was done effectively by toggling the heteronuclear interaction, i.e., “off” = natural abundance  $^{13}\text{C}$ , whereas “on” = 99 %  $^{13}\text{C}$ , at the  $\text{C}_3$  site bonded to the MN protons of Glu. Figure 4.2 shows the effect of switching the heteronuclear coupling on and off for three different echo-time combinations of the PRESS sequence alone. The broad spectral regions of the Glu MN and PQ multiplets which are delineated in Fig. 4.2, are both seen to change significantly as the  $^{13}\text{C}$  coupling to the MN protons is switched “on” or “off”, even though the PQ spins are not coupled to a  $^{13}\text{C}$  spin. This is because the M, N, P, and Q protons are strongly-coupled to each other and thus in-phase coherence of one pair of the spins can transform into antiphase coherence of one of the other pair of spins, and vice-versa (23). For example, when  $\{\text{TE}_1, \text{TE}_2\} = \{20 \text{ ms}, 10\text{ms}\}$  and the “on” and “off” lineshapes are fairly similar, the PQ signal (integrated between 2.25 and 2.55 ppm) is  $\approx 18 \%$  less than when heteronuclear  $^{13}\text{C}$ - $^1\text{H}_{\text{MN}}$  coupling is “on”, and the MN signal (integrated between 1.8 and 2.25 ppm) is  $\approx 27 \%$  less in this same “on” state. This change in signal results from an alteration in the distribution of single quantum coherences (SQCs) present at the onset of acquisition. Each SQC contributes its individual lineshape component to the overall measured lineshape in proportion to the amplitude of that SQC, and hence changes in the SQC distribution give rise to changes in multiplet lineshape. Figure 4.3a shows the contributing lineshapes of four P SQCs and how these SQCs can arise by polarization transfer, for example, from in-phase  $M_Y$  magnetization (present directly after PRESS excitation) due to the strong coupling between the M and P protons.

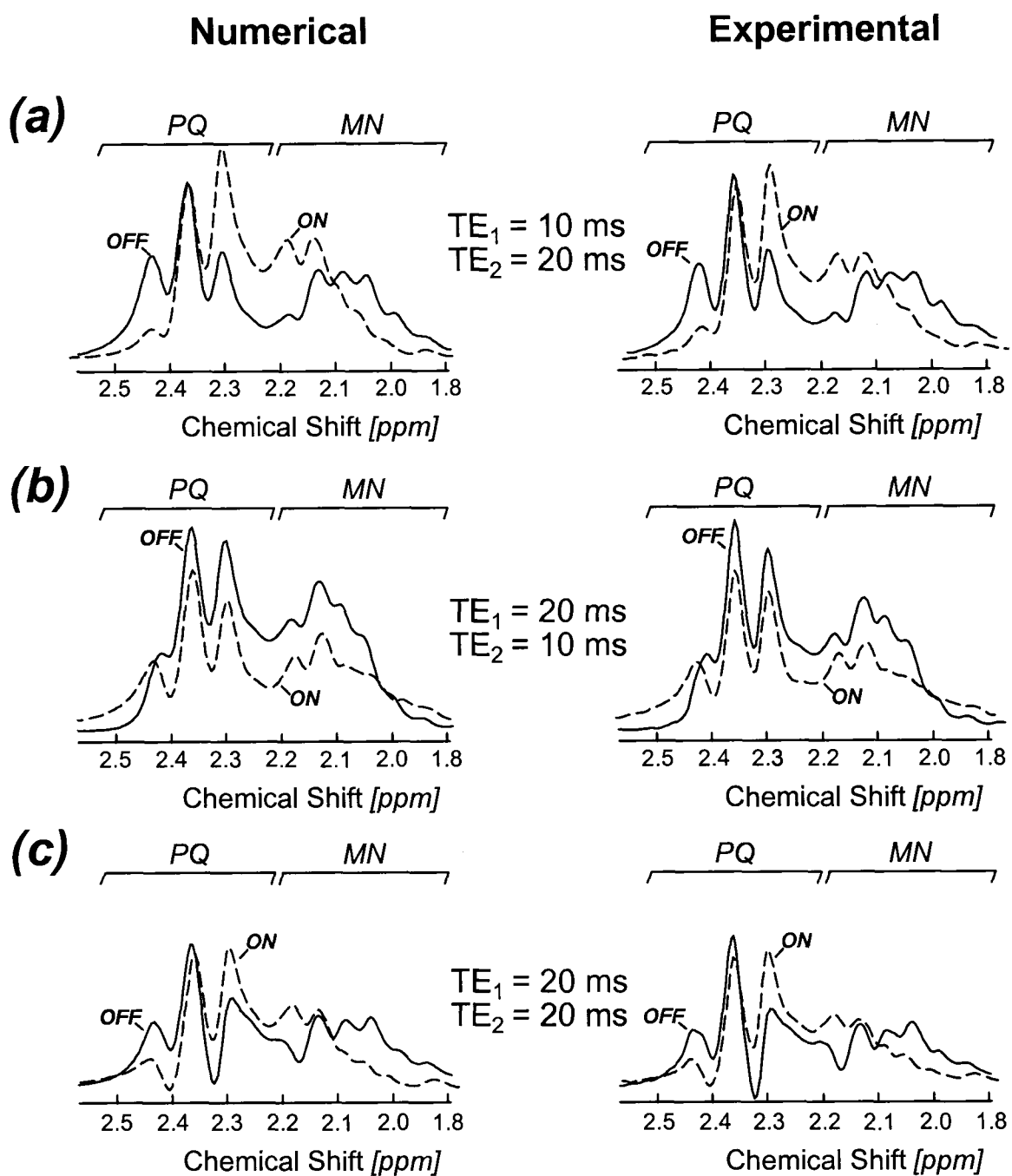


Figure 4.2: An illustration of the different response to a proton PRESS sequence by the MNPQ protons of Glu, depending on whether the  $C_3$  carbon (bonded to the MN protons) is labelled with  $^{13}C$  or not. The figure also demonstrates the variability of these responses to small changes in the echo times of PRESS. Both theoretical and experimental results are compared, where the OFF state for heteronuclear coupling is represented experimentally by natural abundance  $^{13}C$ , and the ON state by 99%  $^{13}C_3$  enriched Glu. For the phantom experiments, a total of 128 averages were acquired for each spectrum. Both numerical and experimental spectra were line broadened to 5 Hz. The small differences between theory and experiment are likely to be due to imperfect pulse calibrations. In particular the RF pulses involved in the  $^{13}C$  decoupling sequence were provided by a surface coil and therefore may not have excited all the spins uniformly in the selected voxel.

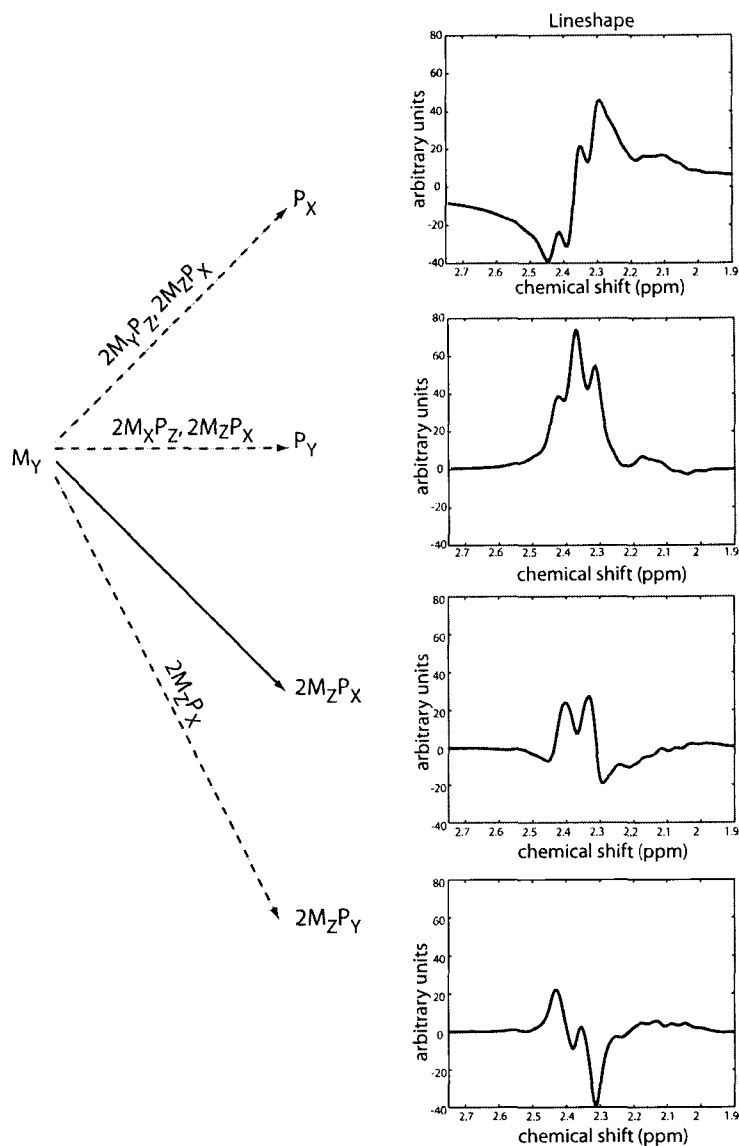


Figure 4.3: The lineshapes of four P SQC terms, namely,  $P_X$ ,  $P_Y$ ,  $2M_ZP_X$ , and  $2M_ZP_Y$ , are shown illustrating how each SQC term, if present at the onset of acquisition, can contribute a net positive or negative area to the final signal. Considering only the MP strongly-coupled protons of Glu, the arrows show how these SQCs can arise by polarization transfer from in-phase  $M_Y$  magnetization present directly after the PRESS excitation pulse, through many pathways. The dashed arrows along with the terms above them indicate the indirect path through which the P SQC is yielded.



In principle, 256 possible SQC terms arise for the four protons (M, N, P, and Q) of the six spin AMNPQX system of Glu, when incorporating a single  $^{13}\text{C}$  spin. However, not all 256 SQC terms have a significant contribution to the MN and PQ multiplets of the Glu proton spectrum. Figure 4.4 shows the distribution of 17 MNPQ SQCs at the onset of acquisition that significantly change in the presence and in the absence of heteronuclear coupling (in response to PRESS,  $\{\text{TE}_1, \text{TE}_2\} = \{20 \text{ ms}, 10 \text{ ms}\}$ ) and that affect the lineshape and intensity of the resulting signal. Apart from the change in the levels of  $2N_yP_z$ ,  $2N_yQ_z$ ,  $2P_yM_z$ , and  $2P_yN_z$ , which cause an increase in signal (based on their sign, amplitude, and contributing lineshapes), the increased negativity of the remaining antiphase coherences and the decrease in the in-phase coherences  $M_y$ ,  $N_y$ ,  $P_y$ , and  $Q_y$  are what is responsible for the overall reduction in signal intensity when the MN protons are  $^{13}\text{C}$ -coupled. This alteration in the SQC distribution can be explained by the proliferation of antiphase coherences involving  $^{13}\text{C}$  (some of which are included in Fig. 4.4) that do not contribute to any signal under conditions of  $^{13}\text{C}$  decoupling. Note the existence of such antiphase coherences for the P and Q protons even though they are not  $^{13}\text{C}$ -coupled. This is a result of the polarization transfer that takes place between the strongly-coupled MN and PQ protons as illustrated below for a simple MPX spin system, where the MP protons are strongly-coupled, the M spin exhibits heteronuclear coupling with the X spin, and there is no coupling between the P and X spin.

$$M_y \rightarrow \begin{cases} 2M_xP_z \\ 2M_yP_z \end{cases} \rightarrow \begin{cases} 4M_xP_zX_z \\ 4M_yP_zX_z \end{cases} \rightarrow \begin{cases} 2P_xX_z \\ 2P_yX_z \end{cases} \quad (4.1)$$

$$M_y \rightarrow 2M_xX_z \rightarrow \begin{cases} 4M_xP_zX_z \\ 4M_yP_zX_z \\ 4M_zP_yX_z \end{cases} \rightarrow \begin{cases} 2P_xX_z \\ 2P_yX_z \end{cases} \quad (4.2)$$

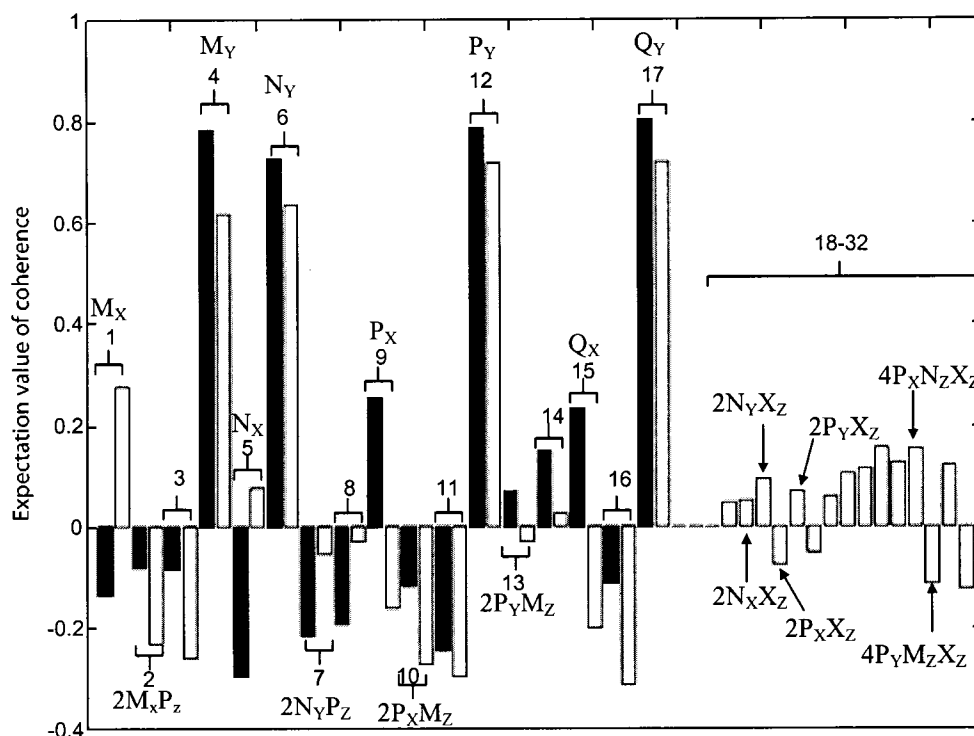


Figure 4.4: Distribution of 17 Glu M, N, P, and Q SQC terms present at the onset of acquisition for a PRESS sequence with  $TE_1 = 20$  ms and  $TE_2 = 10$  ms, in the situation that no heteronuclear scalar coupling exists (solid bars) and in the situation where the MN protons are  $^{13}\text{C}$ -coupled (clear bars). The 17 coherence terms are, respectively,  $M_x$ ,  $2M_xP_z$ ,  $2M_xQ_z$ ,  $M_y$ ,  $N_x$ ,  $N_y$ ,  $2N_yP_z$ ,  $2N_yQ_z$ ,  $P_x$ ,  $2P_xM_z$ ,  $2P_xN_z$ ,  $P_y$ ,  $2P_yM_z$ ,  $2P_yN_z$ ,  $Q_x$ ,  $2Q_xM_z$ , and  $Q_y$ . The fifteen terms on the right side are some of the antiphase terms that arise as a result of the  $^{13}\text{C}$ -coupling, namely,  $2M_yX_z$ ,  $2N_xX_z$ ,  $2N_yX_z$ ,  $2P_xX_z$ ,  $2P_yX_z$ ,  $2Q_xX_z$ ,  $2Q_yX_z$ ,  $4M_xQ_zX_z$ ,  $4M_yQ_zX_z$ ,  $4N_xP_zX_z$ ,  $4N_xQ_zX_z$ ,  $4P_xN_zX_z$ ,  $4P_yM_zX_z$ ,  $4Q_xN_zX_z$ , and  $4P_yN_zX_z$ , respectively.

### 4.3.2 Simultaneous strong homonuclear and weak heteronuclear coupling during POCE

The POCE sequence (16) was described in §1.8.3 and displayed in Fig. 1.2.4. The assumption upon which the action of the POCE inversion pulse is based is that it will invert 100% of the multiplet from  $^{13}\text{C}$ -coupled protons, but none from any uncoupled protons. Subtraction of scans with and without inversion is therefore assumed to give twice the  $^{13}\text{C}$ -coupled proton multiplet, but cancel the uncoupled signal. It is shown here that in situations such as that of the MN or PQ protons of Glu where strong-coupling is involved, POCE does not completely eliminate signal from protons not coupled to  $^{13}\text{C}$  nuclei. This is because the POCE scan which involves application of the  $^{13}\text{C}$  inversion

pulse does not simply invert signal from  $^{13}\text{C}$ -coupled protons with respect to the signal from the other scan. Because of the strong proton coupling, it changes the intensity and the lineshape of the signal from both  $^{13}\text{C}$ -coupled and uncoupled protons so that when the two scans are subtracted, some residual signal from non- $^{13}\text{C}$ -coupled protons remains. This is illustrated in Fig. 4.5, where the response of the MN and PQ protons to the POCE sequence was calculated first for the case where the  $\text{C}_3$  carbon is a  $^{13}\text{C}$  nucleus, and then for the situation where the  $\text{C}_4$  carbon is a  $^{13}\text{C}$  nucleus. The shortest echo time,  $2\tau$ , for the sequence of Fig. 1.2.4 was used ( $\tau=1/2J_{\text{CH}}=3.7\text{ms}$ ) and  $^{13}\text{C}$  decoupling during acquisition was assumed. The dashed lines represent the signal from the two individual POCE scans, the one with the inverted peaks being from the scan where the  $^{13}\text{C}$  inversion pulse was applied. The solid line shows half the difference of the two scans. As can be seen, because of a decrease in the intensity of the signal from non- $^{13}\text{C}$ -coupled protons in the scan where the  $^{13}\text{C}$  inversion pulse was applied there remains some unsuppressed signal in the resulting POCE spectrum from protons that are not coupled to  $^{13}\text{C}$  nuclei. More precisely, by integrating the PQ proton peaks (2.25-2.55ppm) both of the resultant POCE spectrum and of the unedited spectrum shown in Fig. 4.5(a) it was calculated that about 14% of the PQ signal remains unsuppressed. Similar calculations for the MN peaks (1.8-2.25ppm) in Fig. 4.5(b) yield that approximately 11% of the MN signal remains after subtraction of the two scans. In the situation that both  $\text{C}_3$  and  $\text{C}_4$  changes are being monitored and if simple integration is being used for quantification, these unwanted signals can cause errors in  $\text{C}_3$  and  $\text{C}_4$  fractional enrichment level estimates as is described in the following section where a more practical form of the POCE sequence for human *in-vivo* application is considered and where the longer timings involved exacerbate the signal contamination.

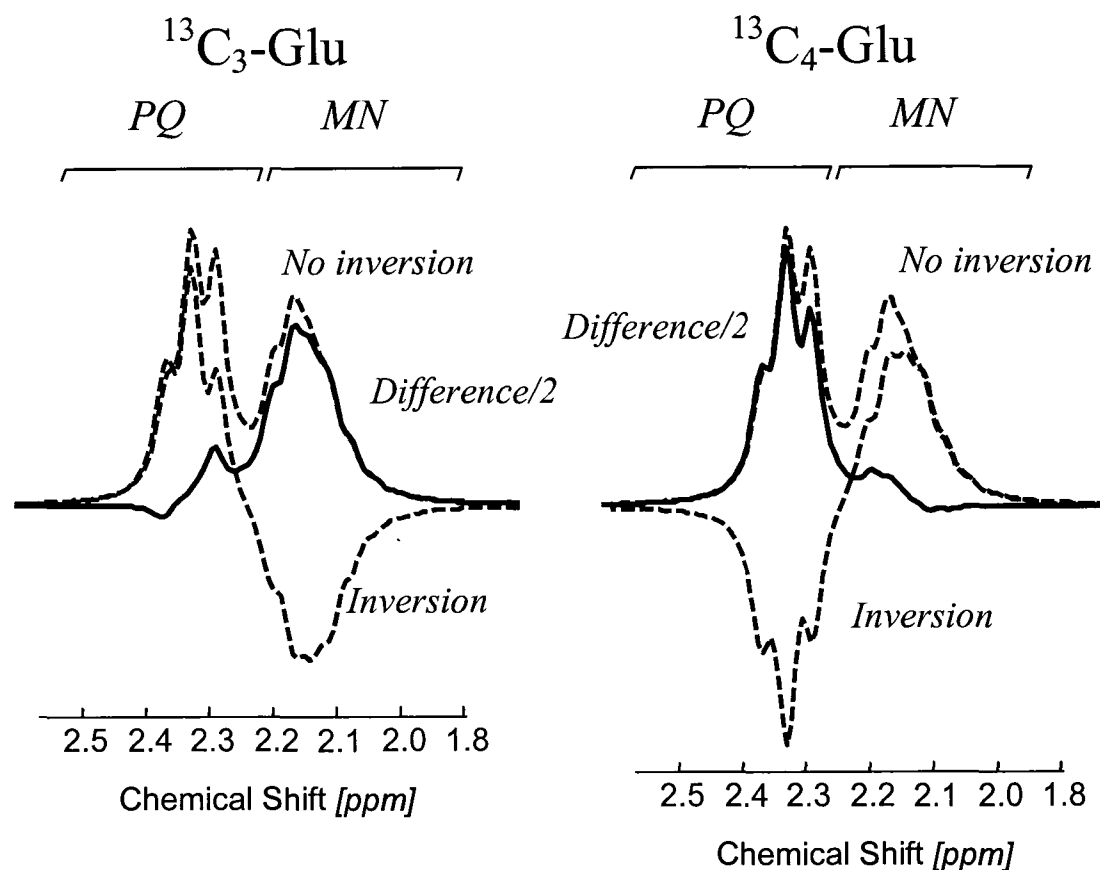


Figure 4.5: The response of Glu to the POCE sequence when a) the MN protons are  $^{13}\text{C}$ -coupled and b) when the PQ protons are  $^{13}\text{C}$ -coupled. The dashed lines are the response to the individual scans of the POCE sequence (the one with the inverted peaks is from the scan with the  $^{13}\text{C}$  inversion pulse). The solid lines represent the result of subtracting the two scans. All spectra were line broadened to 5Hz.

#### 4.3.3 Simultaneous strong homonuclear and weak heteronuclear coupling during PRESS-localized POCE

In the PRESS-Localized POCE sequence of Fig. 4.1, an inversion pulse is applied to the  $^{13}\text{C}$  spins  $1/2J_{\text{CH}}$  prior to an acquisition at the same total echo-time as a PRESS-only sequence. Figure 4.6 displays the changes in SQCs that are brought about by the application of the  $^{13}\text{C}$  inversion pulse. A total echo time of 25 ms was used, i.e.  $\{\text{TE}_1, \text{TE}_2\} = \{10 \text{ ms}, 15 \text{ ms}\}$ , in order to be the closest we could achieve experimentally to the value of 23 ms used by Chen et al (1) at 4.0 T. Although the M or N in-phase and anti-phase SQC with respect to P or Q spins change in sign, as expected, due to the

application of a  $^{13}\text{C}$  inversion pulse  $1/2J_{\text{CH}}$  prior to the start of acquisition, they also change in magnitude. Similarly, the P and Q anti-phase coherences with respect to M or N spins also change in magnitude, but maintain their sign as expected. Equations (4.3-4.8) show the M and N heteronuclear antiphase terms present  $1/2J_{\text{CH}}$  prior to acquisition (their expectation values are given in brackets) and what terms they evolve into after the  $1/2J_{\text{CH}}$  delay. Inversion of those terms  $1/2J_{\text{CH}}$  prior to acquisition will invert the SQCs that evolve from them. Thus the drop in the levels of the in-phase PQ coherences and the more negative amplitudes of the PQ antiphase coherences can be explained by

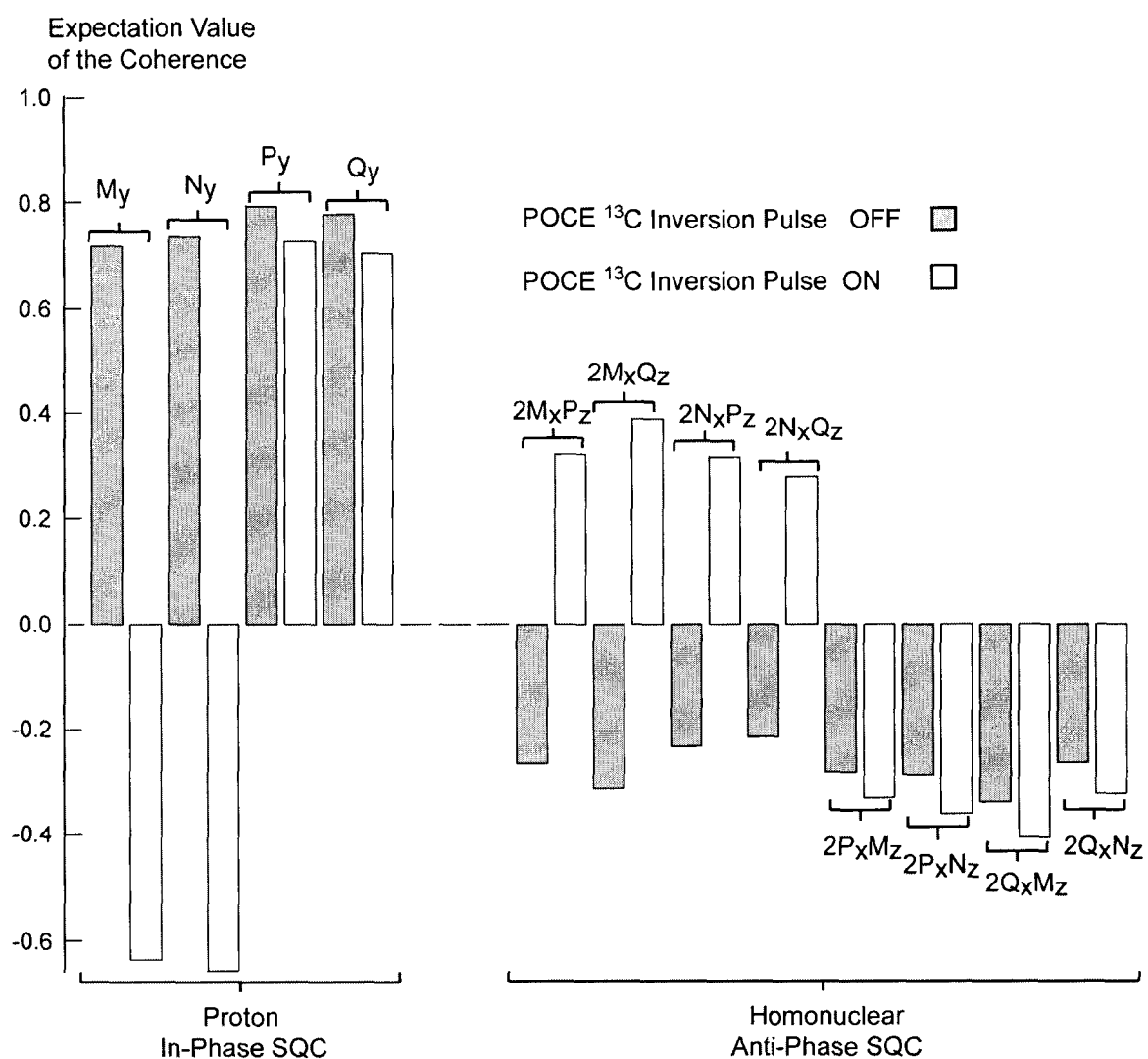


Figure 4.6: A diagram showing the changes in a selection of glutamate SQC that illustrate the consequences of switching the POCE  $^{13}\text{C}$  inversion pulse on or off, in a PRESS-POCE indirect detection sequence. The diagram shows the SQC at the start of acquisition in a PRESS,  $\{\text{TE}_1, \text{TE}_2\} = \{10 \text{ ms}, 15 \text{ ms}\}$ , localizing sequence and demonstrates the impact of applying a  $^{13}\text{C}$  inversion pulse  $1/2J_{\text{CH}}$  before that time.

the inversion of the M and N heteronuclear antiphase coherences that give rise to the PQ SQCs by polarization transfer.

$$(0.76)2M_xX_z \xrightarrow{1/2J_{CH}} \begin{cases} (0.73)M_y \\ (-0.05)2M_xP_z \\ (-0.07)2M_xQ_z \\ (0.03)2P_xM_z \\ (0.04)2Q_xM_z \end{cases} \quad (4.3)$$

$$(0.15)4M_xP_zX_z + (0.25)4M_yP_zX_z \xrightarrow{1/2J_{CH}} \begin{cases} (-0.23)2M_xP_z \\ (0.015)P_y \end{cases} \quad (4.4)$$

$$(0.17)4M_xQ_zX_z + (0.30)4M_yQ_zX_z \xrightarrow{1/2J_{CH}} \begin{cases} (-0.29)2M_xQ_z \\ (0.02)Q_y \end{cases} \quad (4.5)$$

$$(0.75)2N_xX_z + (0.18)2N_yX_z \xrightarrow{1/2J_{CH}} \begin{cases} (0.73)N_y \\ (-0.07)2N_xP_z \\ (-0.06)2N_xQ_z \\ (0.04)2P_xN_z \\ (0.03)2Q_xN_z \end{cases} \quad (4.6)$$

$$(0.10)4N_xP_zX_z + (0.24)4N_yP_zX_z \xrightarrow{1/2J_{CH}} \begin{cases} (-0.20)2N_xP_z \\ (0.015)P_y \end{cases} \quad (4.7)$$

$$(0.09)4N_xQ_zX_z + (0.23)4N_yQ_zX_z \xrightarrow{1/2J_{CH}} \begin{cases} (-0.19)2N_xQ_z \\ (0.01)Q_y \end{cases} \quad (4.8)$$

These changes in the relative magnitudes of proton SQC, brought about by the action of the strong homonuclear proton coupling, lead to the changes in their respective lineshape contributions which prevent the doubling and the cancellation of  $^{13}\text{C}$ -coupled multiplets and  $^{12}\text{C}$ -bonded multiplets, respectively. The degree of lineshape imbalance is demonstrated experimentally by Fig. 4.7 which shows the response of the MNPQ protons of Glu at 3.0 T to the sequence shown in Fig. 4.1. with a total echo time of 25 ms, i.e.  $\{\text{TE}_1, \text{TE}_2\} = \{10 \text{ ms}, 15 \text{ ms}\}$ . While demonstrating the close agreement between theory

and experiment, Figs. 4.7(a) and (b) corresponding to  $^{13}\text{C}_3$  labelling, emphasise changes to both coupled and uncoupled multiplet structures. Subtraction of the experimental spectra, with and without the POCE inversion, leaves a 22 % residual PQ signal (23 % numerically) instead of zero. Figure 4.7(c) demonstrates the converse using  $^{13}\text{C}_4$  labelling, namely, that when only the PQ protons are bonded to  $^{13}\text{C}$ , the residual MN proton signal after subtraction of alternate POCE scans (1.8 - 2.25 ppm) instead of going to zero, still constitutes  $\approx 19$  % by area of the original, unedited MN multiplet. Figure 4.7(d), also using  $^{13}\text{C}_4$  labelling, demonstrates the marked difference between the PQ multiplet of the unlabelled Glu spectrum and the “apparent PQ multiplet” obtained from 100%  $^{13}\text{C}_4$  labelled Glu by subtraction of alternate POCE scans, i.e., carried over from Fig. 4.7(c). Both magnitude and multiplet structure are different.

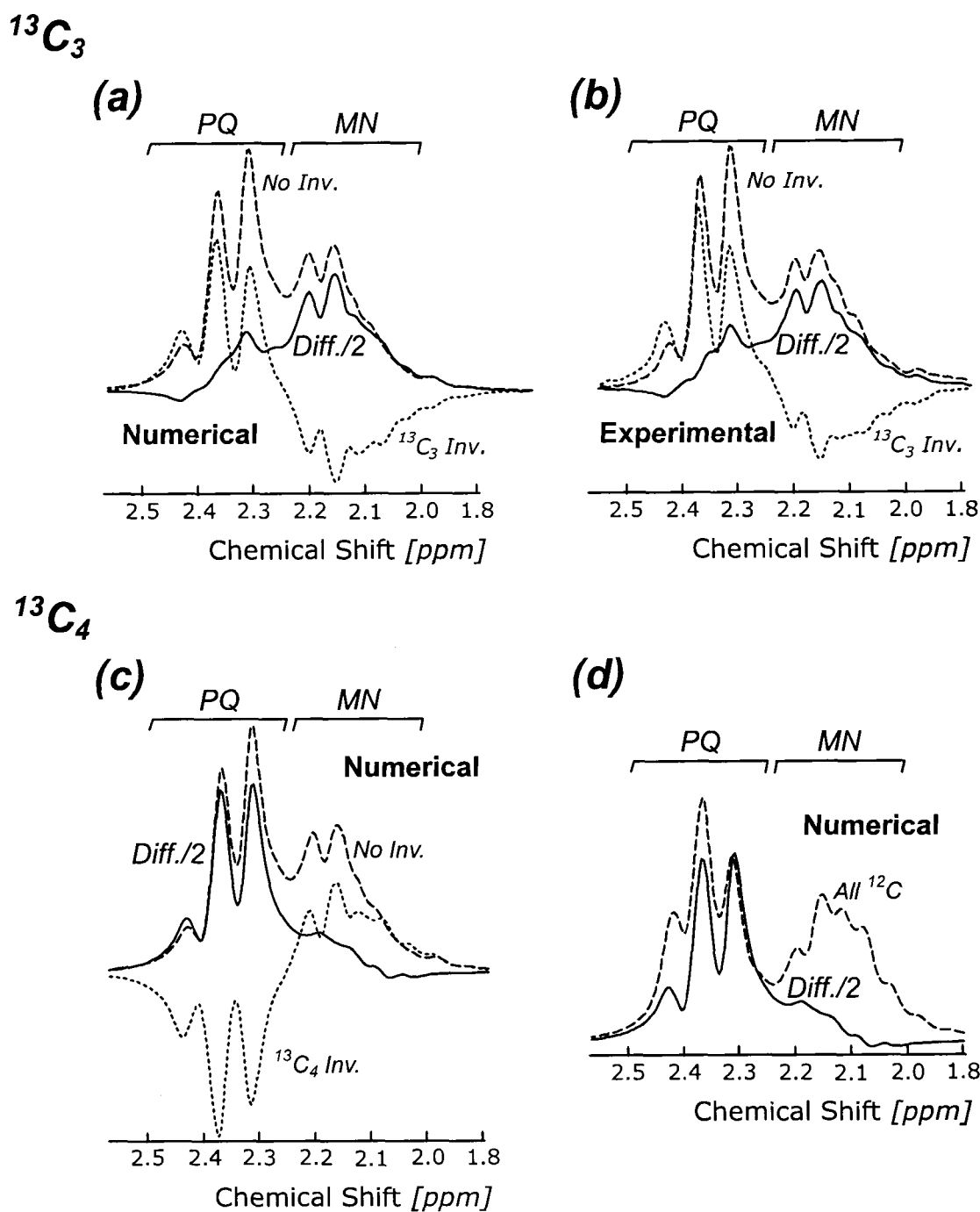


Figure 4.7: A diagram showing the spectral consequences of the POCE inversion pulse on the MN and PQ multiplets of Glu, when either the  $\text{C}_3$  (bonded to the MN protons) or the  $\text{C}_4$  (bonded to the PQ protons) carbon is labelled with a  $^{13}\text{C}$  carbon. In (a) and (b), the  $^{13}\text{C}_3$  case, the data confirm the close similarity between theory and experiment, and demonstrate marked deviation of half the difference-spectrum, labelled Diff./2, from the POCE expectation of a cancellation of the un-bonded (PQ) proton multiplet, and of a normal multiplet from the MN protons bonded to  $\text{C}_3$ . In the  $^{13}\text{C}_4$  case, a similar perturbation of the bonded- and un-bonded-proton multiplets is illustrated in (c), and the half difference-spectrum is compared in panel (d) with a fully  $^{12}\text{C}$  labelled Glu proton signal. This final comparison emphasizes the changing response of the Glu protons to PRESS alone, as a Glu carbon is enriched. The effect is therefore enrichment dependent. Both numerically and experimentally acquired spectra were line broadened to 5 Hz.



#### 4.3.4 Field strength dependence

Because the mechanism for these changes is the strong homonuclear proton coupling, their significance is magnetic field dependent. A measure of this dependence can be seen from the numerical predictions of the decrease, with increasing field strength, of the residual PQ contamination arising from  $^{13}\text{C}_3$  labelled Glu responding to a PRESS-POCE sequence employing hard pulses with  $\{\text{TE}_1, \text{TE}_2\} = \{10 \text{ ms}, 15 \text{ ms}\}$ . At 3.0 T (corresponding to the remainder of this chapter) the integrated residual signal is  $\sim 24\%$  of that of the PQ multiplet obtained from a PRESS only experiment. At 4.7 T, 7.0 T and 9.4 T, the residual declines to  $\sim 14\%$ ,  $\sim 9\%$  and  $\sim 6\%$  respectively, as shown in Fig. 4.8.

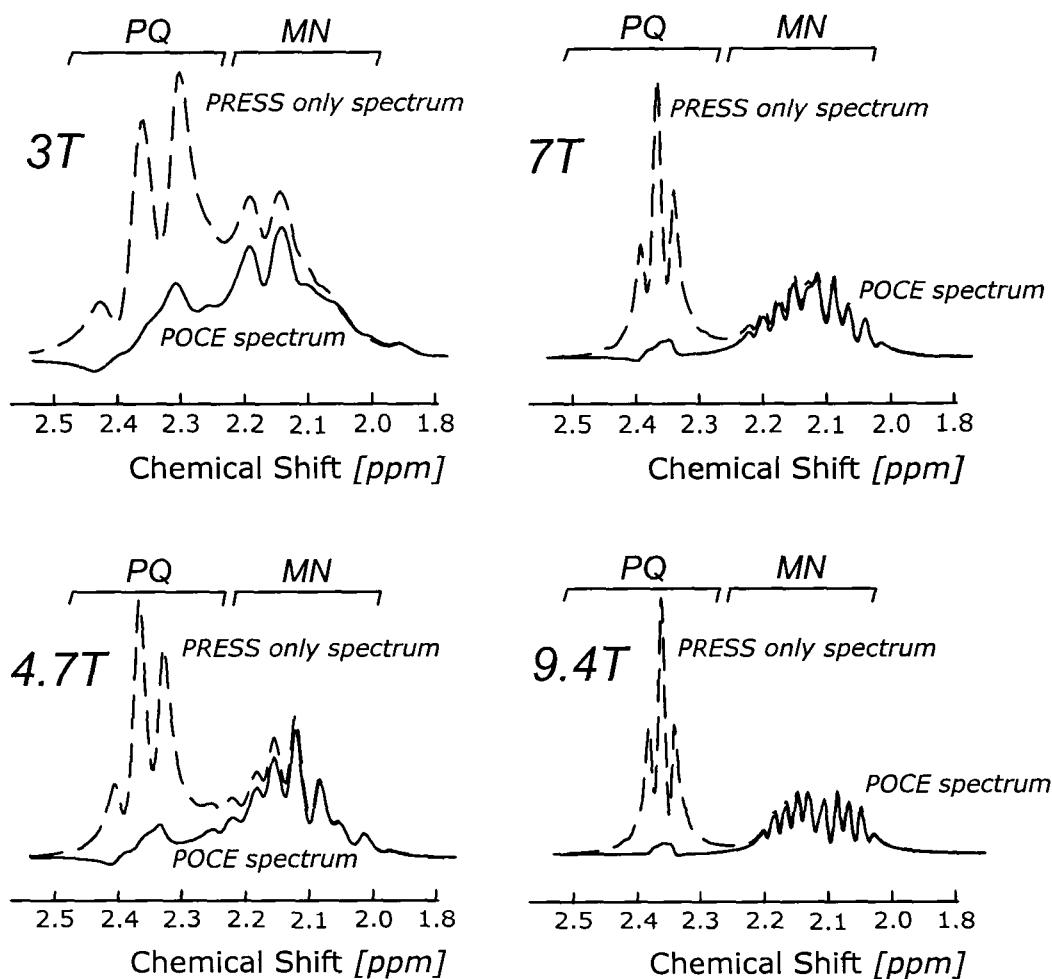


Figure 4.8: Numerically calculated response of the MNPQ protons of  $^{13}\text{C}_3$ -Glu to a hard pulse PRESS-POCE sequence with  $\{\text{TE}_1, \text{TE}_2\} = \{10 \text{ ms}, 15 \text{ ms}\}$  at four different field strengths. As the field strength increases, the residual PQ signal in the PRESS-POCE spectrum decreases as a result of the coupling between the MN and the PQ protons becoming less strong. All spectra were line broadened to 5 Hz.

## **4.4 Discussion**

It is clear from the preceding analysis that when metabolite protons are not only engaged in heteronuclear coupling with  $^{13}\text{C}$  spins, but are also participating in strong homonuclear coupling with their proton neighbours, the  $^{13}\text{C}$  measures derived from the indirect PRESS-POCE sequence is significantly altered by the proton homonuclear coupling. The strong homonuclear proton coupling indirectly links the  $^{12}\text{C}$ -bonded protons to the  $^{13}\text{C}$  spin, and in consequence causes a change in their MRS response. This is in addition to the changes that are seen in the response of the  $^{13}\text{C}$ -bonded protons. As a result of all of these changes, the POCE strategy fails to produce either a complete elimination of signal from protons not bonded to  $^{13}\text{C}$  nuclei, or a doubling of the signal from protons that are.

One example that demonstrates this was shown in Figs. 4.7(c) and (d), where, in Fig. 4.7(c) the individual POCE scans from 100%  $^{13}\text{C}_4$  Glu sample are shown, together with their subtraction. Not only is the integrated intensity of the  $^{13}\text{C}$ -bonded PQ multiplet after POCE subtraction only  $\sim 79\%$  of that of the doubled, no-inversion (PRESS only) scan, but a residual (19%) MN multiplet also remains in the PRESS-POCE subtraction spectrum. Figure 4.7(d) goes further, to demonstrate the  $^{13}\text{C}$  concentration dependence of the PRESS-derived Glu proton spectrum by showing that the 100%  $^{13}\text{C}_4$ , subtraction, PQ multiplet bears a different lineshape and amplitude from the  $^{12}\text{C}$ -bonded, PRESS-only, PQ multiplet. If the in-vivo fractional enrichment of Glu  $\text{C}_4$  were to be calculated assuming that the PRESS-POCE-derived 100%-labelled PQ multiplet were identical to that of the PQ multiplet of Glu with natural abundance  $^{13}\text{C}$ , a significant underestimate of enrichment would occur ( $\approx 30\%$ ). A second practical consequence would manifest itself if the relative enrichments of  $^{13}\text{C}_3$  and  $^{13}\text{C}_4$  were being measured from the same sequence as a function of time following the start of venous administration of  $^{13}\text{C}_1$  labelled glucose. The contamination of the labelled MN multiplet, bonded to  $^{13}\text{C}$  after the second circuit of the TCA cycle, by the residual MN signal from the Glu molecules labelled with  $^{13}\text{C}_4$  on the first round, can be significant. Moreover, the contamination of the PQ multiplet by build up of  $^{13}\text{C}_3$  labelled Glu molecules will also occur. If the MN and PQ multiplet intensities during an enrichment experiment are determined by integration of the observed lineshapes between fixed frequency limits, as in Ref. (1), the contamination of

one multiplet by residue from the other can be as much as 30% for an equal number of C<sub>3</sub> and C<sub>4</sub> labelled molecules. Accurate relative fractional enrichments can really only be obtained by using spectral modelling, e.g., LC model (24), equipped with the precise basis lineshapes for all spins (as in Refs. (15) and (10)), both bonded and not bonded to a <sup>13</sup>C nucleus.

## **4.5 Conclusion**

By means of a numerical solution of the equation of motion of the nuclear spin density matrix we have been able to predict, and then confirm through phantom experiments on aqueous <sup>13</sup>C labelled and unlabelled glutamate solutions at 3.0 T, that when the proton spins of a metabolite molecule are strongly scalar coupled (as they are for example in glutamate, glutamine, aspartate, myo-Inositol, etc.,) the interaction between the strong homonuclear proton coupling and the weak heteronuclear coupling causes a mutual perturbation that significantly alters the spectroscopic outcome of standard experiments (for example, PRESS-POCE *indirect* <sup>13</sup>C detection) to determine the rates of <sup>13</sup>C incorporation from <sup>13</sup>C labelled substrates *in vivo*. These spectral changes are dependent on molecular labelling site, on sequence timing parameters and on field strength, and can affect multiplet intensities by several tens of percent.

## **4.6 References**

1. Chen W, Zhu X-H, Gruetter R, Seaquist ER, Adriany G, Ugurbil K. Study of tricarboxylic acid cycle flux changes in human visual cortex during hemifield visual stimulation using  $^1\text{H}$ - $\{^{13}\text{C}\}$  MRS and fMRI. *Magnetic Resonance in Medicine* 2001;45:349-355.
2. Chhina N, Kuestermann E, Halliday J, Simpson LJ, Macdonald IA, Bachelard HS, Morris PG. Measurement of human tricarboxylic acid cycle rates during visual activation by  $^{13}\text{C}$  magnetic resonance spectroscopy. *Journal of Neuroscience Research* 2001;66:737-746.
3. Gruetter R, Seaquist ER, Kim S, Ugurbil K. Localized *in vivo*  $^{13}\text{C}$ -NMR of glutamate metabolism in the human brain: initial results at 4 tesla. *Developmental Neuroscience* 1998;20:380-388.
4. Shen J, Petersen KF, Behar KL, Brown P, Nixon TW, Mason GF, Petroff OAC, Shulman GI, Shulman RG, Rothman DL. Determination of the rate of the glutamate/glutamine cycle in the human brain by *in vivo*  $^{13}\text{C}$  NMR. *Proc Natl Acad Sci USA* 1999;96:8235-8240.
5. Hyder F, Renken R, Rothman DL. *In vivo* carbon-edited detection with proton echo-planar spectroscopic imaging (ICED PEPSI):  $[3,4\text{-}^{13}\text{CH}_2]$  glutamate/glutamine tomography in rat brain. *Magnetic Resonance in Medicine* 1999;42:997-1003.
6. Sibson NR, Dhankar A, Mason GF, Behar KL, Rothman DL, Shulman RG. *In vivo*  $^{13}\text{C}$  NMR measurements of cerebral glutamine synthesis as evidence for glutamate-glutamine cycling. *Proc Natl Acad Sci USA* 1997;94:2699-2704.
7. Sibson NR, Dhankar A, Mason GF, Rothman DL, Behar KL, Shulman RG. Stoichiometric coupling of brain glucose metabolism and glutamatergic neuronal activity. *Proc Natl Acad Sci USA* 1998;95:316-321.
8. Fitzpatrick SM, Hetherington HP, Behar KL, Shulman RG. The flux from glucose to glutamate in the rat brain *in vivo* as determined by  $^1\text{H}$ -Observed,  $^{13}\text{C}$ -Edited NMR spectroscopy. *Journal of Cerebral Blood Flow and Metabolism* 1990;10:170-179.
9. Mason GF, Rothman DL, Behar KL, Shulman RG. NMR determination of the TCA cycle rate and alpha-ketoglutarate exchange rate in rat brain. *Journal of Cerebral Blood Flow and Metabolism* 1992;12:434-447.

10. De Graaf RA, Brown PB, Mason GF, Rothman DL, Behar KL. Detection of [1,6-<sup>13</sup>C<sub>2</sub>]-Glucose Metabolism in Rat Brain by In Vivo <sup>1</sup>H-<sup>13</sup>C-NMR Spectroscopy. *Magnetic Resonance in Medicine* 2003;49:37-46.
11. Canet D. *Nuclear Magnetic Resonance, Concepts and Methods*. Ontario: John Wiley & Sons; 1996.
12. Ordidge RJ, Connelly A, Lohman JAB. Image-selected in vivo spectroscopy (ISIS). A new technique for spatially selective NMR spectroscopy. *Journal of Magnetic Resonance* 1986;66:283-294.
13. Ordidge RJ, Bendall MR, Gordon RE, Connelly A. *Magnetic Resonance in Biology and Medicine*. In: Govil G, Khetrapal CL, Saran A, editors. New Delhi: McGraw-Hill; 1985. p 387-397.
14. Bottomley PA; Selective volume method for performing localized NMR spectroscopy. US Patent 4, 480,228. 1984.
15. Boumezbeur F, Besret L, Valette J, Vaufrey F, Henry PG, Slavov V, Giacomini E, Hantraye P, Bloch G, Lebon V. NMR measurement of brain oxidative metabolism in monkeys using <sup>13</sup>C-labelled glucose without a <sup>13</sup>C radiofrequency channel. *Magnetic Resonance in Medicine* 2004;52:33-40.
16. Bendall MR, Pegg DT, Doddrell DM, Field J. NMR of protons coupled to <sup>13</sup>C nuclei only. *Journal of the American Chemical Society* 1981;103:934-936.
17. Chen W, Adriany G, Zhu X-H, Gruetter R, Ugurbil K. Detecting Natural Abundance Carbon Signal of NAA Metabolite Within 12-cm<sup>3</sup> Localized Volume of Human Brain Using <sup>1</sup>H-<sup>13</sup>C NMR Spectroscopy. *Magnetic Resonance in Medicine* 1998;40:180-184.
18. Henry P-G, Marjanska M, Gruetter R, Ugurbil K. Effect of strong scalar coupling in Proton-Observed Carbon-Edited NMR Spectroscopy. *Proceedings Annual Meeting ISMRM, Miami, 2005*, p57.
19. Thompson RB, Allen PS. A new multiple quantum filter design procedure for use on strongly coupled spin systems found in vivo: its application to glutamate. *Magnetic Resonance in Medicine* 1998;39:762-771.
20. Gruetter R, Adriany G, Merkle H, Andersen PM. Broadband decoupled, <sup>1</sup>H-localized <sup>13</sup>C MRS of the human brain at 4 tesla. *Magnetic Resonance in Medicine* 1996;36:659-664.
21. Matson GB. An integrated program for amplitude-modulated RF pulse generation and re-mapping with shaped gradients. *Magnetic Resonance Imaging* 1994;12:1205-1225.

22. Shaka AJ, Keeler J, Freeman R. Evaluation of a New Broadband Decoupling Sequence: WALTZ-16. *Journal of Magnetic Resonance* 1983;53:313-340.
23. Kay LE, McClung RED. A product operator description of AB and ABX spin systems. *Journal of Magnetic Resonance* 1988;77:258-273.
24. Provencher SW. Estimation of metabolite concentrations from localized *in vivo* proton NMR spectra. *Magnetic Resonance in Medicine* 1993;30:672-679.

# Chapter 5

## Indirect $^{13}\text{C}$ Observation II: Single-Shot PRESS-Localized ge-HMQC

### 5.1 Introduction

The previous chapter dealt with the POCE sequence which has been employed in a few brain studies (1-4). However, the POCE technique is a difference method (it relies on the subtraction of alternate scans) and thus is susceptible to motion artifacts and subtraction errors due to hardware instabilities. Moreover, as with most proton spectroscopy sequences, it requires additional pulses for water suppression and, therefore, proton resonances close to water such as the  $\text{H}_1$  glucose peak may also be suppressed along with water.

Coherence selection gradients can be used to suppress signals from  $^{12}\text{C}$ -bonded protons in a single scan while maintaining signal only from protons coupled to  $^{13}\text{C}$  nuclei, and therefore can inherently suppress water while avoiding subtraction errors (5). The gradient-enhanced heteronuclear multiple quantum coherence sequence (ge-HMQC) has been successfully applied *in vivo* to obtain indirect  $^{13}\text{C}$  1D and 2D spectra of a localized slice in cat brain by making the excitation pulse slice selective (6).

In this chapter, it is demonstrated that by combining the ge-HMQC technique with the PRESS sequence, indirect  $^{13}\text{C}$  spectra of 3D volumes can be obtained in a single scan while suppressing resonances from  $^{12}\text{C}$  bonded protons. A summary of this sequence has been previously presented (7). Using Glu at 3.0 T as an illustrative example, the effects of the simultaneous homo- and heteronuclear scalar couplings on the spectral response to the basic ge-HMQC and to the PRESS-localized ge-HMQC sequences is investigated. It is shown that when polarization transfer (through strong coupling) takes place between protons that are coupled to  $^{13}\text{C}$  and those that are not, significant changes occur to the proton multiplets that arise both from protons that are  $^{13}\text{C}$ -coupled and from those that are not. These multiplet lineshape and intensity changes

ultimately affect the estimates of  $^{13}\text{C}$  enrichment made by the indirect HMQC method, just as they did with the POCE technique (see previous chapter).

## 5.2 Theory

### 5.2.1 Ge-HMQC pulse sequence

#### 5.2.1.1 General overview of the sequence

Figure 5.1 displays the standard 2D ge-HMQC pulse sequence (8). In the 2D experiment,  $t_1$  is varied in increments and data is collected at a number of different  $t_1$  values. Since there is a  $180^\circ$   $^1\text{H}$  pulse in the middle of the sequence, proton chemical shifts are refocused at the beginning of acquisition and thus the effective chemical shift evolution depends only on the  $^{13}\text{C}$  chemical shift during  $t_1$ , namely,  $e^{-i\omega_c t}$  or  $e^{i\omega_c t}$  depending on the  $^{13}\text{C}$  coherence state during  $t_1$  ( $\omega_c$  is the chemical shift of the  $^{13}\text{C}$  nucleus in question). Thus the resulting  $^1\text{H}$  spectrum is phase modulated as a function of this shift. The pulse sequence can be employed for 1D experiments by keeping  $t_1$  fixed. Appendix 4 contains a thorough product operator analysis of the sequence for a simple CH spin pair using the product operator rules for a weakly coupled two spin system (appendix 1). A conceptual explanation is given in the following paragraph.

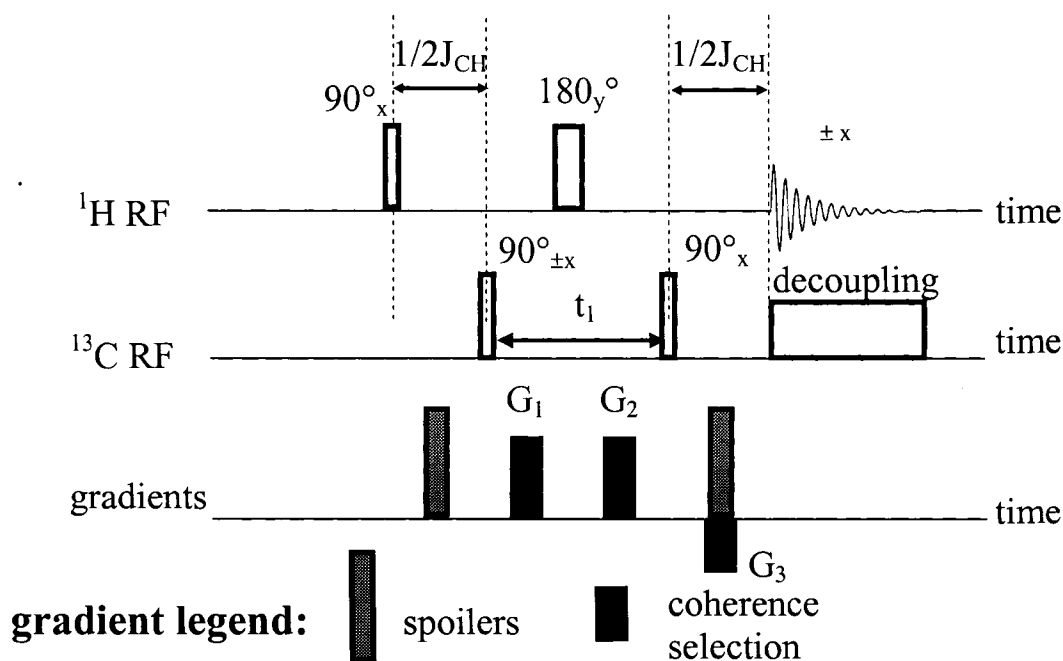


Figure 5.1: Standard 2D ge-HMQC pulse sequence. All pulses are hard pulses.



Consider a weakly coupled AX spin system where A and X represent a proton and its coupled  $^{13}\text{C}$  nucleus, respectively. Proton longitudinal magnetization is converted to in-phase transverse magnetization by the  $90^\circ_x$  proton excitation pulse. The  $1/(2J_{CH})$  delay followed by the first  $^{13}\text{C}$   $90^\circ_x$  pulse generates both zero and double quantum states for protons coupled to  $^{13}\text{C}$  nuclei. The ratio of the gradient strengths (assuming that their lengths are constant)  $G_1:G_2:G_3$  determines what coherence pathway is selected for detection. The second  $^{13}\text{C}$  pulse along with the  $1/(2J_{CH})$  delay convert the coherence states back to in-phase detectable proton magnetization. Any signal from protons not coupled to  $^{13}\text{C}$  nuclei are dephased by the coherence selection gradients. The spoiler gradients are there to eliminate any effects arising from an imperfect proton refocussing pulse.  $^{13}\text{C}$  decoupling may be applied during acquisition in order to simplify the spectrum.

#### 5.2.1.2 Gradient ratios

For an AX spin system, the phase acquired during a rectangular gradient of length  $\tau$  is given by the equation below (6), where  $p$  is the coherence order of the individual nucleus and  $r$  is the nucleus position with respect to the origin of the gradient.

$$\phi = (p_A\gamma_A + p_X\gamma_X)Gr\tau \quad (5.1)$$

During the time interval  $t_1$ , there exists the zero quantum and double quantum coherence terms  $A^+X^-$ ,  $A^-X^+$ ,  $A^+X^+$ , and  $A^-X^-$ . The  $180^\circ$  proton refocussing pulse changes  $A^+$  to  $A^-$  and vice versa, thus interchanging zero quantum and double quantum coherence terms. Therefore, during  $t_1$  the effect of  $G_1$  and  $G_2$  is a phase accumulation of  $\phi_1$  for the double quantum to zero quantum pathway  $A^+X^+ \rightarrow A^-X^+$ .

$$\phi_1 = (\gamma_A + \gamma_X)G_1r\tau + (-\gamma_A + \gamma_X)G_2r\tau \quad (5.2)$$

For the zero quantum to double quantum pathway ( $A^+X^- \rightarrow A^-X^-$ ) a phase accumulation of  $\phi_2$  is acquired.

$$\phi_2 = (\gamma_A - \gamma_X)G_1r\tau + (-\gamma_A - \gamma_X)G_2r\tau \quad (5.3)$$

In quadrature detection, only either the  $A^-$  or the  $A^+$  terms are detected (9). Assuming the detector is tuned to detect only  $A^-$  terms, the pathways  $A^-X^+ \rightarrow A^+X^+$  and  $A^-X^- \rightarrow A^+X^-$  (that evolve during  $t_1$ ) will not be considered, and only those terms containing  $A^-$  will be

considered during the last time interval where the effect of  $G_3$  is to introduce a phase accumulation given by Eq. (5.4).

$$\phi_3 = -\gamma_A G_3 r \tau \quad (5.4)$$

For rephasing of the desired signal, the sum of the accumulated phases must be zero.

$$\Rightarrow (\gamma_A + \gamma_X)G_1 + (-\gamma_A + \gamma_X)G_2 - \gamma_A G_3 = 0 \quad (5.5a)$$

$$(\gamma_A - \gamma_X)G_1 + (-\gamma_A - \gamma_X)G_2 - \gamma_A G_3 = 0 \quad (5.5b)$$

Equations (5.5a) and (5.5b) yield eight different gradient combinations that can be used to rephase the desired signal (8). Table 5.1 summarizes these different combinations. The gradient ratios are calculated for the case of a  $^{13}\text{C}$  nucleus coupled to a  $^1\text{H}$  nucleus, where  $\gamma_A \approx 4\gamma_X$ .

Table 5.1: Gradient ratios in a ge-HMQC sequence for rephasing of selected pathways

Pathway that is rephased	Ratio of $G_1:G_2:G_3$
$A^+X^+ \rightarrow A^-X^+ \rightarrow A^-$	2:2:1
$A^+X^- \rightarrow A^-X^- \rightarrow A^-$	2:2:-1
$A^+X^+ \rightarrow A^-X^+ \rightarrow A^-$	0:4:-3
$A^+X^- \rightarrow A^-X^- \rightarrow A^-$	4:0:3
$A^+X^+ \rightarrow A^-X^+ \rightarrow A^-$	4:0:5
$A^+X^- \rightarrow A^-X^- \rightarrow A^-$	0:4:-5
$A^+X^+ \rightarrow A^-X^+ \rightarrow A^-$	3:5:0
$A^+X^- \rightarrow A^-X^- \rightarrow A^-$	5:3:0

All of the above gradient combinations will dephase any signal from protons not coupled to  $^{13}\text{C}$  nuclei and therefore only signal from  $^{13}\text{C}$ -coupled protons is detected. However, note that since only one of the pathways that leads to observable signal is selected by any one of the gradient combinations, the ge-HMQC sequence suffers from a loss in signal by a factor of two compared to non-gradient methods (8).

### 5.2.2 Combining PRESS and the ge-HMQC technique

Figure 5.2 displays how the PRESS sequence can be combined with the ge-HMQC technique in order to obtain signal from  $^{13}\text{C}$  coupled protons from a three dimensional localized volume. The difference between this sequence and the ge-HMQC sequence is that the first hard proton excitation pulse is replaced by the PRESS single-shot localization sequence, so that by the end of the PRESS part of the sequence there exists in phase transverse proton magnetization in the voxel of interest (the effects of proton homonuclear coupling during the echo times are ignored for now). This magnetization then evolves as described in §5.2.1 so that at acquisition only signal from  $^{13}\text{C}$  coupled protons from the desired volume is acquired.

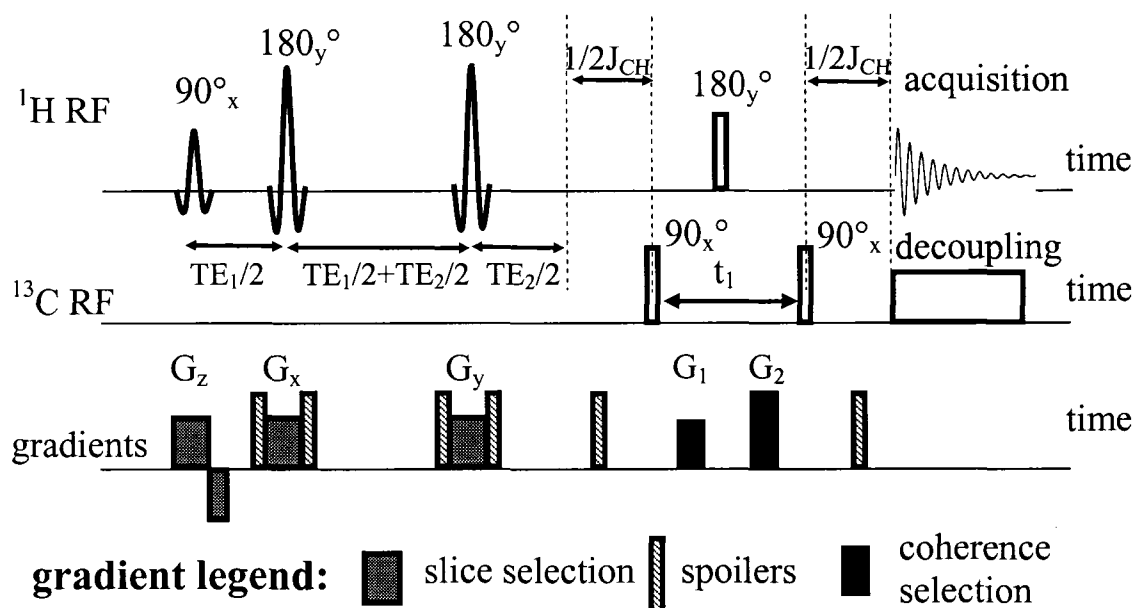


Figure 5.2: The combined PRESS and ge-HMQC pulse sequence. The shaped pulses represent slice selective pulses while the rectangular ones represent hard pulses.  $G_3 = 0$  in this case.

### 5.3 Methods

The method of numerical analysis used in this chapter was outlined in chapter 3. The chemical shift and scalar coupling constants used are the same as those displayed in Table 4.1.

All phantom experiments were carried out in an 80 cm bore, 3.0 T magnet system (Magnex Scientific PLC, Abingdon, UK), using a SMIS spectrometer (Surrey Medical Imaging Systems PCL, Guildford, UK) with a home-built 7 cm diameter  $^1\text{H}$  birdcage RF

coil, and a 3.5 cm diameter  $^{13}\text{C}$  surface coil. The efficacy of the pulse sequence was verified on a 2.7 cm diameter, 10 M natural abundance acetic acid phantom. To verify the numerical calculations, two 2 cm diameter aqueous-solution phantom of  $\text{pH} \approx 7$  was made, one containing 35 mM labelled Glu with the  $\text{C}_3$  carbon enriched 99% in  $^{13}\text{C}$  (Sigma-Aldrich Canada), and the other containing 1.8 M natural abundance Glu.

The PRESS part of the sequence consisted of a sinc-gaussian  $90^\circ$  slice selective excitation pulse of length 2.6 ms (bandwidth  $\approx 1500$  Hz) followed by two slice selective 2.75 ms sinc refocussing pulses (bandwidth  $\approx 1500$  Hz) each applied in conjunction with 3.6 mT/m gradients in order to refocus a slice thickness of 1 cm. The refocusing pulses were numerically optimized using the software MATPULSE (10) to minimize the spatial extent of the tip-angle transition region. The relatively short pulse lengths along with spoiler gradients of length 1 ms allowed a minimum total echo time of 20 ms ( $\text{TE}_1 = \text{TE}_2 = 10$  ms) to be achieved. A preceding hyperbolic secant inversion pulse was employed, when necessary, to minimize water contamination at the appropriate inversion time. To improve suppression of unwanted resonances the phase of the first  $90^\circ$   $^{13}\text{C}$  pulse as well as that of the receiver was alternated between  $\pm x$ . For acetic acid  $1/2J_{\text{CH}} = 3.85$  ms, and for glutamate  $1/2J_{\text{CH}} = 3.7$  ms. A ratio of  $G_1:G_2$  of 3:5 ( $G_3 = 0$ ) was used for coherence selection and these gradients were applied in three orthogonal directions with a duration of 2 ms each. The total length of  $t_1$  including post gradient delays, gradient lengths, and the  $^1\text{H}$   $180^\circ$  pulse (500  $\mu\text{s}$ ) was 5 ms. The  $^{13}\text{C}$  pulses were 150  $\mu\text{s}$  long. All experiments employed a repetition time of 3 s, and a WALTZ-16 segment (11) for  $^{13}\text{C}$  decoupling during acquisition.

## **5.4 Results**

### **5.4.1 Verification of sequence efficacy**

Figure 5.3 displays the results obtained with the acetic acid phantom described above. Figure 5.3(a) shows the PRESS spectrum of the acetic acid phantom with no  $^{13}\text{C}$  editing, while 5.3(b) shows the result of applying the sequence shown in Fig. 5.2, without the decoupling pulses. Symmetric echo times of 10 ms were employed and no water suppression pulses were applied. The efficiency of the sequence in suppressing signal

from water as well as from protons bonded to  $^{12}\text{C}$  nuclei while maintaining only signal from protons coupled to  $^{13}\text{C}$  nuclei is clearly demonstrated. The two satellite proton peaks are  $^{13}\text{C}$  decoupled in Fig. 5.3(c). The protons on the methyl group are not J-coupled and therefore there is no loss in signal due to J-evolution during the echo times of the PRESS sequence. Since  $^{13}\text{C}$  is 1.1% naturally abundant and the ge-HMQC sequence involves a loss in signal by a factor of two, the height of each satellite peak in Fig. 5.3(b) should be 0.0028 times that of the height of the peak in Fig. 5.3(a), taking into account the extra reduction by a factor of 2 because no decoupling was applied. Experimentally the satellite peak heights were determined to be 0.0025 times that of the peak obtained with PRESS which agrees well with theory.

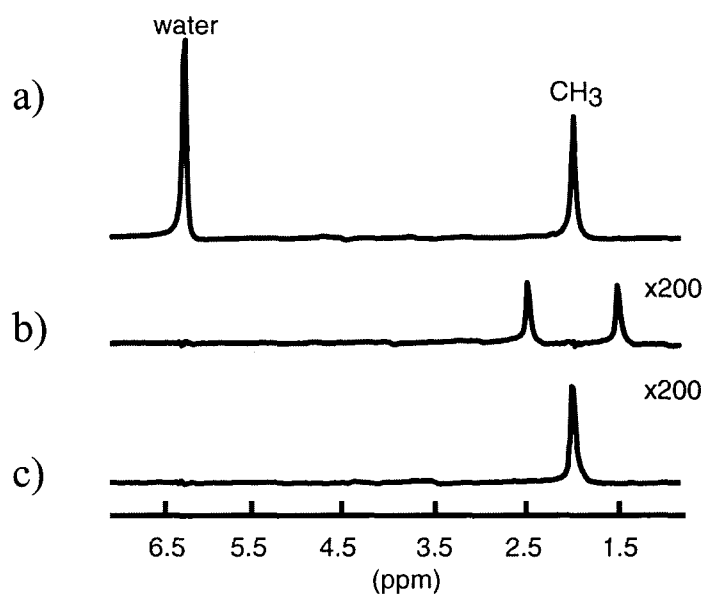


Figure 5.3: The top spectrum is a PRESS spectrum of the acetic acid phantom; the  $\text{CH}_3$  peak is from  $^{12}\text{C}$ -bonded protons. (b) is the spectrum obtained with the sequence shown in Fig. 5.2 but without decoupling, showing the two satellite peaks. (c) is the same as (b) but with  $^{13}\text{C}$  decoupling. All spectra were acquired in 32 averages.

### 5.4.2 Comparing the efficiency of PRESS-localized ge-HMQC to that of PRESS-localized POCE

The sequences of Figs. 4.1 and 5.2 were applied to the acetic acid phantom in order to compare the performances of the two sequences in suppressing unwanted signal. The PRESS part of the sequence was applied as described in the methods section with symmetrical echo times of 15 ms in order to allow time for the application of the  $^{13}\text{C}$  inversion pulse  $1/(2J_{CH})$  (about 3.85 ms) prior to acquisition in the localized POCE sequence. Figure 5.4(a) shows the spectrum obtained using the difference POCE method while that of Fig. 5.4(b) shows the result of applying the PRESS sequence combined with the ge-HMQC technique. The efficiency of the latter sequence over the difference method in suppressing unwanted resonances is clearly demonstrated. However, as mentioned before the disadvantage of using the coherence selection gradients is a loss in signal by a factor of two as can be seen in Fig 5.4.

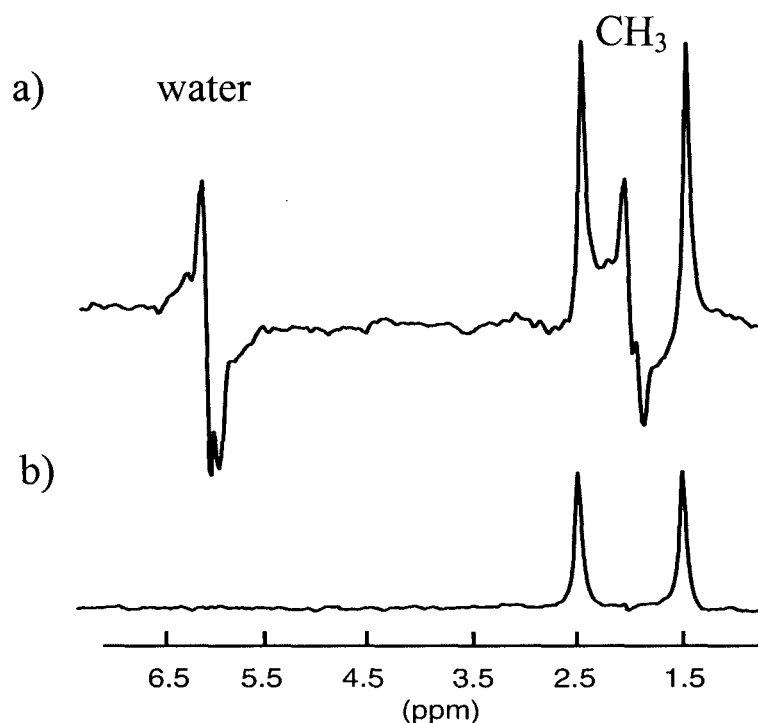


Figure 5.4: (a) is a spectrum of the acetic acid phantom obtained using the localized POCE sequence of Fig. 4.1, while (b) is the result of applying the PRESS sequence that incorporates the ge-HMQC technique. Both spectra were acquired in 32 averages.

### 5.4.3 Effect of strong homonuclear proton coupling on the outcome of the basic ge-HMQC sequence

The ge-HMQC sequence is assumed to dephase any signal from  $^{12}\text{C}$ -bonded protons while retaining signal from only  $^{13}\text{C}$ -coupled protons (with a 50% yield) in a single application of the sequence. It is shown here that in situations such as that of the MN or PQ protons of Glu at 3.0 T where strong-coupling is involved, ge-HMQC does not completely eliminate signal from protons not coupled to  $^{13}\text{C}$  nuclei, but because of the strong proton coupling, some residual signal from non- $^{13}\text{C}$ -coupled protons remains. This is illustrated in Fig. 5.5, where the response of the MN and PQ protons to the ge-HMQC sequence (Fig. 5.1) was numerically calculated first for the case where the  $\text{C}_3$  carbon is a  $^{13}\text{C}$  nucleus, and then for the situation where the  $\text{C}_4$  carbon is a  $^{13}\text{C}$  nucleus. The delay  $1/2J_{\text{CH}}$  was set to 3.7 ms and coherence selection gradients of length 2 ms were assumed. Spectra were calculated under the condition of  $^{13}\text{C}$  decoupling during acquisition. The dashed spectra show the response of the MN and PQ protons to a single  $90^\circ$  proton excitation pulse, while the solid spectra show the outcome of applying the ge-HMQC sequence. As can be seen, there remains some unsuppressed signal in the resulting spectrum from protons that are not coupled to  $^{13}\text{C}$  nuclei. More precisely, by integrating the PQ proton peaks (2.25-2.55ppm) of the ge-HMQC spectrum and of the unedited spectrum shown in Fig. 5.5(a) it was calculated that about 11% of the PQ signal remains unsuppressed, and only 38% of the MN multiplet (1.8-2.25ppm) is retained (instead of the expected 50%). Similar calculations for the peaks in Fig. 5.5(b) indicate that approximately 43% of the PQ signal remains, and although there is some unsuppressed MN signal, upon integration the net residual signal is negligible. Thus it is apparent that when the  $^{13}\text{C}$ -coupled protons are involved in strong homonuclear coupling, not only is the signal yield of  $^{13}\text{C}$ -coupled protons less than expected, but there also remains some residual unsuppressed signal from  $^{12}\text{C}$ -bonded protons. In the next section, it is shown how these effects of strong proton coupling are exacerbated when ge-HMQC is combined with PRESS to allow for three dimensional localization.

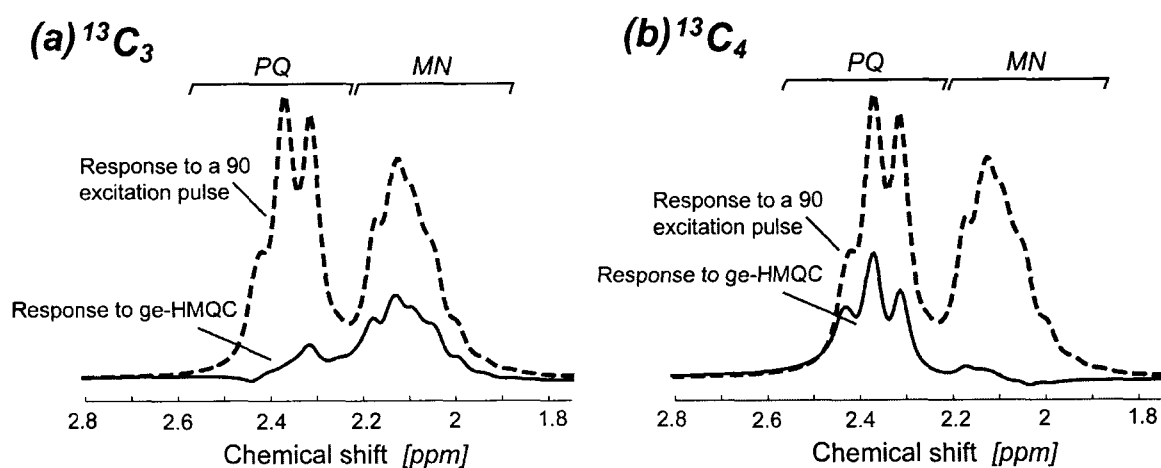


Figure 5.5: The response of Glu to the ge-HMQC sequence when a) the MN protons are  $^{13}\text{C}$ -coupled and b) when the PQ protons are  $^{13}\text{C}$ -coupled. The dashed lines are the response to a  $90^\circ$  excitation pulse. The solid lines are the responses to ge-HMQC. All spectra were line broadened to 5 Hz.

#### 5.4.4 Effect of strong homonuclear proton coupling on the outcome of a PRESS-localized ge-HMQC sequence

Figures 5.6 and 5.7 show the peak intensities of the MN and the PQ multiplets in response to the PRESS-localized ge-HMQC sequence as a function of the PRESS echo times. As can be seen there is a drop in signal with increasing echo times. Note the higher secondary intensity maximum for the PQ protons in the area of  $\text{TE}_1 = \text{TE}_2 = 60$  ms than seen for the MN protons. This is due to the absence of an interaction between the PQ protons and any other proton, similar to that between the MN protons and the A proton (bonded to  $\text{C}_2$ ) of Glu. The drop in signal in general mirrors the decrease of in-phase terms such as  $M_y$  and  $N_y$  (for  $^{13}\text{C}_3$  labelling) or  $P_y$  and  $Q_y$  (for  $^{13}\text{C}_4$  labelling) at the end of PRESS as the strong homonuclear coupling facilitates polarization transfer to other Glu protons (12). It is apparent that for optimal signal from both  $\text{C}_3$  and  $\text{C}_4$  labelled carbons it is desirable to minimize the echo times of the PRESS sequence. Practical timings for a human *in-vivo* experiment would be symmetric echo times of 10 ms. Figure 5.8(a) shows the numerically calculated response of natural abundance Glu to a PRESS sequence alone with those timings, while Fig. 5.8(b) illustrates the response when the ge-HMQC sequence is attached to PRESS for an equal number of singly labeled  $^{13}\text{C}_3$ - and  $^{13}\text{C}_4$ -Glu molecules. Figure 5.8(c) shows experimental confirmation of Fig. 5.8(b) using



the 1.8 M natural abundance phantom. The parameters described in the methods section were used in both the numerical and experimental situations.

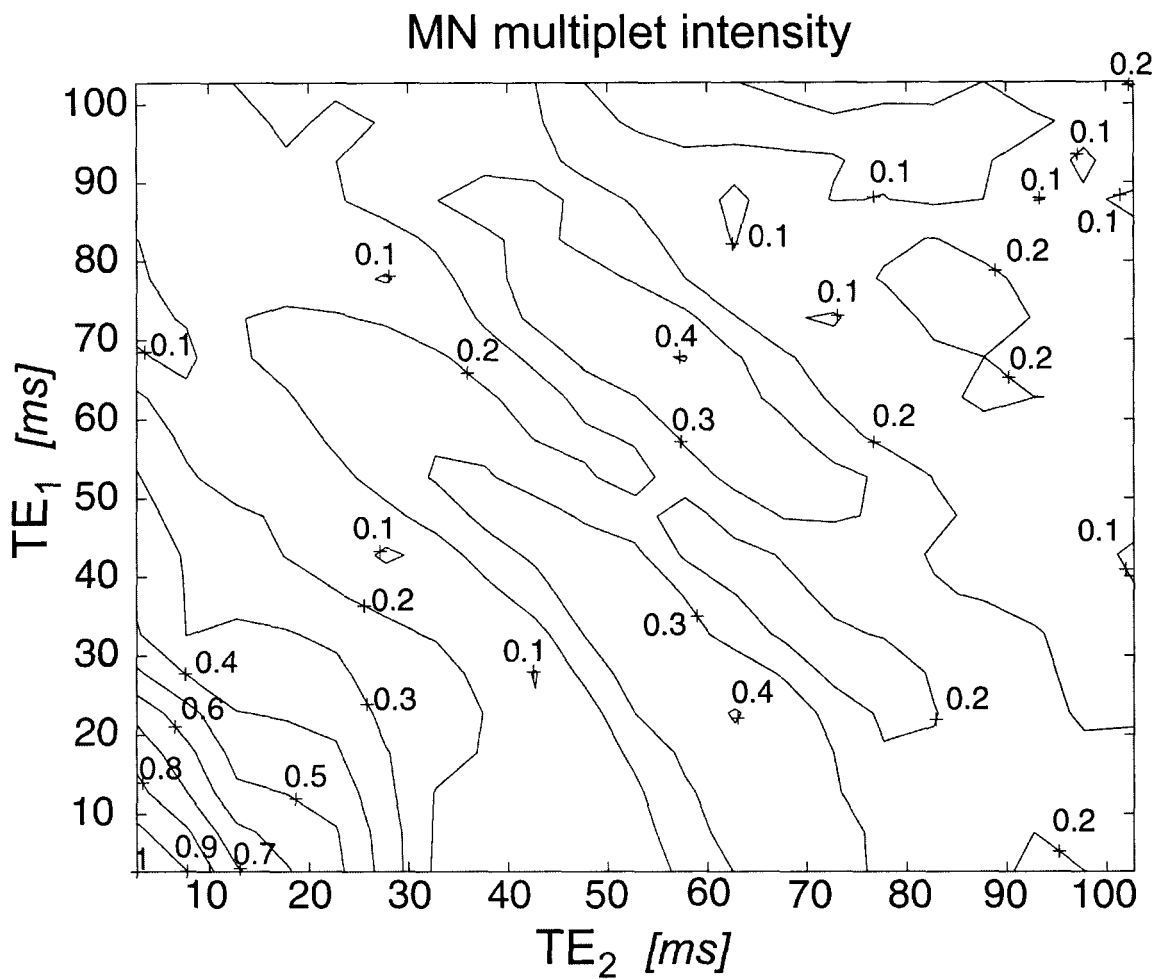


Figure 5.6: A map of the MN multiplet intensity in response to the PRESS-ge-HMQC sequence as a function of PRESS echo times.

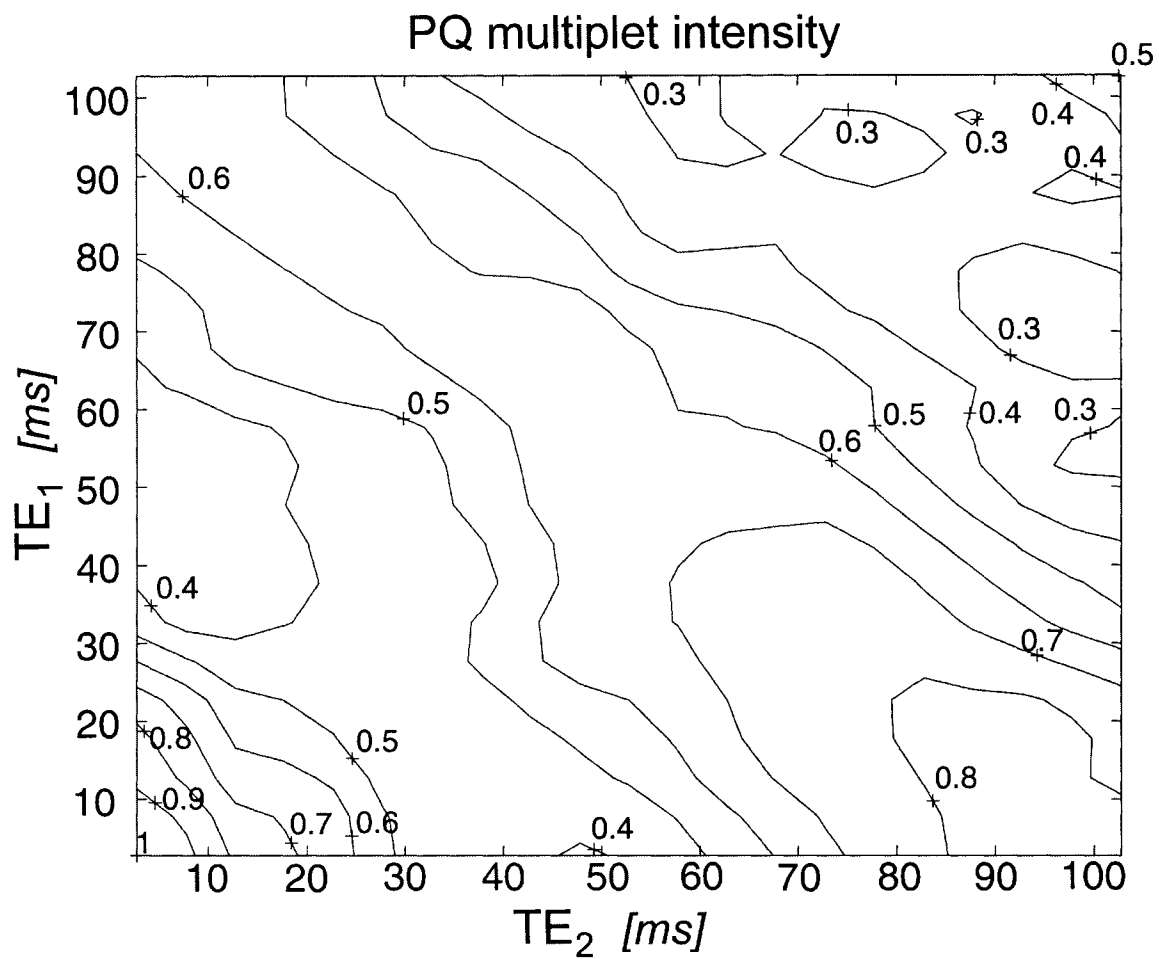


Figure 5.7: A map of the PQ multiplet intensity in response to the PRESS-ge-HMQC sequence as a function of PRESS echo times. The recovery of the intensity at longer PRESS echo times is much broader and higher than that of the MN intensities shown in Fig. 5.6, a phenomenon due to the absence (for PQ protons) of the 'A' spin coupling experienced by the MN protons.

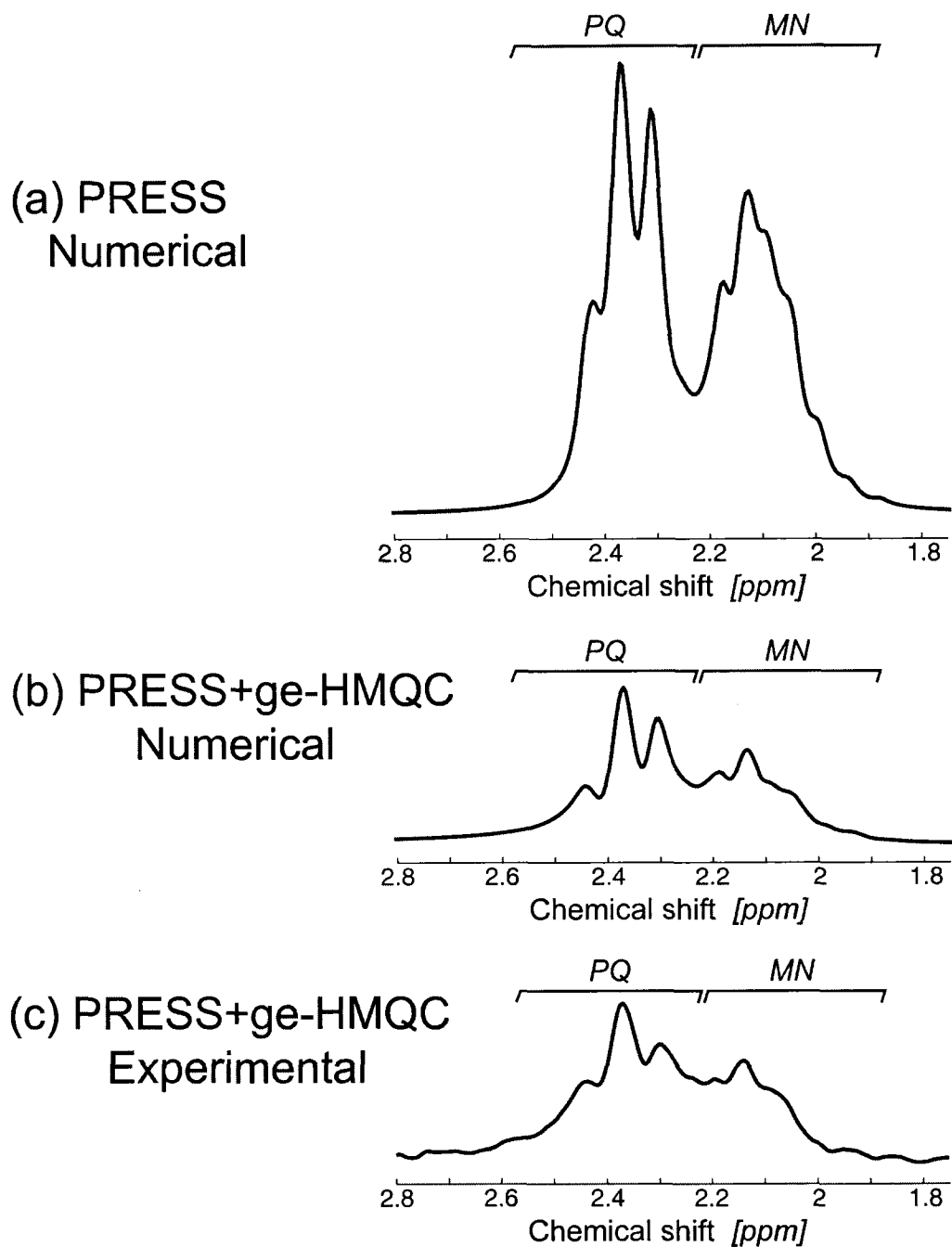


Figure 5.8: The response of natural abundance Glu to the PRESS sequence alone,  $TE_1 = TE_2 = 10$  ms, is shown in (a), while (b) shows the response when PRESS is combined with ge-HMQC. Panel (c) shows experimental confirmation of the lineshape of (b) using the 1.8 M natural abundance Glu phantom (acquired with 256 averages). All spectra were line broadened to 6 Hz. The MN and PQ multiplets of the spectrum shown in (b) are about 28% and 38%, by area, of the corresponding multiplets in (a), respectively.

The natural abundance spectrum of Fig. 5.8(b) shows the response when there are an equal number of C<sub>3</sub> and C<sub>4</sub> singly-labelled Glu molecules. Figure 5.9 shows the contribution from C<sub>3</sub> and C<sub>4</sub> labelled Glu molecules individually. Note that the PRESS spectra in Fig. 5.9 are not the same as the one in Fig. 5.8(a) where the natural abundance situation was considered (essentially no heteronuclear coupling). In Fig. 5.9(a), the response of a C<sub>3</sub>-labelled Glu molecule to the PRESS sequence and to the PRESS-localized ge-HMQC sequence is calculated. Approximately 30% of the MN signal is retained (instead of the ideal 50%) and about 8.5% of the PQ peak remains (instead of zero) compared to the PRESS spectrum. Experimental verification of the spectra in Fig. 5.9(a) are shown in Fig. 5.9(b). Figure 5.9(c) shows the expected response of a C<sub>4</sub>-labelled Glu molecule, where about 30% of the PQ peak is retained and about 9% of the MN peak remains unsuppressed.

## **5.5 Discussion**

The objective of this work was to explore an alternative technique that yields indirect <sup>13</sup>C spectra from three dimensional volumes and that does not rely on the subtraction of alternate scans, thereby reducing its susceptibility to motion artifacts and subtraction errors. The superiority of the sequence over that of the PRESS-localized POCE sequence (topic of the previous chapter) in suppressing unwanted signal from <sup>12</sup>C-bonded protons was demonstrated on a 10 M natural abundance acetic acid phantom. The effects of strong homonuclear coupling on the outcome of this sequence was also investigated. If it is assumed that the only interaction taking place during the PRESS-localized ge-HMQC sequence is the heteronuclear coupling then the sequence suffers from a loss in signal by a factor of two compared to the POCE technique because the coherence selection gradients can only select one of two possible coherence pathways that lead to observable signal. This still renders the sequence twice as sensitive as a direct <sup>13</sup>C detection sequence with polarization transfer (enhances <sup>13</sup>C signal by about  $\gamma_H / \gamma_C \approx 4$ ). Moreover, there is the additional sensitivity that comes from the proton multiplicity (often two or three protons are coupled to the same <sup>13</sup>C nucleus).

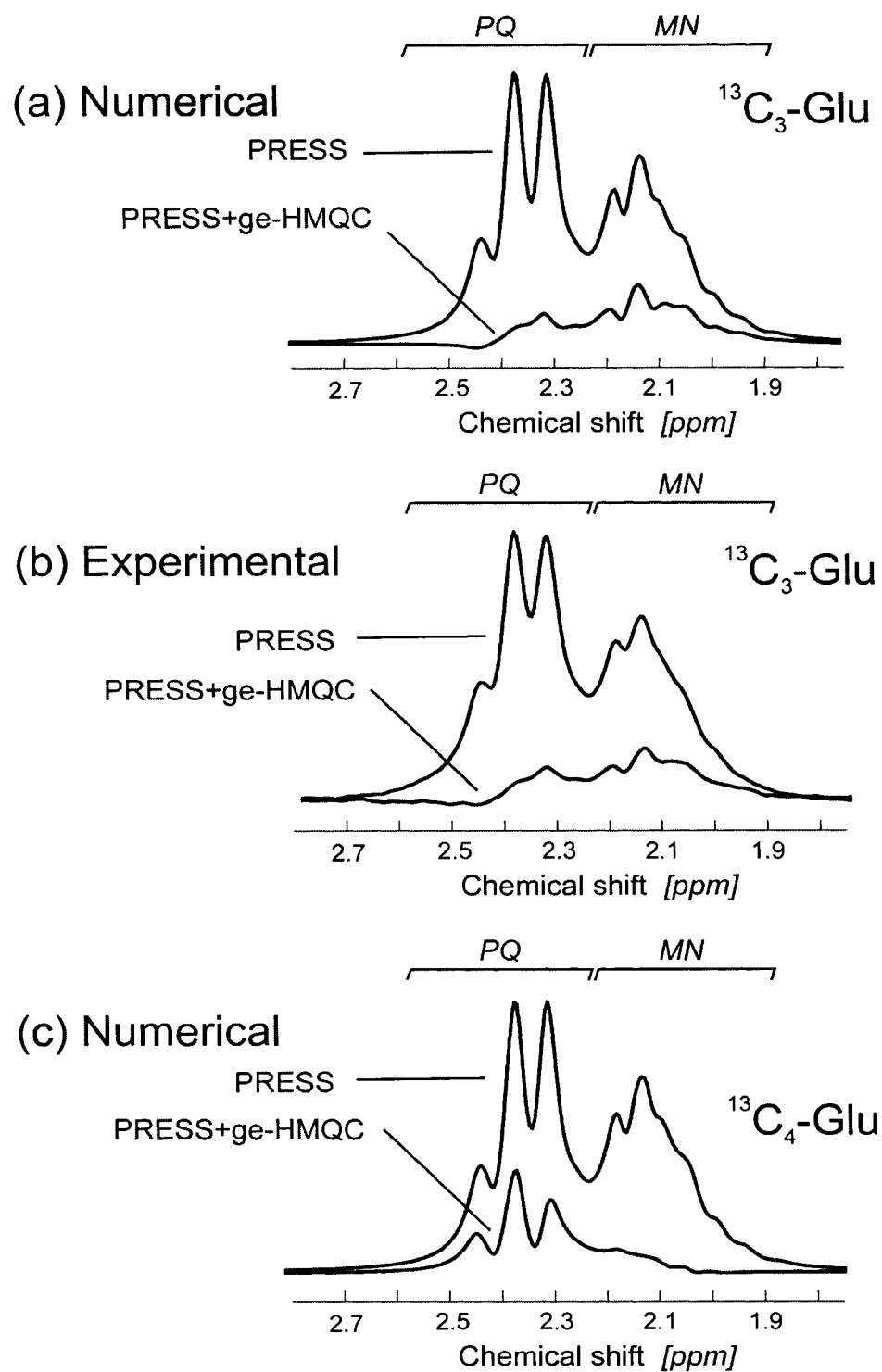


Figure 5.9: The numerical response of a  $\text{C}_3$ -labelled Glu molecule to the PRESS sequence ( $\text{TE}_1 = \text{TE}_2 = 10$  ms) and to the PRESS-localized ge-HMQC is shown in (a). Experimental confirmation of (a) using the 35mM  $^{13}\text{C}_3$ -labelled Glu phantom is shown in (b) where the MN peak constitutes about 28% of the PRESS spectrum (30% numerically in (a)), and a 7.5% residual PQ peak remains (8.5% numerically in (a)). Both experimental spectra were acquired with 128 averages. The numerical response of a  $\text{C}_4$ -labelled Glu molecule is shown in (c), where the PQ peak of the edited spectrum is about 30% that of the PRESS spectrum and the residual MN peak is about 9%. All spectra were line broadened to 5 Hz.

We illustrated in this chapter that when the  $^{13}\text{C}$ -coupled protons are also involved in strong homonuclear coupling the signal yield of the basic ge-HMQC sequence is less than the expected 50%, and furthermore not all the signal from  $^{12}\text{C}$ -bonded protons involved in strong coupling with the  $^{13}\text{C}$ -coupled protons is eliminated (as was the case with the POCE sequence discussed in chapter 4). It was also demonstrated that when the PRESS sequence is combined with the ge-HMQC sequence, the resulting signal is highly dependent on the echo times of the PRESS part of the sequence and the temporal variation is different for the MN and the PQ protons. In particular, for the MN protons (because of the additional coupling it exhibits with the A proton), there is a sharp drop in signal with increasing echo times. Therefore, for maximum signal it is desirable to minimize the echo times of PRESS. Practical short timings are  $\text{TE}_1 = \text{TE}_2 = 10$  ms. At these timings, it was shown in Fig. 5.9 that the  $^{13}\text{C}_4$ -Glu PQ peak is about 30% that of the PRESS spectrum, while a residual 9% MN signal remains unsuppressed. Similar signal yields were obtained with  $^{13}\text{C}_3$ -Glu. The loss in signal of  $^{13}\text{C}$ -coupled protons is a result of the proton scalar coupling evolution that takes place during PRESS and then during ge-HMQC itself which is quite significant. For example, using the same  $^{13}\text{C}_4$ -Glu example above but shortening the coherence selection gradient lengths from 2 ms to 1 ms results in an increase of PQ signal by approximately 13%.

The variations of the MN and PQ signal yields can be used to advantage, for example, if only the rate of  $\text{C}_4$ -Glu labelling is of interest, then instead of employing short echo times, alternative timings that retain a significant amount of PQ signal while eliminating most of the MN signal can be employed. One example is  $\{\text{TE}_1, \text{TE}_2\} = \{70$  ms, 30 ms $\}$ . From Figs. 5.6 and 5.7 it can be seen that the signal yield for the PQ peak at these timings is about 75% of that when  $\text{TE}_1 = \text{TE}_2 = 10$  ms, while the MN signal yield is minimal. The calculated response of natural abundance Glu to the sequence at these timings is shown in Fig. 5.10(a) and its experimental confirmation is illustrated in Fig. 5.10(b).

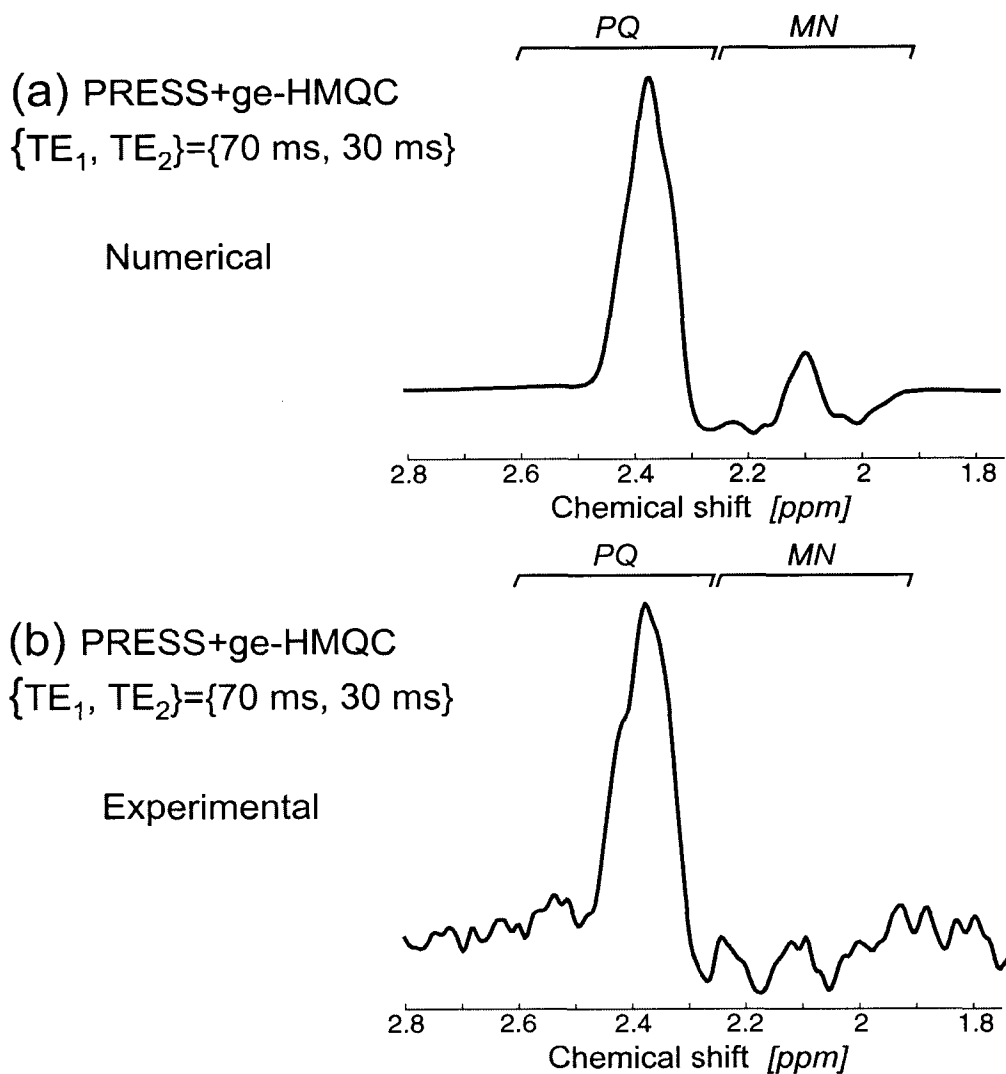


Figure 5.10: The calculated response of natural abundance Glu to the PRESS-localized ge-HMQC sequence with  $\{TE_1, TE_2\} = \{70 \text{ ms}, 30 \text{ ms}\}$  for the PRESS part of the sequence. The spectrum shows a PQ peak that reflects  $C_4$  labelling and that is uncontaminated by signal from the  $^{13}C_3$ -coupled MN protons. Experimental confirmation of the spectrum is shown in (b), acquired with 256 averages. All spectra were line broadened to 6 Hz.

## **5.6 Conclusion**

The PRESS-localized ge-HMQC sequence offers better suppression of  $^{12}C$ -bonded protons because of its ability to filter through signal from  $^{13}C$ -coupled protons in a single application of the sequence without needing to rely on the subtraction of scans. However, the ge-HMQC sequence suffers from a loss in signal by a factor of two. Furthermore, the strong homonuclear coupling present in many of the metabolites detected by  $^{13}C$  NMR at clinical field strengths such as glutamate and glutamine causes a

further loss in signal that further reduces the improvement in SNR expected with indirect  $^{13}\text{C}$  detection. The strong homonuclear coupling also indirectly links the  $^{13}\text{C}$  spin to protons attached to the neighboring  $^{12}\text{C}$  nucleus, so that there is incomplete elimination of signal from the  $^{12}\text{C}$ -bonded protons. If integration between fixed frequency limits is being used as the method of quantifying  $^{13}\text{C}$  fractional enrichments then it is likely that overestimations will take place and a more accurate method of quantification would be to use a spectral fitting routine like LC model (13) with correct basis lineshapes (1,14).



## **5.7 References**

1. De Graaf RA, Brown PB, Mason GF, Rothman DL, Behar KL. Detection of [1,6-<sup>13</sup>C<sub>2</sub>]-Glucose Metabolism in Rat Brain by In Vivo <sup>1</sup>H-[<sup>13</sup>C]-NMR Spectroscopy. *Magnetic Resonance in Medicine* 2003;49:37-46.
2. Rothman DL, Behar KL, Hetherington HP, DEN Hollander JA, Bendall MR, Petroff OAC, Shulman RG. <sup>1</sup>H-Observe/<sup>13</sup>C-decouple spectroscopic measurements of lactate and glutamate in the rat brain *in vivo*. *Proc Natl Acad Sci* 1985;82:1633-1637.
3. Pfeuffer J, Tkac I, Choi IY, Merkle H, Ugurbil K, Garwood M, Gruetter R. Localized In Vivo <sup>1</sup>H NMR Detection of Neurotransmitter Labeling in Rat Brain During Infusion of [1-<sup>13</sup>C] D-Glucose. *Magnetic Resonance in Medicine* 1999;41:1077-1083.
4. Chen W, Zhu X-H, Gruetter R, Seaquist ER, Adriany G, Ugurbil K. Study of Tricarboxylic Acid Cycle Flux Changes in Human Visual Cortex During Hemifield Visual Stimulation Using <sup>1</sup>H-<sup>13</sup>C} MRS and fMRI. *Magnetic Resonance in Medicine* 2001;45:349-355.
5. Hurd RE, Boban JK. Gradient-enhanced proton-detected heteronuclear multiple quantum coherence spectroscopy. *Journal of Magnetic Resonance* 1991;91:648-653.
6. Van Zijl PCM, Chesnick SA, DesPres D, Moonen CTW, Ruiz-Cabello J, Van Gelderen P. *In Vivo* Proton Spectroscopy and Spectroscopic Imaging of {1-<sup>13</sup>C}-Glucose and Its Metabolic Products. *Magnetic Resonance in Medicine* 1993;30:544-551.
7. Yahya A, Allen PS. Single-Shot 3D Localized Indirect <sup>13</sup>C Detection. Proceedings of the 12<sup>th</sup> annual meeting of the International Society for Magnetic Resonance in Medicine 2004:680.
8. Ruiz-Cabello J, Vuister GW, Moonen CT, Van Gelderen P, Cohen JS, Van Zijl PCM. Gradient-Enhanced Heteronuclear Correlation Spectroscopy. Theory and Experimental Aspects. *Journal of Magnetic Resonance* 1992;100:282-302.
9. Nakashima TT, McClung RED. Simulation of Two-Dimensional NMR Spectra Using Product Operators in the Spherical Basis. *Journal of Magnetic Resonance* 1986;70:187-203.
10. Matson GB. An integrated program for amplitude-modulated RF pulse generation and re-mapping with shaped gradients. *Magnetic Resonance Imaging* 1994;12:1205-1225.

11. Shaka AJ, Keeler J, Freeman R. Evaluation of a New Broadband Decoupling Sequence: WALTZ-16. *Journal of Magnetic Resonance* 1983;53:313-340.
12. Thompson RB, Allen PS. Sources of variability in the response of coupled spins to the PRESS sequence and their potential impact on metabolite quantification. *Magnetic Resonance in Medicine* 1999;41:1162-1169.
13. Provencher SW. Estimation of metabolite concentrations from localized *in vivo* proton NMR spectra. *Magnetic Resonance in Medicine* 1993;30:672-679.
14. Boumezbeur F, Besret L, Valette J, Vaufrey F, Henry PG, Slavov V, Giacomini E, Hantraye P, Bloch G, Lebon V. NMR measurement of brain oxidative metabolism in monkeys using  $^{13}\text{C}$ -labelled glucose without a  $^{13}\text{C}$  radiofrequency channel. *Magnetic Resonance in Medicine* 2004;52:33-40.

# Chapter 6

## Direct $^{13}\text{C}$ Observation I: PRESS Combined with a Modified DEPT Sequence<sup>1</sup>

### 6.1 Introduction

Chapters 4 and 5 described techniques used in the indirect detection of  $^{13}\text{C}$  signal (monitoring  $^{13}\text{C}$  labelling through the protons coupled to the  $^{13}\text{C}$  nuclei of interest). Although indirect  $^{13}\text{C}$  detection offers more sensitivity, it suffers from poor spectral resolution, particularly at the relatively lower field strengths, such as 3.0 T, used clinically. Direct  $^{13}\text{C}$  NMR spectra, on the other hand, exhibit much better spectral resolution and eliminate the problems associated with water suppression. Moreover, the signal-to-noise ratio (SNR) of the  $^{13}\text{C}$  spectra can be improved by using polarization transfer techniques such as DEPT (1), Distortionless Enhancement by Polarization Transfer, and INEPT (2), Insensitive Nuclei Enhanced by Polarization Transfer, where there is a transfer of polarization from the more sensitive protons to their less sensitive coupled  $^{13}\text{C}$  nuclei (enhances signal by about  $\gamma_H/\gamma_C \approx 4$ ). Since in *in-vivo* experiments it is desirable to obtain signal from a spatially well defined region, DEPT and INEPT have been combined with proton localization techniques, whereby localization is performed on the protons in the region of interest and polarization transfer is then used to transfer the magnetization to the coupled  $^{13}\text{C}$  nuclei. This clever technique not only allows for enhancement of the  $^{13}\text{C}$  signal but also reduces the otherwise large chemical shift displacement errors associated with localizing directly on  $^{13}\text{C}$ . Though the feasibility of combining INEPT with one-dimensional ISIS (3) and with PRESS (4) has been demonstrated, the INEPT sequence does distort the line intensities of the  $^{13}\text{C}$  multiplets and the refocused INEPT sequence (5) requires more RF pulses than DEPT does. DEPT has also been combined with one-dimensional ISIS (6), and then later the full three dimensional ISIS localization sequence (7) was incorporated with DEPT at 4.0 T and was

---

<sup>1</sup> Part of this chapter has been published. Yahya A, Allen PS. Effect of strong homonuclear proton coupling on localized  $^{13}\text{C}$  detection using PRESS. *Magnetic Resonance in Medicine* 2005; 54, 1340-1350.

used to obtain localized natural abundance  $^{13}\text{C}$  spectra of the human brain (8). More recently, the latter sequence was applied to rat brain (9) with some modifications to the DEPT part. Dephasing gradients were applied around both the proton and carbon  $180^\circ$  refocussing pulses in order to eliminate any off-resonance effects due to imperfect refocussing pulses. The incorporation of these gradients removed the need to rely on a phase cycling scheme, which mitigated the sequence's vulnerability to motion artifacts. However, the ISIS technique itself requires eight separate add/subtract scans in order to localize signal from a voxel, and thus such a sequence is still susceptible to motion artifacts and subtraction errors.

In this work, we demonstrate at 3.0 T that  $^{13}\text{C}$  signal from a three dimensional localized volume can be obtained in a single scan by combining the single shot localization PRESS sequence with a similarly modified DEPT sequence. A summary of this sequence has been previously presented (10). Furthermore, in this report, we show using glutamate (Glu) at 3.0 T as an illustrative example, how the strong homonuclear proton coupling gives rise to a reduction in the  $^{13}\text{C}$  signal enhancement from a basic DEPT sequence, and how this enhancement is further reduced when PRESS is combined with DEPT. The reduction in signal enhancement is a sensitive and non-monotonic function of the PRESS echo times and it does not have the same temporal dependence for each of the carbon positions in Glu. This latter difference would complicate relative  $^{13}\text{C}$  incorporation measurements on different carbon sites that might be made from the same carbon spectrum. The outcome of a sequence combining PRESS and refocussed INEPT is also examined and compared to that of the PRESS-DEPT sequence.

## **6.2 Theory**

### **6.2.1 INEPT**

#### **6.2.1.1 The basic INEPT sequence**

Figure 6.1(a) shows a diagram of the basic INEPT pulse sequence. To understand the mechanism of the sequence, consider an IS spin system, where I represents the proton, and S the coupled  $^{13}\text{C}$  nucleus. Using the product operator approach (Appendix 1), the evolution of the spin system can be followed. At thermal equilibrium the density

operator equals  $\gamma_I I_Z + \gamma_S S_Z$  (the  $\gamma$  factor is usually not included; however it is included here to demonstrate the source of signal enhancement). Upon application of the proton excitation pulse,  $\gamma_I I_Z + \gamma_S S_Z \xrightarrow{90_x(I)} -\gamma_I I_Y + \gamma_S S_Z$ , and following the delay  $1/2J_{IS}$ ,  $-\gamma_I I_Y + \gamma_S S_Z \xrightarrow{1/2J_{IS}} \gamma_I 2I_X S_Z + \gamma_S S_Z$ , forming proton antiphase magnetization. The proton  $180^\circ$  pulse is there to refocus any chemical shift evolutions, while the simultaneous  $^{13}\text{C}$   $180^\circ$  pulse allows the formation of antiphase heteronuclear coherence. The  $^{13}\text{C}$  excitation pulse forms a multiple quantum state and in-phase transverse magnetization for uncoupled  $^{13}\text{C}$  nuclei,  $\gamma_I 2I_X S_Z + \gamma_S S_Z \xrightarrow{90_x} -\gamma_I 2I_X S_Y - \gamma_S S_Y$ . The proton  $90^\circ$  pulse transforms the coherences as follows,  $-\gamma_I 2I_X S_Y - \gamma_S S_Y \xrightarrow{90_y(I)} \gamma_I 2I_Z S_Y - \gamma_S S_Y$ , resulting in a  $^{13}\text{C}$  antiphase coherence state which has benefited from a  $\gamma_I / \gamma_S \approx 4$  enhancement in signal. To eliminate signal from uncoupled  $^{13}\text{C}$  nuclei, the phase of the last proton pulse is alternated between  $\pm y$  and the two scans are subtracted.

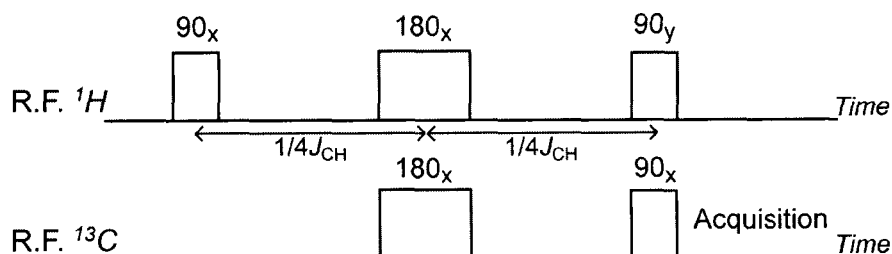
The enhanced antiphase  $^{13}\text{C}$  signals, however, have line intensities that are distorted. Signal from a CH group have line intensities of 1:-1, while those from a  $\text{CH}_2$  group have the ratios 1:0:-1, and those from a  $\text{CH}_3$  group have ratios of 1:1:-1:-1, instead of the standard 1:1, 1:2:1, and 1:3:3:1 ratios, respectively (11). Furthermore, proton decoupling cannot be applied during acquisition because this would simply collapse the multiplets causing the enhanced antiphase signals to cancel out. In order to allow decoupling the enhanced antiphase signals must be refocussed so that they are brought back into phase. This is done by attaching a spin echo to the sequence, yielding the refocussed INEPT sequence.

#### 6.2.1.2 The refocussed INEPT sequence

The refocussed INEPT sequence is shown in Fig. 6.1(b). For CH molecular groups, the delay  $\tau$  for optimal in-phase  $^{13}\text{C}$  signal is  $1/2J_{\text{CH}}$ , yielding signal enhanced by  $\gamma_I / \gamma_S \approx 4$ . For  $\text{CH}_2$  molecular groups, the delay  $\tau$  needs to be  $1/4J_{\text{CH}}$  for maximum signal enhancement which again is  $\gamma_I / \gamma_S \approx 4$ . For  $\text{CH}_3$  molecular groups, the optimal

signal enhancement is  $1.15\gamma_I/\gamma_S \approx 4.6$ , and is achieved when  $\tau$  is equal to  $\cos^{-1}(\sqrt{2/3})/(\pi J_{CH}) \approx 0.2/J_{CH}$  (12).

### (a) Basic INEPT



### (b) Refocussed INEPT

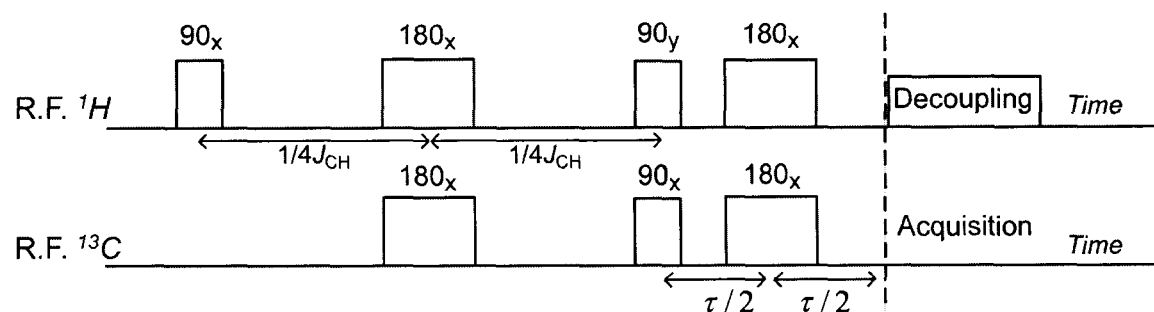


Figure 6.1: The basic INEPT sequence is displayed in (a), while the refocussed INEPT sequence with proton decoupling during acquisition is shown in (b).

## 6.2.2 DEPT

### 6.2.2.1 The basic DEPT sequence

Figure 1.23 displays the basic DEPT pulse sequence and a description of the mechanism of the sequence is given in §1.8.2.

### 6.2.2.2 The modified DEPT sequence

The figure below shows the additional spoilers added to the basic DEPT sequence. The purpose of the spoiler gradients around both the proton and carbon  $180^\circ$  pulses in DEPT is to eliminate any off-resonance effects due to imperfect refocussing pulses (9). The additional  $90^\circ$   $^{13}\text{C}$  pulse at the end of the sequence has the same phase as

the  $^{13}\text{C}$  excitation pulse and transforms any  $^{13}\text{C}$  signal that is directly excited by the  $^{13}\text{C}$  excitation pulse into unobservable longitudinal magnetization. Conventionally, this signal is eliminated by phase cycling the final proton pulse between  $\pm y$  and subtracting alternate scans. The modified DEPT sequence does not need to rely as heavily on phase cycling in order to eliminate  $^{13}\text{C}$  signal not arising via polarization transfer from the coupled protons.

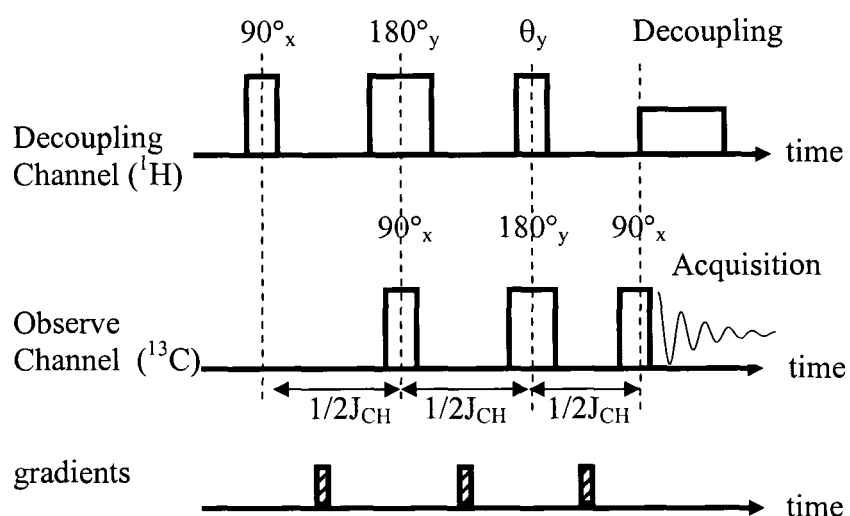


Figure 6.2: The modified DEPT sequence.

### 6.2.3 PRESS combined with modified DEPT

Figure 6.3 illustrates the PRESS sequence combined with the modified DEPT sequence. Localization is performed on the protons in the voxel of interest by PRESS; DEPT polarization transfer is then used to transfer the magnetization to the coupled  $^{13}\text{C}$  nuclei in that voxel. To illustrate the single-shot nature of this sequence, let us revisit the IS (I is a proton, and S the coupled  $^{13}\text{C}$  nucleus) spin system. The refocussing pulses are there to refocus any chemical shift evolution which shall be ignored in the following. At the end of PRESS, there exists transverse proton magnetization  $I_y$  which after the first  $1/2J_{\text{CH}}$  time interval transforms into antiphase proton magnetization with carbon  $2I_xS_z$ . The carbon excitation pulse converts this coherence state into a multiple quantum state, namely,  $2I_xS_y$ . The excitation pulse also creates outer volume signal  $S_y$ . The antiphase state is then transformed into antiphase carbon magnetization with proton,  $2I_zS_y$ , by the proton theta pulse which would be set to  $90^\circ$  for maximum signal from a CH molecular

group. The final delay yields transverse carbon  $S_x$  magnetization which is not influenced by the final  $^{13}\text{C}$   $90^\circ_x$  pulse. Any outer volume carbon  $S_y$  magnetization, however, will be converted back to unobservable longitudinal magnetization by the final carbon  $90^\circ_x$  pulse. Thus we see that by combining PRESS with this modified DEPT sequence,  $^{13}\text{C}$  signal can be acquired from a localized volume in a single scan without the need to rely on any phase cycling scheme or on the addition or subtraction of alternate scans.

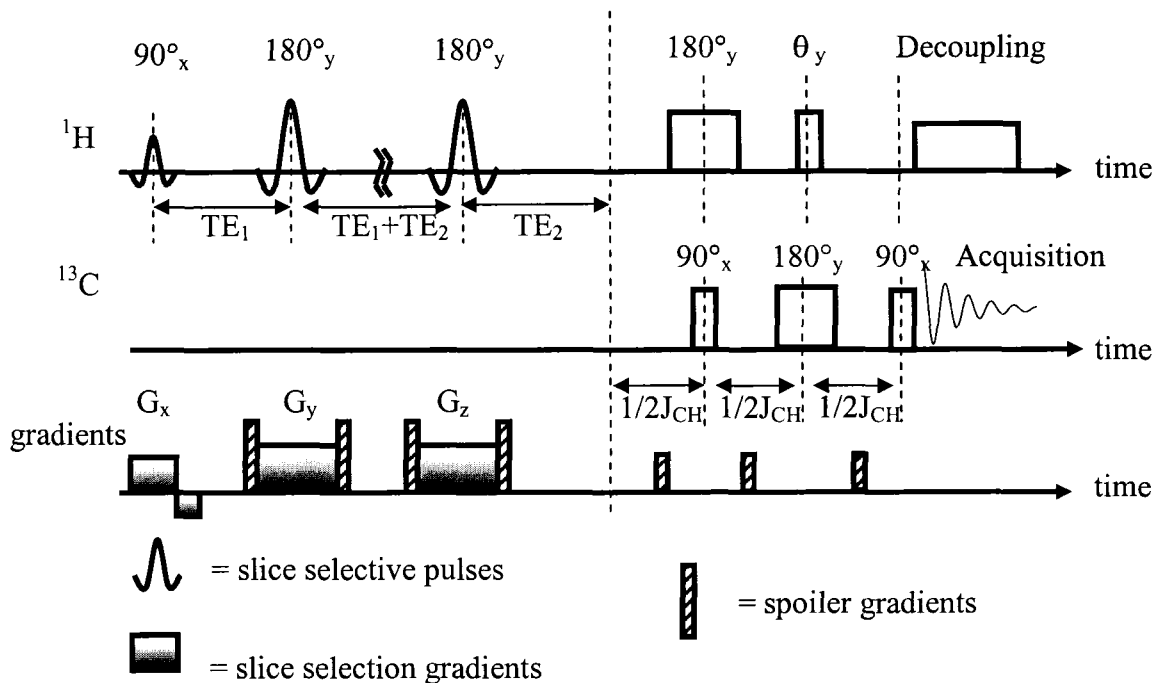


Figure 6.3: Schematic diagram illustrating the PRESS sequence combined with DEPT, where essentially the  $90^\circ$  proton excitation pulse of the DEPT sequence has been replaced by PRESS.

## 6.3 Methods

The method of numerical analysis used in this chapter was outlined in chapter 3. The chemical shift and scalar coupling constants used are the same as those displayed in Table 4.1.

All experiments were carried out in an 80 cm bore, 3.0 T magnet system (Magnex Scientific PLC, Abingdon, UK) using a SMIS spectrometer (Surrey Medical Imaging Systems PCL, Guildford, UK). Two sets of experiments were conducted. One set was to verify the efficacy of the sequence and the other was to investigate the effects of proton homonuclear coupling on the outcome of the sequence. The experiments verifying the



efficacy of the sequence employed a dual-tuned  $^{13}\text{C}/^1\text{H}$  open coil (see chapter 2 for details) and a phantom consisting of a 6 cm diameter sphere containing 10 M acetic acid immersed in a container of canola oil, as shown in Fig. 6.4. The PRESS sequence consisted of a sinc-gaussian  $90^\circ$  slice selective excitation pulse followed by two slice selective pulses of length 5.5 ms (bandwidth  $\approx 750$  Hz) and applied in conjunction with 0.9 mT/m gradients in order to refocus a slice thickness of 2 cm (a voxel of  $2 \times 2 \times 2$  cm<sup>3</sup> was achieved). The pulses were numerically optimized using the software MATPULSE (13) to minimize the spatial extent of the tip-angle transition region. The  $90^\circ$  proton and carbon DEPT pulses were respectively 500  $\mu\text{s}$ , and 400  $\mu\text{s}$  in length and the  $\theta^\circ$  pulse was set to  $45^\circ$  for optimal detection of  $\text{CH}_2$  molecular groups. The spoilers in the DEPT part of the sequence were 2 mT/m in strength and were applied simultaneously for 1 ms in three orthogonal directions. A sixteen step phase-cycling scheme shown to be efficient for DEPT (14) was also incorporated into the sequence (see Table 6.1). The delay  $1/2J_{\text{CH}}$  was set to 3.85 ms and all experiments employed a repetition time, TR, of 3 s, and a WALTZ-16 (15) decoupling component for  $^1\text{H}$  decoupling during acquisition. To achieve optimal signal it is important that the phase of the DEPT  $\theta^\circ$  pulse be orthogonal to that of the PRESS excitation pulse. Since spatial localization changes the relative phases of the two pulses (16-18) a phase calibration routine on the water peak from the desired voxel was carried out initially using the proton-only part of the sequence (see Fig. 6.5). In this routine the tip angle of the last DEPT pulse was set to  $\theta = 90^\circ$  and the phase,  $\alpha$ , of the PRESS excitation pulse was varied until the signal from the water peak reached a maximum. At this point orthogonality had been reached between the phase of the excitation pulse and that of the last proton pulse. This phase was then employed when applying the dual-frequency PRESS-DEPT combination.

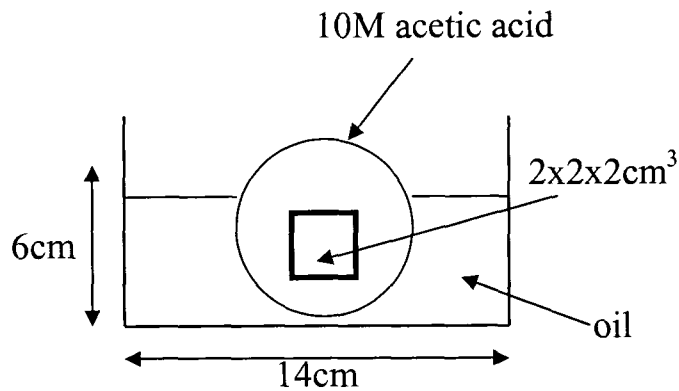


Figure 6.4: Phantom used to verify the efficacy of the PRESS-DEPT sequence.

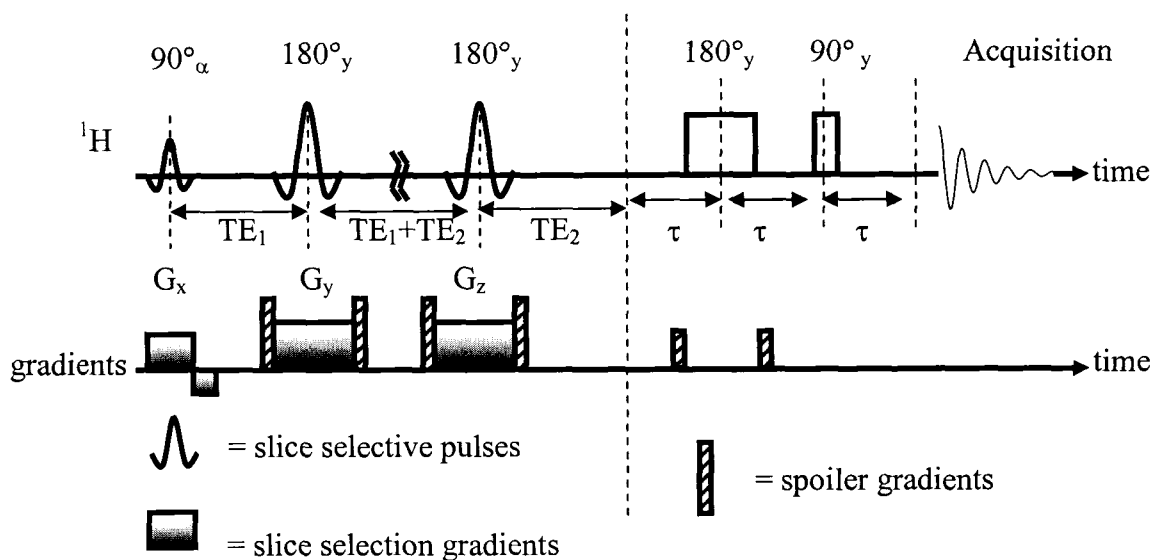


Figure 6.5: Sequence used to calibrate the relative phases of the PRESS excitation pulse and the final proton hard pulse.

The efficacy of the sequence was verified *in vivo* on a  $3 \times 3 \times 7 \text{ cm}^3$  voxel of a human calf using all the parameters above, except that the localization gradient strengths were reduced to  $0.6 \text{ mT/m}$ . The phase calibration routine was not as efficient *in vivo* because of the large amount outer volume signal, and an improvement could be made by employing the method of Choi et al. where two additional  $180^\circ$  slice-selective pulses are appended to the end of the calibration routine shown in Fig. 6.5 (19).

To investigate the effect of strong homonuclear coupling on the outcome of the sequence, the two PRESS refocussing slice selective pulses were reduced to  $2.75 \text{ ms}$  in length (bandwidth  $\approx 1500 \text{ Hz}$ ) and each was applied in conjunction with  $3.6 \text{ mT/m}$  gradients in order to refocus a slice thickness of  $1 \text{ cm}$  (a voxel of  $1 \times 1 \times 1 \text{ cm}^3$  was used).

The relatively short pulse lengths along with spoiler gradients of length 1 ms allowed a minimum total echo time of 20 ms ( $TE_1 = TE_2 = 10$  ms) to be achieved. The  $90^\circ$  proton and carbon DEPT pulses were respectively 200  $\mu$ s, and 150  $\mu$ s in length and the  $\theta^\circ$  pulse was again set to  $45^\circ$  for optimal detection of  $CH_2$  molecular groups. A home-built 7 cm diameter  $^1H$  birdcage RF coil, and a 3.5 cm diameter  $^{13}C$  surface coil were employed for these experiments along with two 2 cm diameter aqueous-solution phantoms of pH  $\approx 7$ , one containing 1.8 M Glu, with  $^{13}C$  in natural abundance and another containing 35 mM labelled Glu with the  $C_3$  carbon enriched 99% in  $^{13}C$  (Sigma-Aldrich Canada).

Table 6.1: Phase cycling scheme implemented for the DEPT part of the sequence.

Phase of DEPT $^1H$ $180^\circ$ pulse	Phase of DEPT $^1H$ $\theta^\circ$ pulse	Phase of DEPT $^{13}C$ $180^\circ$ pulse	Receiver phase
x	y	x	x
y	y	x	-x
-x	y	x	x
-y	y	x	-x
y	-y	x	x
x	-y	x	-x
-y	-y	x	x
x	-y	x	-x
x	y	-x	x
y	y	-x	-x
-x	y	-x	x
-y	y	-x	-x
y	-y	-x	x
x	-y	-x	-x
-y	-y	-x	x
x	-y	-x	-x

## 6.4 Results

### 6.4.1 Efficacy of the sequence

To verify the efficacy of the sequence shown in Fig. 6.3 it was applied to the phantom displayed Fig. 6.4. Figure 6.6(a) shows the result of applying a single  $^{13}\text{C}$  hard pulse (no decoupling pulses were applied during acquisition). Large signal from the  $\text{CH}_2$  groups of oil is visible as are the smaller peaks from the  $\text{CH}_3$  group of the acetic acid solution. The spectrum shown in Fig. 6.6(b) was obtained from a  $2 \times 2 \times 2 \text{ cm}^3$  voxel of the acetic acid phantom by a single-application of the PRESS-DEPT sequence of Fig. 6.3 (no signal averaging). It is clear that in one application of the sequence almost all of the outer volume oil signal is suppressed. The spectrum in Fig. 6.6(c) displays the result of signal averaging and phase cycling.

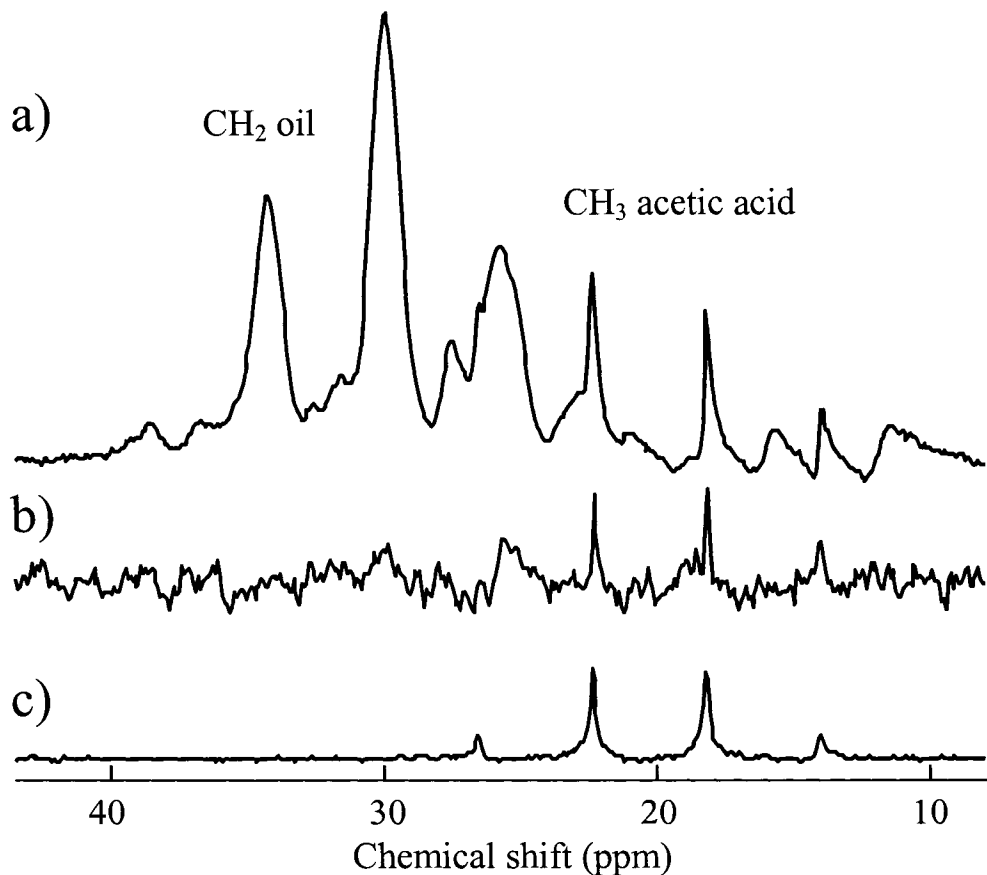


Figure 6.6: The spectrum in (a), acquired in 64 averages, shows the result of applying a single  $^{13}\text{C}$  hard pulse to the phantom shown in Fig. 6.4. The result of a single application of the sequence of Fig. 6.3 ( $\text{TE}_1 = \text{TE}_2 = 30 \text{ ms}$ ); a  $2 \times 2 \times 2 \text{ cm}^3$  voxel in the acetic acid phantom was chosen. It is clear that the sequence efficiently eliminates nearly all outer volume signal. The spectrum in (c) shows the effect of signal averaging (64 averages) and phase cycling. No proton decoupling during acquisition was applied in any of the cases.

### 6.4.2 Feasibility of applying the sequence *in vivo*

To demonstrate the feasibility of applying the sequence of Fig. 6.3 *in vivo*, it was applied to a human calf. Figure 6.7 shows the natural abundance  $^{13}\text{C}$  peaks of creatine (Cr) and choline (Cho) obtained from a  $3\times 3\times 7\text{ cm}^3$  volume from a human calf muscle.

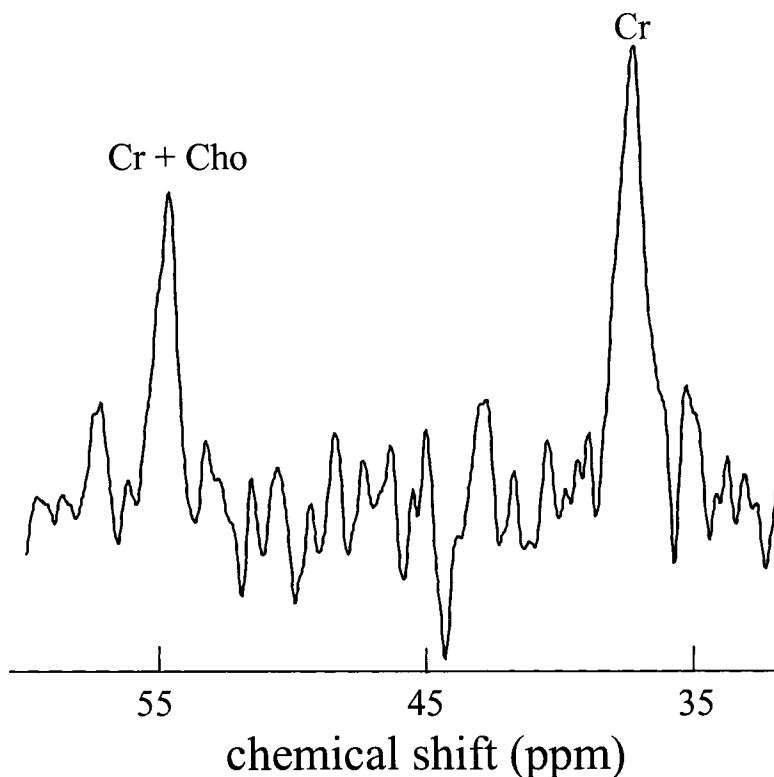


Figure 6.7: Natural abundance  $^{13}\text{C}$  spectrum acquired from a  $3\times 3\times 7\text{ cm}^3$  voxel of a human calf using the sequence of Fig. 6.3 ( $\text{TE}_1 = \text{TE}_2 = 30\text{ ms}$ , 1600 acquisitions). The spectrum shows peaks from the creatine methyl group at 37.5 ppm, and from the creatine methylene and choline methyl groups at 54.8 ppm.

### 6.4.3 The effect of strong homonuclear proton coupling on the outcome of the sequence, illustrated with glutamate at 3.0 T

At 3.0 T, Glu can be represented as a strongly-coupled AMNPQ proton spin system (see Fig. 1.9). When one of its carbons is  $^{13}\text{C}$ -labelled, it can be denoted as an AMNPQX spin system, where X is the  $^{13}\text{C}$  nucleus (see Table 4.1). It is demonstrated in this section that the PRESS localization is not benign and that it affects the localized  $^{13}\text{C}$  outcome through its influence on the coherence distribution of the localized protons, upon which the polarization transfer is dependent. There are therefore two coupling-

dependent processes affecting the intensity of the localized  $^{13}\text{C}$  spectrum. One is the efficiency of the DEPT enhancement and the other is the PRESS-governed coherence distribution of the localized protons.

Under the substantially simplified conditions of an unlocalized DEPT enhancement in which the strong homonuclear proton coupling in Glu is switched “off”, the Glu in-phase SQC,  $M_y$  and  $N_y$  (for  $^{13}\text{C}_3$  labelling) or  $P_y$  and  $Q_y$  (for  $^{13}\text{C}_4$  labelling), would, at the end of DEPT, each contribute 0.5 towards the expectation value of unity for  $X_x$  (corresponding to a factor of  $\gamma_H / \gamma_C \approx 4$  enhancement), but nothing to that for  $X_y$ . In contrast, under strong proton homonuclear coupling, although there can in principle be up to 256 MNPQ Glu SQC terms at the start of DEPT (when preceded by PRESS), only eight (for  $^{13}\text{C}_3$  labelling) or six (for  $^{13}\text{C}_4$  labelling) are significant in producing in-phase  $^{13}\text{C}$  magnetization at the end of DEPT, in addition that is, to the dominating,  $M_y$  and  $N_y$  (for  $^{13}\text{C}_3$  labelling) or  $P_y$  and  $Q_y$  (for  $^{13}\text{C}_4$  labelling). Table 6.2 summarizes these significant SQC and quantifies their maximal ability to contribute to the  $^{13}\text{C}$  yield under the proton homonuclear coupling in Glu during DEPT. The maximal ability is governed by the evolutionary pathways followed during DEPT, and the pathways of the 10 significant terms for  $^{13}\text{C}_3$  labelling, are listed in Fig. 6.8. The simple  $^{13}\text{C}$  Lorentzian resonance lines, when proton decoupling is applied during acquisition, enables us to isolate the impact of strong homonuclear proton coupling on the  $^{13}\text{C}$  enhancement,  $\xi$ , due to an unlocalized DEPT sequence. The enhancements were reduced from the often assumed,  $\xi \approx \gamma_H / \gamma_C \approx 4$ , to  $\xi \approx 3.6 \approx 0.88 \times 4$ , for  $\text{C}_3$  and  $\text{C}_4$ , and to  $\xi \approx 3.9$  for  $\text{C}_2$ .

$$\begin{aligned}
M_Y(1) &\xrightarrow{\frac{1}{2J_{CH}}} \begin{cases} 2M_X X_Z (-0.95) \\ 2M_Y X_Z (-0.07) \\ 4M_X N_Z X_Z (-0.01) \\ 4M_Y N_Z X_Z (0.17) \\ 4M_Z N_X X_Z (-0.01) \\ 4M_Z N_Y X_Z (-0.17) \end{cases} \xrightarrow{\begin{matrix} 180^\circ_Y (^1H) \\ 90^\circ_X (^{13}C) \end{matrix}} \begin{cases} 2M_X X_Y (0.95) \\ 2M_Y X_Y (-0.07) \\ 4M_X N_Z X_Y (-0.01) \\ 4M_Y N_Z X_Y (-0.17) \\ 4M_Z N_X X_Y (-0.01) \\ 4M_Z N_Y X_Y (0.17) \end{cases} \xrightarrow{\frac{1}{2J_{CH}}} \begin{cases} 4M_X N_Z X_X (-0.85) \\ 4M_Z N_X X_X (-0.08) \end{cases} \\
&\xrightarrow{\begin{matrix} 45^\circ_Y (^1H) \\ 180^\circ_Y (^{13}C) \end{matrix}} \{4M_Z N_Z X_X (0.46)\} \xrightarrow{\frac{1}{2J_{CH}}} X_X (-0.46)
\end{aligned}$$

$$\begin{aligned}
N_Y(1) &\xrightarrow{\frac{1}{2J_{CH}}} \begin{cases} 2N_X X_Z (-0.94) \\ 2N_Y X_Z (0.15) \\ 4M_Z N_X X_Z (0.03) \\ 4M_Z N_Y X_Z (0.16) \\ 4M_X N_Z X_Z (-0.01) \\ 4M_Y N_Z X_Z (-0.17) \end{cases} \xrightarrow{\begin{matrix} 180^\circ_Y (^1H) \\ 90^\circ_X (^{13}C) \end{matrix}} \begin{cases} 2N_X X_Y (0.94) \\ 2N_Y X_Y (0.15) \\ 4M_Z N_X X_Y (0.03) \\ 4M_Z N_Y X_Y (-0.16) \\ 4M_X N_Z X_Y (-0.01) \\ 4M_Y N_Z X_Y (0.17) \end{cases} \xrightarrow{\frac{1}{2J_{CH}}} \{4M_Z N_X X_X (-0.85)\} \\
&\xrightarrow{\begin{matrix} 45^\circ_Y (^1H) \\ 180^\circ_Y (^{13}C) \end{matrix}} \{4M_Z N_Z X_X (0.43)\} \xrightarrow{\frac{1}{2J_{CH}}} X_X (-0.43)
\end{aligned}$$

$$\begin{aligned}
2M_X A_Z(1) &\xrightarrow{\frac{1}{2J_{CH}}} \begin{cases} 4M_X A_Z X_Z (-0.07) \\ 4M_Y A_Z X_Z (0.95) \\ 2M_Y X_Z (-0.004) \\ 2M_X X_Z (-0.05) \end{cases} \xrightarrow{\begin{matrix} 180^\circ_Y (^1H) \\ 90^\circ_X (^{13}C) \end{matrix}} \begin{cases} 4M_X A_Z X_Y (-0.07) \\ 4M_Y A_Z X_Y (-0.95) \\ 2M_Y X_Y (-0.004) \\ 2M_X X_Y (0.05) \end{cases} \xrightarrow{\frac{1}{2J_{CH}}} \{4M_X N_Z X_X (-0.10)\} \\
&\xrightarrow{\begin{matrix} 45^\circ_Y (^1H) \\ 180^\circ_Y (^{13}C) \end{matrix}} \{4M_Z N_Z X_X (0.05)\} \xrightarrow{\frac{1}{2J_{CH}}} X_X (-0.05)
\end{aligned}$$

$$\begin{aligned}
2M_X P_Z(1) &\xrightarrow{\frac{1}{2J_{CH}}} \begin{cases} 4M_X P_Z X_Z (-0.07) \\ 4M_Y P_Z X_Z (0.91) \\ 2M_Y X_Z (-0.01) \\ 2M_X X_Z (-0.07) \end{cases} \xrightarrow{\begin{matrix} 180^\circ_Y (^1H) \\ 90^\circ_X (^{13}C) \end{matrix}} \begin{cases} 4M_X P_Z X_Y (-0.07) \\ 4M_Y P_Z X_Y (-0.91) \\ 2M_Y X_Y (-0.01) \\ 2M_X X_Y (0.07) \end{cases} \xrightarrow{\frac{1}{2J_{CH}}} \{4M_X N_Z X_X (-0.14)\} \\
&\xrightarrow{\begin{matrix} 45^\circ_Y (^1H) \\ 180^\circ_Y (^{13}C) \end{matrix}} \{4M_Z N_Z X_X (0.07)\} \xrightarrow{\frac{1}{2J_{CH}}} X_X (-0.07)
\end{aligned}$$

$$2M_x Q_z (1) \xrightarrow{\frac{1}{2J_{CH}}} \begin{cases} 4M_x Q_z X_z (-0.07) \\ 4M_y Q_z X_z (0.92) \\ 2M_y X_z (-0.01) \\ 2M_x X_z (-0.09) \end{cases} \xrightarrow{\begin{matrix} 180^\circ_y ({}^1H) \\ 90^\circ_x ({}^{13}C) \end{matrix}} \begin{cases} 4M_x Q_z X_y (-0.07) \\ 4M_y Q_z X_y (-0.92) \\ 2M_y X_y (-0.01) \\ 2M_x X_y (0.09) \end{cases} \xrightarrow{\frac{1}{2J_{CH}}} \{4M_x N_z X_x (-0.17)\}$$

$$\xrightarrow{\begin{matrix} 45^\circ_y ({}^1H) \\ 180^\circ_y ({}^{13}C) \end{matrix}} \{4M_z N_z X_x (0.09)\} \xrightarrow{\frac{1}{2J_{CH}}} X_x (-0.09)$$

$$2N_x A_z (1) \xrightarrow{\frac{1}{2J_{CH}}} \begin{cases} 4N_x A_z X_z (0.15) \\ 4N_y A_z X_z (0.94) \\ 2N_y X_z (0.01) \\ 2N_x X_z (-0.08) \end{cases} \xrightarrow{\begin{matrix} 180^\circ_y ({}^1H) \\ 90^\circ_x ({}^{13}C) \end{matrix}} \begin{cases} 4N_x A_z X_y (0.15) \\ 4N_y A_z X_y (-0.94) \\ 2N_y X_y (0.01) \\ 2N_x X_y (0.08) \end{cases} \xrightarrow{\frac{1}{2J_{CH}}} \{4M_z N_x X_x (-0.15)\}$$

$$\xrightarrow{\begin{matrix} 45^\circ_y ({}^1H) \\ 180^\circ_y ({}^{13}C) \end{matrix}} \{4M_z N_z X_x (0.08)\} \xrightarrow{\frac{1}{2J_{CH}}} X_x (-0.08)$$

$$2N_x P_z (1) \xrightarrow{\frac{1}{2J_{CH}}} \begin{cases} 4N_x P_z X_z (0.15) \\ 4N_y P_z X_z (0.90) \\ 2N_y X_z (0.01) \\ 2N_x X_z (-0.09) \end{cases} \xrightarrow{\begin{matrix} 180^\circ_y ({}^1H) \\ 90^\circ_x ({}^{13}C) \end{matrix}} \begin{cases} 4N_x P_z X_y (0.15) \\ 4N_y P_z X_y (-0.90) \\ 2N_y X_y (0.01) \\ 2N_x X_y (0.09) \end{cases} \xrightarrow{\frac{1}{2J_{CH}}} \{4M_z N_x X_x (-0.17)\}$$

$$\xrightarrow{\begin{matrix} 45^\circ_y ({}^1H) \\ 180^\circ_y ({}^{13}C) \end{matrix}} \{4M_z N_z X_x (0.09)\} \xrightarrow{\frac{1}{2J_{CH}}} X_x (-0.09)$$

$$2N_x Q_z (1) \xrightarrow{\frac{1}{2J_{CH}}} \begin{cases} 4N_x Q_z X_z (0.14) \\ 4N_y Q_z X_z (0.90) \\ 2N_y X_z (0.01) \\ 2N_x X_z (-0.07) \end{cases} \xrightarrow{\begin{matrix} 180^\circ_y ({}^1H) \\ 90^\circ_x ({}^{13}C) \end{matrix}} \begin{cases} 4N_x Q_z X_y (0.14) \\ 4N_y Q_z X_y (-0.90) \\ 2N_y X_y (0.01) \\ 2N_x X_y (0.07) \end{cases} \xrightarrow{\frac{1}{2J_{CH}}} \{4M_z N_x X_x (-0.14)\}$$

$$\xrightarrow{\begin{matrix} 45^\circ_y ({}^1H) \\ 180^\circ_y ({}^{13}C) \end{matrix}} \{4M_z N_z X_x (0.07)\} \xrightarrow{\frac{1}{2J_{CH}}} X_x (-0.07)$$

$$2P_y X_z (1) \xrightarrow{\frac{1}{2J_{CH}}} \begin{cases} 2P_y X_z (0.69) \\ 2P_x X_z (-0.66) \end{cases} \xrightarrow{\begin{matrix} 180^\circ_y ({}^1H) \\ 90^\circ_x ({}^{13}C) \end{matrix}} \begin{cases} 2P_y X_y (0.69) \\ 2P_x X_y (0.66) \end{cases} \xrightarrow{\frac{1}{2J_{CH}}} \begin{cases} 4M_z N_x X_y (-0.05) \\ 4M_x N_z X_y (-0.04) \\ 8M_z N_z P_y X_y (-0.9) \end{cases}$$

$$\xrightarrow{\begin{matrix} 45^\circ_y ({}^1H) \\ 180^\circ_y ({}^{13}C) \end{matrix}} \begin{cases} 4M_z N_z X_y (-0.05) \\ 8M_z N_x P_y X_y (0.45) \\ 8M_x N_z P_y X_y (0.45) \end{cases} \xrightarrow{\frac{1}{2J_{CH}}} X_y (0.09)$$



$$\begin{aligned}
2Q_y X_z (1) &\xrightarrow{\frac{1}{2J_{CH}}} \begin{cases} 2Q_y X_z (0.72) \\ 2Q_x X_z (-0.62) \end{cases} \xrightarrow{\begin{matrix} 180_y(^1H) \\ 90_x(^{13}C) \end{matrix}} \begin{cases} 2Q_y X_y (0.72) \\ 2Q_x X_y (0.62) \end{cases} \xrightarrow{\frac{1}{2J_{CH}}} \begin{cases} 4M_z N_x X_y (-0.04) \\ 4M_x N_z X_y (-0.06) \\ 8M_z N_z Q_y X_y (-0.9) \end{cases} \\
&\xrightarrow{\begin{matrix} 45_y(^1H) \\ 180_y(^{13}C) \end{matrix}} \begin{cases} 4M_z N_z X_y (-0.05) \\ 8M_z N_x Q_y X_y (0.45) \\ 8M_x N_z Q_y X_y (0.45) \end{cases} \xrightarrow{\frac{1}{2J_{CH}}} X_y (0.10)
\end{aligned}$$

Figure 6.8: It was determined that in the PRESS localized DEPT sequence of Fig. 6.3, that primary responsibility for yielding in-phase observable  $^{13}\text{C}$  signal for  $^{13}\text{C}_3$ -Glu rests with 10 proton SQCs that are present following PRESS localization. The diagram above shows the dominant coherence pathways taken by those 10 SQCs during the DEPT part of the sequence. The expectation value of each term is placed beside it in brackets. To simplify calculations, it was assumed that the  $^{13}\text{C}$  pulses were on resonance and thus no chemical shift evolution was occurring at the carbon frequency. Similar pathways can be calculated for the eight SQC terms that yield  $^{13}\text{C}_4$  in-phase observable signal.

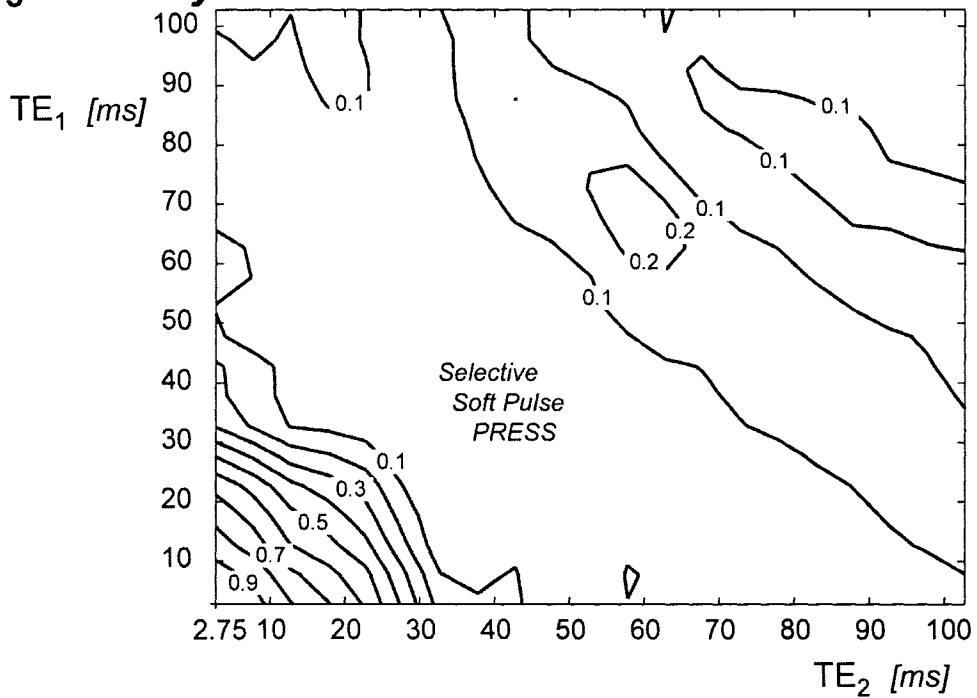
The maximal contributions to the  $^{13}\text{C}$  yield will not, however, be realized in a PRESS-localized-DEPT sequence. This is because by the start of DEPT the amplitude of each of the coherence terms will be governed by its evolution during PRESS. In essence, the strong homonuclear proton coupling modulates the amplitude of each of the significant SQCs as a function of the PRESS echo times, and therefore pre-ordains the distribution of coherences at the start of DEPT. This is the principal source of the  $^{13}\text{C}$  yield variations illustrated in the contour diagram of Fig. 6.9(a) for  $^{13}\text{C}_3$  labelling. The remainder stems from the continued effect of coupling on the coherence distribution throughout the DEPT sub-sequence. The strong influence of PRESS evolution is borne out by the echo-time symmetry of Fig. 6.9(a), which is strongly reminiscent of that obtained for protons in Glu with natural abundance  $^{13}\text{C}$  (20). The deviation from a monotonic dependence of yield on echo time is clarified in Fig. 6.9(b), which shows the intensity change along a diagonal cut ( $\text{TE}_1 = \text{TE}_2$ ) of symmetric PRESS. Figure 6.9(b) includes two intensity cuts, one calculated for PRESS with selective pulses, and the other calculated with all hard pulses. Their difference emphasizes that the additional evolution going on during the selective pulses cannot be ignored. The experimental points displayed in Fig. 6.9(b) were obtained using hard-pulse PRESS in order to reflect more clearly the transverse relaxation of the MN protons, which was not included in the numerical analysis. A  $T_{2\text{MN}} \approx 300$  ms was estimated for the MN protons in the Glu phantom solution. The  $^{13}\text{C}$  yield variations for  $^{13}\text{C}_4$  labelling, shown in Figure 6.10, are

significantly different in amplitude from Fig 6.9(a), although similar in temporal symmetry. The secondary intensity maximum in the region of  $TE_1 = TE_2 \approx 60$  ms is both higher and wider than that seen for  $^{13}\text{C}_3$ . This is due to the absence of an interaction between the PQ protons and any other proton, similar to that between the MN protons and the A proton (bonded to  $\text{C}_2$ ) of Glu.

Table 6.2: A list of proton SQC terms that, when present at the end of the PRESS part of the PRESS-DEPT combined sequence, yield in-phase  $^{13}\text{C}$  magnetization for the  $\text{C}_3$  and  $\text{C}_4$  carbons of Glu through DEPT polarization transfer. The expectation values of the in-phase  $^{13}\text{C}$  terms  $X_X$  or  $X_Y$  are given in brackets.

<b>C<sub>3</sub>-labelled Glu</b>		<b>C<sub>4</sub>-labelled Glu</b>	
<b>SQC</b>	<b><sup>13</sup>C yield</b>	<b>SQC</b>	<b><sup>13</sup>C yield</b>
$M_Y$	$X_X (-0.44)$	$P_Y$	$X_X (-0.44)$
$N_Y$	$X_X (-0.44)$	$Q_Y$	$X_X (-0.44)$
$2M_X A_Z$	$X_X (-0.05)$		
$2M_X P_Z$	$X_X (-0.09)$	$2P_X M_Z$	$X_X (-0.09)$
$2M_X Q_Z$	$X_X (-0.11)$	$2P_X N_Z$	$X_X (-0.11)$
$2N_X A_Z$	$X_X (-0.07)$		
$2N_X P_Z$	$X_X (-0.11)$	$2Q_X M_Z$	$X_X (-0.11)$
$2N_X Q_Z$	$X_X (-0.09)$	$2Q_X N_Z$	$X_X (-0.09)$
$2P_Y X_Z$	$X_Y (0.09)$	$2M_Y X_Z$	$X_Y (0.09)$
$2Q_Y X_Z$	$X_Y (0.10)$	$2N_Y X_Z$	$X_Y (0.09)$

**(a)  $^{13}\text{C}_3$  Intensity**



**(b)  $^{13}\text{C}_3$  Intensity**

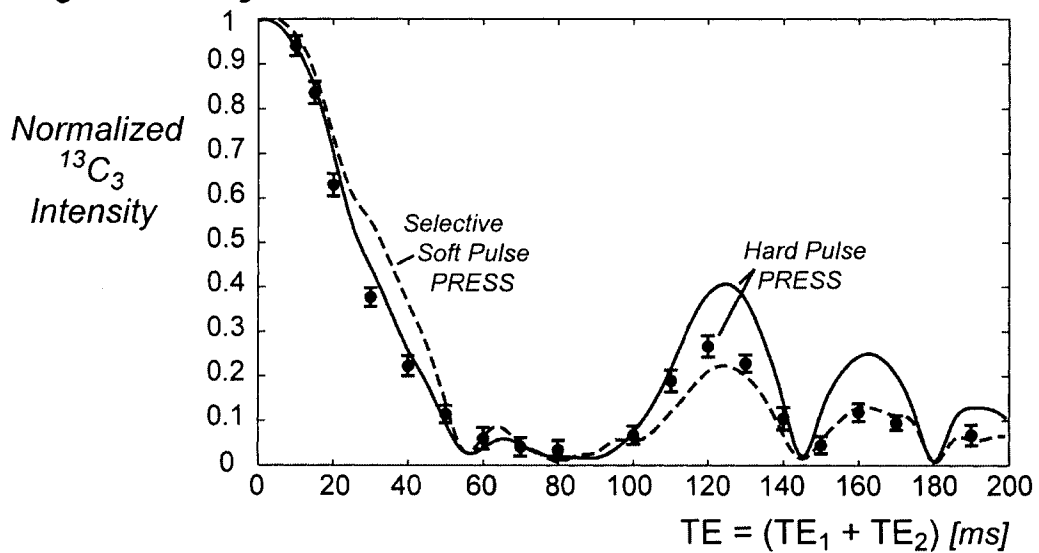


Figure 6.9: A clarification of the effect of the proton localization sequence, PRESS, on the  $^{13}\text{C}$  response to a proton-PRESS-DEPT  $^{13}\text{C}$  observation sequence. Panel (a) maps the  $^{13}\text{C}_3$  peak intensity as a function of the PRESS echo times when the three PRESS pulses are spatially selective. A cut along the  $\text{TE}_1 = \text{TE}_2$  diagonal is shown in panel (b) and compared with the equivalent cut through a contour plot derived assuming hard PRESS pulses. The data points, from a hard pulse PRESS experiment, confirm the temporal variation determined numerically and also reflect the signal loss due to transverse relaxation. The error bars are half the peak-to-peak noise.

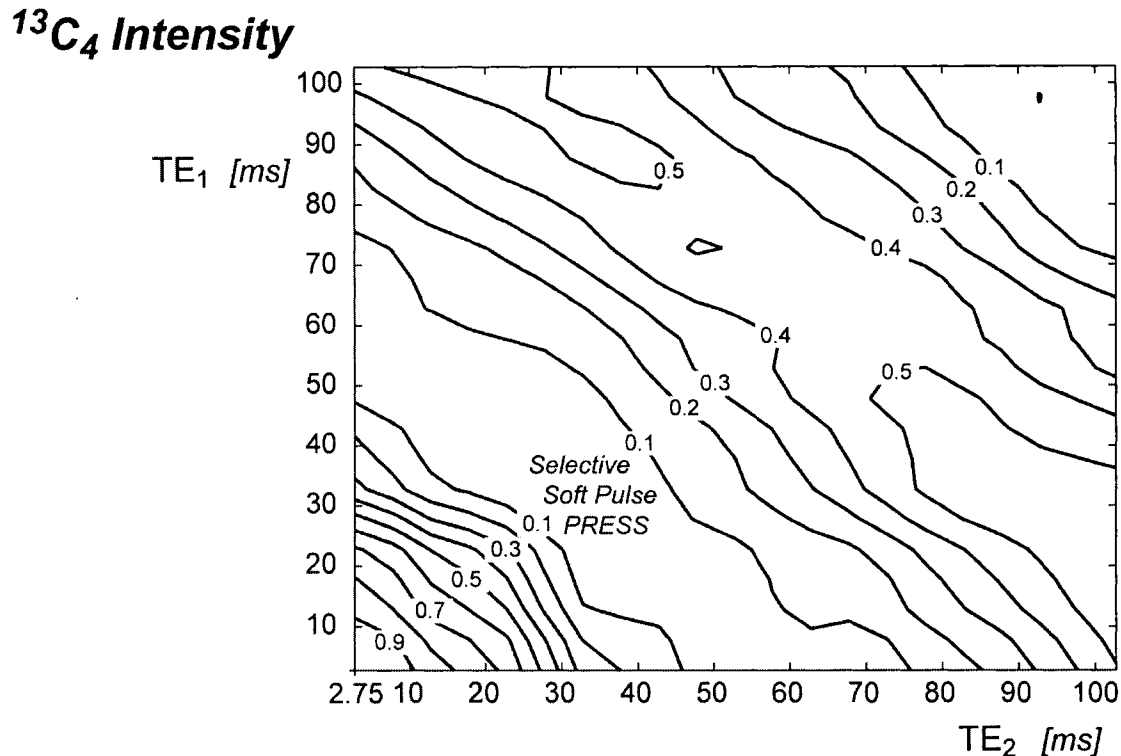
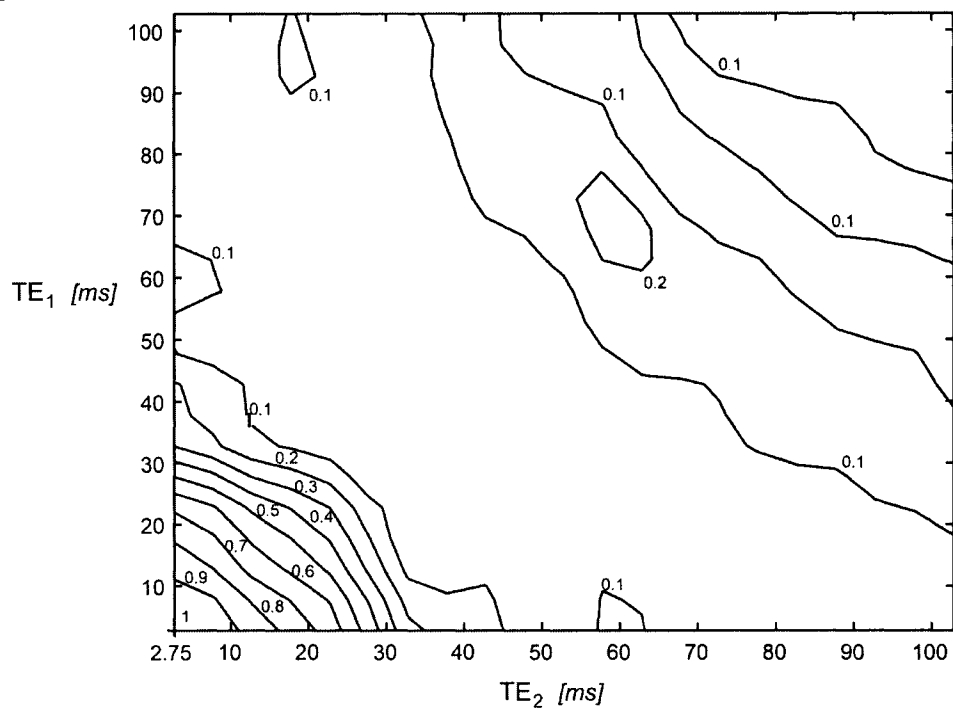


Figure 6.10: The corresponding contour plot for  $^{13}\text{C}_4$  carbon, again using selective PRESS pulses, is illustrated. The recovery of the  $^{13}\text{C}$  intensity at longer PRESS echo times is much broader and higher than that of  $^{13}\text{C}_3$  shown in panel (a), a phenomenon due to the absence (for PQ protons) of the 'A' spin coupling experienced by the MN protons.

The INEPT sequence is much shorter than the DEPT sequence. A refocussed INEPT sequence for a  $\text{CH}_2$  group is about 5.55 ms (using  $J_{\text{CH}} = 135$  Hz), compared to a DEPT length of 11.1 ms. The effect of proton homonuclear coupling during an unlocalized refocussed INEPT sequence on the  $^{13}\text{C}$  signal enhancement was calculated to be negligible. However, if PRESS is combined with a refocussed INEPT sequence, then the  $^{13}\text{C}$  enhancement is again highly dependent on the PRESS echo times. The intensity contour plots for PRESS-refocussed INEPT are very similar to those presented for PRESS-DEPT (see Fig. 6.11). The shorter INEPT sequence (than DEPT) gives rise only to differences in fine detail.

**(a)  $^{13}\text{C}_3$  Intensity**



**(b)  $^{13}\text{C}_4$  Intensity**

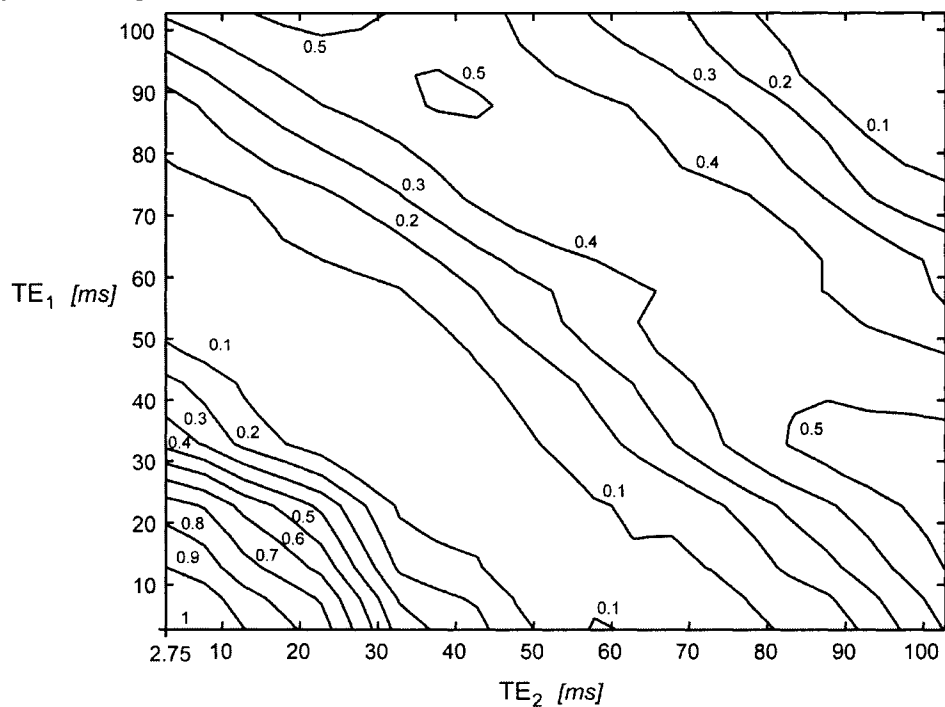


Figure 6.11: The  $^{13}\text{C}_3$  and  $^{13}\text{C}_4$  intensity contour plots for a PRESS sequence combined with a refocused INEPT sub-sequence. The contour plots are very similar to those shown in Figs. 6.9(a) and 6.10 for the PRESS-DEPT sequence.

## **6.5 Discussion**

This work demonstrates that by combining the single-shot PRESS localization sequence with a modified DEPT sequence,  $^{13}\text{C}$  signal can be obtained from a three dimensional volume in a single scan without the need to entirely rely upon phase cycling or upon the subtraction and addition of alternate scans. This sequence would be less susceptible to motion artifacts and subtraction errors than a sequence that involves the ISIS localization technique. However, we showed that the  $^{13}\text{C}$  enhancement of a PRESS-DEPT sequence is significantly modulated as a consequence of the proton coherence evolution taking place during the PRESS localization, as well as suffering a minor reduction due to the further coherence evolution that takes place during the short period of the DEPT sub-sequence ( $\approx 10\%$ ). Unless the role of proton homonuclear coupling is accurately accounted for, quantification errors in  $^{13}\text{C}$  incorporation into Glu can easily arise using either technique.

The biggest challenge to the direct  $^{13}\text{C}$  detection method using the PRESS-DEPT combination is the sharp loss of enhancement as the PRESS  $\text{TE}_1$  and  $\text{TE}_2$  increase. This loss mirrors the decrease of in-phase terms such as  $M_y$  and  $N_y$  (for  $^{13}\text{C}_3$  labelling) or  $P_y$  and  $Q_y$  (for  $^{13}\text{C}_4$  labelling) as the strong homonuclear coupling facilitates polarization transfer to other Glu protons. The rapid decrease of Glu in-phase SQC involving M,N,P and Q spins during a PRESS sequence was previously reported in Ref. (20). Because the contour diagrams (see Figs. 6.9(a) and 6.10) for  $^{13}\text{C}_3$  and  $^{13}\text{C}_4$  labelling are not identical (as is also the case for  $^{13}\text{C}_2$ ), it becomes necessary to correct for the differences in enhancement between label positions, if identical PRESS sequences are used to measure both fractional enrichments, even though the different label positions may both be methylene groups. For example, to efficiently employ the PRESS-DEPT sequence, it is apparent from the contour plots that a short PRESS echo time, e.g.  $\{\text{TE}_1 = \text{TE}_2 = 10 \text{ ms}\}$ , would be the wisest choice for the simultaneous detection of  $\text{C}_3$  and  $\text{C}_4$  labelling of Glu. At these timings the  $^{13}\text{C}$  enhancement is about 84% and 74% for the  $^{13}\text{C}_4$  and  $^{13}\text{C}_3$  carbons of Glu, respectively (see Fig. 6.12 for experimental confirmation). If it was assumed that the  $^{13}\text{C}_3$  yield is identical to that of  $^{13}\text{C}_4$ , then all  $^{13}\text{C}_3$  fractional enrichments would be underestimated by about 12% (for those specific PRESS timings).

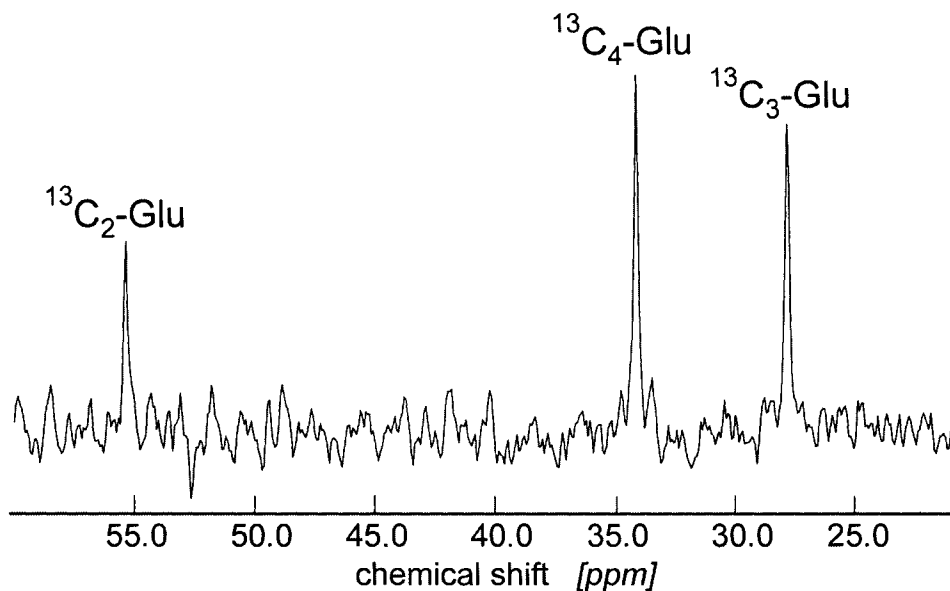


Figure 6.12:  $^{13}\text{C}$  spectrum from a  $1 \times 1 \times 1 \text{ cm}^3$  volume of the 1.8 M natural abundance Glu phantom obtained using the PRESS-DEPT sequence ( $\text{TE}_1 = \text{TE}_2 = 10 \text{ ms}$ , 128 averages). The  $^{13}\text{C}_3$  peak intensity is about 86% that of the  $^{13}\text{C}_4$  peak (agrees well with the 88% obtained numerically). The  $^{13}\text{C}_2$  peak is lower in intensity because for optimum signal from a CH molecular group, the  $\theta^\circ$  proton pulse needs to be set to  $90^\circ$ , here it was set to  $45^\circ$  (which is the optimal setting for  $\text{CH}_2$  molecular groups).

## **6.6 References**

1. Doddrell DM, Pegg DT, Bendall MR. Distortionless enhancement of NMR signals by polarization transfer. *Journal of Magnetic Resonance* 1982;48:323-327.
2. Morris GA, Freeman R. Enhancement of nuclear magnetic resonance signals by polarization transfer. *Journal of the American Chemical Society* 1979;101:760-762.
3. Norris DG, Schuff N, Leibfritz D. INEPT-enhanced  $^{13}\text{C}$  spectroscopy using double-tuned surface coils. *Journal of Magnetic Resonance* 1988;78:362-366.
4. Kries R, Slotboom J, Felblinger J, Boesch C.  $^{13}\text{C}$ -MR spectroscopy on a 1.5T scanner with  $^1\text{H}$ -localization using PRESS, INEPT polarization transfer, adiabatic pulses and WALTZ decoupling, in "Proc. ISMRM, 5th Annual Meeting, Vancouver, 1997,". 1997:1438.
5. Morris GA. Sensitivity enhancement in nitrogen-15 NMR: polarization transfer using the INEPT pulse sequence. *Journal of American Chemical Society* 1980;102:428-429.
6. Beckmann N, Muller S. Analysis of localized polarization transfer for  $^{13}\text{C}$  volume-selective spectroscopy with surface coils. *Journal of Magnetic Resonance* 1991;93:299-318.
7. Ordidge RJ, Connelly A, Lohman JAB. Image-selected in vivo spectroscopy (ISIS). A new technique for spatially selective NMR spectroscopy. *Journal of Magnetic Resonance* 1986;66:283-294.
8. Gruetter R, Adriany G, Merkle H, Andersen PM. Broadband decoupled,  $^1\text{H}$ -localized  $^{13}\text{C}$  MRS of the human brain at 4 tesla. *Magnetic Resonance in Medicine* 1996;36:659-664.
9. Henry P-G, Tkac I, Gruetter R.  $^1\text{H}$ -localized broadband  $^{13}\text{C}$  NMR spectroscopy of the rat brain in vivo at 9.4 T. *Magnetic Resonance in Medicine* 2003;50:684-692.
10. Yahya A, Allen PS. 3D localized direct  $^{13}\text{C}$  detection using PRESS and a modified DEPT sequence. ISMRM 2005.
11. Harris RK. *Nuclear Magnetic Resonance Spectroscopy, a Physicochemical View*. London: Pitman Books Limited; 1983.
12. Levitt MH. *Spin Dynamics, Basics of Nuclear Magnetic Resonance*. Chichester: John Wiley & Sons; 2001.



13. Matson GB. An integrated program for amplitude-modulated RF pulse generation and re-mapping with shaped gradients. *Magnetic Resonance Imaging* 1994;12:1205-1225.
14. Pegg DT, Bendall MR. Theory of localized polarization transfer. *Magnetic Resonance in Medicine* 1985;2:453-468.
15. Shaka AJ, Keeler J, Freeman R. Evaluation of a New Broadband Decoupling Sequence: WALTZ-16. *Journal of Magnetic Resonance* 1983;53:313-340.
16. Keltner JR, Wald LL, Frederick BdB, Renshaw PF. *In vivo* detection of GABA in human brain using a localized double-quantum filter technique. *Magnetic Resonance in Medicine* 1997;37:366-371.
17. Keltner JR, Wald LL, P.J. L, Chen YCI, Matthews RT, Kuestermann EHGK, Baker JR, Rosen BR, Jenkins BG. A localized double-quantum filter for the *in vivo detection of brain glucose*. *Magnetic Resonance in Medicine* 1998;39:651-656.
18. Trabesinger AH, Weber OM, Duc CO, Boesiger P. Detection of glutathione in the human brain *in vivo* by means of double quantum coherence filtering. *Magnetic Resonance in Medicine* 1999;42:283-289.
19. Choi C, Coupland NJ, Hanstock CC, Ogilvie CJ, Higgins ACM, Gheorghiu D, Allen PS. Brain gamma-aminobutyric acid measurement by proton double-quantum filtering with selective J rewinding. *Magnetic Resonance in Medicine* 2005;54:272-279.
20. Thompson RB, Allen PS. Sources of variability in the response of coupled spins to the PRESS sequence and their potential impact on metabolite quantification. *Magnetic Resonance in Medicine* 1999;41:1162-1169.

# Chapter 7

## Direct $^{13}\text{C}$ Observation II: Modified INEPT

### 7.1 Introduction

$^{13}\text{C}$  NMR spectroscopy has proven to be a powerful method of determining metabolic flux rates in both human and animal brain. Time courses of  $^{13}\text{C}$  label incorporation into metabolic products have been acquired either by directly observing the  $^{13}\text{C}$  signal, or by indirectly detecting the  $^{13}\text{C}$ -coupled protons in order to benefit from the higher sensitivity of the  $^1\text{H}$  nucleus. The Insensitive Nuclei Enhanced by Polarization Transfer (INEPT) pulse sequence (1) allows for the detection of enhanced  $^{13}\text{C}$  signal, and also forms the building block of the Heteronuclear Single Quantum Coherence (HSQC) indirect detection sequence (2). In INEPT (see §6.2.1 in the previous chapter), the  $^{13}\text{C}$  inversion pulse responsible for heteronuclear proton antiphase magnetization forming immediately prior to the polarization transfer pulses ( $1/2J_{\text{CH}}$  seconds after proton excitation), is applied simultaneously with the proton refocussing pulse. Both the INEPT and the HSQC sequences have been modified to allow three dimensional localization by replacing the proton hard pulses with slice selective pulses (3,4). These pulses along with their gradients were incorporated into the sequence by separating the  $^{13}\text{C}$  inversion pulse and the  $^1\text{H}$  refocussing pulse in time which allowed the proton echo time to be longer than  $1/2J_{\text{CH}}$  ( $\approx 3.7$  ms for the  $\text{C}_3$  and  $\text{C}_4$  of Glu). The pulses were separated based on product operator calculations which ignored proton homonuclear coupling. The results indicate that whether the  $^{13}\text{C}$  inversion pulse is placed  $1/4J_{\text{CH}}$  ( $J_{\text{CH}}$  is the heteronuclear scalar coupling constant) after the first proton pulse or  $1/4J_{\text{CH}}$  prior to the third proton pulse (the proton echo time) of the modified INEPT sequence, optimal heteronuclear coupling evolution will occur for polarization transfer (3,4).

The purpose of this report is to use glutamate (Glu) at 3.0 T to illustrate, both numerically and experimentally, how concurrent strong homonuclear proton coupling affects the heteronuclear scalar coupling evolution that takes place during the preparatory period of such a modified INEPT sequence. It is demonstrated how the  $^{13}\text{C}$  signal

obtained by a refocussed INEPT sequence (5) incorporating the modifications of Ref. (3) is echo time dependent and is significantly different when the  $^{13}\text{C}$  inversion pulse is applied towards the beginning of the proton spin echo compared to when it is applied towards its end, with the signal from the former case being higher. This shows the relevance of taking homonuclear proton coupling into account when modifying or designing new  $^{13}\text{C}\{^1\text{H}\}$  pulse sequences, as failure to do so can lead to sequences that yield less than optimal  $^{13}\text{C}$  signal.

## **7.2 Methods**

### **7.2.1 Numerical method**

At 3.0 T, four of the five protons of Glu are strongly-coupled and the molecule can therefore be represented as an AMNPQ spin system, where A, MN, and PQ, are the protons bonded to the  $\text{C}_2$ ,  $\text{C}_3$  and  $\text{C}_4$  carbons, respectively. The numerical analysis was carried out in MATLAB after extending a program that carries out density matrix calculations for proton only systems (6-8) to incorporate a  $^{13}\text{C}$  nucleus, denoted by X to indicate weak coupling to the protons, into the Hamiltonian operator and thereby predict the composite effects of both homonuclear and heteronuclear scalar coupling on the spin responses (9). The Hamiltonian operator involves all the interactions under which spin evolution can occur, namely, those due to the static field, the radiofrequency (RF) fields, the gradient field, as well as the chemical shielding, and the scalar coupling interactions. The numerical method of evaluating the response of the spins to a particular pulse sequence, evaluates the time dependent density matrix by solving the Liouville-von Neumann equation. A more detailed description of the numerical method of analysis (see chapter 3) along with the chemical shift and scalar coupling constants used (Table 4.1) in the calculations are given in Ref. (9).

### **7.2.2 Experimental methods**

Figure 7.1(a) displays the basic INEPT sequence. Heteronuclear proton antiphase coherence formed  $1/2J_{\text{CH}}$  after proton excitation, is converted into enhanced heteronuclear  $^{13}\text{C}$  antiphase coherence by the simultaneous  $90^\circ$  pulses on both channels.

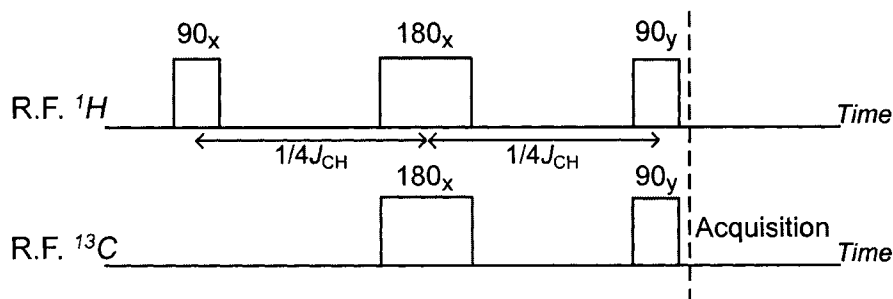
The timing modifications introduced to the INEPT sequence by Watanabe et al (3) in order to allow slice selective pulses to be incorporated is shown in Fig. 7.1(b). Figure 7.1(c) illustrates the refocussed version of the sequence of 7.1(b) optimized for a CH<sub>2</sub> molecular group (10). The extra delay is required to allow the formation of <sup>13</sup>C in-phase magnetization and thus proton decoupling during acquisition can be applied. In the work reported here, the sequence of Fig. 7.1(c) was implemented, once with the <sup>13</sup>C inversion pulse applied 1/4J<sub>CH</sub> after proton excitation, and once with it applied 1/4J<sub>CH</sub> prior to the echo time, TE, for the purpose of demonstrating that when strong proton homonuclear coupling exists along with heteronuclear coupling, the final signal yield depends on the location of the <sup>13</sup>C inversion pulse and on the TE employed. Since this was the sole objective of this report, no localization was incorporated into the numerical and experimental analysis, and all pulses used were hard pulses. The sequences employed 200 μs and 150 μs, <sup>1</sup>H and <sup>13</sup>C 90° pulses, respectively. The delay 1/4J<sub>CH</sub> was set to 1.85 ms (J<sub>CH</sub> ≈ 135 Hz for C<sub>3</sub> and C<sub>4</sub> of Glu), and a repetition time, TR, of 3 seconds was used. WALTZ-16 proton decoupling was applied during acquisition (11), and to eliminate off-resonance effects, a 16 step phase cycling scheme shown in Table 7.1 was implemented (12).

All experiments were carried out in an 80 cm bore, 3.0 T magnet system (Magnex Scientific PLC, Abingdon, UK) using a SMIS spectrometer (Surrey Medical Imaging Systems PCL, Guildford, UK) with a home-built 7 cm diameter <sup>1</sup>H birdcage RF coil, and a 3.5 cm diameter <sup>13</sup>C surface coil. To verify the numerical calculations, a 2 cm diameter aqueous-solution phantom of pH ≈ 7 was made, containing 35 mM labelled Glu with the C<sub>3</sub> carbon enriched 99% in <sup>13</sup>C (Sigma-Aldrich Canada). Although [1-<sup>13</sup>C] glucose yields labelled C<sub>4</sub>-Glu on the first round of the TCA cycle, the idea we wish to convey can be illustrated by C<sub>3</sub>-labelled Glu which is readily available commercially.

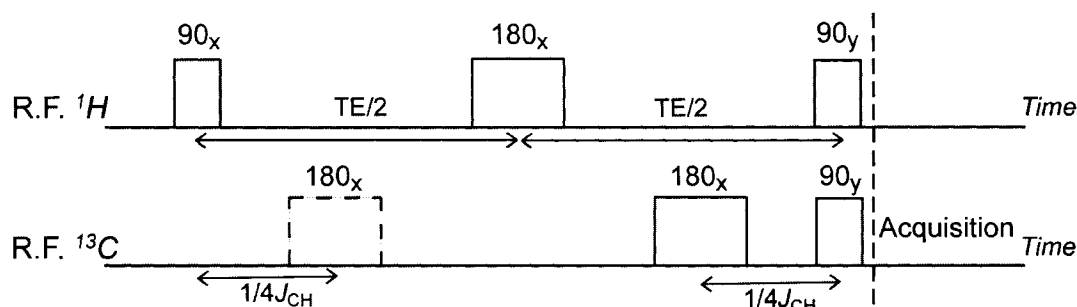
Table 7.1: Phase cycling scheme implemented in the modified INEPT sequence.

Phase of first $^1\text{H}$ 180° pulse	Phase of $^{13}\text{C}$ 90° pulse	Phase of second $^1\text{H}$ 90° pulse	Phase of second $^{13}\text{C}$ 180° pulse	Receiver phase
x	y	y	x	x
x	-y	y	x	-x
-x	y	y	-x	x
-x	-y	y	-x	-x
x	-y	-y	x	x
x	y	-y	x	-x
-x	-y	-y	-x	x
-x	y	-y	-x	-x
x	-y	y	y	x
x	y	y	y	-x
-x	-y	y	y	x
-x	y	y	y	-x
x	y	-y	-y	x
x	-y	-y	-y	-x
-x	y	-y	-y	x
-x	-y	-y	-y	-x

**(a) Basic INEPT**



**(b) Modified INEPT**



**(c) Modified Refocussed INEPT**

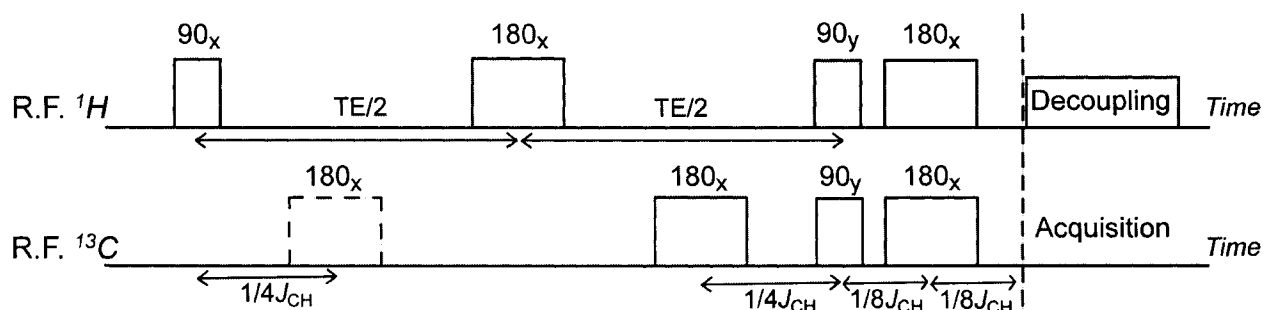


Figure 7.1: The basic INEPT sequence is shown in (a), while (b) illustrates the timing modifications introduced to the sequence in order to allow replacement of all proton hard pulses with slice selective pulses (3). Reference (3) states that the  $^{13}\text{C}$  inversion pulse can be placed at either of the two indicated positions in time but experimentally the pulse was applied  $1/4J_{\text{CH}}$  prior to the third proton pulse as shown by the solid lines. A refocussed INEPT sequence incorporating the timing modifications is shown in (c), where essentially a delay of  $1/4J_{\text{CH}}$  (optimum for  $\text{CH}_2$  molecular groups) is added to the end of the sequence of (b) to allow  $^{13}\text{C}$  heteronuclear antiphase coherences to evolve into in-phase magnetization. The two versions of this sequence (corresponding to the two  $^{13}\text{C}$  pulse locations) were implemented for the work presented here.

## 7.3 Results

The response of  $^{13}\text{C}_3\text{-Glu}$  to the sequence of Fig. 7.1(c) was numerically calculated at a number of echo times within the practical range of 10-30 ms, first when the  $^{13}\text{C}$  inversion pulse was applied  $1/4J_{\text{CH}}$  after the first proton pulse, and then when it was applied  $1/4J_{\text{CH}}$  prior to the third proton pulse. The simple  $^{13}\text{C}$  Lorentzian resonance lines acquired under conditions of proton decoupling, made it simple to compare relative intensities. The results of the analysis are displayed in Fig. 7.2, with all intensities normalized to the maximum intensity (TE = 10 ms, solid curve). The calculations were experimentally verified by applying the two sequences to the 99%  $^{13}\text{C}_3\text{-Glu}$  phantom at five different echo times. These experimental data points are displayed in Fig. 7.2. Apart from the fact that the  $^{13}\text{C}$  signal decreases with increasing echo time, it is interesting to observe that at every echo time, the signal is lower when the  $^{13}\text{C}$  inversion pulse is applied  $1/4J_{\text{CH}}$  prior to third proton pulse. For example, at TE = 30 ms, the resulting signal drops by more than 50% when the  $^{13}\text{C}$  inversion pulse is moved towards the end of the sequence.

The intensity of the  $^{13}\text{C}$  signal is governed by the amount of heteronuclear proton antiphase coherence,  $2M_xX_z$  and  $2N_xX_z$ , present immediately prior to the two  $90^\circ$  pulses responsible for polarization transfer. From Fig. 7.3, it can be seen, as expected, that the expectation values of these two coherences follow the same trend of the curves in Fig. 7.2. The decrease in these antiphase coherences with increasing echo time can be explained by loss of signal to other Glu protons via polarization transfer as a result of strong homonuclear coupling (9,13). What is not so intuitive is why the signal is lower at a given echo time when the  $^{13}\text{C}$  inversion pulse is applied  $1/4J_{\text{CH}}$  prior to the third proton pulse. This also is a result of strong coupling between the MN and PQ protons. In the absence of this coupling, only the terms  $M_y$  and  $N_y$  formed by the proton excitation pulse are responsible for the creation of antiphase coherences  $2M_xX_z$  and  $2N_xX_z$  at the echo time. Although in the presence of strong coupling,  $M_y$  and  $N_y$  are still major contributors to the formation of these antiphase coherences, the two in-phase terms  $P_y$  and  $Q_y$  also add a significant contribution as shown in Fig. 7.4.

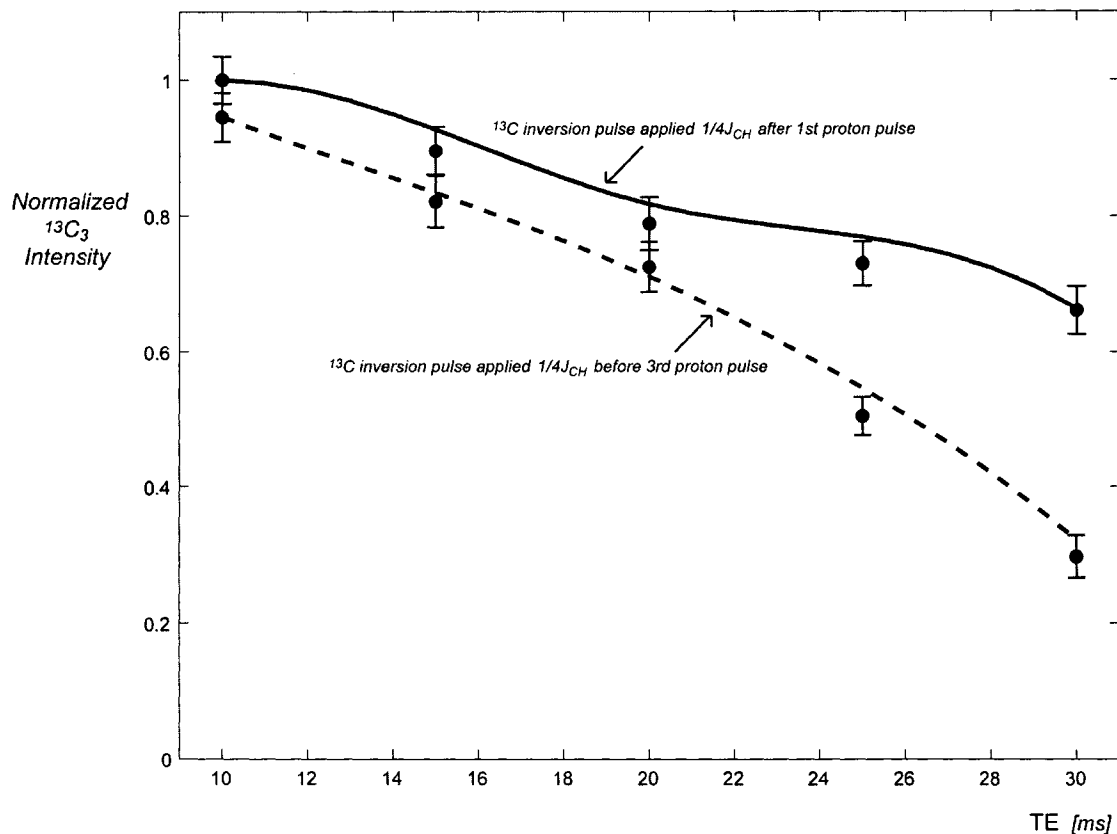


Figure 7.2: The two curves demonstrate how the  $^{13}\text{C}$  signal varies as a function of the echo time of the sequence of Fig. 7.1(c). Moreover, the significant reduction in signal yield when the  $^{13}\text{C}$  inversion pulse is applied towards the end of the spin echo is apparent. The data confirm the temporal variation determined numerically. The error bars are half the peak-to-peak noise.

Figure 7.4 shows the expectation value of  $2M_x X_z$  at different echo times arising from the evolution of  $M_y$ ,  $N_y$ ,  $P_y$ , and  $Q_y$ . The curves for  $\langle 2N_x X_z \rangle$  are quite similar. The contribution from the  $^{13}\text{C}$ -coupled MN protons is the same whether the  $^{13}\text{C}$  inversion pulse is applied towards the beginning of the echo time or towards its end; however the situation is different for the non- $^{13}\text{C}$ -coupled PQ protons. Considering the situation where no  $^{13}\text{C}$  inversion pulse is applied, the in-phase terms  $P_y$  and  $Q_y$  evolve during the echo time and form some positive amount of  $2M_x X_z$  at the echo time by polarization transfer as a result of strong coupling with the MN protons (9). When the  $^{13}\text{C}$  inversion pulse is applied  $1/4J_{\text{CH}} \approx 1.85$  ms after the proton excitation pulse,  $P_y$  and  $Q_y$  have not evolved much during this short delay and thus their evolution over the echo time is only slightly perturbed by the  $^{13}\text{C}$  pulse, as is illustrated in Fig. 7.4 by the dashed curve. However, if the  $^{13}\text{C}$  pulse is applied 1.85 ms before the third proton pulse, then by this



time  $P_y$  and  $Q_y$  have evolved into some heteronuclear terms which will be affected by the  $^{13}\text{C}$  inversion pulse. The inversion of these terms causes the net amount of  $2M_xX_z$  that is formed at TE to drop in comparison to the previous situations. Therefore, because  $P_y$  and  $Q_y$  contribute more to the amount of  $2M_xX_z$  (as shown in Fig. 7.4) and  $2N_xX_z$  when the  $^{13}\text{C}$  inversion pulse is applied towards the beginning of the sequence (because it perturbs the evolution less), the  $^{13}\text{C}$  signal is higher in this situation.

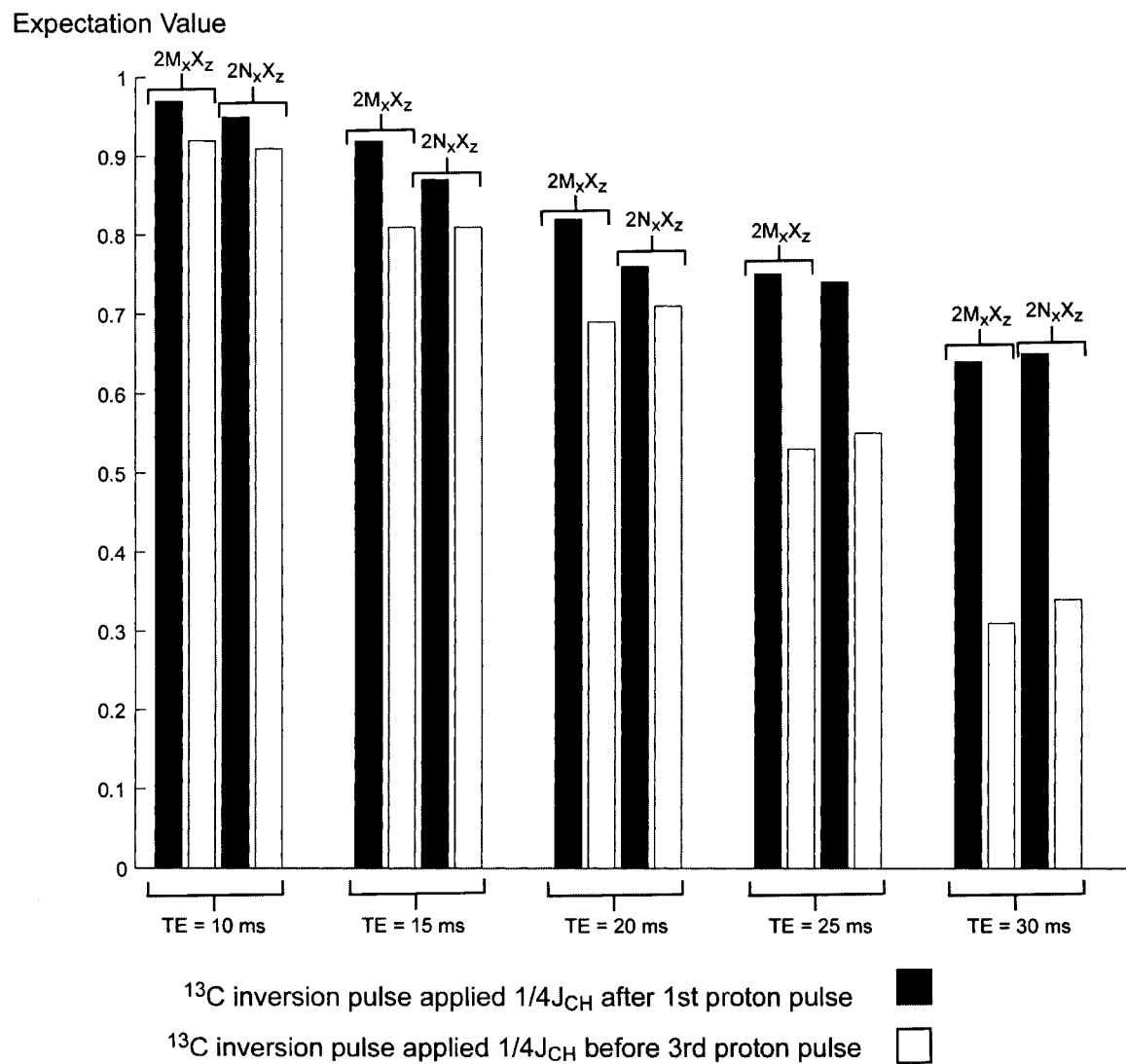


Figure 7.3: A diagram showing the expectation value of the two critical antiphase coherences,  $2M_xX_z$  and  $2N_xX_z$ , immediately prior to the third proton pulse in the sequence of Fig. 7.1(c). These coherences are responsible for the generation of  $^{13}\text{C}$  signal by polarization transfer. The expectation value of each coherence is shown at five different echo times, and how their values change depending on echo time and on the location of the  $^{13}\text{C}$  inversion pulse.

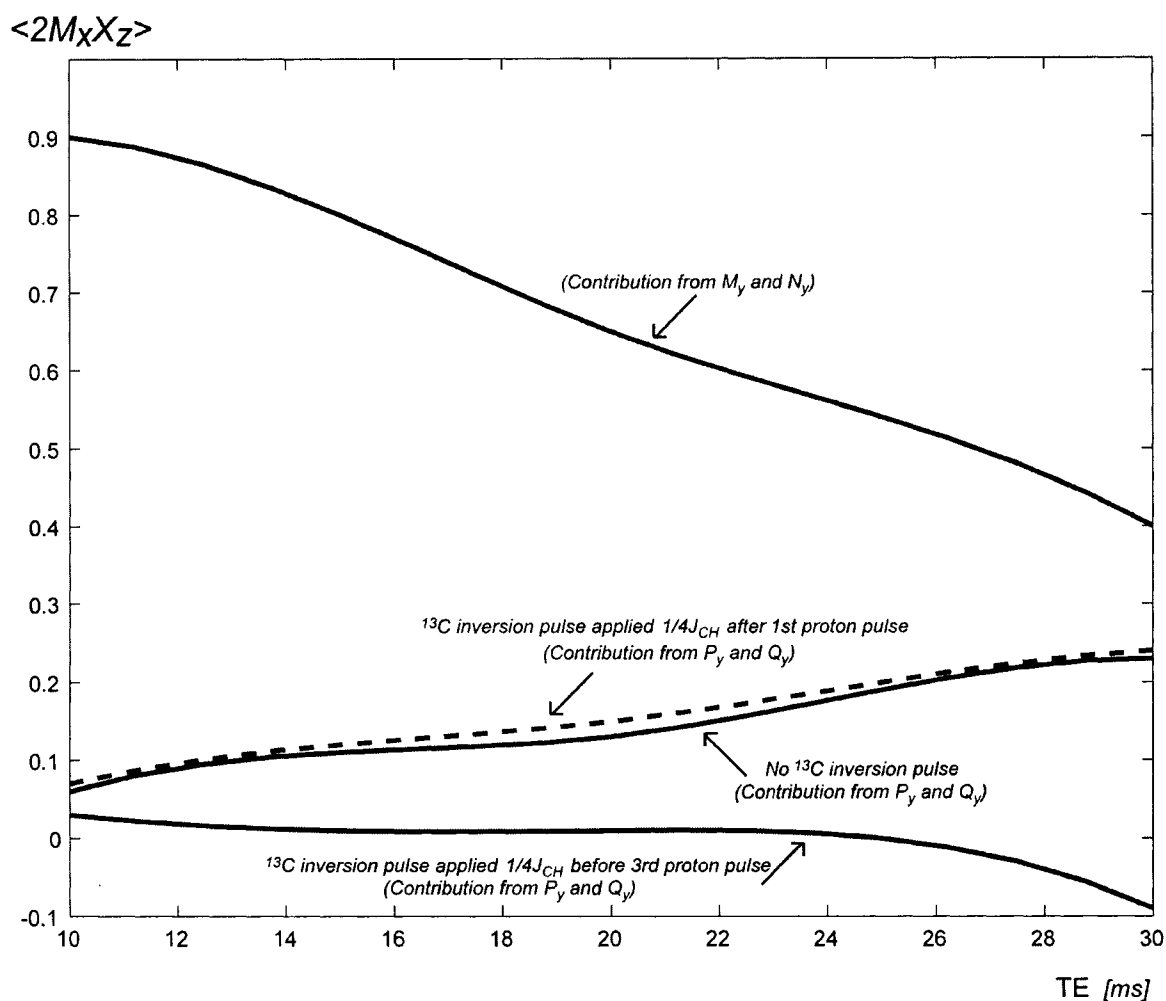


Figure 7.4: The curves show the contributions of the in-phase terms  $M_y$ ,  $N_y$ ,  $P_y$  and  $Q_y$ , present immediately after the excitation pulse, to the formation of the heteronuclear proton antiphase term  $2M_x X_z$  at the echo time, TE, of the sequence of Fig. 7.1(c).  $M_y$  and  $N_y$  form the same amount of  $2M_x X_z$  regardless of the location of the  $^{13}\text{C}$  inversion pulse. However,  $P_y$  and  $Q_y$ , contribute a larger positive amount when the  $^{13}\text{C}$  pulse  $1/4J_{\text{CH}}$  after the first proton pulse.

## 7.4 Discussion

The preceding analysis has demonstrated that when  $^{13}\text{C}$ -coupled protons are also involved in strong coupling with other protons, the expected  $^{13}\text{C}$  responses derived from calculations that consider only the heteronuclear coupling are significantly altered. This is because the strong homonuclear proton coupling indirectly links the  $^{12}\text{C}$ -bonded protons to the  $^{13}\text{C}$  spin. We illustrated this by evaluating the response of  $^{13}\text{C}_3\text{-Glu}$  at 3.0 T to a refocussed INEPT sequence incorporating the timing modifications made by Watanabe et al (3), shown in Fig. 7.1(c). Product operator calculations excluding proton

homonuclear coupling show that whether the  $^{13}\text{C}$  inversion pulse of INEPT is placed  $1/4J_{\text{CH}}$  after the first proton pulse or  $1/4J_{\text{CH}}$  prior to the third proton pulse, the desired proton heteronuclear antiphase coherences for polarization transfer will be formed at TE. We numerically calculated and experimentally verified that the  $^{13}\text{C}_3\text{-Glu}$  signal intensity is not the same in the two situations. In fact, over the range of echo times 10-30 ms, the signal is lower when the  $^{13}\text{C}$  pulse is applied towards the end of the sequence. This is because the  $P_y$  and  $Q_y$  terms contribute (by being strongly-coupled to the MN protons) less to the formation of the critical antiphase coherences for polarization transfer,  $2M_xX_z$  and  $2N_xX_z$ , in this situation. Reference (3) implemented the modified sequence at 2.0 T with a TE = 20 ms and chose to place the  $^{13}\text{C}$  inversion pulse  $1/4J_{\text{CH}}$  prior to the third proton pulse. Our numerical calculations show that had the  $^{13}\text{C}$  pulse been placed  $1/4J_{\text{CH}}$  after the first proton pulse instead, the signals from  $^{13}\text{C}_3\text{-Glu}$  and from  $^{13}\text{C}_4\text{-Glu}$  would have been approximately 31 % and 26% larger, respectively. This is a significant improvement in signal and is larger than the 15% improvement at 3.0 T for the same echo time (see Fig. 7.2) because at 2.0 T the protons of Glu are more strongly-coupled. The higher signal again results from the larger positive contributions to  $2M_xX_z$  and  $2N_xX_z$  from  $P_y$  and  $Q_y$  (for  $^{13}\text{C}_3\text{-Glu}$ ) and to  $2P_xX_z$  and  $2Q_xX_z$  from  $M_y$  and  $N_y$  (for  $^{13}\text{C}_4\text{-Glu}$ ) at TE when the  $^{13}\text{C}$  inversion pulse is applied towards the beginning of the pulse sequence.

## **7.5 Conclusion**

We have shown by means of a numerical solution of the equation of motion of the nuclear spin density matrix, and through phantom experiments on an aqueous  $^{13}\text{C}$ -labelled glutamate solution at 3.0 T, that when the proton spins of a metabolite molecule are strongly scalar coupled (for example in glutamate and glutamine) the interaction between the strong homonuclear proton coupling and the weak heteronuclear coupling causes a perturbation that alters the expected  $^{13}\text{C}$  response. By specifically addressing a modified INEPT sequence, we have shown how a consequence of sequence design that fails to incorporate the effects of strong homonuclear proton coupling can be a loss in signal that could otherwise be avoided.

## **7.6 References**

1. Morris G, Freeman R. Enhancement of nuclear magnetic resonance signals by polarization transfer. *Journal of the American Chemical Society* 1979;101:760-762.
2. Ruiz-Cabello J, Vuister GW, Moonen CT, Van Gelderen P, Cohen JS, Van Zijl PCM. Gradient-Enhanced Heteronuclear Correlation Spectroscopy. Theory and Experimental Aspects. *Journal of Magnetic Resonance* 1992;100:282-302.
3. Watanabe H, Ishihara Y, Okamoto K, Oshio K, Kanamatsu T, Tsukada Y. *In Vivo* Localized  $^{13}\text{C}$  Spectroscopy Using Modified INEPT and DEPT. *Journal of Magnetic Resonance* 1998;134:214-222.
4. Watanabe H, Ishihara Y, Okamoto K, Oshio K, Kanamatsu T, Tsukada Y. 3D Localized  $^1\text{H}$ - $^{13}\text{C}$  Heteronuclear Single-Quantum Coherence Correlation Spectroscopy In Vivo. *Magnetic Resonance in Medicine* 2000;43:200-210.
5. Morris GA. Sensitivity enhancement in nitrogen-15 NMR: polarization transfer using the INEPT pulse sequence. *Journal of American Chemical Society* 1980;102:428-429.
6. Thompson RB, Allen PS. The response of metabolites with coupled spins to the STEAM sequence. *Magnetic Resonance in Medicine* 2001;45:955-965.
7. Thompson RB, Allen PS. A new multiple quantum filter design procedure for use on strongly coupled spin systems found in vivo: its application to glutamate. *Magnetic Resonance in Medicine* 1998;39:762-771.
8. Thompson RB, Allen PS. The role of the N-acetylaspartate multiplet in the quantification of brain metabolites. *Biochemistry and Cell Biology* 1998;76:497-502.
9. Yahya A, Allen PS. Effect of strong homonuclear proton coupling on localized  $^{13}\text{C}$  detection using PRESS. *Magnetic Resonance in Medicine* 2005;54:1340-1350.
10. Levitt MH. *Spin Dynamics, Basics of Nuclear Magnetic Resonance*. Chichester: John Wiley & Sons; 2001.
11. Shaka AJ, Keeler J, Freeman R. Evaluation of a New Broadband Decoupling Sequence: WALTZ-16. *Journal of Magnetic Resonance* 1983;53:313-340.
12. Shenker KV, Von Philipsborn W. Off-resonance effects and their compensation in the multiple-pulse sequences INEPT, DEPT, and INADEQUATE. *Journal of Magnetic Resonance* 1986;66:219-229.

13. Thompson RB, Allen PS. Sources of variability in the response of coupled spins to the PRESS sequence and their potential impact on metabolite quantification. *Magnetic Resonance in Medicine* 1999;41:1162-1169.

# Chapter 8

## Concluding Remarks

The research conducted in this thesis is the first part of a research programme the aim of which is to develop the means to acquire dynamic measurements of neurotransmitter metabolism by  $^{13}\text{C}$  MRS. These techniques of measuring the dynamics of metabolism will then be employed in collaborative projects with psychiatrists and neurologists on patients with brain disorders or diseases. Two objectives of this thesis were to enhance the volume range and sensitivity of dynamic  $^{13}\text{C}$  measurements by designing, constructing, and testing a dual-tuned  $^{13}\text{C}/^1\text{H}$  RF coil based on the half-birdcage design. The advantage of this design is that it provides uniform RF fields at both the  $^{13}\text{C}$  and  $^1\text{H}$  frequencies over deeper regions of the brain, relevant in the study of neurological disorders, than the commonly used RF probe design. The third objective of this thesis was to improve the specificity of dynamic  $^{13}\text{C}$  measurements by calculating numerically and experimentally verifying the effect of simultaneous strong homonuclear proton coupling and weak heteronuclear coupling on the outcome of a number of  $^{13}\text{C}/^1\text{H}$  double resonance sequences, two of which we designed to be single-shot sequences. Previously, when implementing and predicting spin responses to these sequences, it has been assumed that the only interaction taking place is the heteronuclear coupling.

### 8.1 A $^{13}\text{C}/^1\text{H}$ Dual-Tuned Half-Birdcage Coil

The commonly used RF coil system in  $^{13}\text{C}$  studies is the design of Adriany and Gruetter (1) which consists of three separate surface coils (one resonating at the  $^{13}\text{C}$  frequency and the other two operating in quadrature at the  $^1\text{H}$  frequency). This RF probe is efficient primarily over the occipital region of the brain. Because the deeper midbrain area is the region of interest for the study of neurological disorders, we investigated an alternative RF coil design that would be able to excite and receive signal from regions deeper than the occipital lobe, namely, a dual-tuned, half-birdcage coil. The half birdcage was designed and constructed as a low-pass network and it was tuned in such a

way that each of the two resonant modes arise from alternate birdcage conductors. The two frequency modes were isolated by placing trap circuits resonating at the frequency to be blocked in every leg. The Adriany-Gruetter design was also implemented and the performance of the two coils was compared. It was found that the half-birdcage provided a more uniform field at both frequencies, which is an important feature because it allows control over the spin dynamics. Specifically, from proton axial and sagittal images of an oil phantom obtained with the half-birdcage it was found that the approximately linear rate of decay of the field was reduced to  $\approx 66\%$  of that of the Adriany-Gruetter design. The half birdcage was also found to be more sensitive than the  $(10 \times 10 \text{ cm}^2)$   $^{13}\text{C}$  surface coil at depths greater than 5 cm, i.e. regions deeper than the occipital lobe that are of neurological relevance. For example, the SNR of a spectrum obtained with the half-birdcage from an acetic acid phantom located 7 cm above the coil surface (along its axis) was  $\approx 37\%$  higher than the corresponding SNR obtained with the  $^{13}\text{C}$  surface coil.

## **8.2 The Effect of Simultaneous Strong Homonuclear Proton Coupling and Heteronuclear Coupling on Spin Responses**

To enhance the specificity of dynamic  $^{13}\text{C}$  measures, the effect of simultaneous strong homonuclear proton coupling and heteronuclear coupling on spin responses to a number of  $^{13}\text{C}/^1\text{H}$  double resonance pulse sequences, both direct and indirect, was numerically calculated using glutamate at 3.0 T as an illustrative example. Although the metabolites detected by  $^{13}\text{C}$  MRS such as Glu and Gln exhibit strong homonuclear proton coupling at clinical field strengths, this interaction has previously been neglected in the analysis of  $^{13}\text{C}/^1\text{H}$  double resonance sequences. In the work presented in this thesis, it was found that when the  $^{13}\text{C}$ -coupled protons are also involved in strong homonuclear coupling with adjacent protons possibly bonded to  $^{12}\text{C}$ , the presence of the  $^{13}\text{C}$  spin is conveyed to those  $^{12}\text{C}$ -bonded protons through the strong homonuclear interactions. This inter-proton communication manifests itself in both ‘direct’ and ‘indirect’ experiments to observe  $^{13}\text{C}$ . In indirect  $^{13}\text{C}$  detection (where the  $^{13}\text{C}$ -coupled protons are observed), this linkage between  $^{12}\text{C}$ -bonded protons and the  $^{13}\text{C}$  spin was found to result in incomplete elimination of signal from  $^{12}\text{C}$ -bonded protons and a reduction in signal from  $^{13}\text{C}$ -coupled

protons. For example, the response of  $^{13}\text{C}_4\text{-Glu}$  to a PRESS-localized POCE sequence,  $\text{TE}_1 = 10\text{ ms}$ ,  $\text{TE}_2 = 15\text{ ms}$ , yielded  $\approx 79\%$  PQ signal with a residual 19% MN signal. Thus the multiplets that change during  $^{13}\text{C}$  incorporation are not specific to the  $^{13}\text{C}$  incorporation sites, and lack of anticipation of this can lead to potential cross-contamination on the order of several tens of percent between  $\text{Glu } ^{13}\text{C}_4$  and  $^{13}\text{C}_3$  measures. To determine neurotransmitter cycle rates accurately this cross-contamination resulting from the effects of strong proton coupling needs to be incorporated into the kinetic model.

For direct, but polarization-transfer-enhanced detection of  $^{13}\text{C}$ , e.g. using DEPT (2), it was shown that the consequence of the proton homonuclear coupling was a reduction in signal enhancement. Although the enhancement factors of the basic DEPT sequence for  $^{13}\text{C}_3\text{-}$  and  $^{13}\text{C}_4\text{-Glu}$  are only reduced by  $\approx 10\%$ , this reduction in enhancement is exacerbated when DEPT is combined with PRESS localization on protons. The enhancement factors then become strong functions of the PRESS echo times,  $\text{TE}_1$  and  $\text{TE}_2$ , and are reduced for  $^{13}\text{C}_2\text{-}$ ,  $^{13}\text{C}_3\text{-}$ , and  $^{13}\text{C}_4\text{-Glu}$ , but not equally. For example, the signal yield of  $^{13}\text{C}_3\text{-Glu}$  to the PRESS-localized DEPT sequence with  $\text{TE}_1 = \text{TE}_2 = 10\text{ ms}$  is approximately 74% whereas that of  $^{13}\text{C}_4\text{-Glu}$  is about 84%. To avoid quantification errors in  $^{13}\text{C}$  fractional enrichments the different enhancement factors for the individual  $^{13}\text{C}$  sites need to be taken into account.

### **8.3 Future Directions**

The research programme initiated by the work reported in this thesis will be extended in order to reach our ultimate objective of providing the appropriate tools for conducting patient studies of brain diseases in collaboration with psychiatrists and neurologists. To date  $^{13}\text{C}$  MRS has been primarily exploited to evaluate the metabolism of normal brain. In the hands of the spectroscopy group at Yale University it has been extremely successful in providing metabolic data that has within the last decade totally changed our understanding of amino acid neurotransmitter metabolism and the synergistic role of neurons and astrocytes (3-8). Often the region of study has been restricted to the occipital lobe by the use of surface coils. For brain diseases, however, the areas of interest are the midbrain region and the prefrontal cortex, for the study of



neurological disorders and psychiatric disorders, respectively. The half-birdcage coil design described in this thesis can be extended to a three-quarters birdcage in order to further improve uniformity and sensitivity to relevant interior brain structures, while still remaining patient friendly.

To further comply with patient tolerance, experiment durations will need to be constrained to less than one hour as opposed to experiments conducted on normal volunteers that can last approximately two hours in length in order to encompass steady state measurements. Brian Ross's group at the Huntington Medical Research Institutes in Pasadena have also recognized the patient-tolerance time constraint (9-11). Our aim is to identify unambiguous dynamic measures of metabolic abnormalities within the pre-steady-state enrichment phase. Such an identification will likely be sought through an evaluation of the coupled simultaneous equations of the neuron-astrocyte metabolic model (4).

For the localized detection of the  $^{13}\text{C}$  signal by either indirect or direct means, optimal pulse sequences will need to be designed to mitigate the effects of strong homonuclear proton coupling discussed in this thesis. The numerical quantum mechanical methods employed in this thesis will be utilized to manipulate the RF pulse designs and the time intervals between them so that the most desirable coherence distribution can be created at the onset of acquisition. For indirect  $^{13}\text{C}$  detection, the localization sequences will need to be optimized to mitigate non-incorporation-site specific contamination due to strong proton coupling, in addition to separating target peaks from any contaminating background peaks, particularly Glu from Gln (12-14). For the direct detection of  $^{13}\text{C}$ , loss of polarization transfer enhancement will need to be reduced by investigating alternative (single-shot) localization sequences that suffer less degradation of in-phase single quantum coherences than PRESS. For example, one possibility is the LASER (15) sequence which exploits adiabatic pulses and minimizes inter-pulse intervals to limit strong coupling evolution.

## **8.4 References**

1. Adriany G, Gruetter R. A half-volume coil for efficient proton decoupling in humans at 4T. *Journal of Magnetic Resonance* 1997;125:178-184.
2. Doddrell DM, Pegg DT, Bendall MR. Distortionless enhancement of NMR signals by polarization transfer. *Journal of Magnetic Resonance* 1982;48:323-327.
3. Magistretti PJ, Pellerin L, Rothman DL, Shulman RG. Energy on Demand. *Science* 1999;283:496-497.
4. Mason GF, Rothman DL, Behar KL, Shulman GI. NMR determination of the TCA cycle rate and alpha-ketoglutarate exchange rate in rat brain. *Journal of Cerebral Blood Flow and Metabolism* 1992;12:434-447.
5. Rothman DL. Studies of metabolic compartmentation and glucose transport using *in vivo* MRS. *NMR in Biomedicine* 2001;14:149-160.
6. Mason GF, Pan JW, Chu WJ, Newcomer BR, Zhang Y, Orr R, Hetherington HP. Measurement of the tricarboxylic acid cycle rate in human grey and white matter in-vivo by  $^1\text{H}$ - $^{13}\text{C}$  magnetic resonance spectroscopy at 4.1T. *Journal of Cerebral Blood Flow and Metabolism* 1999;19:1179-1188.
7. Sibson N, Dhankar A, Mason G, Rothman D, Behar K, Shulman G. Stoichiometric coupling of brain glucose metabolism and glutamatergic neuronal activity. *Proc Natl Acad Sci USA* 1998;95:316-321.
8. Sibson NR, Shen J, Mason GF, Rothman DL, Behar KL, Shulman RG. Functional energy metabolism: In vivo  $^{13}\text{C}$ -NMR spectroscopy evidence for coupling of cerebral glucose consumption and glutamatergic neuronal activity. *Developmental Neuroscience* 1998;20:321-330.
9. Lin AP, Shic F, Enriquez C, Ross BD. Reduced glutamate neurotransmission in patients with Alzheimer's disease-an in vivo  $^{13}\text{C}$  magnetic resonance study. *Magnetic Resonance Materials in Physics, Biology and Medicine* 2003;16:29-42.
10. Bluml S, Moreno-Torres A, Ross BD.  $[1-^{13}\text{C}]$  Glucose MRS in Chronic Hepatic Encephalopathy in Man. *Magnetic Resonance in Medicine* 2001;45:981-993.
11. Moreno A, Ross BD, Bluml S. Direct determination of the *N*-acetyl-L-aspartate synthesis rate in the human brain by  $^{13}\text{C}$  MRS and  $[1-^{13}\text{C}]$  glucose infusion. *Journal of Neurochemistry* 2001;77:347-350.
12. Choi C, Coupland NJ, Hanstock CC, Ogilvie CJ, Higgins ACM, Gheorghiu D, Allen PS. Brain gamma-aminobutyric acid measurement by proton double-

quantum filtering with selective J rewinding. *Magnetic Resonance in Medicine* 2005;54:272-279.

13. Thompson RB, Allen PS. A new multiple quantum filter design procedure for use on strongly coupled spin systems found in vivo: its application to glutamate. *Magnetic Resonance in Medicine* 1998;39:762-771.
14. Kim H, Wild JM, Allen PS. Strategy for the spectral filtering of myo-inositol and other strongly coupled spins. *Magnetic Resonance in Medicine* 2004;51:263-272.
15. Garwood M, DelaBarre L. The return of the frequency sweep: Designing adiabatic pulses for contemporary NMR. *Journal of Magnetic Resonance* 2001;153:155-177.

# Appendix 1

## Transformation Tables for Two Weakly-Coupled Spins

### Precession in $B_o$

The Zeeman Hamiltonian is given by  $H_Z = -\gamma\hbar B_o I_z = -\hbar\omega_1 I_z$ . For a single spin state  $I_\alpha$ , where  $\alpha = x, y, \text{ or } z$ , solutions to the equation  $\exp(-iH_Z t / \hbar) I_\alpha \exp(iH_Z t / \hbar)$  are given by the transformation table below.

$$\begin{aligned} I_x &\xrightarrow{\omega_1 t} I_x \cos(\omega_1 t) + I_y \sin(\omega_1 t) \\ I_y &\xrightarrow{\omega_1 t} I_y \cos(\omega_1 t) - I_x \sin(\omega_1 t) \\ I_z &\xrightarrow{\omega_1 t} I_z \end{aligned} \quad (\text{A1.1})$$

### Rotation by RF pulses

The solutions to  $\exp(-iH_{RF} t / \hbar) I_\alpha \exp(iH_{RF} t / \hbar)$ , where  $H_{RF} = -\gamma\hbar B_1 I_\lambda = -\hbar\omega_1 I_\lambda$ , and  $\lambda = x, y, \text{ or } z$ , are given by the following table where  $\beta = -\omega_1 t$ .

$$\begin{aligned} I_x &\xrightarrow{\beta I_x} I_x \\ I_y &\xrightarrow{\beta I_x} I_y \cos(\beta) + I_z \sin(\beta) \\ I_z &\xrightarrow{\beta I_x} I_z \cos(\beta) - I_y \sin(\beta) \\ I_x &\xrightarrow{\beta I_y} I_x \cos(\beta) - I_z \sin(\beta) \\ I_y &\xrightarrow{\beta I_y} I_y \\ I_z &\xrightarrow{\beta I_y} I_z \cos(\beta) + I_x \sin(\beta) \end{aligned} \quad (\text{A1.2})$$

### Evolution under J Coupling

If we have two weakly coupled spins I and S, then the spin system can be in the following states,:  $A = I_\alpha, S_\alpha, 2I_\alpha S_\lambda$ , or  $2S_\alpha I_\lambda$  where  $\alpha = x, y$ , or  $z$  and  $\lambda = x, y$ , or  $z$ . The scalar coupling Hamiltonian is given by  $H_J = \hbar J_{IS} I_z S_z / 2\pi$ . Solutions to  $\exp(-iH_J t / \hbar) A \exp(iH_J t / \hbar)$  are given by the table below.

$$\begin{aligned}
 I_x &\xrightarrow{2\pi J_{IS} I_z S_z t} I_x \cos(\pi J_{IS} t) + 2I_y S_z \sin(\pi J_{IS} t) \\
 I_y &\xrightarrow{2\pi J_{IS} I_z S_z t} I_y \cos(\pi J_{IS} t) - 2I_x S_z \sin(\pi J_{IS} t) \\
 I_z &\xrightarrow{2\pi J_{IS} I_z S_z t} I_z \\
 \\ 
 2I_x S_z &\xrightarrow{2\pi J_{IS} I_z S_z t} 2I_x S_z \cos(\pi J_{IS} t) + I_y \sin(\pi J_{IS} t) \\
 2I_y S_z &\xrightarrow{2\pi J_{IS} I_z S_z t} 2I_y S_z \cos(\pi J_{IS} t) - I_x \sin(\pi J_{IS} t) \\
 2I_z S_z &\xrightarrow{2\pi J_{IS} I_z S_z t} 2I_z S_z \\
 \\ 
 2I_x S_x &\xrightarrow{2\pi J_{IS} I_z S_z t} 2I_x S_x \\
 2I_x S_y &\xrightarrow{2\pi J_{IS} I_z S_z t} 2I_x S_y \\
 2I_y S_y &\xrightarrow{2\pi J_{IS} I_z S_z t} 2I_y S_y
 \end{aligned} \tag{A1.3}$$

# Appendix 2

## The Difference in Evolution between Strongly-Coupled spins and Weakly-Coupled Spins

To illustrate the difference in spin evolution between a weakly-coupled spin pair and a strongly-coupled spin pair we first consider the response of an uncoupled spin I to a simple spin-echo sequence with total echo time TE. Relaxation is ignored in all of the following analysis. Figure A2.1 illustrates that the expectation value of in-phase transverse magnetization for the spin,  $I_y$ , will be unity for any choice of sequence timing.

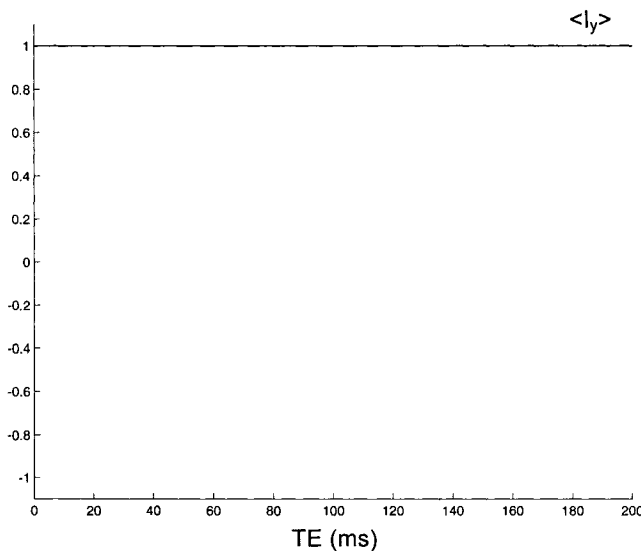


Figure A2.1: The response of an uncoupled spin I to a simple spin-echo experiment at a number of different echo times. Because the spin experiences no scalar coupling interactions, the expectation value for in-phase transverse magnetization,  $I_y$ , is unity for any choice of echo time. Relaxation is ignored.

If we now consider a weakly-coupled AX spin system,  $J_{AX} = 15.4\text{Hz}$ ,  $\delta_1 = 2.54\text{ppm}$ , and  $\delta_2 = 30\text{ppm}$  ( $J_{AX} / \delta \approx 0.004$  where  $\delta$  is the chemical shift difference of the two spins) then the response of the spins varies sinusoidally as a function of TE and depends on the scalar coupling constant as illustrated in Fig. A2.2, where for simplicity only the response of spin A is displayed. The variations can be understood by referring to the transformation tables in Appendix 1.

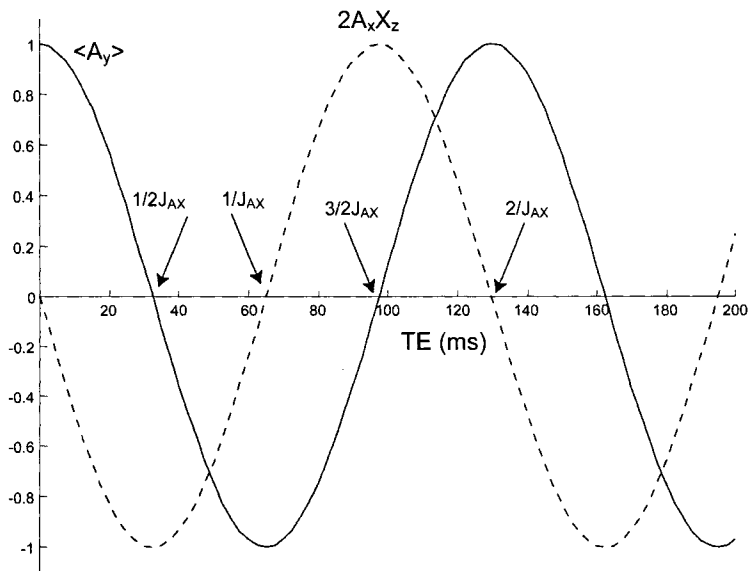


Figure A2.2: The response of the A spin of a weakly-coupled AX spin system to a simple spin-echo experiment at a number of different echo times. In phase  $A_y$  and antiphase  $2A_xX_z$  magnetization oscillate periodically. The in-phase term is maximized at TEs that are integral multiples of  $1/J_{AX}$ , and the antiphase term is maximized at TEs that are half integrals of  $1/J_{AX}$ .

Finally, the evolution of a strongly-coupled AB spin system,  $J_{AB} = 15.4\text{Hz}$ ,  $\delta_1 = 2.54\text{ppm}$ , and  $\delta_2 = 2.79\text{ppm}$  ( $J_{AX} / \delta \approx 0.5$  where  $\delta$  is the chemical shift difference of the two spins) is calculated. This time the response is much more complicated because for strongly-coupled spins, in-phase terms of one spin can evolve into antiphase terms of the other spin and vice versa. Because of the polarization transfer that takes place between the two spins, the magnetization can evolve into many different coherences. The pattern of evolution is no longer easy to predict and the response depends on both the scalar coupling constant and the chemical shift difference between the two spins.

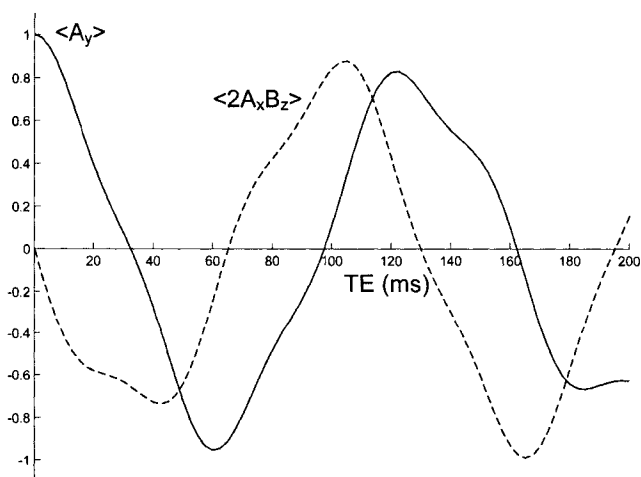


Figure A2.3: The response of the A spin of a strongly-coupled AB spin system to a simple spin-echo experiment at a number of different echo times. In-phase  $A_y$  magnetization oscillates; however, it never regains its maximum intensity because it not only evolves into antiphase  $2A_xB_z$  (shown by the dashed line) but also into B in-phase and antiphase terms shown in the next two figures.

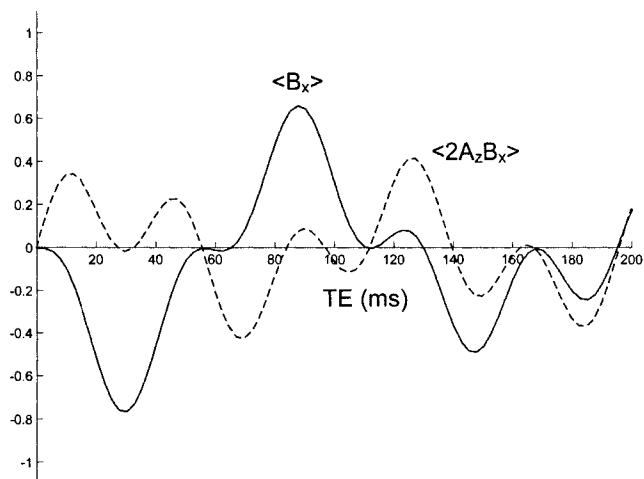


Figure A2.4: The evolution of in-phase  $B_x$  and antiphase  $2A_z B_x$  magnetization terms of a strongly-coupled AB spin system with increasing echo times of a spin echo experiment. These terms evolved by polarization transfer from the A spin via the strong homonuclear coupling.

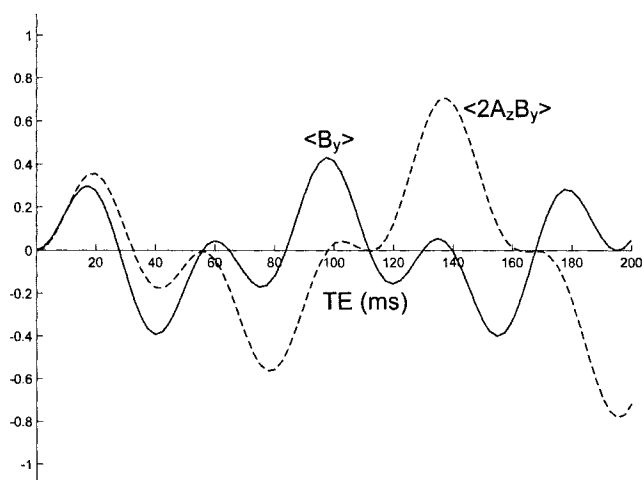


Figure A2.5: The evolution of in-phase  $B_y$  and antiphase  $2A_z B_y$  magnetization terms of a strongly-coupled AB spin system with increasing echo times of a spin echo experiment. These terms evolved by polarization transfer from the A spin via the strong homonuclear coupling.



# Appendix 3

## Transformation Under the Influence of a Gradient Pulse

The gradient Hamiltonian is given by  $H_{Grad} = -\gamma\hbar\vec{G}\cdot\vec{r}I_z$ , where  $G$  is the gradient strength, and  $r$  the displacement vector measured from the origin of the linear gradient field. It is simplest to write the transformation equations in terms of the raising and lowering operators,  $I_+$  and  $I_-$ .

$$\begin{aligned} I_+ &\xrightarrow{\gamma G r I_z} I_+ \exp(-i\gamma\vec{G}\cdot\vec{r}t) \\ I_- &\xrightarrow{\gamma G r I_z} I_- \exp(i\gamma\vec{G}\cdot\vec{r}t) \end{aligned} \quad (\text{A3.1})$$

As an example if we consider a double quantum coherence term of a homonuclear spin system  $I_S$ , we see that the gradient pulse encodes the coherence according to its order.

$$I_S \xrightarrow{\gamma G r I_z} \xrightarrow{\gamma G r I_z} I_S \exp(2i\gamma\vec{G}\cdot\vec{r}t) \quad (\text{A3.2})$$

# Appendix 4

## Evolution of an IS Heteronuclear Spin System during the ge-HMQC Sequence

Using the transformation tables given in Appendices 1 and 3, the evolution of an IS spin system (I denotes a  $^1\text{H}$  spin and S denotes a  $^{13}\text{C}$  spin) to the basic ge-HMQC sequence shown in Fig. , with  $G_3$  set to zero, can be followed. The initial density operator is given by  $I_z + S_z$ . Since  $^{13}\text{C}$  spins directly excited by the  $^{13}\text{C}$  pulse will be dephased by the coherence selection gradients, the term  $S_z$  will be ignored. The length of the gradient is  $\tau$ .

$$I_z \xrightarrow{90_x(^1\text{H})} -I_y \xrightarrow{1/2J_{IS}} 2I_xS_y \quad (\text{A4.1})$$

$$2I_xS_y \xrightarrow{90_x(^{13}\text{C})} -2I_xS_y \quad (\text{A4.2})$$

$$-2I_xS_y = -2\left(\frac{I_+ + I_-}{2}\right)\left(\frac{S_+ - S_-}{2i}\right) = \frac{-1}{2i}(I_+S_+ - I_+S_- + I_-S_+ - I_-S_-) \quad (\text{A4.3})$$

$$\begin{aligned} \frac{-1}{2i}(I_+S_+ - I_+S_- + I_-S_+ - I_-S_-) \xrightarrow{G_1} & \frac{-1}{2i}[I_+S_+ \exp(-i\gamma_I G_1 \tau - i\gamma_S G_1 \tau) \\ & - I_+S_- \exp(-i\gamma_I G_1 \tau + i\gamma_S G_1 \tau) \\ & + I_-S_+ \exp(i\gamma_I G_1 \tau - i\gamma_S G_1 \tau) \\ & - I_-S_- \exp(i\gamma_I G_1 \tau + i\gamma_S G_1 \tau)] \end{aligned} \quad (\text{A4.4})$$

$$\begin{aligned} & \frac{-1}{2i}[I_+S_+ \exp(-i\gamma_I G_1 \tau - i\gamma_S G_1 \tau) - I_+S_- \exp(-i\gamma_I G_1 \tau + i\gamma_S G_1 \tau) \\ & + I_-S_+ \exp(i\gamma_I G_1 \tau - i\gamma_S G_1 \tau) - I_-S_- \exp(i\gamma_I G_1 \tau + i\gamma_S G_1 \tau)] \xrightarrow{180_x(^1\text{H})} \\ & \frac{-1}{2i}[I_-S_+ \exp(-i\gamma_I G_1 \tau - i\gamma_S G_1 \tau) - I_-S_- \exp(-i\gamma_I G_1 \tau + i\gamma_S G_1 \tau) \\ & + I_+S_+ \exp(i\gamma_I G_1 \tau - i\gamma_S G_1 \tau) - I_+S_- \exp(i\gamma_I G_1 \tau + i\gamma_S G_1 \tau)] \end{aligned} \quad (\text{A4.5})$$

$$\begin{aligned}
& \frac{-1}{2i} [I_- S_+ \exp(-i\gamma_I G_1 \tau - i\gamma_S G_1 \tau) - I_- S_- \exp(-i\gamma_I G_1 \tau + i\gamma_S G_1 \tau) \\
& \quad + I_+ S_+ \exp(i\gamma_I G_1 \tau - i\gamma_S G_1 \tau) - I_+ S_- \exp(i\gamma_I G_1 \tau + i\gamma_S G_1 \tau)] \xrightarrow{G_2} \\
& \frac{-1}{2i} [I_- S_+ \exp(-i\gamma_I G_1 \tau - i\gamma_S G_1 \tau + i\gamma_I G_2 \tau - i\gamma_S G_2 \tau) \\
& \quad - I_- S_- \exp(-i\gamma_I G_1 \tau + i\gamma_S G_1 \tau + i\gamma_I G_2 \tau + i\gamma_S G_2 \tau) \\
& \quad + I_+ S_+ \exp(i\gamma_I G_1 \tau - i\gamma_S G_1 \tau - i\gamma_I G_2 \tau - i\gamma_S G_2 \tau) \\
& \quad - I_+ S_- \exp(i\gamma_I G_1 \tau + i\gamma_S G_1 \tau - i\gamma_I G_2 \tau + i\gamma_S G_2 \tau)] \tag{A4.6}
\end{aligned}$$

Letting  $a = \gamma_I G_1 \tau, b = \gamma_S G_1 \tau, c = \gamma_I G_2 \tau, \text{ and } d = \gamma_S G_2 \tau$ , the right hand side of Eq. (A4.6) can be rewritten as

$$\begin{aligned}
& \frac{-1}{2i} [I_- S_+ \exp(-ia - ib + ic - id) \\
& \quad - I_- S_- \exp(-ia + ib + ic + id) \\
& \quad + I_+ S_+ \exp(ia - ib - ic - id) \\
& \quad - I_+ S_- \exp(ia + ib - ic + id)] \tag{A4.7}
\end{aligned}$$

$$\begin{aligned}
& \frac{-1}{2i} [I_- S_+ \exp(-ia - ib + ic - id) - I_- S_- \exp(-ia + ib + ic + id) \\
& \quad + I_+ S_+ \exp(ia - ib - ic - id) - I_+ S_- \exp(ia + ib - ic + id)] \xrightarrow{90^\circ (^{13}\text{C})} \\
& \frac{-1}{2i} \{ I_- [\frac{1}{2}(S_- + S_+) + iS_z] \exp(-ia - ib + ic - id) \\
& \quad - I_- [\frac{1}{2}(S_- + S_+) - iS_z] \exp(-ia + ib + ic + id) \\
& \quad + I_+ [\frac{1}{2}(S_- + S_+) + iS_z] \exp(ia - ib - ic - id) \\
& \quad - I_+ [\frac{1}{2}(S_- + S_+) - iS_z] \exp(ia + ib - ic + id) \} \tag{A4.8}
\end{aligned}$$

If  $a + b - c + d = 0$  then the middle two terms on the right hand side of the above equation will be dephased, whereas if  $a - b - c - d = 0$  then the first and last terms will be dephased. Solving  $a + b - c + d = 0$ , implies that  $\gamma_I G_1 \tau + \gamma_S G_1 \tau - \gamma_I G_2 \tau + \gamma_S G_2 \tau = 0$ .

$$\begin{aligned}
& \Rightarrow \frac{G_1}{G_2} = \frac{\gamma_I - \gamma_S}{\gamma_I + \gamma_S} \\
& \Rightarrow \frac{G_1}{G_2} \approx \frac{3}{5} \tag{A4.9}
\end{aligned}$$

Similarly solving  $a - b - c - d = 0$  yields  $\Rightarrow \frac{G_1}{G_2} \approx \frac{5}{3}$ . The analysis will be pursued with

$\Rightarrow \frac{G_1}{G_2} \approx \frac{3}{5}$ , and by considering only the terms involving  $S_z$  which will contribute to observable magnetization.

$$\begin{aligned}
 & \frac{-1}{2i} \{iI_- S_z \exp(-ia - ib + ic - id) \\
 & \quad + iI_+ S_z \exp(ia + ib - ic + id)\} \xrightarrow{1/2J_{IS}} \\
 & \frac{-1}{2i} \{i(2iS_z I_-)S_z + i(-2iS_z I_+)S_z\} \tag{A4.10} \\
 & = \frac{-1}{2i} (-2I_- S_z S_z + 2I_+ S_z S_z) \\
 & = \frac{-1}{2i} \left( \frac{-I_-}{2} + \frac{I_+}{2} \right) = \frac{-I_y}{2}.
 \end{aligned}$$

Thus the outcome of the sequence is half the signal from  $^{13}\text{C}$ -coupled protons. Any signal from  $^{12}\text{C}$ -bonded protons will be dephased by the gradients.